
THE UNIVERSITY *of* EDINBURGH

# Cavitation Dynamics of Surface Nanobubbles

*Duncan Dockar*


*Doctor of Philosophy*

THE UNIVERSITY OF EDINBURGH

2020

# Abstract

Cavitation is the fluid phenomenon where a bubble of gas or vapour can spontaneously form in a liquid in response to a local drop or variation in pressure. Unlike bubbles formed from other types of processes such as boiling, cavitation bubbles can become highly unstable due to their sensitivity to fluctuations in pressure. These cavitation bubbles can very rapidly expand many orders of magnitude in size, in what is sometimes referred to as "explosive" growth; when they collapse, they often release a high-speed liquid jet, which can lead to pitting and erosion if directed onto a solid surface. Cavitation is a problem often encountered in engineering, such as in turbomachinery, where the repeated formation and collapse of these bubbles can cause major structural damage. More recently, engineers have aimed to exploit the high-speed jet dynamics during cavitation bubble collapse for novel applications at the nano to microscale, such as in surface cleaning, diagnostics and cancer treatment.

Around 20 years ago, spherical-cap shaped nanoscale bubbles were found to be able to exist long-term on solid substrates under certain experimental conditions. These newly discovered "surface nanobubbles" were of scientific interest as their resistance to dissolution seemed to contradict previous Epstein-Plesset theory on the general unstable diffusive equilibrium of bubbles. They were confirmed to be diffusively stable if the surrounding liquid was supersaturated with dissolved gas, and the substrate had surface heterogeneities, such as roughness or chemical patterning, such that the bubble's three-phase contact line was pinned to the substrate. This contact line pinning resulted in a constant contact radius (CCR) mode of growth unique to surface nanobubbles, where the radius of curvature would begin to decrease during expansion, contrary to the radial growth typically found in spherical bubbles.

Surface nanobubbles initially seemed to provide a convenient explanation for the heterogeneous nucleation of cavitation bubbles. However, early experiments found that they did not respond as expected to pressure drops intended to induce cavitation growth. Most of the classical analyses for cavitation assume a spherical bubble immersed in an infinite liquid. This results in models which are mathematically simple and usually suitable for most applications, however, surface nanobubbles have a spherical cap shape and typically grow with a pinned contact line, and so the classical spherical bubble models were found not to be suitable for these cases.

The research in this thesis investigates the cavitation dynamics of pinned surface nanobubbles using Molecular Dynamics (MD) simulations. The cavitation threshold for unstable growth, the growth rate and oscillation dynamics, and finally the collapse of pinned surface nanobubbles are simulated and investigated further here. Results are compared to the corresponding classical spherical bubble equations, and improved models are proposed, where appropriate, to account

for their different observed cavitation dynamics.

Most of the surface nanobubbles' unique behaviour arises from their pinned mode of growth. The surface tension contribution across the liquid-gas interface (the Laplace pressure) is found to increase during growth of the surface nanobubble due to the CCR mode of growth, which is the opposite effect to spherical bubbles. Surface nanobubbles are found to be able to resist pressures many mega-Pascals (MPa) lower than that predicted by the classical Blake threshold equation for unstable growth of spherical bubbles. A new model is derived to more accurately predict this cavitation threshold for surface nanobubbles, which captures their spherical cap shape and pinned growth. The proposed model suggests that the smallest surface nanobubbles can be resistant to pressures as low as $-28\,\mathrm{MPa}$. Critical discussions are also made on experimental findings that suggested that $300\,\mathrm{nm}$ bubbles were resistant to pressures of $-6\,\mathrm{MPa}$.

The classical Rayleigh-Plesset equation for spherical bubbles is modified to be more suitable for surface nanobubbles, accounting for their spherical cap shape and Laplace pressure variation, which could accurately predict their growth rate and oscillation dynamics. The natural frequency of surface nanobubbles is also found through linearised analyses of this newly derived growth rate model. The proposed natural frequency is compared to other models for bubbles, such as the classical Minnaert frequency, and was found to be better at capturing the surface nanobubble's oscillation dynamics. The MD simulation set-up is also critically examined for accurately modelling the pressure variations acting on the surface nanobubbles.

The surface nanobubbles are found to collapse less violently than spherical bubbles, since the cavitation jets have less time to develop before impacting the solid surface. Despite the collapsing surface nanobubbles causing less damage, the resulting pit shapes were found to be similar to the pit shapes from spherical bubble collapse, with the perimeters of the pits typically scaling with the maximum bubble size before collapse. The internal gas phase is found to decelerate the jet formation, and reduce the resulting damage, through comparisons to the collapse of vapour bubbles. No toroidal rebounding bubbles were observed in the collapsing surface nanobubbles, which is a common occurrence in spherical bubble collapse, as the jets do not flow outward from the impact centre after impact on the substrates.

The findings presented here should provide an improved understanding for the design of microfluidic engineering processes where the cavitation dynamics of pinned surface nanobubbles are to be utilised.

# Lay Summary

Bubbles are a surprisingly complex problem for engineers in fluid mechanics, due to their sensitivity to a variety of factors. For example, boiling is a process in which bubbles can spontaneously form in a liquid by increasing temperature, typically past 100 °C for water. Cavitation (which this thesis is concerned with) is similar to boiling, except bubbles are formed by a drop in pressure. A simple example of cavitation is when opening a fizzy drink, and watching all the bubbles form as the bottle is de-pressurised. What makes this difference important is that pressures can change a lot more rapidly than temperature. Boiling water usually takes a few minutes, whereas pressure can change in milliseconds, such as from a ship propeller spinning many hundreds of revolutions per minute. The result is that cavitation bubbles are often unstable, in that they experience "explosive" or very rapid growth, and they also collapse violently. It is this violent collapse that causes the most problems for engineers, as this recurring process can cause wear and even structural failure of pumps and propellers if uncontrolled. However, with improved understanding of the growth and collapsing phases, there are many beneficial proposed applications of cavitation, such as "ultrasonic cleaning" of high precision devices, medical diagnostics, non-invasive cancer treatment, and waste-water treatment.

One of the reasons for the currently limited understanding of cavitation is that it occurs so rapidly, and occurs for such small bubble sizes, that properly observing the full process is very difficult in either experiments or computer modelling. Bubbles can form at the nanoscale, grow to a millimetre (equivalent to one million times their initial size), and then collapse, all within a matter of milliseconds. Several mathematical models exist to predict the bubble's cavitation behaviour; however, they are simplistic and rely on the assumption that the bubble remains spherical throughout. This is usually suitable for "free" bubbles which are completely surrounded by liquid, however, are less realistic for cavitation near a solid surface, where most of the problems associated with cavitation occur.

This thesis specifically investigates the dynamics of "surface nanobubbles", which are hemispherical bubbles, measured in millionths of millimetres across, that rest on solid surfaces. They are special because classical fluid mechanics would expect these bubbles to dissolve almost instantly, due to the increased effects of surface tension from their size, however, they have been shown to exist for days to even weeks at a time. Due to their extremely small size, they were only confirmed to exist around 20 years ago through sophisticated experiments. The reason for this stability was found to be due to the stabilising effect of the solid, on which the bubble rests, as well as a nearby *supersaturation*, where there is a surplus of dissolved gas within the surrounding liquid. Due to the solid, the bubbles grow in such a way that the surface

tension effects work to prevent excessive growth, which is the opposite to normal bubbles, and it is found in this thesis that this strongly affects their cavitation dynamics.

In this research, it is shown that the typical mathematical models for cavitation do not work for these surface nanobubbles, due to their unique shape and form of growth. Instead, updated equations are proposed to correctly account for these effects, and comparisons are made to Molecular Dynamics (MD) simulations. This technique accurately models the individual motions of atoms, where many of the complex fluid phenomena influencing bubble behaviour arise naturally within the simulations, which would otherwise need to be manually incorporated in other modelling methods. The disadvantage is that MD requires a lot of computational resources, such as the use of a supercomputer, with results only obtained in the nanometre and nanosecond range. While these modelled bubble sizes may appear irrelevant to most practical situations, cavitation bubbles begin their unstable growth at these sizes, and this is arguably one of the most important areas to be investigating.

This thesis covers the unstable growth phase of surface nanobubbles, in which it is found that surface nanobubbles are more resistant to drops in pressure compared to equivalently sized spherical bubbles. Then the growth rate and resonance of these bubbles are modelled. Surface nanobubbles are found to have a higher resonant frequency than spherical bubbles, which could provide further insight into the diagnostics application which rely on this behaviour. Finally, the surface nanobubbles are found to cause less damage during collapse than spherical bubbles, due to the nearby solid surface restricting their collapsing shape.

# Acknowledgements

I would first like to thank our late Professor Jason Reese, who passed away in March 2019. Jason was a role model for how to conduct myself in an academic setting, and I appreciate he always made time for us, despite his busy schedule. I would not be in this position without the early backing from Jason, and I feel privileged to have been able to share briefly in his impressive career.

I would also like to thank my supervisors: Matthew, for the continued support from my Master's degree and into the beginning of my academic career, and Livio, who had the difficult task of having to quickly familiarise himself with my research (and hectic work-style!). Again, thanks to all our colleagues and collaborators in Edinburgh, Warwick, and Daresbury laboratory for their encouraging feedback, and general sounding board for some of my more ambitious research ideas.

Finally, I would like to thank my close friends and family for their support over the last four years. The topic of bubbles always seems to draw in some enthusiastic questions from people, and is a constant reminder of how lucky I have been to study such an interesting topic.

# Declaration

I declare that this thesis was composed by myself, that the work contained herein is my own except where explicitly stated otherwise in the text, and that this work has not been submitted for any other degree or professional qualification except as specified.

**Duncan Dockar**

# Contents

# Figures and Tables

## Figures

## Tables

# List of Acronyms

**AFM** Atomic Force Microscopy
**CCA** constant contact angle
**CCR** constant contact radius
**CFD** Computational Fluid Dynamics
**DoF** degree of freedom
**FCC** face-centred cubic
**FFT** Fast Fourier Transform
**HPC** High Performance Computer
**LJ** Lennard-Jones
**MEMS** Micro-Electro-Mechanical Systems
**MD** Molecular Dynamics
**PDMS** polydimethylsiloxane
**SW** Stillinger-Weber
**VOF** Volume of Fluid
**LCA** low contact angle
**HCA** high contact angle

# Chapter 1

# Introduction

Cavitation is the fluid phenomenon where a bubble of gas or vapour can spontaneously form within a liquid in response to a local drop in pressure. These cavitation bubbles may appear harmless, with maximum sizes of the order of millimetres, however, when they collapse, they can release a supersonic jet of liquid, which, if directed on a solid substrate, can cause pitting and wear. This behaviour is accentuated by oscillating pressure fields and as such cavitation is a significant problem for turbomachinery, e.g. turbines and ship propellers, where the repeated formation and collapse of these bubbles over many cycles can cause major structural damage (Brennen, 2013; Fivel *et al.*, 2015). Not only do these damaged surfaces increase hydrodynamic drag, but there is also a vicious cycle where the rough surfaces and cracks that form from collapsing bubbles are preferential nucleation sites for more cavitation bubbles to form, which further accelerates cavitation erosion.

Certainly, if uncontrolled, cavitation can be a problem for the engineering of fluid systems. However, at the nano to microscale, there are novel proposed applications of controlled or targeted cavitation, such as in surface cleaning, and cancer treatment and diagnostics, which harness the concentrated power of the liquid jet (Brems *et al.*, 2014; Lukianova-Hleb *et al.*, 2014, 2016; Martynov *et al.*, 2011; Stride and Saffari, 2003). While some promising results have already been obtained in these applications, cavitation is still not a fully understood problem. This is mainly because bubbles, in general, are sensitive to a wide range of external conditions, such as temperature, concentration of the external liquid, gravitational effects, and pressure (as in cavitation). Small changes to these conditions can have a significant impact on their dynamics and general stability. Similarly, the effects of confinement, particularly in nano and microfluidic systems, can influence bubble oscillation dynamics. Fortunately for this work, dynamics due to cavitation tend to occur at the fastest time-scales (Brennen, 2013), which make this behaviour easy to isolate.

There are three stages to cavitation growth:

1. instability, where the bubble becomes unstable due to pressure imbalances at the liquid-gas interface, typically from a reduction in the external liquid pressure;
2. rapid growth and oscillation, where the bubble has already become unstable and can increase in size many orders of magnitude; and

3. collapse, where the bubble rapidly and violently decreases in size, usually as the external liquid pressure is restored to its original ambient conditions.

While the collapsing stage of the bubble is most commonly associated with cavitation, all three stages will be considered in this thesis and the term "cavitation" will be used to describe any bubble growth dynamics governed by the instantaneous imbalance of pressures across the bubble surface.

Elsewhere, around the turn of the millennium, scientists were performing Atomic Force Microscopy (AFM) experiments on liquid covered hydrophobic surfaces and observing unusual "stepwise" and hysteresis features in force measurements (Lohse and Zhang, 2015b; Theodorakis and Che, 2019). While some speculated that these could be simple artefacts of AFM measurement, there was growing evidence to suggest the presence of long-lived spherical cap-shaped "interfacial gaseous" domains, which simply became known as "surface nanobubbles" (Ishida *et al.*, 2000; Lohse and Zhang, 2015b; Lou *et al.*, 2000; Theodorakis and Che, 2019; Tyrrell and Attard, 2001; Zhang *et al.*, 2008). However, this presented a problem for fluid dynamics; the classical understanding of diffusive bubble equilibrium (the stability governed by gas concentrations within the external liquid), predicts that *all* bubbles should be in unstable diffusive equilibrium. Furthermore, the predicted life-time of a nanoscale bubble is of the order of microseconds; yet these experiments demonstrated that surface nanobubbles had lifetimes of hours, up to several days at a time. Further research confirmed that these were the hypothesised nanobubbles, along with improved models of their diffusive stability, which critically relied on pinning of the three-phase contact line, i.e. the line where the solid, gas and liquid phases all meet.

Rounding all these points together, it had long been known that cavitation preferentially occurred on solids, i.e. heterogeneous nucleation, and more recently surface nanobubbles have been shown to exist stably on solid surfaces, rather than dissolving away like bubbles in the bulk. So, it would be natural to assume that these surface nanobubbles act as the nucleation sites for cavitation. However, when this hypothesis was tested, these surface nanobubbles did not respond as expected in cavitation experiments (Borkent *et al.*, 2007). The reason for this anomalous behaviour, as well as the discrepancy from the diffusive equilibrium theory, is that most classical analyses of bubbles assume a perfectly spherical bubble within an infinite liquid field. The spherical cap-shaped surface nanobubbles have been observed to grow differently to bulk spherical bubbles; most notably the pinned contact line alters the surface tension effects during growth, which has increased prominence at the nanoscale. Also, the presence of the solid surface on which the bubble rests influences the dynamics of the multiphase fluids, such that a radially symmetric infinite surrounding liquid cannot be assumed, as is common in the classical models for cavitation. It is found that cavitation dynamics are strongly dependent on the inertial and viscous contributions from the liquid, as well as the balance of gas, liquid and surface tension pressure contributions across the bubble interface, and so it becomes necessary to

account for these differences in bubble shape and liquid flow conditions for surface nanobubble cavitation.

Given that the effects of cavitation are more widely observed on solids, e.g. in heterogeneous nucleation and pitting erosion, these classical models will need to be re-examined so they are suitable for more realistic cavitation events involving surface nanobubbles. This thesis aims to investigate the common discrepancies between cavitation growth of surface nanobubbles and the classical understanding which typically assumes spherical bubbles; where appropriate, new models for their unique behaviour will be proposed. The research in this thesis will roughly outline the lifetime of a cavitating surface nanobubble: from the threshold for instability, to rapid growth and oscillatory effects, and finally to eventual collapse.

The scientific work in this thesis is purely theoretical and simulation-based, however, references will be made to experimental works, which elaborate on some of the unusual behaviour exhibited by surface nanobubbles. The majority of the simulations are performed using Molecular Dynamics (MD) software, giving an unparalleled view into atomic processes which cannot be achieved by traditional experimental or simulation techniques. The disadvantage of MD is its relatively high computational cost which limits its use to only nanoscale systems and theoretical timescales, and so these simulations are used as the reference for validating the improved models of surface nanobubble cavitation dynamics.

## 1.1 Thesis outline

The remainder of this thesis will cover the following:

**Chapter 2 – Background** gives an overview of the previous research in bubble dynamics, including cavitation and surface nanobubble stability. Some of the key concepts relevant to the physics of bubbles will also be introduced.

**Chapter 3 – Molecular Dynamics Simulation** introduces the principle of Molecular Dynamics (MD), the primary simulation technique employed in this research. The various models used in this work will be discussed, including some standard calibration techniques and benchmark tests.

**Chapter 4 – Cavitation Threshold of Surface Nanobubbles** investigates how the threshold for unstable growth differs between surface nanobubbles and equivalent spherical bubbles in the bulk. A new model for this cavitation threshold is proposed and compared to the classical Blake threshold, with a critical discussion of the effects of contact line pinning on the mechanical stability of surface nanobubbles.

**Chapter 5 – Oscillation and Growth Dynamics of Surface Nanobubbles** examines the commonly used Rayleigh-Plesset equation for spherical bubbles, and critically evaluates its

relevance for surface nanobubbles. A new model is proposed for surface nanobubble cavitation growth, drawing on similar concepts to the Rayleigh-Plesset equation, although accounting for the effects of the pinned contact line, and spherical cap-shaped volume.

**Chapter 6 – Shock-Induced Collapse of Surface Nanobubbles** investigates the differences between the shock wave induced collapses of spherical bubbles and surface nanobubbles on a nearby solid substrate. Both fluid and solid responses will be analysed, with a detailed study of the liquid jet and resulting pitting damage for different cases.

**Chapter 7 – Summary and Concluding Remarks** concludes the main findings of this work, with discussions on the implications for surface nanobubbles in some of the proposed applications of cavitation.

# Chapter 2

# Background

## 2.1 Bubbles

A bubble can be defined as a volume of gas or vapour entrapped within a fluid interface[1], as shown in Figure 2.1. We are generally used to seeing bubbles floating in air, with a temporary thin liquid film preventing them from bursting. In the context of cavitation, however, bubbles are always submerged within a surrounding liquid; it is the interplay between the internal gas and external liquid phases which provide most of the interesting behaviour of bubbles for engineering purposes.

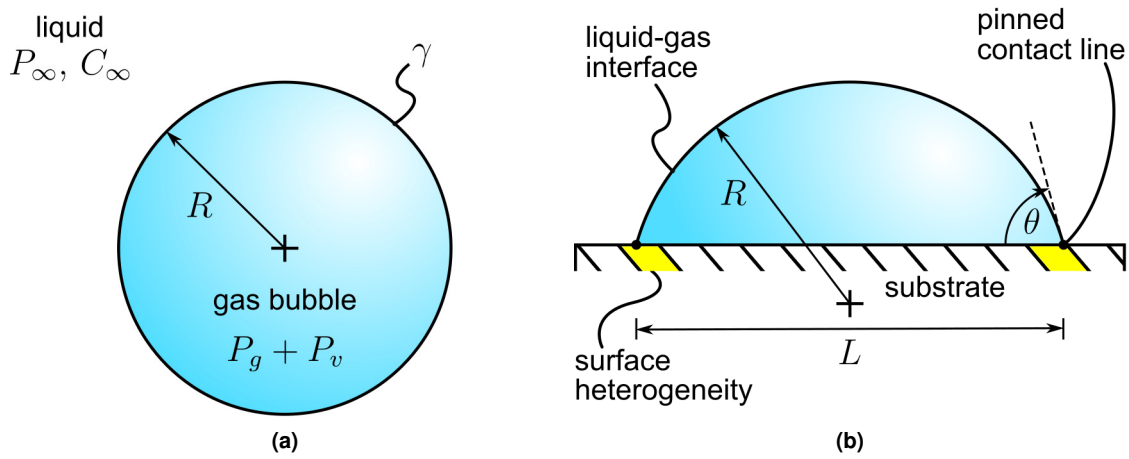


**Figure 2.1:** Schematic of (a) a spherical bubble, and (b) a surface nanobubble.

The effects of surface tension tend to minimise the surface area of a fluid interface for a particular volume, and so bubbles typically form a naturally spherical shape. The Laplace pressure is one of the most important concepts in cavitation and relates the pressure difference across a curved liquid-gas interface:

$$\Delta P \equiv P_g + P_v - P_l = \frac{2\gamma}{R}, \tag{2.1}$$

1. From hereon, the interface between the liquid and gas/vapour phases will be simply referred to as the liquid-gas interface unless otherwise stated.

where $P_g$ is the pressure of the internal gas phase of the bubble (not including vapour from the surrounding liquid), $P_v$ is the vapour pressure of the surrounding liquid, usually a function of temperature, and $P_l$ is the liquid pressure immediately outside of the bubble interface. The interface has a surface tension $\gamma$, and the bubble's radius of curvature is given by $R$ (Brennen, 2013). The surface tension of water is relatively high, $\gamma = 71.69\,\mathrm{mJ/m^2}$ at 300 K (Lemmon *et al.*, 2017), and for nanobubbles with sizes of the order of $R \sim 10\,\mathrm{nm}$, this can result in significant pressure differences of several mega-Pascals. For a bubble in mechanical equilibrium, the pressure of the liquid field is considered constant throughout, so the pressure of the liquid just outside the interface is equal to the far-field liquid pressure $P_\infty$.

Bubbles are sensitive to different environmental conditions, the most obvious being temperature. Boiling is a commonly observed phenomenon, where increasing the temperature of a liquid, for example when heating a pot of water, causes bubbles of water vapour to form. Cavitation can be thought of as the corresponding thermodynamic process to boiling, where reducing the pressure, instead, causes bubbles to form. In boiling, an increase in temperature increases the vapour pressure of the fluid, and the gradual increase in internal vapour pressure drives bubble growth, with an associated increased mass content of the bubble. In cavitation, it is typical to assume constant liquid temperature (at least before collapse) and so the vapour pressure within the bubble is generally considered constant; growth is driven by a pressure difference, usually caused by the drop in external liquid pressure. Cavitation often happens so rapidly that the bubble's mass contents remain constant (Brennen, 2013).

For gas flows in or around nano/microscale geometries, the mean free path of the gas is comparable to the geometric flow dimension, and rarefaction has been shown to play a role in the underlying physics of many problems. For fully immersed nanobubbles, it is assumed the liquid's inertia and viscous effects are dominant if the density and viscosity of the liquid both far exceed the respective properties of the internal gas phase, and so the bubble's cavitation dynamics are mostly governed by the external liquid flow. The rarefied gas dynamics do not need to be considered and the internal gas pressure can be considered uniform throughout the bubble (Brennen, 2013). Fortunately, the bubble's gas pressure can usually be estimated by the simple polytropic gas law for a fixed mass:

$$P_g V^k = \text{const.}, \tag{2.2}$$

where $V$ is the bubble volume, and $k$ is the polytropic exponent. Thermodynamic behaviour of the gas phase can be inferred from this exponent, e.g. $k = 1$ indicates isothermal expansion, where adiabatic behaviour is $k = 5/3$ for a monatomic gas, and $k = 7/5$ for a diatomic gas.

## 2.2 Cavitation

### 2.2.1 Cavitation threshold

The earliest references to cavitation involve experiments on the tensile strength of water (Berthelot, 1850; Brennen, 2013; Caupin and Herbert, 2006). The term literally means to form a cavity within a medium, which is the process that ruptures bulk liquids when subjected to a tensile stress. Tension in liquids is defined as the difference between the vapour pressure and external liquid pressure, i.e. $(P_v - P_\infty)$. For experiments at room temperature, where $P_v$ can be considered negligible, tension reduces to: $(P_v - P_\infty) \approx -P_\infty$. The liquid pressure at which cavitation occurs is referred to as the *cavitation threshold* $P_{\infty,c}$, so for this research, the tensile strength can be simply assumed as the negative of the cavitation threshold. As early as the 19$^{\text{th}}$ century, Berthelot (1850) was able to measure this cavitation threshold and find $P_{\infty,c} = -5\,\text{MPa}$ by heating and cooling very pure, degassed water within glass capillary tubes (Brennen, 2013).

#### Negative pressures in liquids

It is important to specify at this point that the cavitation threshold is measured as an *absolute* pressure, and not gauge pressure as is often assumed. Negative absolute pressure is a real concept in liquids, although often becomes a hurdle in many discussions on cavitation, and likely why the field is still poorly understood. Pressure is usually taught in the context of an ideal gas; particles within a closed box collide with each other and impart momentum on the surrounding walls of the box. All these particle-wall collisions can be summed to achieve a total force per unit area on the box, which is typically defined as pressure, and this scales with gas temperature and the inverse of the box volume, Boyle's law. This understanding is still valid, and it is true that gas pressure cannot be below zero.

For liquids, it is useful to understand that pressure can be represented as a force per unit area, or equivalently as energy per unit volume. J. H. Irving and J. G. Kirkwood (1950) provided a statistical approach in which hydrodynamic properties could be obtained from discrete particle dynamics, as used in Molecular Dynamics (MD) (see Chapter 3). Pressure can be split into kinetic and virial components. The kinetic component is dominant for gases, and simply relates the kinetic energy of the particles (i.e. temperature) to the bulk pressure, and Boyle's law (as mentioned above) can be obtained. The virial component sums the specific potential energy of the particles from the interatomic and intermolecular interactions, such as bonds, van der Waals forces, and partial coulombic charges, which becomes the dominant contribution for liquids (J. H. Irving and J. G. Kirkwood, 1950).

This concept was illustrated by Frenkel (1955) who presented the example of the van der Waals interaction between two atoms. The potential energy $U$ as a function of separation $r$ is shown in Figure 2.2. The force between these two atoms is given by $F_r = -\mathrm{d}U/\mathrm{d}r$, and can be seen to be zero at $r_0$, i.e. the atoms are in equilibrium. There is a long-range attraction for $r > r_0$ and

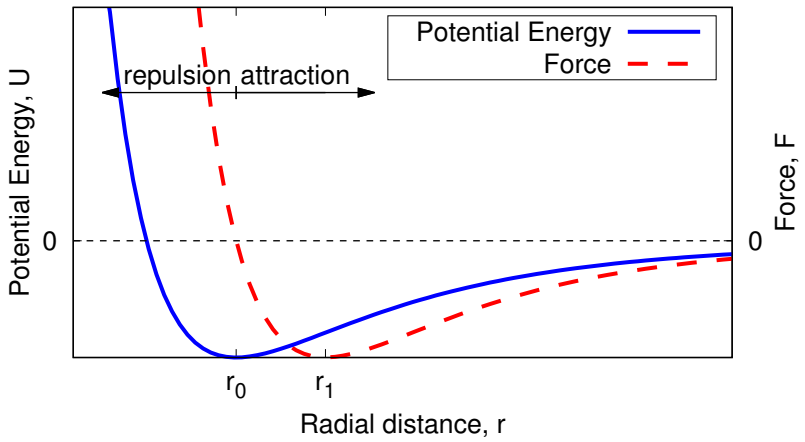


**Figure 2.2:** Variation of potential energy and attractive/repulsive force between two uncharged atoms in a van der Waal interaction.

strong, short-range repulsion for $r < r_0$, which are caused by the attraction (between the nuclei and electrons from the opposite atoms) and Pauli's repulsion, respectively. The maximum attractive force occurs when the radial separation is increased to $r_1$. In between $r_0$ and $r_1$, there is a restoring attractive force resisting the separation of the atoms: they are supporting a tensile force. For $r > r_1$, the attractive force decreases in magnitude, so the interaction pair would not be able to support any increase in tension, i.e. the tensile strength can be assumed when the molecules are separated by $r = r_1$. While this is a simplistic example, this thinking can be extended to a fluid of closely packed atoms. There is still sufficient attraction between all the atoms in the liquid to resist rupture when subjected to a tensile stress, and so the absolute pressure of the liquid will be negative.

The tensioned liquid is in a *meta-stable state*: it can resist small perturbations from thermal fluctuations or impurities, however larger energy fluctuations can induce instability, and the energy barrier for these critical fluctuations decrease with decreasing pressure. This forms the basis of classical nucleation theory (Brennen, 2013), and also fits the general intuition of liquids under negative pressure not being thermodynamically stable. Since thermal fluctuations have some statistical variation, classical nucleation theory can predict the timescale in which a tensioned liquid would be expected to rupture, based on probabilistic means.

It is generally accepted that solids are capable of supporting a tensile load. Liquids have a comparable density and are subject to similar interatomic potentials, and so there is no reason to suggest they cannot also support tensile stresses for short times.

Further experiments on water, using similar methods to Berthelot (1850), have found cavitation thresholds down to $P_{\infty,c} = -30\,\text{MPa}$ (Brennen, 2013; Caupin and Herbert, 2006). Classical nucleation theory predicts at 300 K the cavitation threshold can be as low as $-160\,\text{MPa}$ (Caupin and Herbert, 2006; El Mekki Azouzi *et al.*, 2012; Pallares *et al.*, 2014). More recently inclusion

experiments have measured cavitation thresholds down to −140 MPa in water (El Mekki Azouzi *et al.*, 2012; Pallares *et al.*, 2014), with MD simulations estimating −126 MPa (Menzl *et al.*, 2016).

The cases described above refer to *homogeneous nucleation*; a vapour bubble forming within the bulk of a pure liquid. *Heterogeneous nucleation* is when bubbles form from some external cavitation nuclei, such as a solid substrate or dissolved impurities, and these increase the likelihood of cavitation. The cavitation threshold for water is usually well above the theoretical limit due to the abundant presence of cavitation nuclei in a normal sample liquid, in much the same way that water typically freezes at 0 °C, while pure water can be supercooled down past −40 °C (Debenedetti, 2003). Even cosmic radiation has been shown to induce the formation of cavitation nuclei (Brennen, 2013; Seddon *et al.*, 2012), which is difficult to avoid in most practical situations.

Harvey *et al.* (1944) suggested entrapped gases within microscopic particles and solid impurities in liquids act as cavitation nuclei; these gas-filled particles simply became known as Harvey nuclei, and Atchley and Prosperetti (1989) expanded on this for their crevice theory. Further research in this area has examined cavitation nucleation within carefully controlled nanoscale cylindrical pits (Borkent *et al.*, 2009; Bremond *et al.*, 2005).

Dissolved gases certainly raise the cavitation threshold, and form the basis of some simple cavitation models. Blake (1949) assumed a spherical bulk bubble with initial radius $R_0$ acted as a nucleus for unstable cavitation growth, leading to:

$$P_{\infty,c} = P_v - 2\gamma\left(1 - \frac{1}{3k}\right)\left[\frac{2\gamma}{3kR_0^{3k}P_{g,0}}\right]^{\frac{1}{3k-1}}, \tag{2.3}$$

where $P_{g,0}$ is the initial bubble gas pressure, which can be obtained from Equations (2.1) and (2.2) under equilibrium. For example, a spherical nanobubble with $R_0 = 100\,\text{nm}$, under ambient water conditions: $\gamma = 71.69\,\text{mJ/m}^2$, $P_{\infty,0} = 0.1\,\text{MPa}$, $P_v = 3.54 \times 10^{-3}\,\text{MPa}$, and assuming isothermal growth, $k = 1$, Equation (2.3) predicts the cavitation threshold to be $P_{\infty,c} = -0.53\,\text{MPa}$. This is well above the typical cavitation threshold for the pure water homogeneous nucleation cases as found by Caupin and Herbert (2006); El Mekki Azouzi *et al.* (2012); Menzl *et al.* (2016); Pallares *et al.* (2014), and demonstrates the sensitivity of cavitation to the effects of dissolved gases. The internal gas phase is much more sensitive to variations in pressure than the bubble's vapour content for pure homogeneous nucleation.

### 2.2.2 Growth and oscillation of cavitation bubbles

The most commonly used model for spherical cavitation bubble dynamics is the Rayleigh-Plesset equation:

$$R\ddot{R} + \frac{3}{2}\dot{R}^2 + \frac{4\nu\dot{R}}{R} = \frac{1}{\rho}\left[P_{g,0}\left(\frac{R_0}{R}\right)^{3k} - (P_\infty - P_v) - \frac{2\gamma}{R}\right], \tag{2.4}$$

where $\nu$ is the liquid kinematic viscosity, and $\rho$ is the liquid density. Dot notation is used to denote a time-derivative, e.g. $\dot{R} = \mathrm{d}R/\mathrm{d}t$, and $\ddot{R} = \mathrm{d}^2R/\mathrm{d}t^2$ (Brennen, 2013; Plesset, 1949).

Figure 2.3 shows an example of an isothermal $(k = 1)$ cavitation event, solved using Equation (2.4); a nitrogen bubble with initial radius $1\,\mu$m and immersed in water, is subjected to a pressure drop $P_\infty = -0.1\,$MPa, before restoring to ambient pressure within $1\,\mu$s. The Blake threshold (Equation (2.3)) for this particular bubble is $P_{\infty,c} = -0.043\,$MPa.

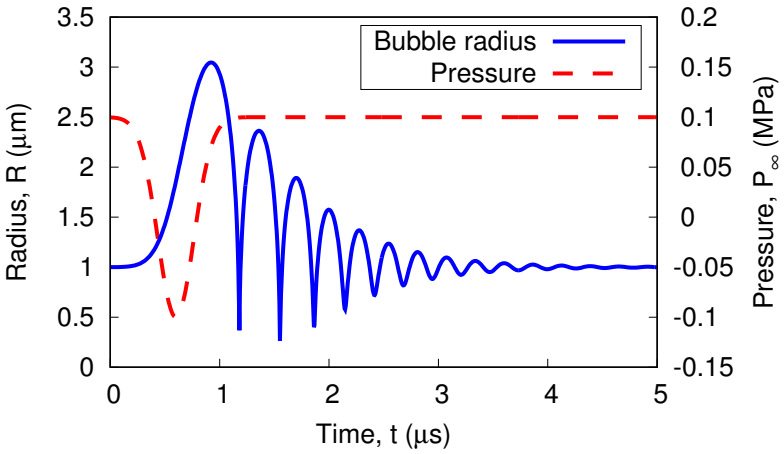


**Figure 2.3:** Typical solution of the Rayleigh-Plesset equation (Equation (2.4)) showing the initial instability, collapse and rebound of a spherical cavitation bubble in a liquid.

Figure 2.3 shows the initial unstable growth, then collapse of the cavitation bubble; there are also decaying oscillations in the bubble radius after the initial collapse (see Section 2.2.3).

Minnaert (1933) determined the natural frequency of these bubble oscillations, neglecting surface tension effects:

$$\omega_{0,m} = \left(\frac{3kP_{\infty,0}}{\rho R_0^2}\right)^{\frac{1}{2}}. \tag{2.5}$$

The Minnaert frequency will be expanded upon in Chapter 5, to account for the effect of surface tension, which becomes more prominent at the nanoscale.

Equation (2.4) assumes a perfectly spherical oscillating bubble within an infinite liquid field. This assumption is usually valid for the initial stages of growth where expansion is slow, for micro and nanobubbles where surface tension effects are strong (see Equation (2.1)), or for

small amplitude oscillations. Gravitational effects, nearby surfaces and large pressure variations, however, can disturb this spherical symmetry, particularly during collapse (Adhikari *et al.*, 2016; Choubey *et al.*, 2011; Klaseboer and Khoo, 2006; Shekhar *et al.*, 2013; Supponen *et al.*, 2016; Vedadi *et al.*, 2010; Zhang and Duncan, 1994). Despite this asymmetric collapse, Equation (2.4) can still give a surprisingly good prediction for the subsequent rebounding and collapsing phases of the bubble (see Section 2.2.3) (Brennen, 2013; Leighton, 2008).

Bubble confinement, such as in Micro-Electro-Mechanical Systems (MEMS) devices, can also influence bubble oscillation dynamics, as the assumption of an infinite external liquid field is no longer valid (Leighton, 2011; Martynov *et al.*, 2011; Tsuda *et al.*, 2015; Vincent and Marmottant, 2017). The effects of confinement are not always so trivial to determine. Confinement typically reduces the liquid inertia, which would result in an increased oscillation frequency, and can be observed when confined by a free surface (Tsuda *et al.*, 2015; Vincent and Marmottant, 2017); however, confinement usually involves a nearby solid surface which can contribute significantly to the system inertia and stiffness (Leighton, 2011; Vincent and Marmottant, 2017). Nearby surfaces can also induce translational motion of spherical bubbles, often just before collapse (Brennen, 2013; Supponen *et al.*, 2016).

Cavitation inception and collapse can usually be induced by (and form) shock waves, and compressibility in the liquid becomes more significant; previous authors have adapted Equation (2.4) to account for some of these compressibility effects, which provides better accuracy for modelling the high-speed collapsing phase (Keller and Miksis, 1980; Trilling, 1952; Vokurka, 1986). Compressibility effects also become significant for oscillation pressures near the bubble's natural frequency, typically enhancing the peak frequency predicted by Equation (2.5) (Brennen, 2013).

Despite all these issues, the Rayleigh-Plesset equation remains one of the most important models in cavitation dynamics; its simplicity makes it easy to understand as well as implement on modern computers. However, as will be shown in Chapter 5, Equation (2.4) in its current form is not suitable for predicting the growth rate of a surface nanobubble.

### 2.2.3 Collapse of cavitation bubbles

Equation (2.4) can predict the collapse of a cavitation bubble, as seen by the sharp troughs in Figure 2.3. By neglecting the effects of surface tension, viscosity and the internal gas phase, Equation (2.4) can be solved analytically to estimate the time for the bubble radius to decrease to zero:

$$\tau_c \approx 0.9147 R_{max} \sqrt{\frac{\rho}{P_\infty - P_v}}, \tag{2.6}$$

where $\tau_c$ is known as the Rayleigh collapse time, and $R_{max}$ is the maximum bubble radius before collapse. Equation (2.6) is a simple approximation, which again assumes spherical symmetry, although is useful in providing an estimate for this collapse time.

The bubble is also seen to "rebound" in Figure 2.3, where it experiences successive growth and collapse phases, which ultimately lead to decaying oscillations. Interestingly, this rebounding behaviour is not just a feature of the Rayleigh-Plesset equation, but can be readily observed experimentally and in simulations (Akhatov *et al.*, 2001; Brennen, 2013; Koukouvinis *et al.*, 2016; Supponen *et al.*, 2016; Zhang and Duncan, 1994).

This rebounding behaviour also occurs even during highly asymmetric collapse, where an impinging liquid jet pierces the bubble surface. The asymmetric collapse and resulting jet formation are common in cavitation, and is considered the main source of damage (Adhikari *et al.*, 2016; Brennen, 2013; Choubey *et al.*, 2011; Shekhar *et al.*, 2013; Vedadi *et al.*, 2010). The jet strength and direction can be influenced by different environmental conditions. Jets typically form: in the opposite direction of gravitational fields, towards solid surfaces, away from free surfaces, and in the direction of shock waves (Adhikari *et al.*, 2016; Choubey *et al.*, 2011; Han *et al.*, 2018; Shekhar *et al.*, 2013; Supponen *et al.*, 2016; Vedadi *et al.*, 2010). Despite the variety of drivers, the cavitation jets formed all have similar shapes which can be characterised by the pressure gradient across the bubble during collapse (Supponen *et al.*, 2016). This gradient is obvious for the hydrostatic pressure caused by gravitational fields; in the case of bubbles collapsing close to surfaces, the surrounding liquid flow is influenced by the nearby solid or free surface that drives the pressure gradient across the bubble (Koukouvinis *et al.*, 2016; Supponen *et al.*, 2016).

Figure 2.4 shows the bubble surface evolution during the collapse of a spherical nanobubble from a shock wave (see Chapter 6); a jet forms, pierces the opposing bubble surface and flows through to the external liquid. This toroidal shape has been commonly observed in experiments

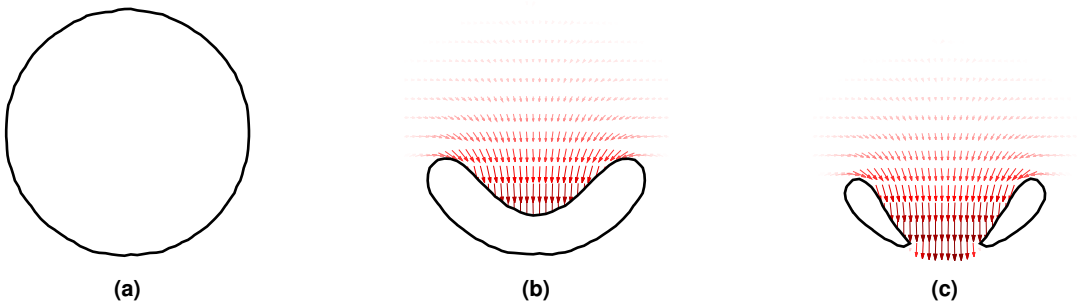


**Figure 2.4:** Evolution of bubble surface showing jet formation during a typical cavitation collapse: (a) initial spherical bubble shape; (b) early stage of bubble collapse and jet formation; (c) the moment just after the jet has pierced the opposing bubble surface. The red arrows show the direction of the jet velocity. The bubble surface is shown as the 50 % isodensity contour obtained from MD simulations, see Chapter 6.

and simulations (Benjamin and Ellis, 1966; Brennen, 2013; Koukouvinis *et al.*, 2016; Supponen *et al.*, 2016; Zhang and Duncan, 1994).

Bubble collapses can be violent, with jet velocities of the order of liquid sound speeds (Suppo-

nen *et al.*, 2016, 2017). While material damage is possible during collapse, a lot of energy is normally dissipated in the form of heat. Flannigan and Suslick (2005) found collapsing argon bubbles could reach temperatures as high as 15 000 K, hot enough to achieve an inertially confined plasma state (Flannigan and Suslick, 2005, 2010) (see Section 2.5). The rebounding behaviour in Figure 2.3 may be enhanced by an increase in vapour pressure, and even boiling effects, caused by high temperatures of the initial collapse (Akhatov *et al.*, 2001).

Damage is caused when these jets are directed onto a solid surface. A coherent model of the damage caused during cavitation has not yet been established. Experimental examination of the final stages of bubble collapse can be difficult due to the extremely high speeds and small scales (Benjamin and Ellis, 1966; Supponen *et al.*, 2016). Simulation is also not so trivial, typical simulation techniques usually either focus on the fluid or the solid only. Many authors have investigated the dynamics of collapsing cavitation bubbles with Computational Fluid Dynamics (CFD) simulations (Koukouvinis *et al.*, 2016; Supponen *et al.*, 2016; Zhang and Duncan, 1994). More recently Fivel *et al.* (2015) modelled the solid response to a pressure loading equivalent to that from an impinging cavitation jet. MD simulations (see Section 2.6) are capable of modelling the fluid and solid together, although are limited to relatively small bubbles and short time-scales (Adhikari *et al.*, 2016; Choubey *et al.*, 2011; Shekhar *et al.*, 2013; Vedadi *et al.*, 2010).

## 2.3 Diffusive equilibrium of bubbles

Before moving on to surface nanobubbles, it is worth examining the classical theory of bubble diffusive equilibrium to understand why surface nanobubbles are so unique. Epstein and Plesset (1950) estimated the diffusive growth mechanics of a bulk bubble surrounded by an infinite liquid, with far-field gas concentration $C_\infty$, and gas solubility $C_s$ given by Henry's law:

$$C_s = HP_\infty, \tag{2.7}$$

where $H$ is Henry's constant for a particular liquid-gas system (Sander, 2017).

At best, a bulk bubble can only ever be in an unstable diffusive equilibrium, by Epstein-Plesset theory, summarised as follows; for a large bubble, at a particular supersaturation (i.e. $C_\infty > C_s$), a bubble can be in diffusive equilibrium when there is a balance in gas concentration just outside the bubble surface (proportional to $P_g$), with the far-field value $C_\infty$. For incremental growth, the Laplace (and gas) pressure (Equation (2.1)) decreases, which results in a drop in gas concentration just outside the bubble surface. The far-field concentration remains constant and so a concentration gradient forms toward the bubble centre, and the bubble continues to grow until buoyancy effects take over (Brennen, 2013; Epstein and Plesset, 1950; Lohse and Zhang, 2015b). During this whole process, the bubble remains in mechanical equilibrium, i.e. Equation (2.1) holds for $P_l = P_\infty$.

Conversely, for an incremental decrease in radius, the Laplace pressure increases, causing a concentration gradient away from the bubble, and the bubble loses mass until it completely dissolves. For small bubbles ($\lesssim 1.4\,\mu$m for air bubbles in water (Lohse and Zhang, 2015b)), the high Laplace pressure always drives dissolution even for high supersaturation ratios (Epstein and Plesset, 1950; Lohse and Zhang, 2015b). Classical Epstein-Plesset theory (Epstein and Plesset, 1950) estimates the time-scale for dissolution of these small bubbles:

$$\tau_D \approx \frac{R_0^2 \rho_g}{3DC_s}, \tag{2.8}$$

where $\rho_g$ is the initial internal gas density, and $D$ is the diffusion constant (Epstein and Plesset, 1950; Lohse and Zhang, 2015a; Maheshwari *et al.*, 2016). For a typical nitrogen nanobubble in water, $R_0 = 100\,\text{nm}$, at ambient atmospheric conditions, $300\,\text{K}$, $P_\infty = 0.1\,\text{MPa}$, $\gamma = 71.69\,\text{mJ/m}^2$, $D = 2\times10^{-9}\,\text{m}^2/\text{s}$ (Lohse and Zhang, 2015b), $C_s = 0.017\,\text{kg/m}^3$ (Sander, 2017), it is found that $\tau_D \sim 1\,\text{ms}$. Contrast that to a typical oscillation period considering Equation (2.5), $\tau_m \sim 2\pi/\omega_{0,m} \approx 30\,\text{ns}$, which is a difference of over four orders of magnitude; cavitation dynamics occur much more rapidly than diffusive based growth (Brennen, 2013). For this thesis, the diffusive timescales were considered too costly to fully investigate with MD simulations, and so run times were purposely kept short enough to neglect the effects of diffusive based growth.

An added complexity of bubble dynamics is that gas solubility typically increases with pressure and decreases with temperature (Sander, 2017). So, a change in one of these environmental conditions might result in a rapid primary growth phase to a new temporary bubble size (e.g. cavitation), with a concurrent, more relaxed phase driven by diffusive growth dynamics.

## 2.4 Surface nanobubbles

Some early Atomic Force Microscopy (AFM) images of immersed hydrophobic surfaces showed spherically capped, nanoscale shapes on the surface (Ishida *et al.*, 2000; Lohse and Zhang, 2015b; Lou *et al.*, 2000; Tyrrell and Attard, 2001). Further experiments, involving: infrared spectroscopy, quartz crystal microbalance, surface plasmon resonance and neutron reflectometry, denied speculation that these were simply artefacts of AFM, and were in fact bubbles (Lohse and Zhang, 2015b; Theodorakis and Che, 2019; Zhang *et al.*, 2008). From Section 2.3 it would appear that no nanobubble can be stable longer than a matter of milliseconds, yet repeated measurements showed some of these surface nanobubbles were stable for several hours to days at a time, completely defying the previous understanding of Epstein-Plesset theory (Lohse and Zhang, 2015b; Theodorakis and Che, 2019; Zhang *et al.*, 2008).

Another unexpected feature of surface nanobubbles was their low contact angle $\theta$ (the angle between the solid substrate and liquid-vapour surface) when measured from the internal, gas-

side of the bubble[2], as shown in Figure 2.1(b). This gas-side contact angle was much lower than the expected equilibrium contact angle from Young's equation, even for hydrophobic surfaces (Lohse and Zhang, 2015b).

After some initial competing theories (see below), there seems to be general agreement that the long-term stability of surface nanobubbles is due to: a) pinning of the three-phase contact line, and b) a local supersaturation of dissolved gas (Attard, 2016; Lohse and Zhang, 2015a,b; Maheshwari *et al.*, 2016; Theodorakis and Che, 2019). Like with classical Epstein-Plesset theory, supersaturation is required to keep the surface nanobubble in some diffusive equilibrium (Attard, 2016; Chan *et al.*, 2015; Lohse and Zhang, 2015a).

The difference in stability arises from the effects of contact line pinning. A pinned contact line means the bubble footprint, or lateral contact diameter $L$, is constant. The associated mode of growth is known as constant contact radius (CCR). An incremental increase in surface nanobubble volume requires an increase in contact angle, which results in a *decrease* in radius of curvature $R$:

$$R = \frac{L}{2\sin\theta}. \tag{2.9}$$

From Equation (2.1), this causes an *increase* in internal gas pressure (for $\theta < 90°$), which drives an external concentration gradient away from the bubble. This is the inverse of the spherical bubble case, and the result is a negative feedback loop, which keeps the surface nanobubble in stable diffusive equilibrium (Attard, 2016; Chan *et al.*, 2015; Lohse and Zhang, 2015a).

The equilibrium contact angle of the surface nanobubble is not given from Young's equation, but instead depends on the gas supersaturation:

$$\sin\theta_e = \zeta\frac{L}{L_c}, \tag{2.10}$$

where $\theta_e$ is the surface nanobubble equilibrium contact angle, the gas supersaturation is given as $\zeta \equiv C_\infty/C_s - 1$, and $L_c$ is the critical lateral diameter, given by $L_c = 4\gamma/P_\infty$ ($\approx 2.84\,\mu$m for water in ambient conditions) (Chan *et al.*, 2015; Lohse and Zhang, 2015a). For 2D cases, the Laplace pressure is half that given in Equation (2.1), and so the critical lateral diameter becomes $L_c = 2\gamma/P_\infty$.

The surface nanobubble contact angle is related to the supersaturation of the surrounding liquid. Given air (mostly nitrogen) is relatively insoluble in water, compared to other gases such as carbon dioxide (Lohse and Zhang, 2015b; Sander, 2017; Zhang *et al.*, 2008), it makes sense that surface nanobubbles would be prevalent in many usual experimental conditions. Carbon dioxide is still commonly used because of its strong identifying signal in Attenuated Total Reflection experiments (Lohse and Zhang, 2015b; Zhang *et al.*, 2008).

---

2. The contact angle is conventionally measured from the liquid side in fluid mechanics. However, for ease of analysis in later chapters, the contact angle will refer to the gas side for the remainder of this thesis.

Contact line pinning is also not difficult to achieve, since no surface is atomically smooth. Pinning usually results from surface heterogeneities, such as hydrophobic patches and chemical patterning, or nanoscale structures on the surface like roughness. Contamination, surface cleaning techniques and erosion can introduce all manner of these heterogeneities and increase the number density of pinning sites. The enablers for pinning are so widespread, it would surely be a greater challenge to create a solid surface which did *not* cause contact line pinning. Pinning is also considered to be the cause of contact angle hysteresis (de Gennes, 1985; Lohse and Zhang, 2015b).

### Alternative explanations for surface nanobubble stability

Some authors dispute the claims that the contact line pinning and supersaturation are necessary for surface nanobubble stability. These arguments typically postulate some mechanism that reduces the surface tension (that would reduce the high Laplace pressure), and usually also impedes gas exchange at the bubble interface.

There is also growing evidence to suggest the possibility of stable bulk nanobubbles, via some of these mechanisms (Seddon *et al.*, 2012). Surface nanobubbles are likely more commonly observed because their pinned contact line limits the effects of Brownian motion and convection, which makes them suitable for measuring with AFM (Che and Theodorakis, 2017; Ishida *et al.*, 2000; Lohse and Zhang, 2015b; Lou *et al.*, 2000; Tyrrell and Attard, 2001), while bulk nanobubbles would likely be more difficult to measure by the same techniques.

Molecules in polar liquids, such as water, naturally order themselves at interfaces, giving the interface a net negative charge (Creux *et al.*, 2007). This charge density can be enhanced in aqueous solutions, forming an electric double layer (Creux *et al.*, 2007), and the repulsion between charged bubble surfaces have been speculated to be the cause of reduced coalescence rates between bubbles (Seddon *et al.*, 2012; Tyrrell and Attard, 2001). Bulk nanobubble stability driven by this ionic shielding mechanism, or some other diffusive shielding mechanism, is plausible. Diffusive shielding, caused by closely spaced bubbles preventing the formation of a steady concentration gradient that would otherwise drive dissolution, has been shown to be dependent on a minimum number density of bulk nanobubbles, which is likely the case for ionic shielding as well (Seddon *et al.*, 2012; Weijs *et al.*, 2012a). Stability driven by an electric double layer should be dependent on salt concentration and pH (Lohse and Zhang, 2015b), however, there are conflicting experimental reports on these effects on surface nanobubble stability and morphology (Tyrrell and Attard, 2001; Zhang *et al.*, 2006).

Other authors have suggested that nanobubbles can be stabilised against dissolution by reducing the surface tension with surfactants, which also inhibits gas outflux (Andersen and Mørch, 2015; Ducker, 2009; Zhang *et al.*, 2012). These surfactants can be naturally occurring from contamination (Ducker, 2009), or be purposefully added for certain engineering applications,

such as ultrasound contrast agents (Martynov *et al.*, 2011; Stride and Saffari, 2003) (see Section 2.5). Contamination may also introduce more pinning sites for the surface nanobubble contact line. While contamination can certainly aid in stabilising surface nanobubbles, it has shown to not be completely essential (Lohse and Zhang, 2015b; Maheshwari *et al.*, 2016; Zhang *et al.*, 2012). Surfactants are not so trivial to simulate, and typically represent quite specific cases in cavitation, so will not be considered in this thesis.

Contamination has also been blamed for some apparent inconsistencies in experiments. Berkelaar *et al.* (2014) found that nanodroplets of polydimethylsiloxane (PDMS), a polymer typically used for plastic syringes and disposable equipment, have a similar morphology and pinning characteristics, and could be mistaken for surface nanobubbles in experiments.

All the above explanations would appear to at least enhance the stability of surface nanobubbles, however, the roles of both contact line pinning and gas supersaturation still seem paramount. Even in the short time-scales of MD simulations, the absence of one or more of these parameters has been shown to result in complete dissolution of a surface nanobubble (Che and Theodorakis, 2017; Maheshwari *et al.*, 2016). It is assumed that this current understanding is fundamental for surface nanobubble diffusive stability in this thesis.

## 2.5 Applications of cavitation bubbles

Cavitation has long been considered a problem in engineering of fluids systems (Brennen, 2013). However, attention is increasingly being focussed on micro and nanoscale systems as technology becomes more sophisticated, and the role of cavitation is becoming more appealing. The highly directional jets and extreme pressures that can be achieved have the potential for a variety of high precision applications.

In medicine, plasmonic nanobubbles can be induced to grow and collapse via pulsing lasers on gold nanoparticles. These nanoparticles can be specially coated to bind to cancerous cells, and bubbles are generated *in vivo* to break up tumours in non-invasive treatment (Lukianova-Hleb *et al.*, 2014, 2016). It has also been suggested that cavitation, induced by shock waves, could be responsible for traumatic brain injuries, where collapsing nanobubbles can create temporary pores in the blood-brain barrier; these pores allow the detrimental exchange of proteins which can have irreversible effects on brain function (Adhikari *et al.*, 2016).

Microbubbles are already used in medicine as “ultrasound contrast agents”. Bubbles which are specially coated to bind to diseased tissue transmit strong non-linear responses to ultrasound waves in medical sonography, which can aid in the diagnosis of cancer and liver abscesses (Martynov *et al.*, 2011; Stride and Saffari, 2003).

Ultrasonic cleaning is the principle of using cavitation bubbles, excited by ultrasound waves, to remove debris and contaminants from the surfaces of mechanical components (Brems *et al.*,

2014). This technique can be particularly useful for cleaning parts with intricate surfaces or features that would make it difficult to clean manually. Care needs to be taken to ensure the cavitation bubbles do not damage the working surfaces, and this is becoming increasingly important as researchers look to this method for cleaning of high-precision technical equipment (Brems *et al.*, 2014).

Surface nanobubbles also have some unique applications. For example, rarefied gas effects are expected to occur in surface nanobubbles with low surface heights, and high-slip lengths could be possible, allowing for low-drag coatings in ships and hydrodynamic structures; however, the potential drag reduction was found to be smaller than previously suggested, and there is still difficulty in ensuring a large surface area coverage of surface nanobubbles for this application to be feasible (Lohse and Zhang, 2015b; Ramisetti *et al.*, 2017). Surface nanobubbles have also been blamed for reduced efficiencies in electrolysis and catalysts. During electrochemical reactions, such as in the production of chlorine gas, the formation of stable surface nanobubbles on electrode surfaces is speculated to be responsible for limiting the reaction rate by reducing the total wetted surface area (Lohse and Zhang, 2015b). The collapse of these bubbles can damage catalytic surfaces, although they can also be used to remove passivated layers and so enhance reaction rates, by controlling frequencies and pressure amplitudes in ultrasonic cleaning (Suslick and Price, 1999). Improved understanding of their cavitation dynamics could lead to methods of detaching these bubbles from the electrodes and maintain high electrolysis efficiencies.

As mentioned in Section 2.2.3, collapsing cavitation bubbles have been able to reach temperatures as high as 15 000 K (Flannigan and Suslick, 2005, 2010). These temperatures are comparable to the surface of the sun, and in some cases, a dim light can be observed in a phenomenon known as *sonoluminescence* (Flannigan and Suslick, 2005). Expanding on this process, *sonofusion* is the theorised process of inducing nuclear fusion via cavitation bubble collapse (Barber *et al.*, 1994; Flannigan and Suslick, 2010). The field has been surprisingly controversial, with one research group claiming they had directly observed nuclear emissions and temperatures exceeding $10^6$ K in cavitation collapse experiments using relatively simple laboratory equipment (Taleyarkhan *et al.*, 2002). These findings proved very difficult to replicate and have been heavily criticised (Levi, 2002; Saltmarsh and Shapira, 2002). The results of Flannigan and Suslick (2005, 2010) remain the highest experimental temperatures observed in the literature with the greatest agreement from the wider scientific community, although still fall well below the theoretical limit of $10^8$ K (Barber *et al.*, 1994).

Sonofusion falls into a broader field known as sonochemistry, where ultrasonic cavitation acts as the catalyst for chemical reactions. Waste-water treatment has commonly used disinfectants such as ozone gas, chlorine gas, and hydrogen peroxide; ultrasonic cavitation can be used in conjunction to increase the efficacy of these cleaning agents (Dular *et al.*, 2016).

## 2.6 Simulation and modelling techniques

Multiphase fluid problems, like in bubbles, typically calls for Navier-Stokes Computational Fluid Dynamics (CFD) simulation techniques (Chakraborty, 2019; Chakraborty *et al.*, 2013; Denner *et al.*, 2017; Koukouvinis *et al.*, 2016; Lauterborn *et al.*, 2018; Zhang and Duncan, 1994). Some of the most popular forms of CFD employ a finite-volume scheme to discretise the fluid domain. One of the challenges in this approach remains in accurately resolving the liquid-gas interface(s), which can be done by a variety of techniques.

The simplest method is Volume of Fluid (VOF) which treats the whole system as one fluid, and applies a volume fraction function to distinguish the liquid and gas properties (Denner *et al.*, 2017; Koukouvinis *et al.*, 2016; Lauterborn *et al.*, 2018). The interface can be reconstructed from the midpoint of the volume fraction. High curvatures can cause discontinuities in the surface reconstruction which drives numerical instabilities, known as "spurious" or "parasitic" currents (Denner *et al.*, 2017). Micro and nanoscale fluids are also prone to these parasitic currents, driven by the high pressure difference across the interface, see Equation (2.1). There are various techniques to more accurately resolve the fluid interfaces, intended to lessen these effects, including the level-set method which employs a smoothed surface function to the bubble surface as it propagates in time (Chakraborty, 2019; Chakraborty *et al.*, 2013).

The boundary element method explicitly tracks the bubble interface; the surrounding liquid is modelled using potential flow, which assumes irrotational flow, and the bubble surface provides the appropriate boundary conditions. Typically, viscous and surface tension effects are not modelled, which may be suitable for high-speed bubble collapse simulations (Zhang and Duncan, 1994), although is not ideal for the initial growth and oscillation stages of cavitation at the nano and microscale. Including viscous effects is possible, although not trivial, to implement (Joseph, 2006; Padrino and Joseph, 2007).

Less common is the use of finite element methods to model the fluid. Extra care is needed to ensure the solutions are conservative in terms of mass, momentum and energy (Zienkiewicz *et al.*, 2014), however, they can be useful for modelling fluids interacting with flexible solid materials (Martynov *et al.*, 2011). They are more commonly associated with solid mechanics and have been previously used to model the pitting damage caused during cavitation bubble collapse (Fivel *et al.*, 2015). Finite element solvers can also be coupled with more conventional CFD techniques to model the solid and fluid responses, respectively, during cavitation bubble collapse (Chahine and Hsiao, 2015).

For the research undertaken in this thesis, Molecular Dynamics (MD) was chosen as the primary simulation method. MD applies Newton's laws of motion on a finite number of particles, with unique potential energy functions between different atomic species. The allure of MD is that nearly all physical processes (neglecting directly solving for quantum effects) can be theoretically simulated with the appropriately chosen potentials. That is, all the issues with

multiphase fluids described above in other simulation methods, e.g. viscosity, energy conservation, surface tension etc., do not exist in MD (although other issues do arise due to limitations of long-range interactions and choice of potentials). Similarly, other fluid behaviour such as surface tension, equations of state, rarefied gas dynamics, stick-slip contact line dynamics, saturation and temperature effects, compressibility and shock waves, are all resolved naturally within MD, since they are all the product of the collective behaviour of the constitutive atoms. One would typically need to manually incorporate these individual properties in other simulation techniques, which could introduce unforeseen errors, such as the parasitic currents discussed earlier (Denner *et al.*, 2017). This wide variety of fluid properties can sometimes become disadvantageous for analysis, however, as *all* physical effects are often present in simulations; isolating the effects which are responsible for a particular phenomenon can be difficult. There is also the benefit of modelling solids within MD for cavitation bubble collapse simulations (see Chapter 6), which is not trivial within CFD without some form of coupling (Chahine and Hsiao, 2015).

Unfortunately, the biggest limitation is that MD is highly computationally expensive for its output, typically requiring High Performance Computers (HPCs) to perform these simulations and store the large data files produced. A very large simulation could contain $20 \times 10^6$ atoms, which might only cover a domain of a 100 nm sized cube, and only span 1 ns of simulation time. Also, MD simulation cost typically scales with the square of the number of atoms, so currently cannot come close to challenging traditional CFD for macroscopic applications and design. However, its high molecular resolution is well suited for modelling individual surface nanobubbles, particularly when the physics behind their behaviour is still not fully understood (Che and Theodorakis, 2017; Chen *et al.*, 2018; Lohse and Zhang, 2015b; Maheshwari *et al.*, 2016, 2018; Weijs *et al.*, 2012b).

Previous MD modelling of surface nanobubbles has typically focussed on their diffusive stability and formation. Weijs *et al.* (2012b) investigated the relative effects of interatomic potentials between the solid, liquid and gas atomic species, and found that surface nanobubbles tended to nucleate in reduced solubility fluid mixtures (i.e. supersaturated solutions), and tended to a specific contact angle on hydrophobic surfaces of 75°. However, with no pinning sites present, the surface nanobubbles dissolved in these simulations (Weijs *et al.*, 2012b). Maheshwari *et al.* (2016) verified that both pinning and gas supersaturation were required for surface nanobubble stability. Pressure was also varied to model the effect of solubility (from Henry's law, see Equation (2.10)) on their morphology. Later, Maheshwari *et al.* (2018) modelled the process of "Ostwald ripening" for surface nanobubbles; a local concentration gradient drives dissolution of smaller bubbles while enhancing larger bubbles in neighbouring cases. Che and Theodorakis (2017) also modelled the nucleation and dissolution process, using more realistic models of water, nitrogen and graphite for the liquid, gas and solid phases respectively. In the absence of pinning sites, these surface nanobubbles also dissolved (Che and Theodorakis, 2017). More

recently, Chen *et al.* (2018) were able to model stable argon gas surface nanobubbles in water *without* pinning sites for over 160 ns, with appropriate hydrophobicity of the solid substrate. They argue that there exists a gas enrichment layer which stabilises the bubble, as was also suggested in Weijs *et al.* (2012b), despite dissolution in that particular case.

Modelling of cavitation introduces another challenge. Equation (2.4) predicts that the nanobubble radius can vary up to three orders of magnitude within a matter of microseconds during unstable growth; a $10^3$ increase in radius is equivalent to a $10^9$ increase in volume. This huge change in scale is a challenge for any simulation (and experimental) method to properly capture, and so many simulations have been limited to particular stages of the cavitation process, e.g. instability, oscillation, and collapse, as is done in this thesis.

## 2.7 Cavitation of surface nanobubbles

As discussed in Section 2.2, cavitation is a process that occurs most often on solid substrates. The origins and exact behaviour of these cavitation bubbles are still not fully understood, particularly in heterogeneous nucleation events. Section 2.4 then describes how spherical cap nanoscale bubbles can remain in long-term diffusive equilibrium resting on a solid substrate, in conditions that are not overly difficult to achieve experimentally. It would be reasonable to assume, then, that in heterogeneous nucleation, these surface nanobubbles may act as the nuclei for cavitation.

However, Borkent *et al.* (2007) found no cavitation activity for surface nanobubbles subjected to a $-6$ MPa drop in pressure, even when the Blake threshold (see Equation (2.3)) predicted a threshold pressure of $-0.55$ MPa; the authors labelled this phenomenon the "superstability" of surface nanobubbles (Borkent *et al.*, 2007). More recently, doubt has been cast on this experiment (plus others) due to the possibility of PDMS droplet contamination (Berkelaar *et al.*, 2014). As these experiments are very challenging to perform, as well as interpret, it is clear that the cavitation dynamics of surface nanobubbles is not a well-understood area. There has been very little research published in this field since. It should now be clear the motivation and the need for the work conducted in this thesis on surface nanobubbles, which is summarised as follows:

- the Blake threshold, Equation (2.3), is found to be inadequate for predicting the cavitation threshold for a surface nanobubble in Chapter 4, as first suggested by Borkent *et al.* (2007), and a more appropriate cavitation threshold model is proposed;
- the Rayleigh-Plesset equation, Equation (2.4), is found to be unsuitable for modelling the dynamic and oscillatory behaviour of the surface nanobubble in Chapter 5, and an alternative, more suitable model is proposed;
- the collapsing dynamics of surface nanobubbles is investigated in Chapter 6 and compared to equivalent spherical bubbles near a solid substrate, as a benchmark in this study.

# Chapter 3

# Molecular Dynamics Simulation

## 3.1 Introduction

Molecular Dynamics (MD) is a simulation technique that can model the dynamics of individual atoms in a system. Its greatest strength is that many complex physics and phenomena, such as surface tension, rarefied effects, and wettability, arise naturally within these high-fidelity simulations, which would otherwise need to be manually implemented into the traditional Navier-Stokes based fluid equations. The LAMMPS software package was used to perform all the MD simulations in this work (Plimpton, 1995).

The basic principle behind MD is quite simple: potential energy functions $U$ are specified between unique pairs, triplets (or more) of atoms and forces can be obtained from these potential interactions $\vec{F} = -\vec{\nabla}U$. Newton's laws of motion are used to track particle trajectories in the system, i.e. $\vec{F} = M\mathrm{d}\vec{u}/\mathrm{d}t$, where $M$ is the particle mass, and the particle velocity is given by $\vec{u} = \mathrm{d}\vec{r}/\mathrm{d}t$, where $\vec{r}$ is the particle position. The velocity-Verlet algorithm is used to update all particle positions at each timestep (Plimpton, 1995).

In practice, however, MD is more complex than it would first appear. Noise from the random thermal motion of atoms is significant and requires more involved averaging methods when obtaining results. Simulations are also at risk of becoming numerically unstable, particularly during initialisation or extreme environmental conditions, e.g. shock waves; if two atoms get unrealistically close to one another, a sharp spike in repulsive force is calculated (see Figure 2.2) which propagates in a chain reaction and causes the simulation to "blow up". This numerical instability can be mitigated by reducing the simulation timestep, although will, of course, require longer to run.

Obtaining continuum-like properties, such as pressure and temperature, from particle dynamics is challenging, as it requires grouping and averaging of discrete atomic quantities, which is often influenced by high statistical variance (J. H. Irving and J. G. Kirkwood, 1950). Likewise, setting up simulations within a nanoscale domain, which can still give good agreement with theoretical models based on infinite and semi-infinite fluids, can be particularly difficult. Often, unusually strong environmental conditions or processes, such as equilibrium pressure and heat flux, are modelled in MD to be able to observe particular phenomena within an acceptable

time. This chapter will examine some of the technical details of MD simulations, including the models and techniques employed in this research. Once all appropriate parameters have been established, the cavitation of surface nanobubbles can be accurately modelled; for example, see Section 3.6 for equilibrium simulations of surface nanobubbles.

### 3.1.1 Thermodynamic ensembles

The thermodynamic properties of groups of atoms are controlled and averaged within "ensembles". The dynamics of particles is constrained such that the average of a particular thermodynamic property within an ensemble matches a prescribed or initialised value. The simplest example is the *microcanonical*, or *NVE*, ensemble, where the number of particles, total volume and total system energy is conserved.

In the *canonical*, or *NVT*, ensemble the number of particles, total volume, and temperature of the system are enforced. The temperature of a group of atoms is related to the system kinetic energy by:

$$\frac{3}{2}k_B T = \bar{E}_k, \tag{3.1}$$

where $k_B$ is the Boltzmann constant, $T$ is the average temperature of a group of atoms, and $\bar{E}_k$ is the average kinetic energy of a group of atoms.

A "thermostat" is an algorithm/numerical device used to control the average temperature of a group of atoms. There are a variety of different thermostats available in MD simulations such as the Nosé-Hoover (Hoover, 1985; Nosé, 1984) and Berendsen (Berendsen *et al.*, 1984) thermostats. Thermostats alter the individual velocities of a group of atoms, via forces or velocity rescaling. Thermostats act like negative feedback loop control systems and hence have an associated relaxation time, typically of the order of $1000\Delta t$, where $\Delta t$ is the integration timestep (Plimpton, 1995). Because of this, and the noise from the atoms' thermal velocities, the average temperature of a group of thermostatted atoms is rarely at the exact target temperature. For the research in this thesis, the Nosé-Hoover thermostat was used for all simulations.

Since MD simulations conserve energy, the work done by external forces incurs changes in kinetic energy, creating anomalous drifts in temperature in the absence of an appropriate thermostat; however, their function effectively limits particle velocities, which can adversely inhibit fluid flows. To counter this, the molecules' centre of mass velocity is subtracted from the kinetic energy formulation in Equation (3.1), thus the change in kinetic energy is applied to the thermal velocity component of the molecule and not its absolute component.

*Isothermal-isobaric*, or *NPT*, ensembles constrain the number of particles, system pressure and system temperature. Analogous to thermostats, "barostats" control the system pressure, usually by varying the positions of the domain boundaries as well as rescaling the particle positions within the domain. Pressure can be obtained from the virial stress tensor of a group of atoms,

derived by J. H. Irving and J. G. Kirkwood (1950):

$$\underline{\underline{\tau}} = -\frac{1}{V}\left[\sum_{i}^{N} M_i \vec{u}_i \otimes \vec{u}_i + \frac{1}{2}\sum_{i}^{N}\sum_{i\neq j}^{N} \vec{r}_{i,j} \otimes \vec{F}_{i,j}\right], \tag{3.2}$$

where $M_i$ is the mass of atom $i$, $\vec{u}_i$ is the velocity vector of atom $i$, $r_{i,j}$ is the distance between atoms $i$ and $j$, and $\vec{F}_{i,j}$ is the force between atoms $i$ and $j$. The volume of the group of atoms is given by $V$. The $\sum_i^N M_i \vec{u}_i \otimes \vec{u}_i$ term is the kinetic component, equivalent to $3k_BT$ from Equation (3.1), and is dominant for gases. The virial contribution is given by $\frac{1}{2}\sum_i^N \sum_{i\neq j}^N \vec{r}_{i,j} \otimes \vec{F}_{i,j}$ and becomes more significant for liquids (Plimpton, 1995).

The pressure of the system of atoms is given by one third of the negative of the trace of the stress tensor, i.e.:

$$P = -\frac{1}{3}\left(\tau_{xx} + \tau_{yy} + \tau_{zz}\right). \tag{3.3}$$

The kinetic contribution to the pressure is always positive, although the virial contribution can become negative in certain environments common to cavitation, as discussed in Chapter 2.

The pressure formulated by Equations (3.2) and (3.3) is dependent on the volume of the system domain. This can be problematic, when attempting to control the pressure of a multiphase system, such as in this research. Due to the Laplace pressure, the internal gas pressure of the bubble is expected to always be at an increased pressure than the external liquid. Similarly, the pressure of the rigid wall atoms cannot be reliably measured. Even if only the liquid atoms are considered, estimating the liquid volume is not so trivial, which can make accurate "on the fly" pressure calculation difficult. Maheshwari *et al.* (2016) employed an NPT ensemble in which the relationship between the input simulation pressure and output measured pressure was obtained after post-processing. Accurate and concurrent determination of the liquid pressure is crucial for modelling the cavitation dynamics of the surface nanobubbles. For this reason, and the fact that the nanobubble systems employed here are generally non-periodic (see Section 3.1.2), the NPT thermostat is *not* used to control the system pressure. Instead, a piston, composed of solid atoms, is used and is more suitable for achieving the desired pressure within the fluid system (see section 3.5).

### 3.1.2 Boundary conditions

To obtain agreement with infinite or semi-infinite fluids, certain boundary conditions are employed that allow the finite simulation domain size to act as if it was part of a much larger system. In continuum-based Computational Fluid Dynamics (CFD) simulations, pressure and velocity boundary conditions are used to allow a continuous flow of fluid through the domain. In MD, this would involve continuous generation and removal of atoms as they enter and leave the domain, respectively. This is not so simple to achieve as sudden additions or removals of atoms can cause instabilities in the potential energy functions if not done correctly (Borg *et al.*,

2010, 2014).

*Periodic* boundary conditions are more common in MD as they conserve mass, energy and linear momentum. In periodic boundary conditions, atoms leaving the domain are automatically placed at the opposite side of the domain, retaining the same velocity and planar position. This limits the domain to simpler box shapes but does allow bulk properties of infinite fluids to be modelled using relatively small system sizes. Interatomic interactions extend across these periodic boundaries and there is no violation in energy conservation.

*Fixed* boundary conditions were also sometimes used in this research, to reduce computational cost. Unlike periodic boundary conditions, atoms leaving through a fixed boundary are not placed back into the opposite end of the domain. Atoms are either simply removed, which can prove problematic for energy, mass and momentum conservation, or reflected off the boundary. In this research fixed boundary conditions were positioned over the piston (see Section 3.5) to prevent unintended interactions with the periodic image of the lower wall atoms.

## 3.2 Potential models

### 3.2.1 Lennard-Jones potential

One of the simplest and most commonly used potentials in MD is the Lennard-Jones (LJ) potential:

$$U_{LJ}(r) = 4\varepsilon \left[ \left(\frac{\sigma}{r}\right)^{12} - \left(\frac{\sigma}{r}\right)^{6} \right], \tag{3.4}$$

where $\varepsilon$ and $\sigma$ are the LJ potential well depth and characteristic length scale, respectively, between two atoms separated by a distance $r$.

This potential accounts for the long-range attraction and short-range repulsion between two uncharged atoms, due to van der Waals interactions (the forces between instantaneous and induced dipoles). The potential energy from Equation (3.4) is plotted in Figure 3.1(a). The potential minimum occurs at $r = 2^{1/6}\sigma$, where the force is zero. The maximum attractive force occurs at $r = (26/7)^{1/6}\sigma$.

### 3.2.2 Coulomb potential

The Coulomb potential models the repulsion and attraction between like and unlike charged particles, respectively:

$$U_C = \frac{1}{4\pi\varepsilon_0}\frac{q_1 q_2}{r}, \tag{3.5}$$

where $q_1$ and $q_2$ are the charges of the two interacting atoms, respectively, and $\varepsilon_0$ is the permittivity of free-space (Plimpton, 1995). Unlike for the LJ potential, the resulting force is either always positive or always negative, depending on the charges involved. The Coulomb potential is shown in Figure 3.1(b).

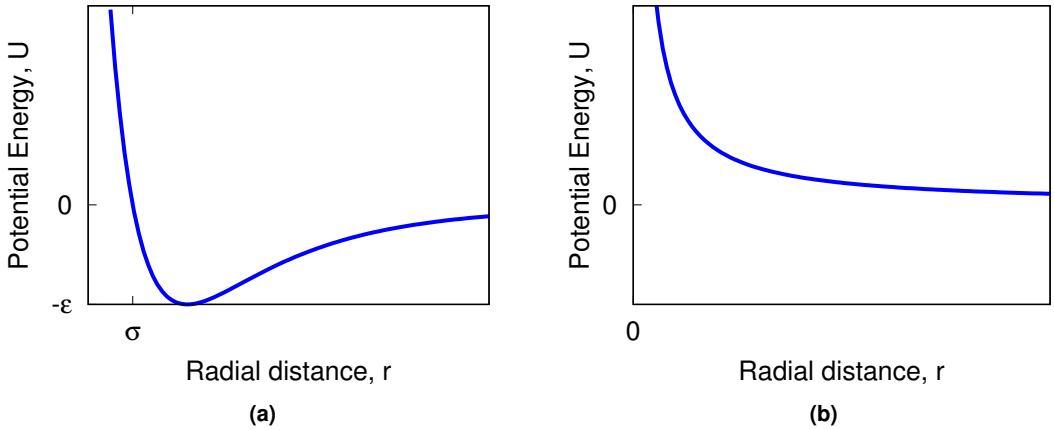


**Figure 3.1:** Variation of potential energy in: (a) Lennard-Jones (LJ) and (b) Coulomb potential models.

### Effect of cut-off

The LJ and Coulomb potentials have long-range interaction components. Theoretically, then, an atom should interact with *all* other atoms in a simulation. Realistically, this is not possible nor necessary in MD simulations; instead, there are techniques developed to reduce the number of interaction calculations and hence the computational cost. A "cut-off" length is introduced in which atoms exceeding a certain separation, $r_{cut}$, are ignored from force and energy calculations. This is often chosen to be large enough that the forces are considered negligible, however, can be a problem for energy conservation as there is a significant accumulated potential energy that is being "lost" through ignoring these long-range interactions. It is common to subtract a correction to "shift" the potential energy equation, which is essentially the potential energy at cut-off distance $r_{cut}$:

$$U = \begin{cases} U_0(r) - U_0(r_{cut}), & \text{for } r \leq r_{cut}, \\ 0, & \text{for } r > r_{cut}, \end{cases} \tag{3.6}$$

where $U_0$ is a generic pair-wise potential function, e.g. the LJ potential, or Coulomb potential as described above. The effect of this shift to the potential energy for the LJ potential is to smooth out the potential function near the cut-off, as shown in Figure 3.2; this can reduce anomalous effects of energy conservation, such as drifts in temperature, and surface tension effects (Cosden and Lukes, 2011; Kitchen *et al.*, 1990).

It is typical to implement a cut-off length of $r_{cut,LJ} = 2.5\sigma$ with the LJ potential for homogeneous systems (Plimpton, 1995); however, for multiphase systems, it is important to capture the interatomic interactions across the extent of the interface, and so a relatively larger cut-off of $r_{cut,LJ} = 5.0\sigma = 1.65\,\text{nm}$ was chosen for all LJ interactions (Maheshwari *et al.*, 2016). A smaller cut-off was used for the Coulomb potential, $r_{cut,C} = 1.45\,\text{nm}$, to improve the efficiency of the

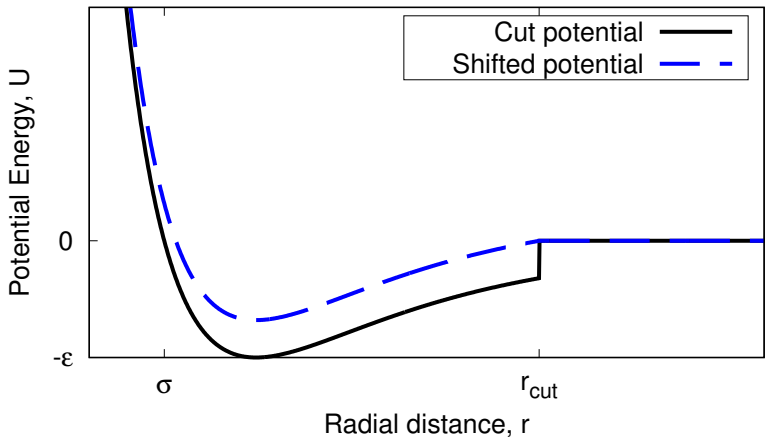


**Figure 3.2:** Effect of cut-off on LJ potential energy. The cut-off length is exaggerated for illustrative purposes.

simulations, specifically for the implementation of the TIP4P/2005 model (see Section 3.3.1) in LAMMPS (Plimpton, 1995).

An additional technique to shifting the potential is to apply long-range solvers to approximate the contribution from long-range forces and energies of far-away atoms, for example using Fast Fourier Transforms (FFTs) to solve Poisson's equation (Hockney and Eastwood, 1988; Plimpton, 1995). This can typically account for some fluid phenomena which rely on long-range interactions, namely surface tension (see Section 3.4.5), and disjoining pressure. Long-range solvers still have an associated cost and are specifically formulated assuming a completely homogeneous, periodic simulation (Matsumoto and Kataoka, 1988). Since any bubble system cannot be considered truly homogeneous, it did not seem appropriate to use long-range solvers in this research, although this could be investigated in future work.

### 3.2.3 Stillinger-Weber potential

The Stillinger-Weber (SW) potential was originally derived to model different phases of silicon (Stillinger and Weber, 1985), and is used for the monatomic water and amorphous silicon models in this thesis (see Section 3.3). It combines a pair-wise potential (between two atoms as in the LJ and Coulomb potential) in the first term and a triple-body potential between three atoms in the second term of the equation:

$$U_{SW} = \sum_i \sum_{j>i} A_{SW}\varepsilon \left[ B_{SW} \left( \frac{\sigma}{r_{ij}} \right)^{p_{SW}} - \left( \frac{\sigma}{r_{ij}} \right)^{q_{SW}} \right] \exp\left( \frac{\sigma}{r_{ij} - a_{SW}\sigma} \right) + \sum_i \sum_{j\neq i} \sum_{k>j} \lambda_{SW}\varepsilon \left[ \cos\theta_{jik} - \cos\theta_{SW} \right]^2 \exp\left( \frac{\gamma_{SW}\sigma}{r_{ij} - a_{SW}\sigma} \right) \exp\left( \frac{\gamma_{SW}\sigma}{r_{ik} - a_{SW}\sigma} \right), \quad (3.7)$$

where atoms $i$ and $j$ are separated by distance $r_{ij}$, and likewise atoms $i$ and $k$ are separated by distance $r_{ik}$; atoms $j$ and $k$ form an angle $\theta_{jik}$, subtended at atom $i$; $\varepsilon$ and $\sigma$ are the characteristic potential and length-scale, respectively. The parameters $A_{SW}$, $B_{SW}$, $a_{SW}$, $p_{SW}$, $q_{SW}$, $\lambda_{SW}$, $\theta_{SW}$ and $\gamma_{SW}$ are for fitting.

Note that Equation (3.7) gives the *total* potential energy between all the interactions in a system by the SW potential, while the potentials in Equations (3.4) and (3.5) are each for one interaction pair.

## 3.3 Atomic models

In all of the bubble simulations, water and nitrogen were used for the liquid and gas phases, respectively. There are various models for these fluids, with particular advantages (and disadvantages) in capturing certain fluid properties such as surface tension, phase changes etc. For example, there are more than 30 models for water, including SPC (Berendsen *et al.*, 1987), TIP3P (Jorgensen *et al.*, 1983), TIP4P/2005 (Abascal and Vega, 2005), TIP5P (Mahoney and Jorgensen, 2000) and monatomic water (mW) (Molinero and Moore, 2009).

There are also various models for the gaseous phase of nitrogen: the single-site "pea", or monatomic nitrogen (mN), model considers the nitrogen molecule as one LJ site (Coasne *et al.*, 2010), while the two-site $N_2$ model accounts for both nitrogen atoms individually in each molecule (Zambrano *et al.*, 2014). The models used in this thesis, as discussed below, represent only a small number of the large variety available.

### 3.3.1 TIP4P/2005 water

One of the more accurate models for capturing the condensed phases of water, TIP4P/2005, consists of four atomic sites: two charged hydrogen (H) sites, one uncharged oxygen (O) site, and one massless charged site (M), offset from the O atom (Abascal and Vega, 2005), as shown in Figure 3.3(a). The positioning of the charged sites is intended to capture the polar nature of water.

The TIP4P/2005 water ($H_2O$) molecules (from here on will be simply referred to as $H_2O$ molecules) interact via the LJ and Coulomb potentials, Equations (3.4) and (3.5), respectively. The H atoms have a net positive charge, while the M sites have a negative charge and interact through the Coulomb potential; the O atoms interact only through the LJ potential. The LJ and Coulomb potential parameters of the TIP4P/2005 model are given in Table 3.1. The bond lengths and angles of the $H_2O$ molecules were kept fixed at $r_{OH} = 0.09572\,\text{nm}$, $r_{OM} = 0.01546\,\text{nm}$ and $\theta_{HOH} = 104.52^\circ$, using the LAMMPS *SHAKE* algorithm (Abascal and Vega, 2005; Plimpton, 1995).

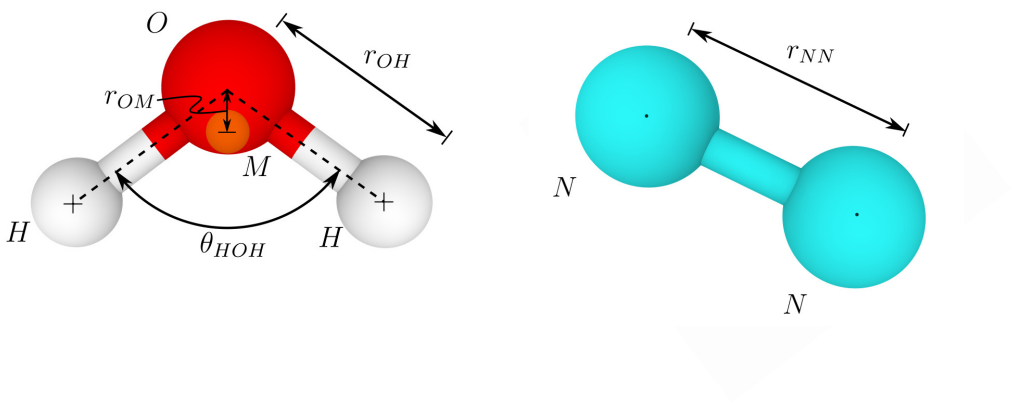


(a) (b)

**Figure 3.3:** Schematics of the: (a) TIP4P/2005 water molecule, and (b) two-site nitrogen molecule.

| **Atom/** interatomic pair | Atom mass $(10^{-26}\,\mathrm{kg})$ | $\varepsilon\ (10^{-21}\,\mathrm{J})$ | $\sigma$ (nm) | $q$ (e) |
|---|---|---|---|---|
| **H** | 0.16738 | 0 | 0 | 0.5564 |
| **M** | 0 | 0 | 0 | −1.1128 |
| **O** | 2.6568 | 1.2867 | 0.3159 | 0 |
| O–$S_o$ | - | 0.9000 | 0.2815 | - |
| O–$S_i$ | - | 2.25 | 0.2815 | - |
| **N** | 2.3259 | 0.50248 | 0.3320 | 0 |
| N–O | - | 0.90632 | 0.3243 | - |
| N–$S_o$ | - | 7.000 | 0.2815 | - |
| N–$S_i$ | - | 1.3984 | 0.2815 | - |

**Table 3.1:** Atom types and parameters for interatomic potential interactions between TIP4P/2005 $H_2O$ model (Abascal and Vega, 2005), two-site $N_2$ model (Zambrano *et al.*, 2014) and LJ solid atoms ($S_i$/$S_o$), as used in Chapter 4. LJ parameters for atoms in bold are given for pairs of like atoms.

### 3.3.2 Two-site nitrogen

Nitrogen gas exists as a diatomic molecule, as shown in Figure 3.3(b). The two-site nitrogen ($N_2$) model (from here on will be simply referred to as $N_2$ model) used for some of the research in this thesis interacts only by the LJ potential, Equation (3.4), and the parameters for these interactions, as well as interactions with the TIP4P/2005 model, are also given in Table 3.1.

Bond lengths were kept fixed at $r_{NN} = 0.1098\,\text{nm}$ using the LAMMPS *SHAKE* algorithm (Plimpton, 1995).

### 3.3.3 Monatomic water (mW)

TIP4P/2005 is generally accepted as one of the most accurate models for water given its ability to capture a wide variety of its fluid properties (see Section 3.4 for some examples); however, the model can be computationally expensive with four atomic sites per molecule to calculate every timestep. For some of the research, where a large number of water molecules was needed to approximate a semi-infinite liquid, the cheaper monatomic water (mW) model was used instead (Molinero and Moore, 2009). The mW model is a single-site water molecule, with dynamics governed by the Stillinger-Weber potential[1]. The parameters for Equation (3.7) for the mW potential are given in Tables 3.2 and 3.3.

| Fitting parameter | Value |
|---|---|
| $A_{SW}$ | 7.049 556 27 |
| $B_{SW}$ | 0.602 224 558 4 |
| $a_{SW}$ | 1.8 |
| $p_{SW}$ | 4 |
| $q_{SW}$ | 0 |
| $\lambda_{SW}$ | 23.15 |
| $\theta_{SW}$ | 109.47° |
| $\gamma_{SW}$ | 1.2 |

**Table 3.2:** Fitting parameters used in Equation (3.7) to obtain a coarse-grained model for monatomic water (Molinero and Moore, 2009; Stillinger and Weber, 1985), as used in Chapters 5 and 6.

The mW model can replicate the hydrogen-bonded structure of water via the tetrahedral, triple-body term in Equation (3.7), without needing to include long-range interactions, as required for the TIP4P/2005 water model (Molinero and Moore, 2009). While mW is successful for reducing computational cost, some of the fluid properties of $H_2O$, such as viscosity, are not as accurately captured (see Section 3.4.6). This is generally one of the compromises of using simpler models in MD, however, if these discrepancies are known in advance, they can still be very useful in validating cavitation models.

1. While it is well known that water and nitrogen are polyatomic molecules, the terms “atoms” and “molecules” will be used interchangeably throughout to denote any single-site body in the MD simulations.

### 3.3.4 Monatomic nitrogen (mN)

A monatomic nitrogen (mN) model (Coasne *et al.*, 2010) was used in conjunction with the mW model to reduce computational cost in some of the research. Interactions between the mN molecules, and also between the mN and mW molecules, were modelled by the LJ potential, Equation (3.4). Interaction parameters for the mN model are also given in Table 3.3.

| **Atom/** Interatomic pair | Interaction type | Molecule mass $10^{-26}$ kg | $\varepsilon\ (10^{-21}\mathrm{J})$ | $\sigma$ (nm) |
|---|---|---|---|---|
| **mW** | SW | 2.9915 | 42.9993 | 0.23925 |
| mW–mN | LJ | - | 0.68497 | 0.30713 |
| mW–$S_o$ | LJ | - | 1.5000 | 0.24318 |
| mW–$S_i$ | LJ | - | 3.1542 | 0.24318 |
| **mN** | LJ | 4.6517 | 1.3144 | 0.37500 |
| mN–$S_o$ | LJ | - | 3.8747 | 0.31105 |
| mN–$S_i$ | LJ | - | 1.8350 | 0.31105 |

**Table 3.3:** Atom types and parameters for interatomic potential interactions between mW model (Molinero and Moore, 2009), mN model (Coasne *et al.*, 2010) and LJ solid atoms ($S_i$/$S_o$), as used in Chapters 5 and 6. Parameters for atoms in bold are given for pairs of like atoms. Any interaction pairs not given are equal to zero.

### 3.3.5 Lennard-Jones solid

The solid substrates' role in the surface nanobubble systems is primarily to provide contact line pinning, as well as the general surface for the bubble to rest on. Fortunately, this can be done with relatively simple models, so the majority of the computational effort can be focussed on the fluid behaviour. The solid substrates were modelled as a face-centred cubic (FCC) crystal structure, with lattice spacing of $a_S = 0.392\,\mathrm{nm}$.

For Chapters 4 and 5, the atoms in the substrate are kept rigid, i.e. they are all fixed in their original position. Since the solid (S) atoms are perfectly immobile the energy of fluid atoms is conserved in a solid-fluid atomic collision; there is no heat transfer from the fluid when in contact with the rigid solid and no temperature drift is observed in the fluid from this interaction. The interaction potentials between like pairs of rigid solid atoms were unimportant and do not need to be listed here. However, the characteristic length ($\sigma_S = 0.2471\,\mathrm{nm}$) is required to determine the surface-liquid and surface-gas interaction potentials, and these were obtained using the Lorentz mixing rule (Lorentz, 1881).

The interactions between the fluid atoms and solid atoms are important, however, as this governs wetting behaviour and general hydrophobicity and hydrophilicity. These interactions

were modelled using Equation (3.4) and can be found for each specific solid-liquid and solid-gas interactions in Sections 3.4.2 and 3.4.4, respectively. This substrate type was also used for the piston that controlled the pressure in all of the surface nanobubble simulations (see section 3.5).

#### Contact line pinning

As discussed in Chapter 2, the surface nanobubble contact line is pinned by surface heterogeneities, typically either surface roughness or chemical patterning on the surface. It was found that the size of the roughness required to pin the contact line was of the order of $\sim 1\,\text{nm}$. Considering this was close to the sizes of the nanobubbles under investigation in the MD simulations, it was deemed more appropriate to employ chemical patterning for contact line pinning in this research, so the volume of the gas phase of the bubble would not be influenced by the rough nano-structured surface it was resting on.

The simplest chemical pattern found to provide this pinning effect was alternating hydrophobic ($S_o$) and hydrophilic ($S_i$) patches (Maheshwari *et al.*, 2016; Wang and Wu, 2013). Hydrophobicity governs the contact angle on the solid, see section 3.4.2. The LJ potential parameters for the $S_o$ and $S_i$ atom types interacting with the different fluid models are also given in Tables 3.1 and 3.3. See Section 3.4 for how these potentials were obtained.

### 3.3.6 Amorphous silicon

The LJ solid model described in the previous section is suitable for simulations where only the fluid behaviour is important. In collapsing cavitation bubble simulations (see Chapter 6) it becomes important to also model the substrate to accurately predict the solid damage. This substrate material was chosen to be amorphous silicon (aSi), which can be modelled using the SW potential in Equation (3.7) (Stillinger and Weber, 1985; Vink *et al.*, 2001).

The parameters used in Equation (3.7) to model aSi are given in Tables 3.4 and 3.5. Chemical patterning was employed again to provide contact line pinning; hydrophobic ($aSi_o$) and hydrophilic ($aSi_i$) silicon atom types were used, with potential parameters between the different silicon atoms and the mW and mN fluid models also given in Table 3.5.

| Fitting parameter | Value |
|---|---|
| $A_{SW}$ | 7.049 556 27 |
| $B_{SW}$ | 0.602 224 558 4 |
| $a_{SW}$ | 1.8 |
| $p_{SW}$ | 4 |
| $q_{SW}$ | 0 |
| $\lambda_{SW}$ | 31.5 |
| $\theta_{SW}$ | 109.47° |
| $\gamma_{SW}$ | 1.2 |

**Table 3.4:** Fitting parameters used in Equation (3.7) to obtain a model for non-rigid amorphous silicon (Stillinger and Weber, 1985; Vink *et al.*, 2001), as used in Chapter 6.

| **Atom/** Interatomic pair | Interaction type | Molecule mass $10^{-26}$ kg | $\varepsilon\ (10^{-21}\mathrm{J})$ | $\sigma$ (nm) |
|---|---|---|---|---|
| **$aSi_o$** | SW | 4.6637 | 264.0921 | 0.20951 |
| **$aSi_i$** | SW | 4.6637 | 264.0921 | 0.20951 |
| mW–$aSi_o$ | LJ | - | 1.7492 | 0.2244 |
| mW–$aSi_i$ | LJ | - | 3.2756 | 0.2244 |
| mN–$aSi_o$ | LJ | - | 7.1416 | 0.27076 |
| mN–$aSi_i$ | LJ | - | 3.9361 | 0.27076 |

**Table 3.5:** Atom types and parameters for interatomic potential interactions between mW (Molinero and Moore, 2009) and mN models (Coasne *et al.*, 2010) with the hydrophilic ($aSi_i$) and hydrophobic ($aSi_o$) amorphous Silicon atom models (Vink *et al.*, 2001), as used in Chapter 6. Parameters for atoms in bold are given for pairs of like atoms. Any interaction pairs not given are equal to zero.

## 3.4 Benchmark results

The potential parameters given in Section 3.3 were either found from literature, or from calibration studies to obtain particular material properties, such as solubility, wettability, etc. The suitability of these potentials is assessed with benchmark tests in the following subsections.

### 3.4.1 Equations of state

The equation of state defines how certain thermodynamic properties of a substance, such as density, vary under different environmental conditions like temperature and pressure. During cavitation events, bubbles are subjected to a wide range of pressures and so it is important to assess how accurate the nitrogen and water MD models are at capturing the fluid densities during these pressure variations. For all the fluids presented here, the equations of state from experiments and other literature are compared to MD simulations, using the models presented in Section 3.3, and thermostatted to $T = 300\,\mathrm{K}$, which is the temperature used in all simulations in this work.

#### Water

A fully periodic cube with lengths of 3.92 nm was filled with $H_2O$ molecules, with timestep $\Delta t = 10^{-6}\,\mathrm{ns}$. Nine simulations were run, with the number of water molecules varying between 1933 and 2094; the bulk density and pressure was measured and is plotted in Figure 3.4, with comparisons to experimental data (Lemmon *et al.*, 2017). Results are also compared to experimental and MD simulation data at reduced pressures (González *et al.*, 2016; Pallares *et al.*, 2016).

The TIP4P/2005 equation of state presented in Figure 3.4 was simulated using shifted LJ and Coulomb potentials, with cut-off lengths $r_{cut,LJ} = 1.65\,\mathrm{nm}$ and $r_{cut,C} = 1.45\,\mathrm{nm}$, respectively. Figure 3.5 shows how the TIP4P/2005 equation of state varies when reducing the LJ and Coulomb potential cut-off lengths to $r_{cut,LJ} = 1.2\,\mathrm{nm}$ and $r_{cut,C} = 1.0\,\mathrm{nm}$, respectively, and also with and without shifting the LJ and Coulomb potentials at these new cut-offs. There are serious errors with the unshifted potential results, as shown in the inset in Figure 3.5, and so are unsuitable for accurately modelling water. The effect of shifting the potentials has a significant effect on increasing the accuracy of the model's equation of state; all further TIP4P/2005 simulations are run with shifted LJ and Coulomb potentials, with cut-off lengths $r_{cut,LJ} = 1.65\,\mathrm{nm}$ and $r_{cut,C} = 1.45\,\mathrm{nm}$, respectively, following this test.

MD simulations of bulk water using the mW model were run with similar parameters as for the TIP4P/2005 case described above, and are also shown in Figure 3.4. The mW simulations were run for the same number of timesteps as the TIP4P/2005 simulations but with an increased timestep of $\Delta t = 10^{-5}\,\mathrm{ns}$. The density of the mW model near ambient pressure (0.1 MPa)

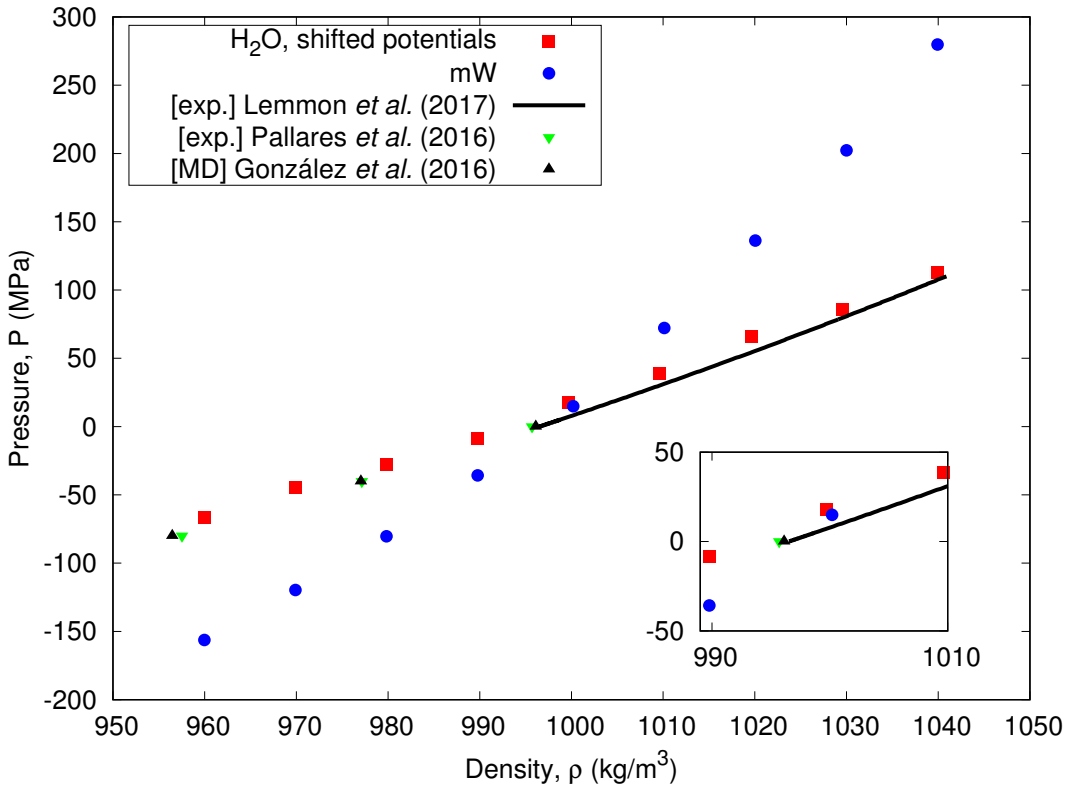


**Figure 3.4:** Equation of state for water using the $H_2O$ and mW models at 300 K. Results are compared to experimental (exp.) and other MD simulation data (González *et al.*, 2016; Lemmon *et al.*, 2017; Pallares *et al.*, 2016). The inset shows results close to the typical range of pressures used in this research.

matches the TIP4P/2005 MD results, and experimental results of Lemmon *et al.* (2017). However, the gradient of the $P$-$\rho$ curve is much steeper for the mW model than other models for water. This anomalous behaviour has been acknowledged by the authors of the mW model, Molinero and Moore (2009). This discrepancy should not present a problem to cavitation simulations, although the steeper curve in Figure 3.4 does cause a higher speed of sound in the liquid (see Section 3.4.7). More significant is that both TIP4P/2005 and mW models can support tensile loading (in liquid state), which is crucial for the cavitation simulations that follow.

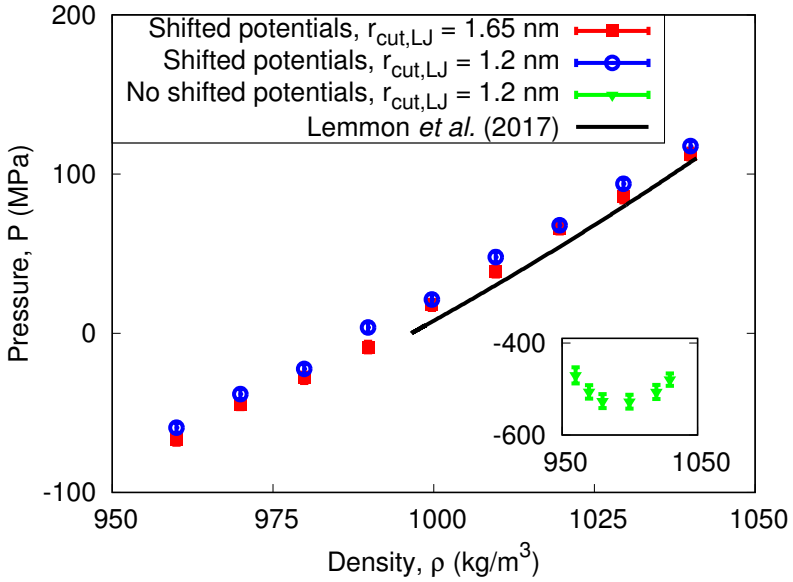


**Figure 3.5:** Equation of state for water using the $H_2O$ models at 300 K, with reduced LJ and Coulomb potential cut-off lengths, and also with and without shifting the LJ and Coulomb potentials. The inset shows the anomalous results when no potential shifting is employed. Results are compared to experimental data (Lemmon *et al.*, 2017).

### Nitrogen

A fully periodic cube with lengths of 7.84 nm was filled with differing numbers of nitrogen molecules, using both the two-site and single-site nitrogen models, respectively. Fifteen simulations were run for each model, with nitrogen molecule counts varying from 5 to 5914. The results of the MD equations of state simulations are shown in Figure 3.6, and compared with experimental data (Lemmon *et al.*, 2017). Also shown in Figure 3.6 is the ideal gas law relation $PV = Nk_BT$.

The inset in Figure 3.6 shows the gas density and pressure at lower pressures, and that both models are in good agreement with the experimental results of Lemmon *et al.* (2017) and also the classical ideal gas law. Results only appear to significantly diverge for pressures over 20 MPa, which is above the operating range of the following surface nanobubble simulations, and so both models should be suitable for investigation.

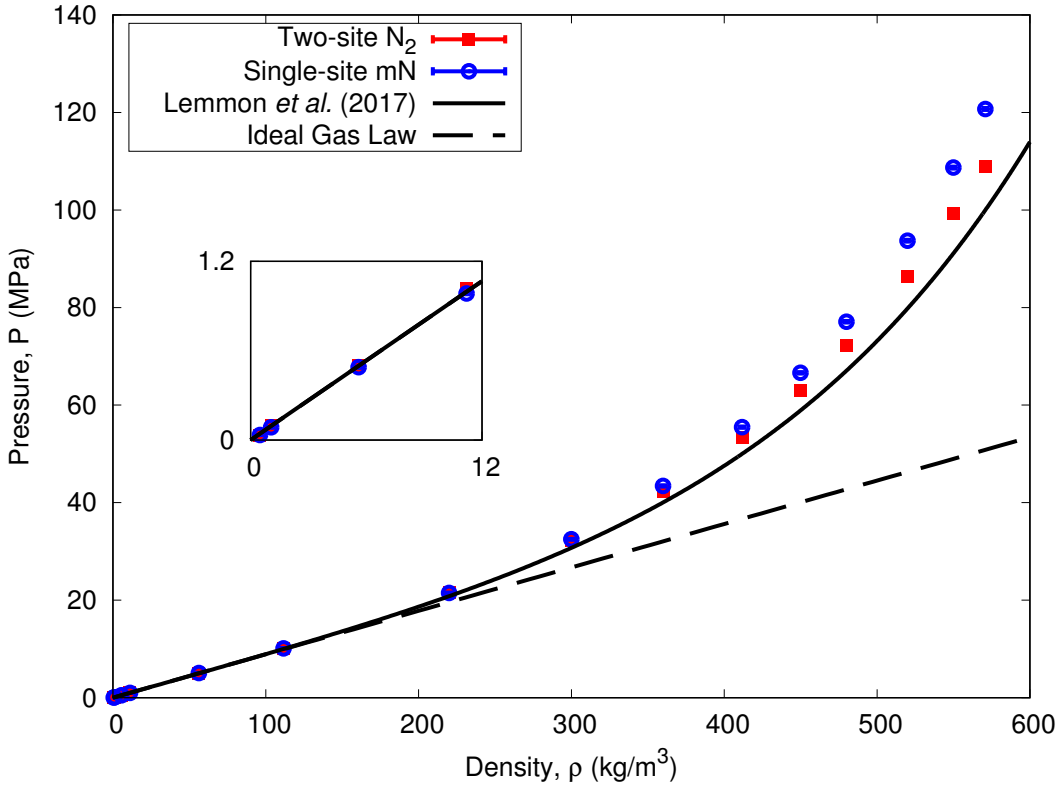


**Figure 3.6:** Equation of state for nitrogen gas using the two-site ($N_2$) and single-site (mN) models at 300 K. Results are compared to experimental data (Lemmon *et al.*, 2017), and the ideal gas law $PV = Nk_BT$. The inset shows results at lower pressures.

### 3.4.2 Contact angle: solid-liquid interactions

It was necessary to determine the contact angle of the water models on each of the different solid models listed in Section 3.3. A liquid droplet was equilibrated on the solid surface, and a spherical cap was fitted to the 50% isodensity contour of the liquid phase. The internal contact angle of a spherical cap can be obtained via geometrical relations:

$$\cos\theta = \frac{-z_c}{R}, \tag{3.8}$$

where $z_c$ is the central coordinate of the spherical cap fit, and $R$ is the fitted radius of curvature.

The LJ potential parameters were varied between the solid (subscript $s$) and liquid (subscript $l$) models, and appropriate values of $\varepsilon_{s,l}$ were chosen based on the desired wettabilities. The $\sigma_{s,l}$ values in the liquid-solid LJ interaction were determined using the Lorentz mixing rule (Lorentz, 1881). For the TIP4P/2005 model (which has four sites), the LJ potential parameters were specified between the O atom and the solid atoms. The unique liquid-solid pairs that were investigated were $H_2O$–S, mW–S and mW–aSi. The variation in liquid-side contact angle $\theta_O$ with LJ interaction potential $\varepsilon_{s,l}$ for each pair is shown in Figure 3.7. Also shown in Figure 3.7

is the equivalent gas-side contact angle, i.e. $\theta = 180 - \theta_O$. As discussed previously, the gas-side contact angle $\theta$ will be used for the rest of this thesis.

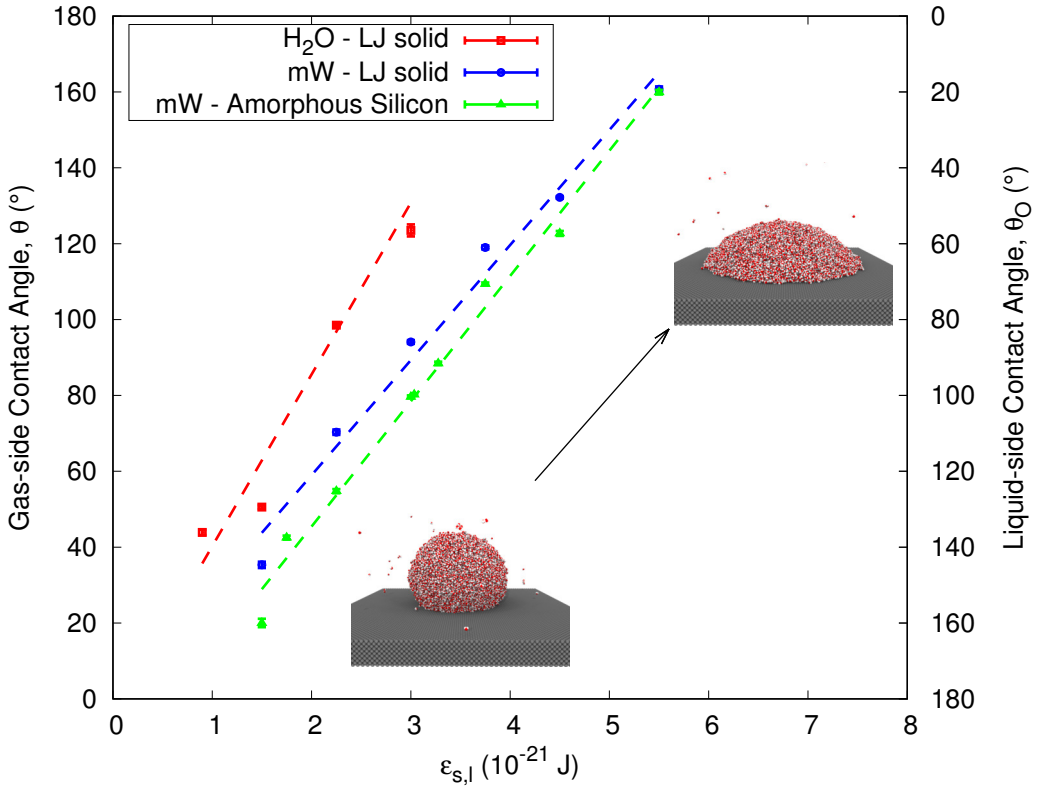


**Figure 3.7:** Variation of droplet contact angle with LJ interaction potential for different atomic model pairs. The dashed lines show the straight lines of best fit. The insets show the typical variation in the droplet contact angle with $\varepsilon_{s,l}$, through renderings of the $H_2O$ droplet simulations (Stukowski, 2010).

The equilibrium gas-side contact angles of the $H_2O$ model, and $S_i$ and $S_o$ substrates were chosen to be 99° and 43°, respectively, as shown in Figure 3.7, with appropriate LJ parameters given in Table 3.1. The gas-side contact angles of the mW $H_2O$ model on the $S_i$ and $S_o$ atom types were chosen to be 99° and 35°, respectively, and with appropriate parameters given in Table 3.3. Finally, the gas-side contact angles for the mW model with $aSi_i$ and $aSi_o$ interactions were chosen to be 88° and 43°, respectively, with appropriate parameters given in Table 3.5.

### 3.4.3 Solubility: liquid-gas interactions

The long-term stability of a surface nanobubble is governed by the surrounding liquid supersaturation, see Equation (2.10). Potentials between the different liquid and gas models were calibrated to match the solubility of nitrogen in water. The different liquid-gas combinations used in this research were the $H_2O$–$N_2$ and mW–mN model pairs.

Simulations were run in a fully periodic box containing a slab of 4740 water molecules, and a slab of nitrogen molecules. A typical simulation is shown for 10 MPa in Figure 3.8. The number

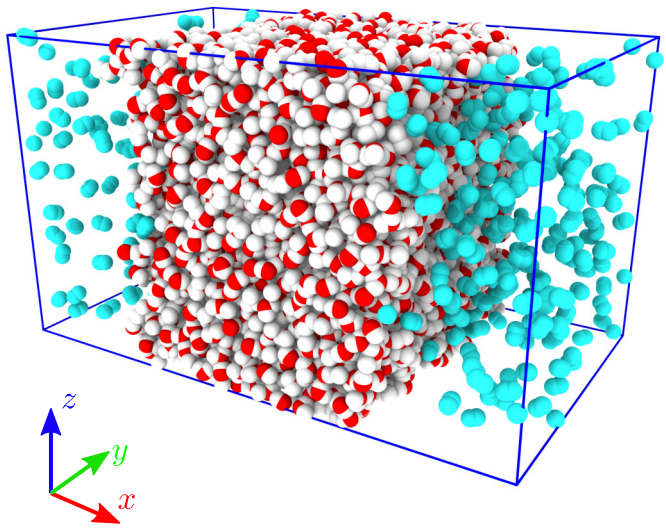


**Figure 3.8:** Rendering of a typical $H_2O$ and $N_2$ solubility simulation. Oxygen atoms are shown in red, hydrogen atoms in white and nitrogen atoms in cyan.

of nitrogen molecules was varied between 345 and 1280 to investigate the effect of pressure, and simulations were run until they had reached diffusive equilibrium.

The LJ interaction potentials between the mW–mN models were varied to achieve agreement in Henry's constant $H$ with experimental results (Sander, 2017), see Equation (2.7). The variation in $H$ with the LJ liquid and gas (subscript $g$) potential $\varepsilon_{l,g}$ is shown in Figure 3.9. The potential was interpolated from results in Figure 3.9 to match Henry's constant from experimental results (Sander, 2017), and is given in Table 3.3. The $\sigma_{l,g}$ value for the mW–mN LJ interactions was determined by the Lorentz mixing rule (Lorentz, 1881).

The variation in solubility with pressure for the mW–mN model pair, using LJ potential parameters from Table 3.3, is shown in Figure 3.10. The $H_2O$–$N_2$ interaction parameters were obtained from Zambrano *et al.* (2014) and confirmed to agree with experimental data (Sander, 2017), as shown in Figures 3.9 and 3.10. The slopes in Figure 3.10 correspond to Henry's constant $H$ in Equation (2.7).

Note that the slope of the mW–mN pair is slightly less than the experimental data of Sander

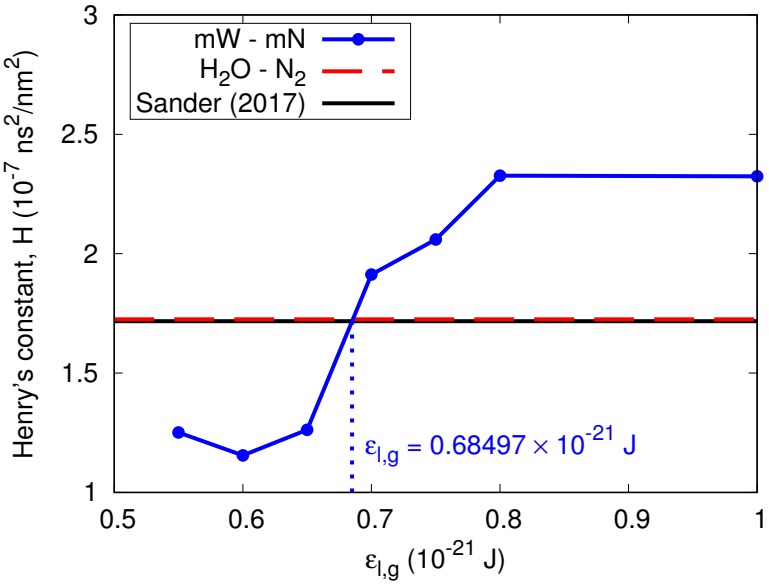


**Figure 3.9:** Variation in Henry's constant with LJ interaction potential $\varepsilon_{l,g}$ for the mW–mN model pairs. The solid black line shows the experimental value of Henry's constant from Sander (2017), and the red dashed line shows the measured value of Henry's constant for the $H_2O$–$N_2$ MD model pairing (Zambrano *et al.*, 2014). The blue dotted line shows the interpolated value for the mW–mN interaction potential, as given in Table 3.3.

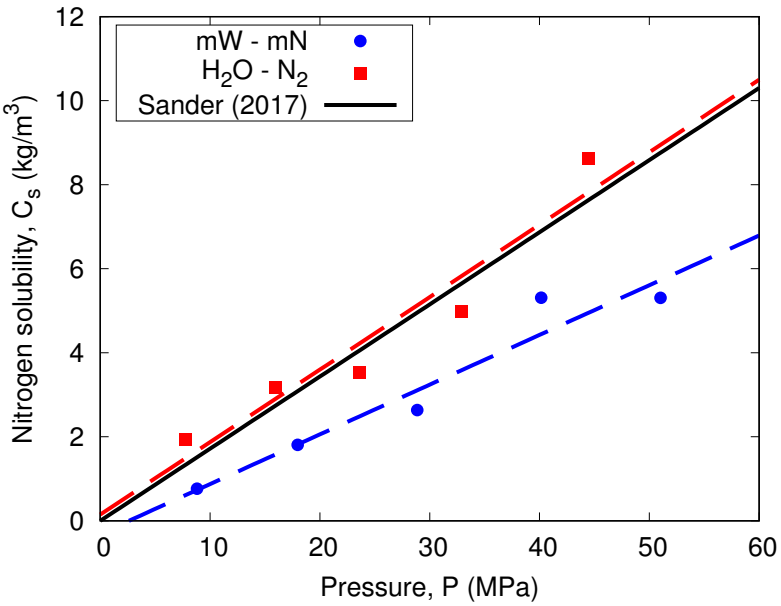


**Figure 3.10:** Variation in nitrogen gas solubility in water for the $H_2O$–$N_2$ and mW–mN MD model pairs. Results are compared to experimental data (Sander, 2017).

(2017). However, as discussed in Chapter 2, the cavitation dynamics of bubbles are much more rapid than the diffusive dynamics, so this should not be a problem for this research.

### 3.4.4 Nitrogen density layering

The solid's interaction with the multi-phase fluid is mostly governed by the liquid-solid potentials $\varepsilon_{s,l}$, as described in Section 3.4.2. The interactions between the solid and gas were considered less important for the surface nanobubbles, provided contact line pinning was achieved with the different liquid-solid interactions; however, appropriate solid-gas potentials could enhance the hydrophobic/hydrophilic nature of the solid surfaces, and so were not completely unimportant (Maheshwari *et al.*, 2016, 2018).

Atoms in fluids tend to order themselves in layers close ($\lesssim 1\,\text{nm}$) to solid boundaries, as shown in Figure 3.11(a); this is most prominent in liquids but can also be observed in gases (Ramisetti *et al.*, 2017; Zambrano *et al.*, 2014). This ordering results in distinct peaks in the measured density close to the solid surface, as shown in Figure 3.11(b), and is dependent on $\varepsilon_{s,g}$. Because

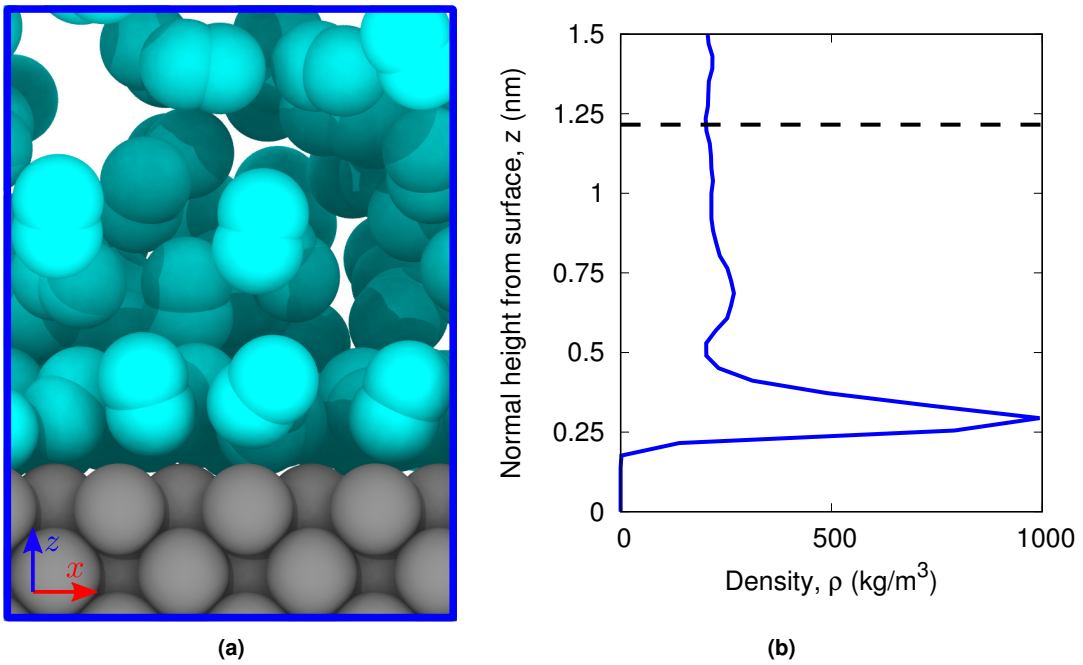


**Figure 3.11:** (a) Schematic of layering of nitrogen molecules on a solid substrate, and (b) typical fluctuating density profile in gas near a solid surface. The black dashed line shows the upper limit ($z = 1.2\,\text{nm}$) of the mean density measurement region.

of this fluctuating layer it is usually important to measure bulk fluid properties, such as density and pressure, outside of this layer, and away from surfaces in general.

The $N_2$–S model pairing was first employed for initial surface nanobubble simulations (see Section 3.6). A similar $\varepsilon_{s,g}$ for the $N_2$–$S_o$ atom pair was used from Ramisetti *et al.* (2017). Similar scaling to Maheshwari *et al.* (2016, 2018) was used for the relative $\varepsilon_{s,g}$ potentials to obtain the $N_2$–$S_i$ for the hydrophilic substrates. These preliminary surface nanobubble simulations showed the gas–solid potentials were suitable, particularly for pinning the contact line

(see Section 3.6), and so the corresponding mean density values for the $S_o$ and $S_i$ LJ solid substrates with the two-site $N_2$ model were used as the benchmark values for the other model pairs, as shown by the dashed and dotted lines in Figure 3.12, respectively. The values for $\varepsilon_{s,g}$ were interpolated from these target densities for the mN–$S_i$, mN–$S_o$, mN–a$Si_i$ and mN–a$Si_o$ model pairs, as given in Tables 3.1, 3.3, and 3.5. The mean density $\bar{\rho}$ was measured within

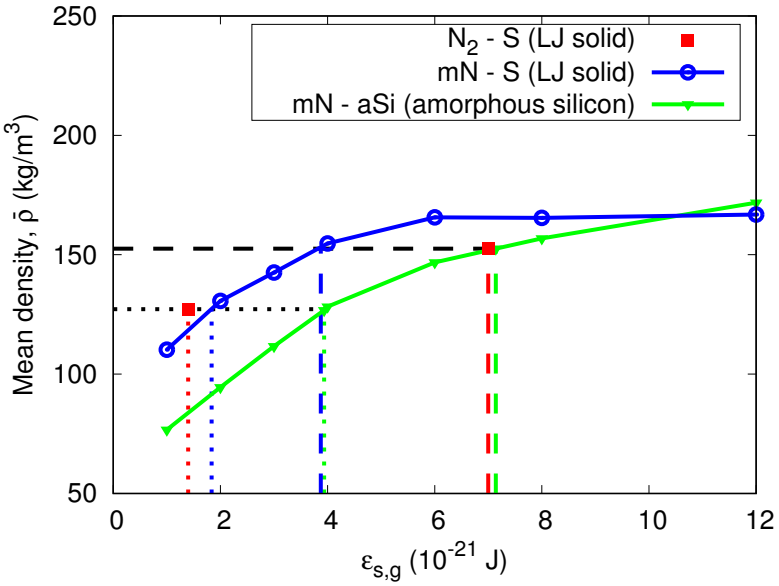


**Figure 3.12:** Variation of mean gas-density near the solid wall as a function of LJ interaction potential $\varepsilon_{s,g}$, for different gas-solid MD model pairs. The black dotted line shows the target mean density on the hydrophilic substrates, and the red, blue and green dotted lines show the chosen $\varepsilon_{s,g}$ values for the $N_2$–$S_i$, mN–$S_i$ and mN–a$Si_i$ model pairs, respectively. The black dashed line shows the target mean density of the hydrophobic substrates, and the red, blue and green dashed lines show the chosen $\varepsilon_{s,g}$ values for the $N_2$–$S_o$, mN–$S_o$ and mN–a$Si_o$ model pairs, respectively.

$z < 1.2\,\text{nm}$, where $z$ is the normal distance from the solid surface, as shown by the dashed line in Figure 3.11(b). The $\sigma_{s,g}$ LJ interaction values were determined by the Lorentz mixing rule (Lorentz, 1881).

### 3.4.5 Surface tension

Surface tension can be calculated from:

$$\gamma = \int_{-\infty}^{\infty} [\tau_t - \tau_n] \mathrm{d}x, \tag{3.9}$$

where $\gamma$ is the surface tension, and $\tau_t$, $\tau_n$ are the diagonal stress tensor elements that act tangentially and normal to the fluid interface, respectively, found from Equation (3.2) (Che and Theodorakis, 2017; Shi *et al.*, 2006). When $x$ is the normal distance from the surface, the

normal stress is given by $\tau_n = \tau_x$, and the mean tangential stress is $\tau_t = (\tau_y + \tau_z)/2$. The integral limits should ideally extend out to an infinite fluid, however, in practice Equation (3.9) typically converges within 1 nm of the interface.

An MD simulation was run for the each of the TIP4P/2005 and mW models, containing a slab of water, interfacing with its own vapour, as shown in Figure 3.13(a) for the mW case. The density and stress tensor components across the two interfaces of the mW slab are also shown in Figures 3.13(b) and 3.13(c), respectively. Another interesting point to note about multiphase fluids at the atomic level is that the interfaces in Figure 3.13(b) are not sharp, as is commonly assumed in some of the continuum-based methods mentioned in Chapter 2. Instead, there is a smooth transition in density between the vapour and liquid phase, which can be approximated as a hyperbolic tangent function (Weijs *et al.*, 2011).

The surface tension was measured and averaged across both of the plane liquid/vapour interfaces using Equation (3.9). The measured surface tension values for the TIP4P/2005 and mW models were $57.35\,\mathrm{mJ/m^2}$ and $65.38\,\mathrm{mJ/m^2}$, respectively. Note that these are lower than the expected experimental value of $71.69\,\mathrm{mJ/m^2}$ at ambient conditions (Lemmon *et al.*, 2017). This is most likely due to the cut-off lengths used in the MD modelling, and also by not implementing long-range interactions, which is not trivial to achieve in multi-phase MD systems (Janeček, 2006; Matsumoto and Kataoka, 1988; Shi *et al.*, 2006).

Some authors also suggest that increasing supersaturation typically reduces surface tension, which may influence the diffusive equilibrium shapes of surface nanobubbles (Attard, 2016). In Section 3.6 and later chapters it is found that the above values for surface tension give good estimates for the internal gas pressure by Equation (2.1), even with high supersaturations to achieve diffusive equilibrium.

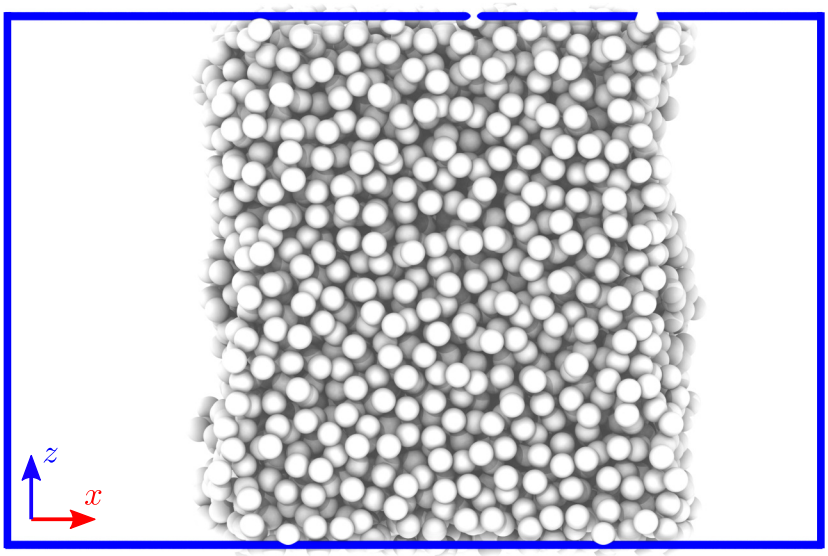


(a)

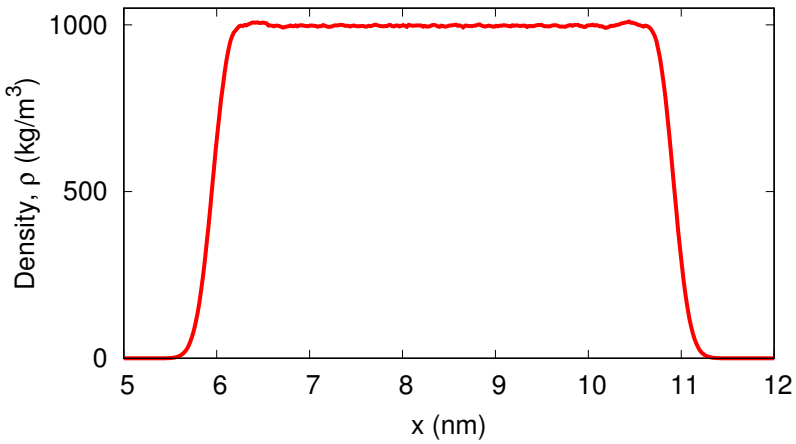


(b)

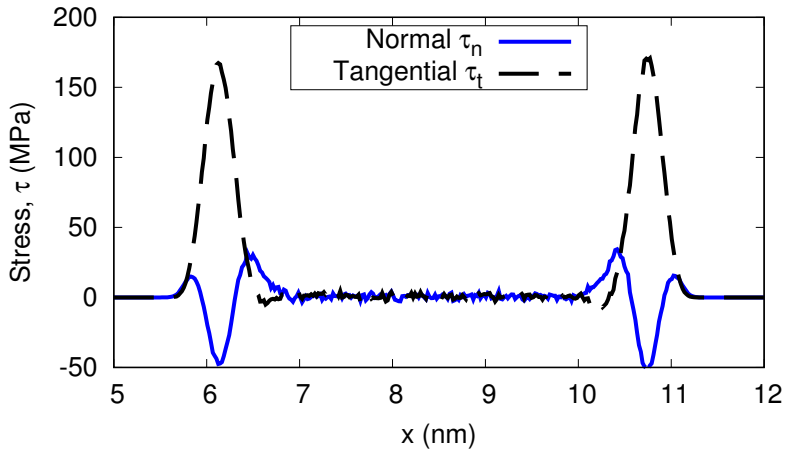


(c)

**Figure 3.13:** (a) Schematic of the mW surface tension simulation, with the variations in: (b) density, and (c) tangential and normal stress tensor contributions across the interfaces.

### 3.4.6 Viscosity

Viscosity is the fluid property that dissipates kinetic energy into heat via shear stresses. In the context of cavitation, the liquid's viscosity is dominant and the gas viscosity can typically be ignored. The effects of viscosity are mostly relevant to the oscillation dynamics of cavitation bubbles, as in Equation (2.4) (see Chapter 5).

In a molecular context, viscosity arises from strong short-range atomic interactions disrupting the mean local flow of the bulk fluid. The viscosity of a liquid can be estimated by the Green-Kubo formulation (Green, 1954; Kirova and Norman, 2015; Kubo, 1957):

$$\mu = \frac{V}{k_B T} \int_0^\infty \langle \tau_{xy}(0) \tau_{xy}(t) \rangle \mathrm{d}t, \tag{3.10}$$

where $\tau_{xy}$ is the sum of the stress tensor shear stress components, for all the atoms within the domain volume $V$. Equation (3.10) is a special case of the Green-Kubo formulation in which transport coefficients can be obtained by an auto-correlation function: $\int_0^\infty \langle \dot{A}(0)\dot{A}(t) \rangle \mathrm{d}t$, where the angle brackets $\langle ... \rangle$ represent the time average of a property, and $\dot{A}$ is some rate-dependent term (Green, 1954; Kubo, 1957). In the MD liquids, Equation (3.10) converges well within 10 ns.

An equilibrium simulation was run for the different liquid models, TIP4P/2005 and mW, of a 165 $\mathrm{nm}^3$ cube containing 5531 water molecules, at a fixed temperature of 300 K. Viscosities of the TIP4P/2005 and mW models were calculated from Equation (3.10) to be 0.8441 mPa s and 0.3350 mPa s, respectively. The TIP4P/2005 model better matches the real viscosity of water, $\mu = 0.853$ mPa s (Lemmon *et al.*, 2017), than the mW model.

### 3.4.7 Shock wave dynamics

The speed of sound in a material can be found from:

$$c_{0,l} = \sqrt{\left(\frac{\partial P}{\partial \rho}\right)_\varsigma}, \tag{3.11}$$

where the subscript $\varsigma$ here means at constant entropy. This can be approximated from the square root of the gradient of the equation of state curves given in Figure 3.4. For the TIP4P/2005 model, $c_{0,l} = (1500 \pm 40)$ m/s from Figure 3.4, which is in good agreement with the experimentally observed value for water sound speed $c_{0,l} = 1501.5$ m/s, at $T = 300$ K and $P_\infty = 0.1$ MPa (Lemmon *et al.*, 2017). This value is mostly insensitive to pressure in the condensed phase. The mW model has an enhanced sound speed $c_{0,l} = (2300 \pm 200)$ m/s, compared to the TIP4P/2005 model and experimental reference, due to the steeper slope in Figure 3.4.

In Chapter 6, spherical and surface nanobubbles are induced to collapse from an incoming shock wave. A shock wave can be propagated within an MD simulation by moving a group

of (piston) atoms at a prescribed particle velocity $u_p$, of the order of the sound speed $c_{0,l}$, as shown in the schematic in Figure 3.14(a). The shock front can be seen from the red colouring scheme of the atoms, which qualitatively shows the magnitude of the virial stress tensor from Equation (3.2). Figure 3.14(b) shows the step-change in pressure due to this shock wave

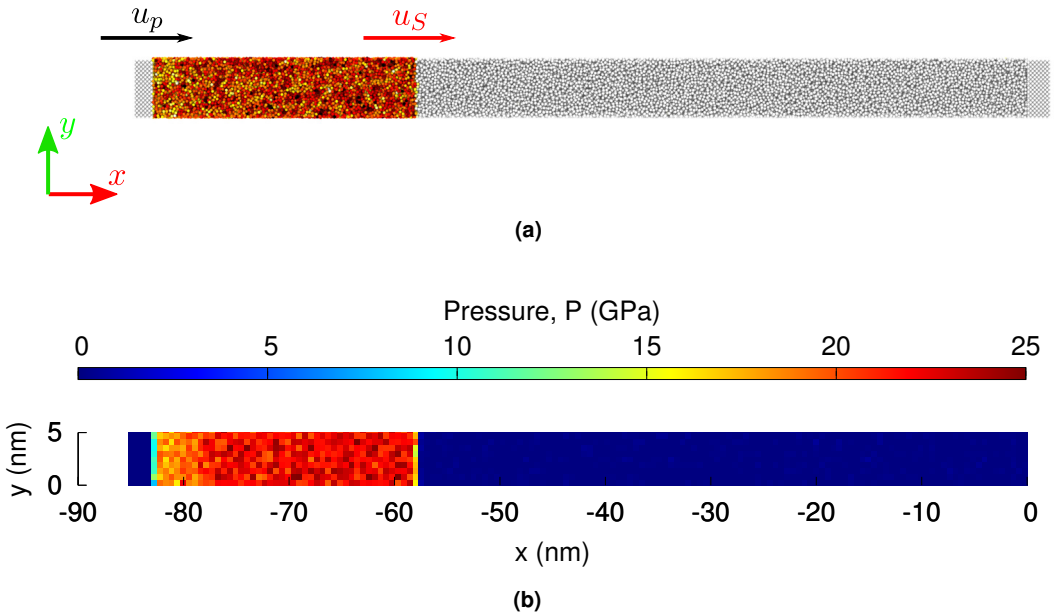


**Figure 3.14:** (a) Schematic showing the propagation of a shock wave with velocity $u_S$ in a long column of liquid, by moving the left group of white piston atoms at $u_p$ (the red colouring qualitatively shows the magnitude of each atom's virial stress to visualise the shock front), and (b) measured pressure in the liquid column.

propagation, for $u_p = 2500\,\mathrm{m/s}$. The shock front can be seen around $x = -58\,\mathrm{nm}$.

The velocity of a shock wave profile $u_S$ can be approximated as a linear function of the particle velocity and sound speed (Grady, 2017; Heymann, 1969; Vedadi *et al.*, 2010):

$$u_S = \mu_S u_p + c_{0,l}, \tag{3.12}$$

where $\mu_S$ is the fitted gradient. Only the mW model is considered here as this is the model used in Chapter 6. Several MD simulations were run in which a shock wave was propagated along the $x$ direction through a column of liquid comprising $10^5$ mW molecules, as shown in Figure 3.14(a). Particle velocities ranged from $u_p = 500\,\mathrm{m/s}$ to $u_p = 2500\,\mathrm{m/s}$. The propagation of the shock wave was measured by tracking the step-change in pressure, as shown in Figure 3.14(b). The velocities of the propagating shock waves were plotted as a function of particle velocity $u_p$, as shown in Figure 3.15.

A straight line of best fit was plotted as per Equation (3.12). Also shown in Figure 3.15 is the estimated speed of sound of the mW model from the equation of state, i.e. at $u_p = 0\,\mathrm{m/s}$. The fitted gradient was found to be $\mu_S = 2.1$, consistent with experiments on water (Heymann,

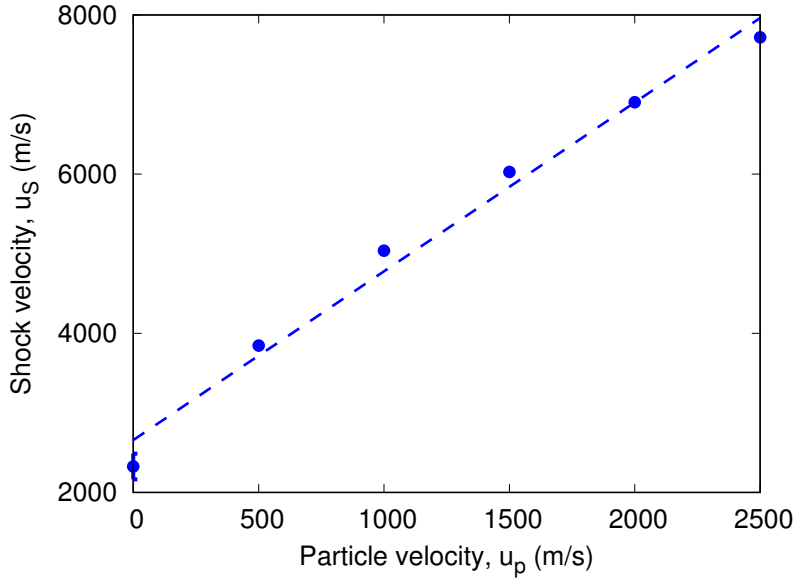


**Figure 3.15:** Variation in developed shock wave velocity $u_S$ with particle velocity $u_p$ for the mW model. The dashed line shows the fitted straight line.

1969). This property is used to predict further shock wave dynamics during spherical and surface nanobubble collapse, see Chapter 6.

### 3.4.8 Tensile strength

The tensile strength of the amorphous silicon model was tested by applying a constant unidirectional strain rate $\dot{e}$ to a solid sample, as is typically done for macroscopic materials (Ivashchenko *et al.*, 2007). A block of 16000 amorphous silicon atoms within periodic boundary conditions was stretched in the $x$ direction, and the stress $s$ and strain $e$ were measured, as shown in Figure 3.16. Strain rate was fixed at $\dot{e} = 5 \times 10^8\,\mathrm{s}^{-1}$, and temperature was thermostatted to 300 K.

The elastic deformation can be seen by the initial linear regime in Figure 3.16, shown by the dashed line. The gradient of this fitted line, the Young's modulus, was found to be $E = 58\,\mathrm{GPa}$. The curve begins to deviate from the elastic regime around 3.6 GPa, which is labelled in Figure 3.16 as the yield stress $s_Y$. The stress peaks at around 5.5 GPa, which can be considered the ultimate tensile strength of the amorphous silicon model. These values are consistent with the ranges observed in previous experiments (Berla *et al.*, 2014), and MD simulations (Ivashchenko *et al.*, 2007; Kilymis *et al.*, 2019).

During the tensile test, the amorphous silicon sample contracted in the $y$ and $z$ directions. The Poisson's ratio was estimated from $\nu_P = -0.5(e_y + e_z)/e_x = 0.33$, where $e_x$ is the strain in the $x$ (axial) direction, and $e_y$ and $e_z$ are the strains in the $y$ and $z$ (transverse) directions, respectively.

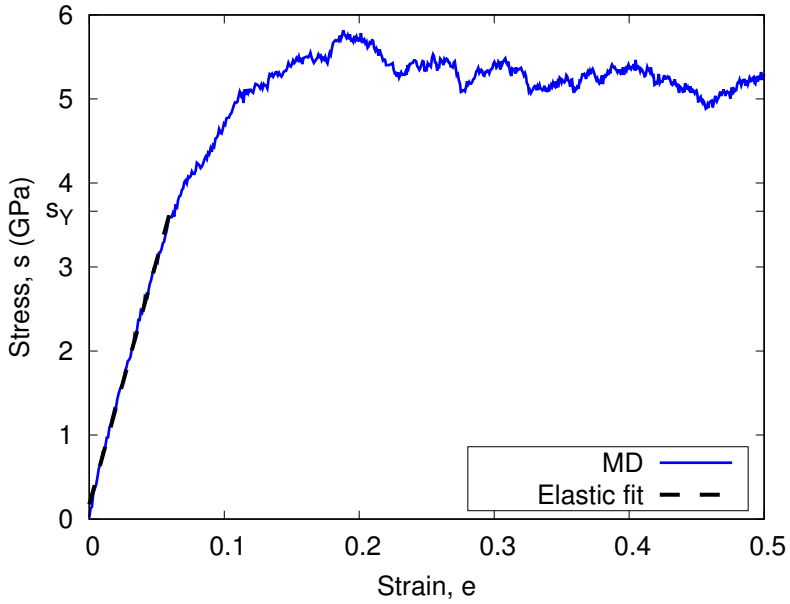


**Figure 3.16:** Stress-strain curve of amorphous silicon model. The dashed black line shows the elastic regime of deformation, up to the yield stress $s_Y$.

The bulk modulus of the material was found from:

$$K_s = \frac{E}{3(1-2\nu_P)}, \tag{3.13}$$

and was calculated to be $K_s = 56\,\text{GPa}$ (De Beer and Maina, 2008). The speed of sound within the amorphous silicon model was then found by modifying Equation (3.11) for solids (De Beer and Maina, 2008):

$$c_{0,s} = \sqrt{\frac{K_s}{\rho_s}}, \tag{3.14}$$

where $c_{0,s}$ is the speed of sound in the solid; the initial solid density was measured at $\rho_s = 2200\,\text{kg/m}^3$. Using Equation (3.14), the speed of sound in the amorphous silicon model was estimated to be $c_{0,s} = 5100\,\text{m/s}$. This is over double the sound speed of the $H_2O$ and mW liquid models, due to the increased modulus of the solid material.

## 3.5 Piston pressure control

Cavitation is highly sensitive to pressure, so methods of accurately determining the input pressure were essential for this research. As already mentioned, setting the liquid pressure in a multiphase system is not trivial with barostats in NPT ensembles, since the domain volume does not correspond with the liquid volume. Also, barostats operate by constantly performing small adjustments to the atom positions throughout the system, which was deemed unsuitable for accurately modelling the dynamic nature of cavitation growth.

Instead, a piston comprising of a simple lattice of solid atoms with LJ potentials between the solid and fluid atoms (see Section 3.3.5) was used to control the pressure in the system. The piston atoms were only allowed to travel vertically in the $z$ direction, as shown in Figure 3.17, and moved as one rigid unit.

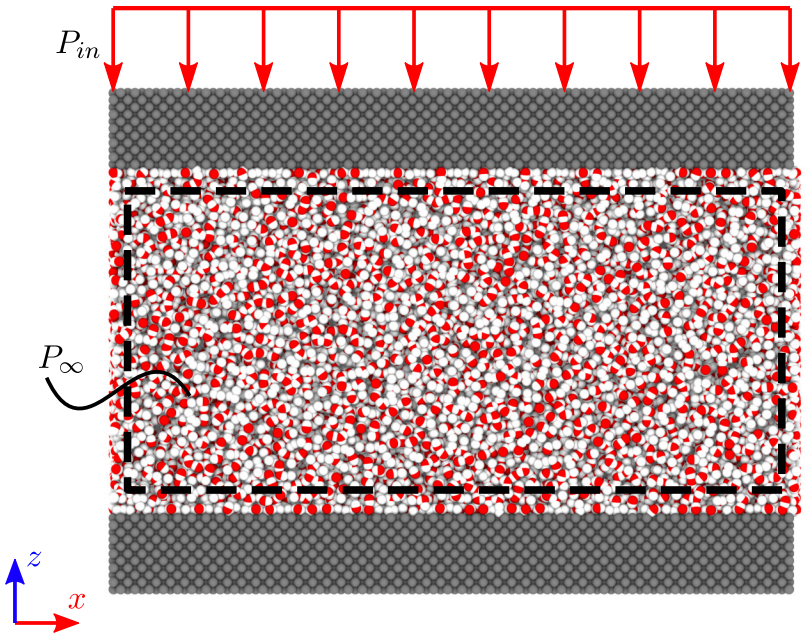


**Figure 3.17:** Schematic of a typical piston set-up used to enforce pressure within the fluid domain. The internal fluid under pressure here is the TIP4P/2005 $H_2O$ model.

The force on each piston atom $F_p$ was determined from:

$$F_p = -\frac{P_{in}A_p}{N_p}, \tag{3.15}$$

where $P_{in}$ is the input pressure, $A_p$ is the plane area of the piston in contact with the fluid, and $N_p$ is the number of piston atoms. In the steady-state, the liquid pressure is equal to the input pressure $P_\infty = P_{in}$. In dynamic cases, it was found that inertia of the piston becomes significant to the resulting liquid pressure, which will be discussed in more detail in Chapter 5. The piston force acts in the $z$ direction; for a positive pressure $P_{in}$, the piston would need to compress the

fluid and so acts downwards, and vice versa.

Simulations were run using the TIP4P/2005 and mW models, where 56 541 water molecules were placed between two horizontal walls, with the top wall acting as the piston. Several simulations were run where the input piston pressure was varied, and the pressure in the liquid was calculated using Equations (3.2) and (3.3). Results of these simulations are shown in Figure 3.18. The agreement between the input and measured pressures was good, even for

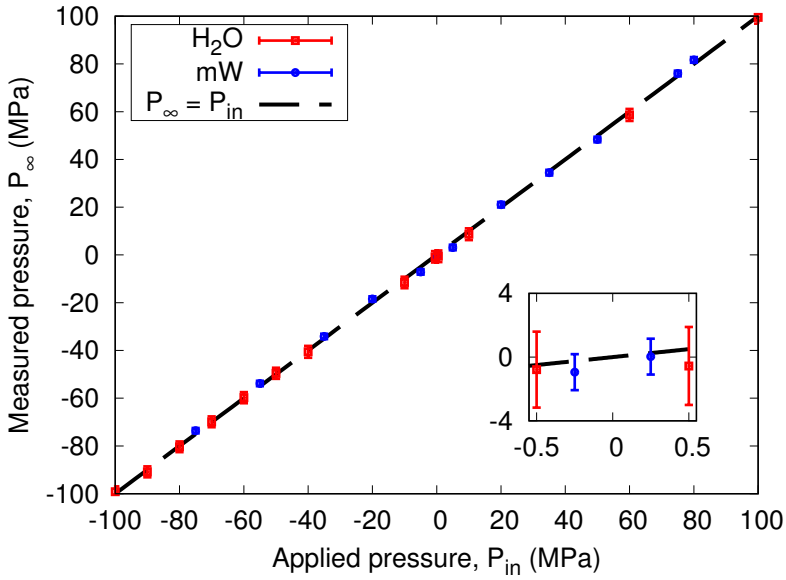


**Figure 3.18:** Variation in measured liquid pressure in MD simulation $P_\infty$ with applied piston pressure $P_{in}$. The inset shows results for the small pressure magnitudes.

negative pressures; in these cases, the force applied on the piston is upwards, yet there is sufficient attraction between the $H_2O$ molecules and piston atoms to prevent detachment at the wall. The size of the error bars in the inset of Figure 3.18 is $\sim 1$ MPa and is indicative of the high level of noise that can be expected in pressure formulations in MD simulations, especially at low absolute pressures.

## 3.6 Equilibrium surface nanobubble simulation

Having established all the simulation parameters above, it was possible to perform a variety of simulations of surface nanobubble cavitation dynamics. This section is a demonstration of the initialisation and equilibration steps of a quasi-2D (cylindrical) surface nanobubble, using the $H_2O$, $N_2$, and $S_o/S_i$ atomic models, with potentials from Table 3.1.

Previous authors have typically initialised MD surface nanobubble simulations using a single supersaturated box of mixed liquid and gas molecules and run until a surface nanobubble naturally formed on a solid substrate, a process that can take up to $\sim 10$ ns (Che and Theodorakis,

2017; Maheshwari *et al.*, 2016; Weijs *et al.*, 2012b). In this research, to reduce the computational cost, it was assumed that Equation (2.10) was suitable to relate the surface nanobubble's contact angle to the surrounding liquid supersaturation, as confirmed by Maheshwari *et al.* (2016). As such, all the MD surface nanobubble simulations presented here were initialised from a cylindrical cap (for the quasi-2D bubble), or spherical cap (for the 3D bubble), filled with gas (Martínez *et al.*, 2009). The surrounding liquid was initialised with appropriate liquid supersaturation ratios calculated from Equation (2.10), using the initialised bubble contact angle. These surface nanobubbles are then run under equilibrium conditions to allow them to reach their diffusive equilibrium size sooner, before the main pressure variation simulations can begin.

This particular surface nanobubble simulation was initialised as a cylindrical cap on a single $S_o$ pinning site with width $L = 7.84\,\text{nm}$, and a gas-side contact angle of $\theta = 65°$. The bubble was initialised with 801 $N_2$ molecules, plus a further 70 $N_2$ molecules dissolved in the surrounding bulk liquid, containing 26 847 $H_2O$ molecules. After initialisation, the bubble was allowed to equilibrate for 0.82 ns at $P_{in} = 10\,\text{MPa}$, before any pressure changes were applied. The equilibrated fluid domain had a size of $18.8 \times 5.88 \times 8.10\,\text{nm}^3$, although was allowed to expand in the $z$ direction during pressure changes. A rendering of the initialised and equilibrated states for this particular simulation is shown in Figures 3.19(a) and 3.19(b), respectively. The Nosé-

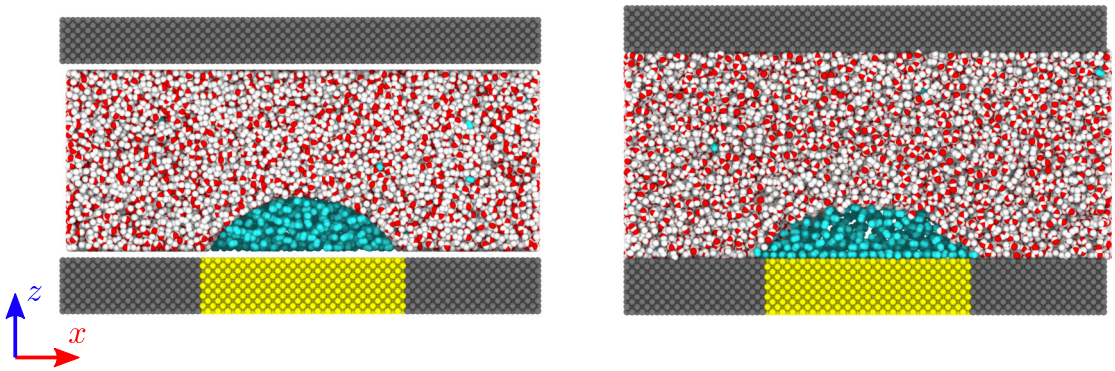


**Figure 3.19:** Rendering of MD surface nanobubble simulation after: (a) initialisation, and (b) equilibration. The oxygen (O) atoms are shown in red, hydrogen (H) atoms in white, nitrogen (N) atoms in cyan, hydrophilic ($S_i$) atoms in grey and hydrophobic ($S_o$) atoms in yellow.

Hoover thermostat was used to maintain the fluid at 300 K, with thermal velocities only scaled in the 2D $(y)$ direction. A timestep of $\Delta t = 1 \times 10^{-6}\,\text{ns}$ was used.

System pressure was controlled by the piston method (see Section 3.5); input piston pressure was varied between 0 MPa and 100 MPa, and held for 0.75 ns. The timescales for these simulations were short, to prevent the diffusive response to alter the bubble size. Pressure in the gas and liquid phases were calculated using Equations (3.2) and (3.3). A circle was fitted to

the fluid 50% isodensity contour, which defined the radius of curvature of the bubble. Note for 2D or cylindrical bubbles, the Laplace pressure is half that given in Equation (2.1) and instead becomes $\Delta P = \gamma/R$, due to the interface only curving in one plane (Maheshwari *et al.*, 2016).

For example, the density and pressure variation of the $P_\infty = 1\,\text{MPa}$ case are shown in Figure 3.20(a) and 3.20(b), respectively. The density and pressure results of the piston and solid

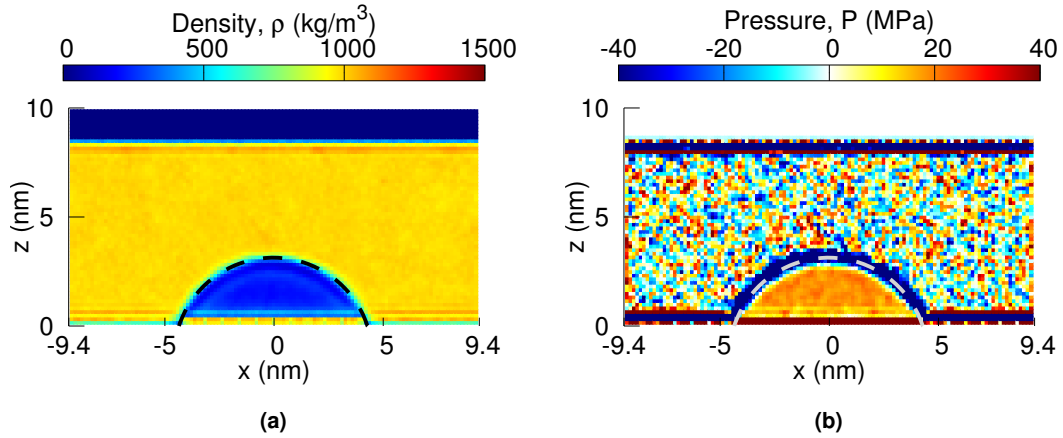


**Figure 3.20:** Surface nanobubble MD simulation at $P_{in} = 1\,\text{MPa}$ with results for (a) density, and (b) pressure. A circle is fitted to the 50% isodensity contour, as shown by the dashed black and grey lines in (a) and (b), respectively.

atoms are not shown in Figure 3.20 for clarity. Also shown is the fitted circle profile to the 50% isodensity contour. Note Equation (3.3) holds for bulk systems; there appear to be anomalous results in the pressure near ($< 1\,\text{nm}$) the bubble and solid surfaces, similar to Figure 3.13(c), which is a result of non-bulk fluid behaviour and is not an accurate representation of the pressure in these regions. The liquid pressure in Figure 3.20(b) is significantly noisier than in the gas phase, despite a greater sampling size with increased density. This difference in noise can be put down to the virial contribution of Equation (3.2).

The different pressure contributions, including from the liquid, gas, and 2D Laplace pressure, are shown in Figure 3.21. Also shown in Figure 3.21 is the difference in these pressure contributions which would be expected to be zero in mechanical equilibrium: $P_g - P_\infty - \gamma/R = 0$.

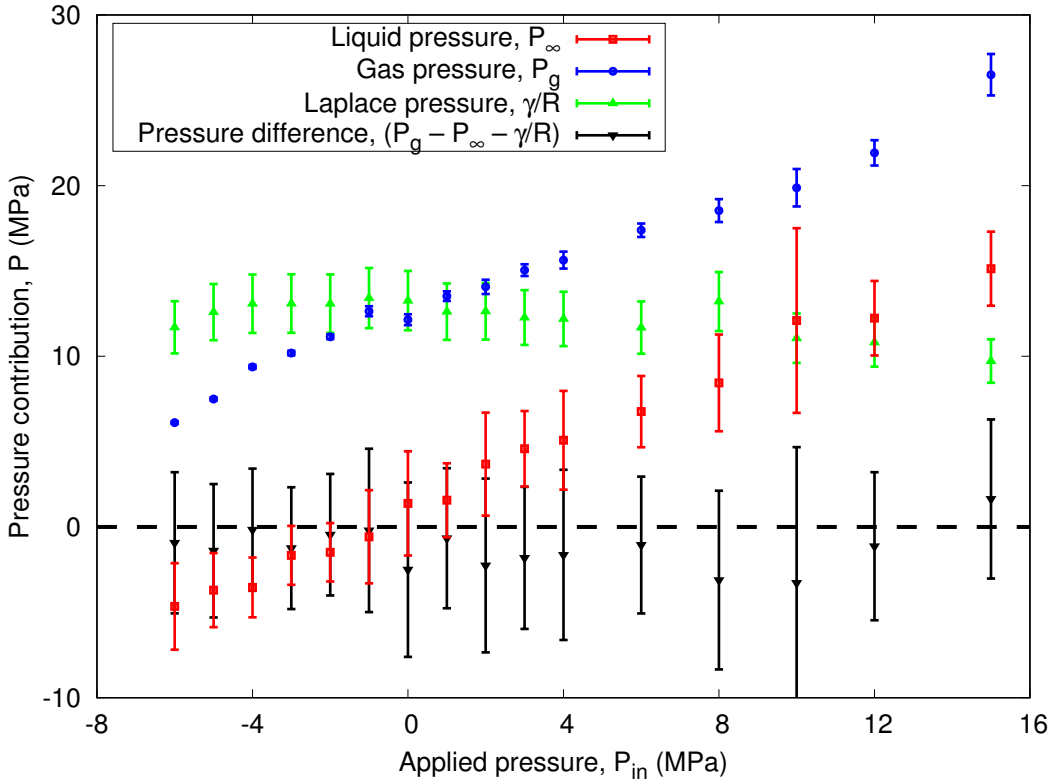


**Figure 3.21:** Variation in pressure contributions in surface nanobubble MD simulations with applied piston pressure $P_{in}$. The difference in measured pressures $P_g - P_\infty - \gamma/R$ is also shown, and the dashed line shows the expected difference (0 MPa).

## 3.7 Summary

This chapter has covered all the simulation parameters and methods required to perform the surface nanobubble cavitation simulations in the remainder of this thesis. MD is a versatile modelling technique that can be used to model both fluid and solid behaviour, which is important for investigating the instability, growth and collapse of cavitating surface nanobubbles. Molecular models based on water (TIP4P/2005, mW) and air ($N_2$, mN) were chosen for modelling the liquid and gas phases respectively of the bubbles, with the simpler models (mW, mN) being employed to reduce the cost of larger simulations. A simple FCC solid and amorphous silicon model were chosen for the solids. The interactions between the fluid and solid models were calibrated and presented here, to obtain results close to previous experimental and simulation literature. Further benchmark tests were performed to obtain bulk properties of these models relevant to simulations in the following chapters, such as equations of state, viscosity and surface tension.

Pressure in the fluid systems was found best to be controlled via a piston mechanism that applied a force proportional to the desired liquid pressure. Preliminary simulations confirmed

this method was suitable for enforcing pressure, and also that the Laplace pressure balance across the surface nanobubble could be obtained. The research in the following chapters makes use of this piston mechanism to investigate the different stages of cavitation, with different input pressure conditions.

Chapter 4

# Cavitation Threshold of Surface Nanobubbles

Parts of this chapter have been published in: Dockar, D., Borg, M. K., and Reese, J. M. "Mechanical Stability of Surface Nanobubbles". *Langmuir*, 35(29):9325–9333, 2019, with permission from *American Chemical Society*. Further supporting information, plus permissions relating to the material, can be found from: `https://pubs.acs.org/doi/10.1021/acs.langmuir.8b02887`.

## 4.1 Introduction

Cavitation bubbles generally nucleate from an instability in the liquid, driven by a drop in pressure. For pure liquids, this instability is governed by thermal effects and the liquid's tensile strength. Pure water is capable of supporting pressures down to $-160\,\mathrm{MPa}$ (Caupin and Herbert, 2006; El Mekki Azouzi *et al.*, 2012; Menzl *et al.*, 2016; Pallares *et al.*, 2014) as discussed in Chapter 2.

In more practical scenarios, cavitation typically nucleates from temporary bubbles of dissolved gases, or on the surfaces of impurities and solids. For engineering applications, where the effects of cavitation are to be mitigated, the phrase "prevention is better than cure" certainly applies, and so it is important to accurately predict this cavitation threshold $P_{\infty,c}$.

Blake (1949) accurately predicted the cavitation threshold of a spherical gas bubble in a bulk liquid, as given in Equation (2.3), depending on the radius of curvature $R$. The Blake threshold predicts the cavitation threshold of $-0.55\,\mathrm{MPa}$ for a bubble with $R \sim 100\,\mathrm{nm}$. However, recent experiments reported surface nanobubbles of this size to be stable against pressures of $-6\,\mathrm{MPa}$, an order of magnitude lower than expected (Borkent *et al.*, 2007).

This chapter will investigate the suitability of the Blake threshold for surface nanobubble cavitation, for 2D and 3D cases, and propose a new cavitation threshold to account for the effects of pinning and the different morphology of the spherically capped surface nanobubbles.

## 4.2 Cavitation threshold derivations

### 4.2.1 2D Blake threshold

Before considering the surface nanobubble case, it is important to show how the 2D Blake threshold is derived, as the surface nanobubble cavitation threshold proposed in this work follows a similar approach.

Equation (2.1) can be combined with Equation (2.2) to obtain the pressure balance at the 2D bubble interface, where the Laplace pressure is half that given in Equation (2.1), i.e. $\gamma/R$ (Maheshwari *et al.*, 2016):

$$P_\infty = P_{g,0}\left(\frac{V_0}{V}\right)^k + P_v - \frac{\gamma}{R}, \tag{4.1}$$

where the subscript 0 denotes the initial state of the bubble's internal gas phase. For a 2D cylindrical bubble, the bubble size is better expressed in terms of its cross-sectional area $A$, since $A \propto V$. In turn, the area is a monotonic function of the radius of curvature, i.e. $A = \pi R^2$, so Equation (4.1) can be rewritten as:

$$P_\infty = P_{g,0}\left(\frac{R_0}{R}\right)^{2k} + P_v - \frac{\gamma}{R}. \tag{4.2}$$

As the liquid pressure decreases, the bubble increases in size such that the pressures balance as in Equation (4.2), and the bubble remains in mechanical stability. The variation in the bubble's gas pressure $P_g$, Laplace pressure $\gamma/R$, and liquid pressure $P_\infty$ with the bubble radius $R$ is shown in Figure 4.1. The vapour pressure $P_v$ is assumed constant for constant temperature, and can be considered negligible at 300 K when compared to the gas and Laplace pressures. The $P_\infty$ solid black line in Figure 4.1 shows the range of sizes the bubble can be in mechanical equilibrium for varying liquid pressure. There is a minimum which occurs at a critical radius $R_c$, indicated by the red cross ($\times$) symbol; the corresponding pressure is the cavitation threshold $P_{\infty,c}$. If the liquid pressure drops below this threshold, there can be no stable bubble, i.e. the internal gas and vapour pressure will always exceed the Laplace pressure and surrounding liquid pressure, and the bubble will experience unstable growth.

Equation (4.2) is differentiated with respect to $R$:

$$\frac{\mathrm{d}P_\infty}{\mathrm{d}R} = -2kP_{g,0}\frac{R_0^{2k}}{R^{2k+1}} + \frac{\gamma}{R^2}, \tag{4.3}$$

which can be solved at the minimum ($\mathrm{d}P_\infty/\mathrm{d}R = 0$) to find $R_c$:

$$R_c = \left(\frac{2kP_{g,0}R_0^{2k}}{\gamma}\right)^{\frac{1}{2k-1}}. \tag{4.4}$$

Substituting the critical radius, $R_c$, into Equation (4.2) for $R$ will give the minimum possible

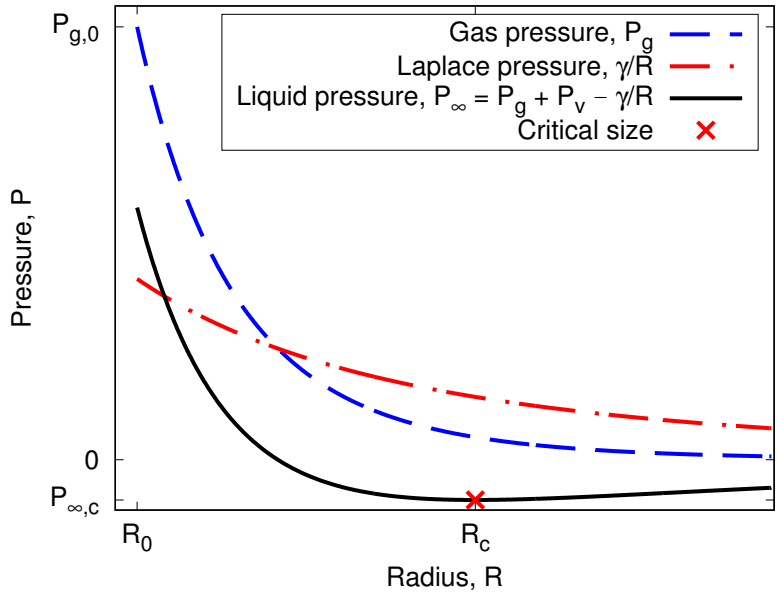


**Figure 4.1:** Variation in pressure contributions acting on a 2D cylindrical bubble.

value of $P_\infty$ that can sustain a bubble in mechanical equilibrium, i.e. the cavitation threshold:

$$P_{\infty,c} = P_v - \gamma\left(1 - \frac{1}{2k}\right)\left[\frac{\gamma}{2kR_0^{2k}P_{g,0}}\right]^{\frac{1}{2k-1}}, \tag{4.5}$$

which is referred to as the 2D Blake threshold.

### 4.2.2 2D surface nanobubble threshold

The cavitation threshold for the 2D surface nanobubble proposed in this work can be derived by considering the limit in which the pressures acting on the bubble interface can be in mechanical equilibrium, as in the 2D Blake threshold case derived above. Equation (4.1) also holds for a surface nanobubble in mechanical equilibrium. Again, 2D bubble volume can be better expressed in terms of its cross-sectional area, since $A \propto V$, i.e.

$$A = \frac{1}{2}R^2\left[2\theta - \sin 2\theta\right], \tag{4.6}$$

where $\theta$ is the cylindrical cap bubble's internal contact angle as measured from the gas side, in radians. For the 2D free cylindrical bubbles, $A$ is a monotonically increasing function of $R$, such that the bubble radius naturally increases with the bubble's size. However, for the surface nanobubbles undergoing constant contact radius (CCR) growth, this is not so simple, as $R$ will *decrease* with increasing size for $\theta < 90°$, and increase with increasing size for $\theta > 90°$. So, for a given $R$ there are two possible values for $A$.

It becomes more convenient to define the surface nanobubble size solely in terms of $\theta$, for a

fixed contact diameter $L$, reproduced from Equation (2.9) below:

$$R = \frac{L}{2\sin\theta}. \tag{2.9}$$

Substituting Equation (2.9) into Equation (4.6) gives:

$$A = \frac{1}{4}L^2\left[\frac{\theta}{\sin^2\theta} - \frac{1}{\tan\theta}\right]. \tag{4.7}$$

Equation (4.1) can then be expressed in terms of $\theta$, using Equations (2.9) and (4.7):

$$P_\infty = P_v + P_{g,0}A_0^k\left[\frac{1}{4}L^2\left(\frac{\theta}{\sin^2\theta} - \frac{1}{\tan\theta}\right)\right]^{-k} - \frac{2\gamma\sin\theta}{L}, \tag{4.8}$$

where the initial bubble area is given by Equation (4.7), i.e.:

$$A_0 = A(\theta_0) = L^2\left[\theta_0/\sin^2\theta_0 - 1/\tan\theta_0\right]/4.$$

Interestingly, there is no direct effect from the solid-fluid surface energies entering these equations, however, there is an implicit assumption that these parameters are suitable to provide contact line pinning throughout the growth process (Attard, 2016).

The variation in the bubble's gas pressure $P_g$, Laplace pressure $\gamma/R$, and liquid pressure $P_\infty$ with the bubble contact angle $\theta$, as given by Equations (2.9) and (4.8) is shown in Figure 4.2. Also shown by the red cross ($\times$) symbol is the critical bubble contact angle $\theta_c$ where the liquid pressure is at a minimum: the cavitation threshold $P_{\infty,c}$. The most important feature of Figure 4.2 is that the Laplace pressure component begins to increase with increasing bubble size, the inverse effect to the 2D cylindrical free bubble case shown in Figure 4.1. The Laplace pressure effectively suppresses excessive growth of the surface nanobubble as it increases in size, and this is the reason that surface nanobubbles can typically resist much lower pressures than equivalently sized spherical bubbles.

There is a minimum in Figure 4.2 which can be found by differentiating Equation (4.8) with respect to $\theta$:

$$\frac{\mathrm{d}P_\infty}{\mathrm{d}\theta} = -kP_{g,0}\left(\frac{4A_0}{L^2}\right)^k\left(\frac{2}{\sin^2\theta} - \frac{\theta\sin 2\theta}{\sin^4\theta}\right)\left(\frac{\theta}{\sin^2\theta} - \frac{1}{\tan\theta}\right)^{-k-1} - \frac{2\gamma\cos\theta}{L}, \tag{4.9}$$

and setting $\mathrm{d}P_\infty/\mathrm{d}\theta = 0$ at the critical contact angle $\theta = \theta_c$, i.e.

$$-\left[\sin^2\theta_c\cos\theta_c\left(\frac{\theta_c}{\sin^2\theta_c} - \frac{1}{\tan\theta_c}\right)^{k+1}\right]^{-1}\left(1 - \frac{\theta_c}{\tan\theta_c}\right) = \left(\frac{L^2}{4A_0}\right)^k\frac{\gamma}{kLP_{g,0}}. \tag{4.10}$$

Equation (4.10) cannot be solved analytically and so must be solved numerically for $\theta_c$. Once obtained, the 2D surface nanobubble cavitation threshold can be determined by substituting $\theta_c$

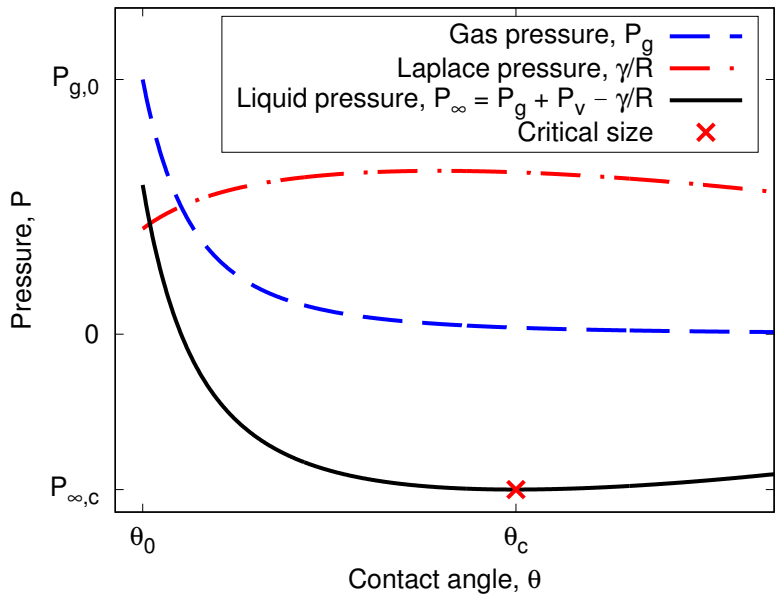


**Figure 4.2:** Variation in pressure contributions acting on a 2D cylindrical cap-shaped surface nanobubble, as a function of its contact angle.

into Equation (4.8):

$$P_{\infty,c} = P_v + P_{g,0}A_0^k \left[\frac{1}{4}L^2\left(\frac{\theta_c}{\sin^2\theta_c} - \frac{1}{\tan\theta_c}\right)\right]^{-k} - \frac{2\gamma\sin\theta_c}{L}. \tag{4.11}$$

### 4.2.3 3D Blake threshold

The 3D Blake threshold can be derived in a similar approach to that shown in Section 4.2.1. The polytropic gas law is employed again, except now the bubble volume is a simple function of a sphere: $V = 4\pi R^3/3$, and substituting this into Equation (2.1) gives:

$$P_\infty = P_{g,0}\left(\frac{R_0}{R}\right)^{3k} + P_v - \frac{2\gamma}{R}. \tag{4.12}$$

The variations in the bubble pressures, Laplace pressure, and liquid pressure are qualitatively similar to those in Figure 4.1. Equation (4.12) is differentiated with respect to $R$:

$$\frac{\mathrm{d}P_\infty}{\mathrm{d}R} = -3kP_{g,0}\frac{R_0^{3k}}{R^{3k+1}} + \frac{2\gamma}{R^2}, \tag{4.13}$$

and can be solved for $\mathrm{d}P_\infty/\mathrm{d}R = 0$ at $R = R_c$:

$$R_c = \left(\frac{3kP_{g,0}R_0^{3k}}{2\gamma}\right)^{\frac{1}{3k-1}}. \tag{4.14}$$

Substituting this critical radius, $R = R_c$, into Equation (4.12) gives the minimum possible value of $P_\infty$ that can sustain a bubble in mechanical equilibrium, and Equation (2.3) is obtained, reproduced below:

$$P_{\infty,c} = P_v - 2\gamma\left(1 - \frac{1}{3k}\right)\left[\frac{\gamma}{3kR_0^{3k}P_{g,0}}\right]^{\frac{1}{3k-1}}. \tag{2.3}$$

The difference between the 3D Blake threshold in Equation (2.3) and the 2D equivalent in Equation (4.5) arises because of the change of the exponent in the polytropic gas law from $2k$ to $3k$, and the change of the surface tension pressure contribution from $\gamma/R$ to $2\gamma/R$.

### 4.2.4 3D surface nanobubble threshold

As with the Blake threshold, the proposed cavitation threshold for the surface nanobubble can be obtained by considering the limits of mechanical stability of a pinned 3D spherical cap. The volume of a spherical cap is:

$$V = \frac{1}{3}\pi R^3\left[2 - 3\cos\theta + \cos^3\theta\right]. \tag{4.15}$$

For pinned CCR growth, it is more appropriate to define the cap volume in terms of $\theta$ using Equation (2.9):

$$V = \frac{\pi L^3}{24\sin^3\theta}\left[2 - 3\cos\theta + \cos^3\theta\right]. \tag{4.16}$$

The pressure balance across the bubble interface can then be expressed in terms of $\theta$ using Equations (2.1), (2.9) and (4.16):

$$P_\infty = P_v + P_{g,0}V_0^k\left[\frac{\pi L^3}{24\sin^3\theta}\left(2 - 3\cos\theta + \cos^3\theta\right)\right]^{-k} - \frac{4\gamma\sin\theta}{L}, \tag{4.17}$$

where the initial bubble volume can be found from Equation (4.16), i.e.:

$$V_0 = V(\theta_0) = \pi L^3[2 - 3\cos\theta_0 + \cos^3\theta_0]/(24\sin^3\theta_0).$$

The variations in the bubble pressures, Laplace pressure, and liquid pressures are qualitatively similar to those shown in Figure 4.2.

Equation (4.17) can be differentiated with respect to $\theta$:

$$\frac{\mathrm{d}P_\infty}{\mathrm{d}\theta} = -3kP_{g,0}\left(\frac{24V_0}{\pi L^3}\right)^k(1+\cos\theta)^{\frac{3k-1}{2}}(1-\cos\theta)^{\frac{-k-1}{2}}(2+\cos\theta)^{-k-1} - \frac{4\gamma\cos\theta}{L}. \tag{4.18}$$

The threshold pressure can be found by solving for $\mathrm{d}P_\infty/\mathrm{d}\theta = 0$ at $\theta = \theta_c$, i.e.

$$-(1+\cos\theta_c)^{\frac{3k-1}{2}}\sec\theta_c(1-\cos\theta_c)^{\frac{-k-1}{2}}(2+\cos\theta_c)^{-k-1} = \frac{4\gamma}{3LkP_{g,0}}\left(\frac{\pi L^3}{24V_0}\right)^k. \tag{4.19}$$

Again, Equation (4.19) cannot be solved analytically and so must be solved numerically. Once $\theta_c$ is obtained, the threshold pressure $P_{\infty,c}$ is determined by substituting it into Equation (4.17):

$$P_{\infty,c} = P_v + P_{g,0}V_0^k \left[\frac{\pi L^3}{24\sin^3\theta_c}\left(2 - 3\cos\theta_c + \cos^3\theta_c\right)\right]^{-k} - \frac{4\gamma\sin\theta_c}{L}. \tag{4.20}$$

## 4.3 Molecular Dynamics (MD) simulation set-up

MD simulations were run to validate the proposed theoretical expressions for the 2D and 3D surface nanobubble cavitation thresholds, in Equations (4.11) and (4.20), respectively. Simulations were performed in quasi-2D (hereon referred to as just "2D") and 3D, with variations in the initialisation to account for the different Laplace pressure contributions (Maheshwari *et al.*, 2016). An example rendering of the (2D) MD simulation set-up is shown in Figure 4.3. The TIP4P/2005 water ($H_2O$), two-site nitrogen ($N_2$), and rigid hydrophilic ($S_i$) and hydrophobic ($S_o$) solid atom models were used, with potentials given in Table 3.1.

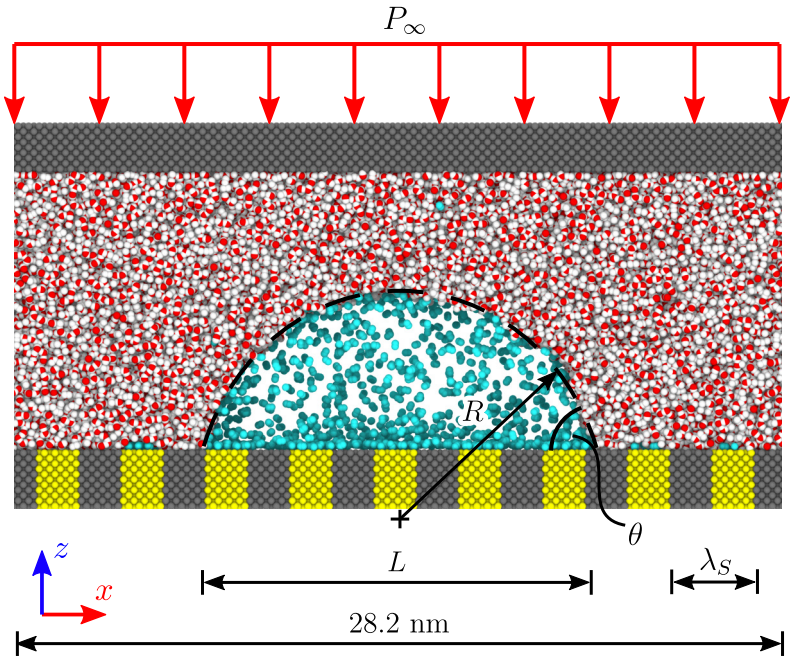


**Figure 4.3:** Annotated rendering of an MD quasi-2D surface nanobubble. The red and white atoms are the O and H atoms of the TIP4P/2005 water molecule, respectively; N atoms of the $N_2$ model are cyan; the grey and yellow atoms are the $S_i$ and $S_o$ LJ solid atoms, respectively. A circle of best fit of the bubble surface is also shown as the black dashed line.

The surface nanobubbles were initialised and equilibrated on the wall surface, and the piston method was used to control the liquid pressure, as discussed in Section 3.5. The lower wall was textured with an alternating pattern of $S_i$ and $S_o$ atom types, with "pattern wavelength"

$\lambda_S = 3.14\,\text{nm}$. For the 2D case, this patterning formed simple horizontal stripes that extended into the $y$ direction, as shown in Figure 4.3; for the 3D case, the patterning formed concentric rings, as shown in Figure 4.4. The substrate patterning allowed the contact-line to move to new pinning sites during growth.

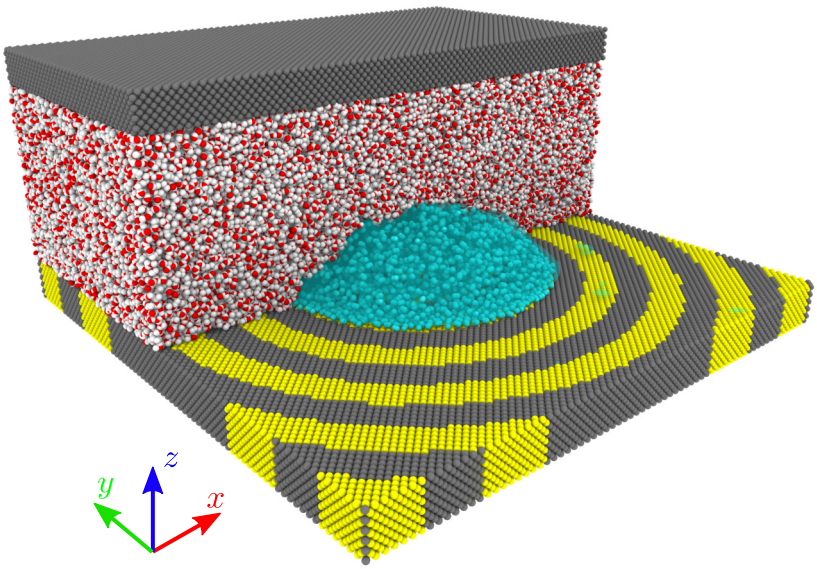


**Figure 4.4:** Rendering of a 3D surface nanobubble from the MD simulations. Some of the water molecules, nitrogen molecules and piston atoms are not shown for visualisation purposes.

All of the simulations were run in an NVT ensemble, with the Nosé-Hoover thermostat used to keep the water molecules at temperature 300 K (see Section 3.1.1). In the 2D simulations, the thermostat only operated on the $y$-component velocities, while in the 3D simulations, the thermostat operated on all thermal velocity components, which is equal to the mean centre of mass velocity subtracted from the velocity of each molecule. The water and nitrogen were collectively thermostatted to 300 K during equilibration. During the main production run (i.e. when the pressure drop is applied), no temperature control was applied to the $N_2$ molecules; this allowed the gas-phase to expand more realistically, without forcing isothermal or adiabatic behaviour as is common in previous cavitation analyses (Borkent *et al.*, 2009; Brennen, 2013). A time-step of $\Delta t = 1 \times 10^{-6}\,\text{ns}$ was used for all simulations in this chapter.

The 2D and 3D surface nanobubble simulations were initialised and equilibrated in a similar process to that described in Chapter 3, Section 3.6. A cylindrical/spherical cap containing $N_2$ gas molecules was initialised on a solid substrate, surrounded by $H_2O$ molecules, similar to that in Figure 3.19(a), for the 2D/3D simulations, respectively. The solid surface was initialised primarily as $S_i$ atom types, with a single patch of $S_o$ atoms below the bubble, with contact diameter $L = 14.11\,\text{nm}$ (equivalent to $4.5\,\lambda_S$). The surface nanobubbles were

allowed to equilibrate at initial pressure $P_{\infty,0} = 10\,\text{MPa}$ for up to 1.4 ns. The end states of the equilibrated 2D and 3D bubbles were used as the starting point for all the subsequent pressure drop simulations in Sections 4.4.1 and 4.4.2, respectively.

The drop in pressure was applied as a smooth hyperbolic tangent function over a period of 0.1 ns to prevent any separation of fluid from the piston. Piston atom forces were obtained from Equation (3.15). Simulations were run for up to 15 ns, or until the bubble had outgrown the MD domain size in the case of the unstable pressure drop simulations. Care was taken not to run the simulations too long to ensure that growth by mass diffusion was unimportant. The timescale for surface nanobubble diffusive growth is of the order of 1 $\mu$s (Chan *et al.*, 2015; Lohse and Zhang, 2015a,b), and so is not considered to influence growth dynamics here (see Chapter 2). The vapour pressure of $H_2O$ at 300 K is $P_v = 3.54 \times 10^{-3}$ MPa (Lemmon *et al.*, 2017), which is several orders of magnitude lower than the liquid, gas, and Laplace pressures ($\sim 10\,\text{MPa}$). Periodic boundary conditions were applied to the $x$ and $y$ direction faces; fixed boundaries were applied in the $z$ direction, sized appropriately such that the piston could move upwards during the pressure drop cases.

## 4.4 Results and discussion

### 4.4.1 2D cavitation threshold

Thirteen simulations were performed in which the equilibrated 2D surface nanobubble was subjected to a drop in pressure, from the initial 10 MPa to a final value in the range $+3$ MPa to $-4.5$ MPa. Each case was held at the target pressure for 15 ns after the initial pressure drop, which was enough time to determine whether the bubble was stable or unstable, in which case it usually outgrew the size of the domain.

The 2D cylindrical cap surface nanobubble was initialised and equilibrated at $P_{\infty,0} = 10\,\text{MPa}$, as discussed in Section 4.3. A total of 43 000 $H_2O$ molecules were used in the liquid phase. 1120 $N_2$ molecules were placed in the initialised bubble, with a further 79 $N_2$ placed in the liquid phase to achieve supersaturation. This supersaturation was sufficient to provide a target equilibrium contact angle of $\theta_e \sim 50°$, using the 2D forms of Equations (2.1) and (2.10). A circular profile was fitted to the equilibrated bubble's 50% isodensity contour, in which the morphological properties could be obtained from Equation (2.9). The equilibrated 2D surface nanobubble had a gas-side contact angle of $\theta_0 = 43°$, and lateral contact diameter $L_0 = 14.37\,\text{nm}$. The equilibrated radius of curvature was $R_0 = 10.52\,\text{nm}$, which could be used to obtain $P_{g,0}$ using the 2D form of Equation (2.1), i.e. $P_{g,0} = P_\infty - P_v + \gamma/R_0$. The final size of the equilibrated 2D surface nanobubble domain was $28.2 \times 5.88 \times 9.1\,\text{nm}^3$ in the $x$, $y$, and $z$ directions, respectively, although was allowed to expand in the $z$ direction to allow changes in pressure.

During the pressure drop simulations, the surface nanobubbles grew with a pinned contact line, or CCR growth as expected (Lohse and Zhang, 2015b), until some point when the contact line unpinned and rapidly expanded to the next pinning site. This behaviour is commonly referred to as "stick-slip" motion for macroscopic droplets and bubbles. However, in these cases, the motion to the next pinning site was so quick this phenomenon is better described as "stick-jump" motion (Maheshwari *et al.*, 2016). The contact line was found to jump in finite increments of $\lambda_S$, such that the lateral contact diameter could be expressed as $L_n = L_0 + n\lambda_S$, where $L_n$ is the contact diameter after $n$ number of jumps. The variations in the contact diameters and cross-sectional areas of three bubble growth cases are shown in Figure 4.5. Figure 4.5(a) shows the stable growth of a 2D surface nanobubble for $P_\infty = -2.75\,\text{MPa}$, remaining on its original pinning site $L_0$; Figure 4.5(b) shows the growth of the 2D surface nanobubble for $P_\infty = -3.75\,\text{MPa}$, which remains stable even after jumping to the next pinning site $L_1$. Figure 4.5(c) shows the unstable growth of the 2D surface nanobubble for $P_\infty = -4\,\text{MPa}$, which jumps across multiple pinning sites before eventually outgrowing the domain[1].

The surface nanobubbles experiencing final applied pressures of $P_\infty = -4\,\text{MPa}$ and lower were all found to exhibit unstable growth, and typically outgrew the domain within around 5 ns. All the other pressure drop cases resulted in stable growth; the final bubble cross-section areas for the stable cases is shown in Figure 4.6. The lowest nominal pressure that could sustain a mechanically stable surface nanobubble was $P_\infty = -3.75\,\text{MPa}$, so it is concluded from the MD simulations that the 2D surface nanobubble cavitation threshold is in between $-3.75\,\text{MPa}$ and $-4\,\text{MPa}$.

The Blake threshold was first used to obtain an estimate for the surface nanobubble cavitation threshold. It was necessary to obtain the exponent to the polytropic gas law, $k$. The variation of the final measured pressure with cross-sectional area of the stable 2D surface nanobubble MD simulations is plotted in Figure 4.7, on logarithmic axes. The polytropic exponent $k = 1.18$ was found from the negative of the gradient of the fitted line in Figure 4.7, which, as expected, is in between the limits for isothermal $(k = 1)$ and adiabatic $(k = 7/5)$ growth for a diatomic gas. With this fitted parameter of $k$, it would be expected that the gas temperature would decrease as the bubbles grew, and this is confirmed in Figure 4.8. Also shown in Figure 4.8 is the final bubble temperatures of the unstable growth cases, which are significantly lower than for the stable cases. This suggests that as the bubble begins to experience unstable growth, it tends to adiabatic growth behaviour rather than isothermal, as this growth phase would be extremely rapid (Brennen, 2013; Plesset and Prosperetti, 1977).

Equation (4.5) could then be used to estimate the cavitation threshold for a cylindrical 2D bubble, with equivalent radius $R_0 = 10.52\,\text{nm}$. The surface tension is obtained from Chapter 3, $\gamma = 57.35\,\text{mJ/m}^2$. The Blake threshold was predicted to be $P_{\infty,c} = -0.78\,\text{MPa}$, which is also

1. Supplementary videos showing the growth cases in Figures 4.5(b) and 4.5(c) can be found at `https://pubs.acs.org/doi/10.1021/acs.langmuir.8b02887`.

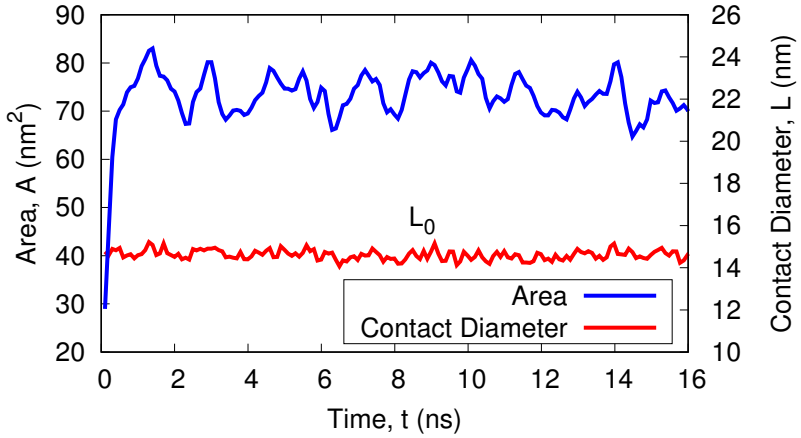


(a)

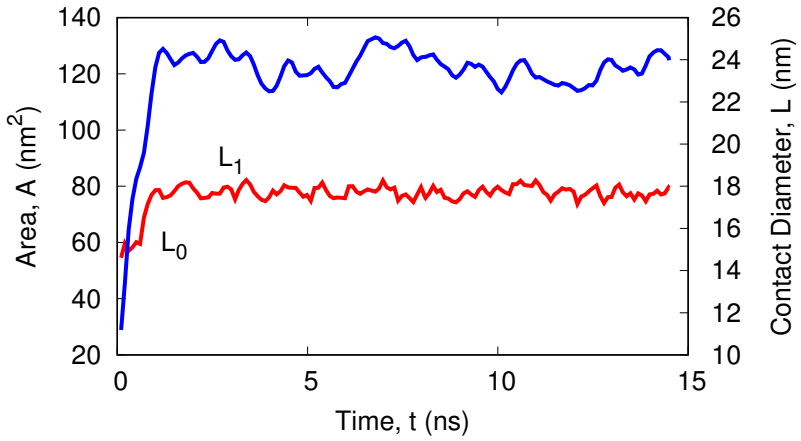


(b)

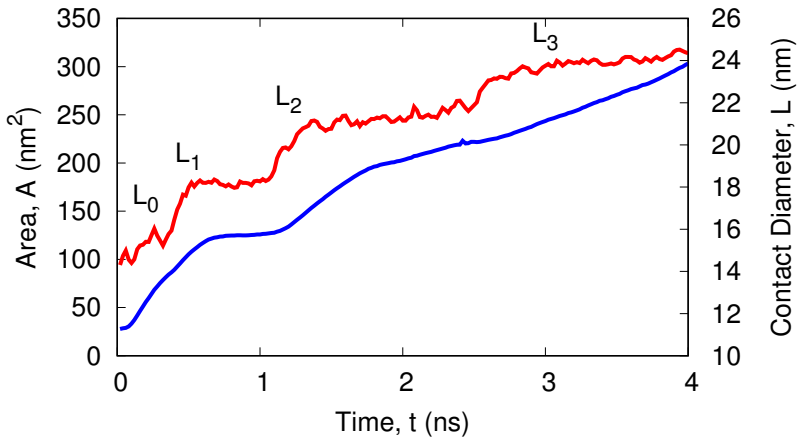


(c)

**Figure 4.5:** Variations in cross-sectional area (blue) and lateral contact diameter (red) for (a) stable, $P_\infty = -2.75\,\mathrm{MPa}$, (b) stable, $P_\infty = -3.75\,\mathrm{MPa}$, and (c) unstable, $P_\infty = -4\,\mathrm{MPa}$, growth cases. The labels correspond to the different discrete pinning sites $L_n$, where $n = 0$ is for no jump, $n = 1$ is for one pinning site jump, etc.

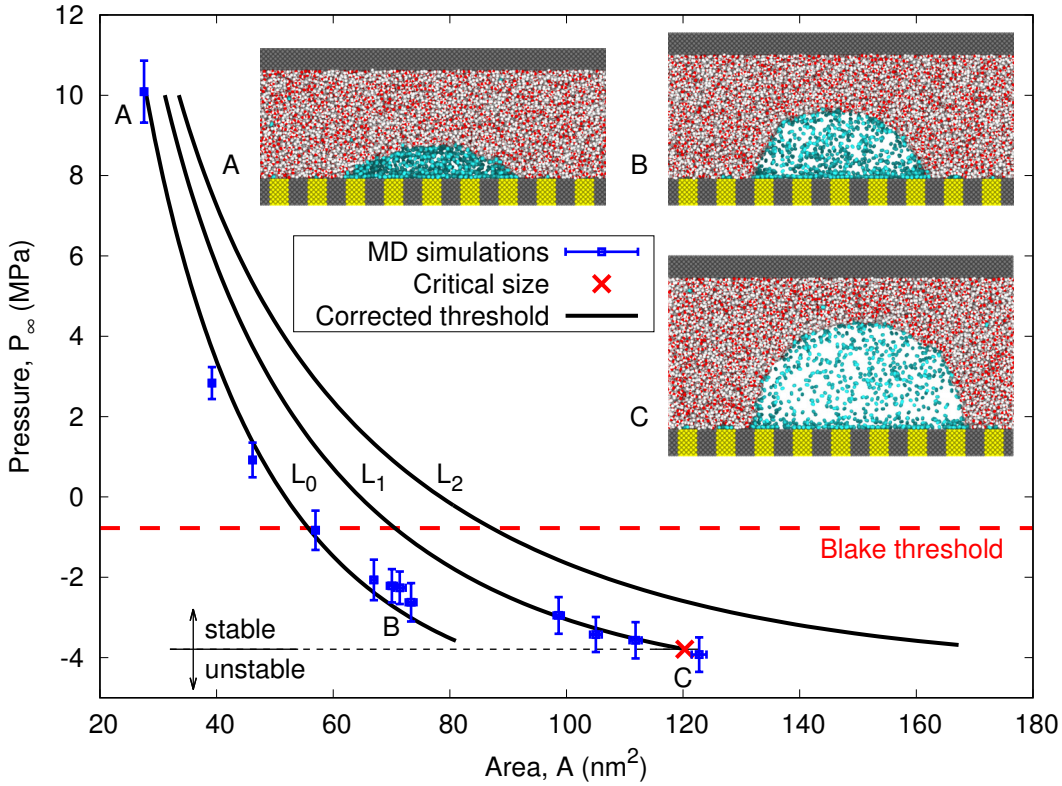


**Figure 4.6:** Variations in the final cross-section areas with final applied pressure for the stable 2D surface nanobubble MD simulation cases. Also shown is the 2D Blake threshold (red dashed line), the predicted growth paths for different pinning sites $L_n$ from the proposed corrected models (black solid lines), and the new predicted threshold pressure by the red cross ($\times$) symbol. Insets show typical renderings of the MD simulations at different pressures, indicated by the A, B, C labels on the graph.

shown as a horizontal reference line in Figure 4.6. The MD simulations showed that the 2D surface nanobubble can resist pressures almost $-3$ MPa lower than this prediction, which confirms other claims that the Blake threshold is unsuitable for estimating the cavitation threshold of surface nanobubbles (Borkent *et al.*, 2007).

Equations (4.10) and (4.11) better predict the cavitation threshold of the 2D surface nanobubble, as shown in Figure 4.6, however, the stick-jump motion of the contact line also needs to be considered in the proposed model, which may not be known *a priori*. None of the bubbles sustained a final contact angle $\theta > 90°$. This has been speculated to be the case for diffusive equilibrium: stable surface nanobubbles must have $\theta < 90°$ (Chan *et al.*, 2015; Lohse and Zhang, 2015a), although there is nothing in the literature to suggest this must be the case for short-term mechanical equilibrium. More likely is that this is near the $S_i$ equilibrium gas-side contact angle of 99°, and the angle at which the contact line jumps is closely linked to the substrate's wettability (de Gennes, 1985).

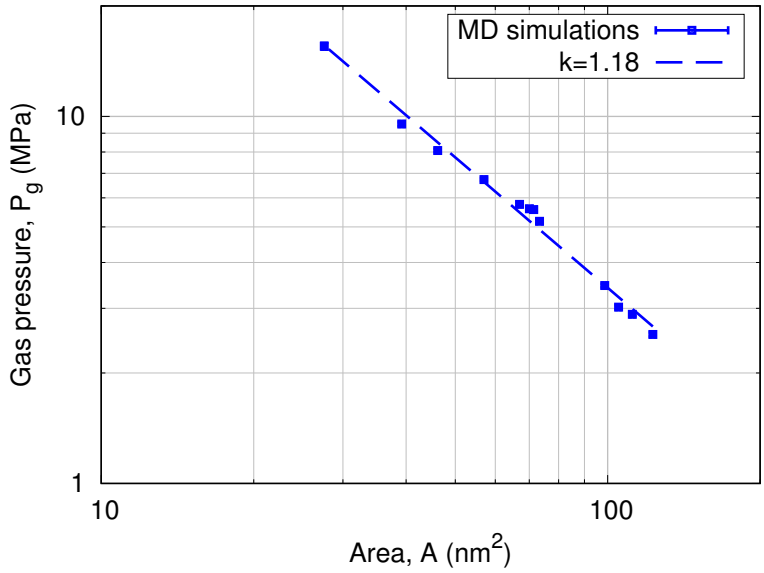


**Figure 4.7:** Variation in gas pressure with bubble cross-sectional area for the stable 2D surface nanobubble MD simulations, on logarithmic axes. A line is also plotted, corresponding to the fitted polytropic exponent $k = 1.18$.

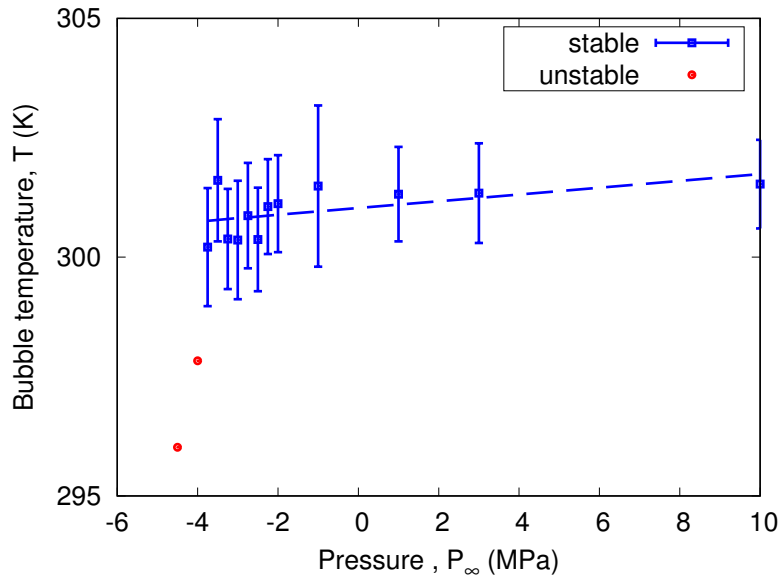


**Figure 4.8:** Variation in internal bubble temperature with pressure drop in the MD simulations. A straight (dashed blue) line is fitted to the stable growth cases.

For this work, it was assumed that the maximum contact angle that a bubble could take on a particular pinning site was 90°, which imposed an additional constraint on Equation (4.10). This does invalidate the assumption that the mode of growth is purely CCR, however, with the $P_{g,0}$ and $A_0$ terms in Equations (4.10) and (4.11) remaining unchanged, different threshold

pressures could be obtained for different pinning sites $L = L_n$; the lowest of these threshold pressures was determined as the cavitation threshold for the 2D surface nanobubble.

The proposed equations predict a cavitation threshold of $P_{\infty,c} = -3.79\,\text{MPa}$, in good agreement with the range of $-3.75\,\text{MPa}$ and $-4\,\text{MPa}$ predicted by the MD simulations. For each pinning site $L_n$, the growth paths predicted by Equations (4.7) and (4.8) are also in good agreement with the stable MD simulation cases, as shown in Figure 4.6. Another pinning site $L_2$ is also shown to demonstrate that the lowest possible pressure for mechanical equilibrium occurs on pinning site $L_1$. The variations in contact angle, radius of curvature, and lateral contact diameter with pressure for the stable MD simulation cases are compared to the predicted cylindrical cap shapes using Equations (2.9) and (4.8), as shown in Figure 4.9. There is strong agreement between the MD simulations and the proposed models for the final surface nanobubble shapes in Figure 4.9, confirming the validity of the cylindrical cap shape assumption for the surface nanobubbles.

The maximum contact angle that was sustained on the first pinning site $L_0$ was $\theta = 84^\circ$, as shown in Figure 4.9(a). After jumping to the next pinning site $L_1$, the contact angle decreases to $\theta = 80^\circ$. For larger surface nanobubbles, where $\lambda_S/L \to 0$, these jumps in pinning sites would appear a lot smoother, and the contact line motion could be approximated as stick-slip instead of stick-jump. In these cases, past some critical contact angle, one might expect to observe constant contact angle (CCA) mode of growth (Li *et al.*, 2014).

The radius of curvature $R$ decreases with decreasing pressure, on a particular pinning site, as shown in Figure 4.9(b). As already discussed, this results in an increase in the Laplace pressure contribution $\gamma/R$, which effectively suppresses excessive growth of the surface nanobubble and allows them to resist much lower pressures compared to 2D cylindrical nanobubbles with same initial radius $R_0$. The Blake threshold assumes spherical geometry, in which the inverse result occurs, and so fails to predict this aspect of the surface nanobubble's mechanical stability, as shown in Figure 4.6.

Figure 4.9(c) confirms that the surface nanobubble is indeed pinned during its growth; the lateral contact diameter remains around the initial pinning site $L_0$, before jumping to the next pinning site $L_1$, with an increase equal to $\lambda_S = 3.14\,\text{nm}$.

The proposed models agree with the MD simulations for $L_0 = 14.37\,\text{nm}$ and $\theta_0 = 43^\circ$, but how does this vary with different 2D surface nanobubble shapes and sizes? Figure 4.10 shows how the *predicted* cavitation threshold varies, using Equations (4.10) and (4.11), for different values of $L_0$ and $\theta_0$. Similar fluid conditions are used as above, with $P_{\infty,0} = 10\,\text{MPa}$, and $\gamma = 57.35\,\text{mJ/m}^2$. Decreasing $\theta_0$ and $L_0$ is equivalent to a decreasing $A_0$ and results in a lower cavitation threshold. For increasing size, the cavitation threshold tends to $P_v$, which is similar to the Blake threshold (Blake, 1949; Brennen, 2013). The effect of the polytropic exponent $k$ is also shown in Figure 4.10 for the $\theta_0 = 43^\circ$ case. Moving from isothermal $(k = 1)$ to adiabatic

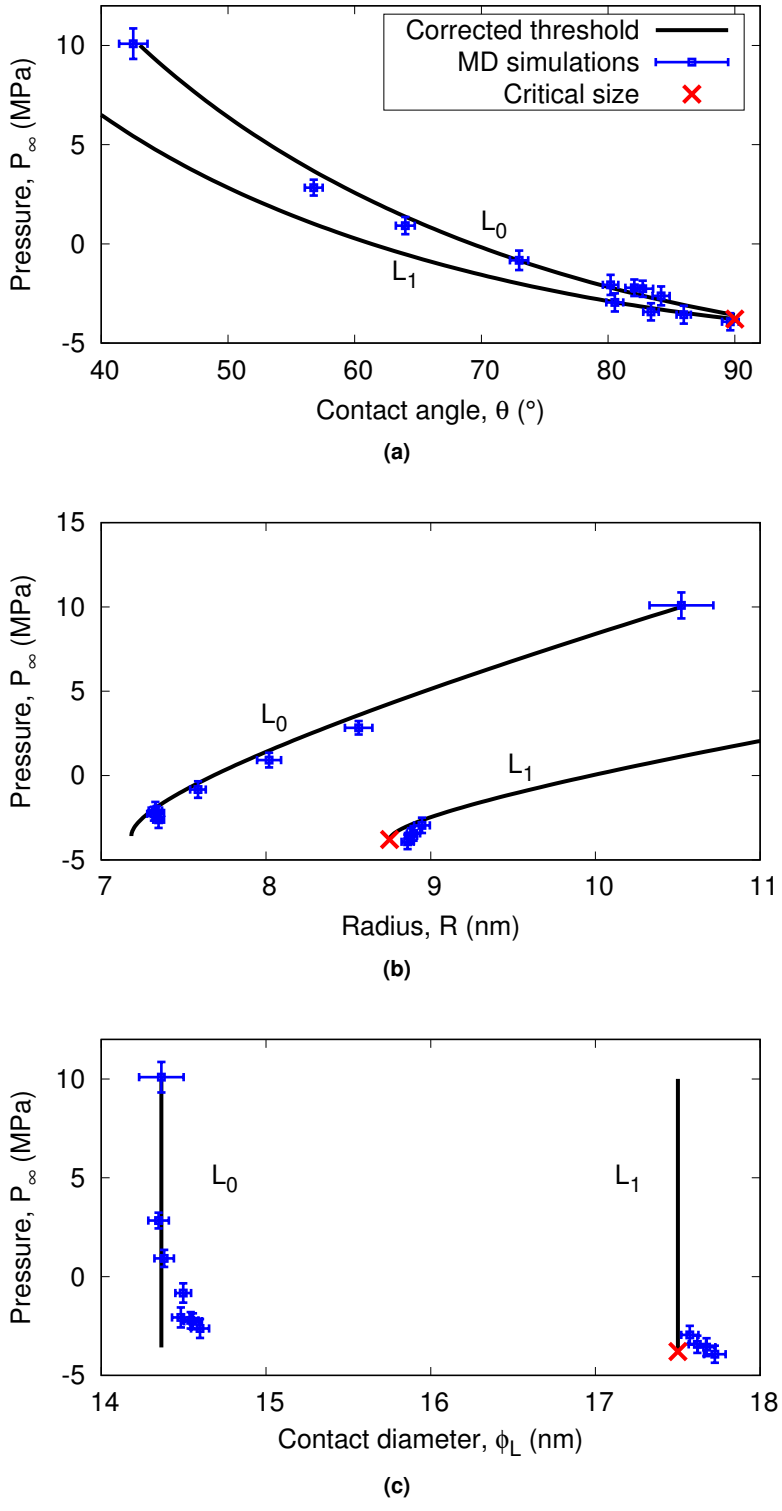


**Figure 4.9:** Variations in: (a) contact angle, (b) radius of curvature, and (c) lateral contact diameter, for the 2D MD surface nanobubble simulations. Results are compared to the proposed corrected threshold model. The labels correspond to the different discrete pinning sites $L_n$.

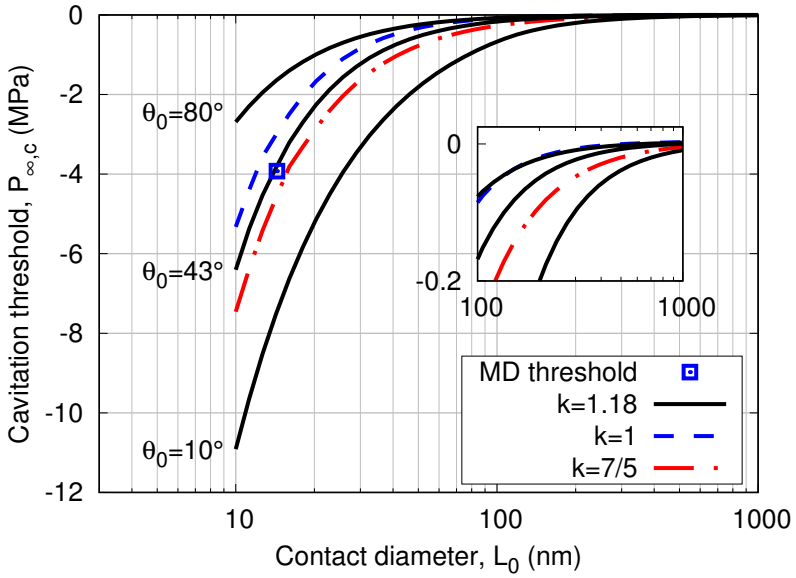


**Figure 4.10:** Variation in the predicted 2D surface nanobubble cavitation threshold with initial contact diameter and contact angle, for $P_{\infty,0} = 10\,\text{MPa}$ and $\gamma = 57.35\,\text{mJ/m}^2$. The inset shows the variations for large surface nanobubbles. Changes in polytropic exponent are also shown for the $\theta_0 = 43^\circ$ bubble.

$(k = 7/5)$ behaviour typically results in a lower cavitation threshold, which is a similar result to the Blake threshold (Blake, 1949; Brennen, 2013). The same 90° limit for pinning site jumps, as explained above, is also used in obtaining the cavitation thresholds for Figure 4.10.

### 4.4.2 3D cavitation threshold

Having confirmed the proposed models accurately predict the cavitation thresholds for 2D surface nanobubbles in Section 4.4.1, it was then appropriate to confirm that the cavitation threshold for a more realistic 3D surface nanobubble could also be predicted. A 3D spherical cap surface nanobubble was equilibrated on a solid substrate, as described in Section 4.3. A concentric ring $S_i/S_o$ patterning was used, equivalent to an axisymmetric form of the patterning used in Section 4.4.1.

A total of 230 000 $H_2O$ molecules were used in the liquid phase. The bubble was initialised as a spherical cap containing 2525 $N_2$ molecules, with a further 575 $N_2$ molecules dissolved in the surrounding bulk liquid to achieve supersaturation. This degree of supersaturation should be sufficient to achieve an equilibrium contact angle of $\theta_e \sim 50^\circ$, using Equations (2.1) and (2.10). The final size of the equilibrated 3D surface nanobubble domain was $28.2 \times 28.2 \times 9.1\,\text{nm}^3$ in the $x$, $y$, and $z$ directions, respectively, although was allowed to expand in the $z$ direction to allow changes in pressure.

At a pressure of $P_{\infty,0} = 10\,\text{MPa}$, the equilibrated 3D surface nanobubble formed a spherical

cap shape with radius of curvature $R_0 = 10.5\,\text{nm}$ and contact angle $\theta_0 = 46^\circ$, pinned to the substrate with initial contact diameter $L_0 = 15.22\,\text{nm}$. The initial gas pressure $P_{g,0}$ could be estimated from Equation (2.1). The other properties $P_v$, $\gamma$, and $k$ were assumed identical to Section 4.4.1.

The 3D simulations were considerably more expensive than the 2D simulations, requiring $\sim 3$ times as many processors per simulation, and so only two cases were run. The applied pressures in these cases were specifically chosen to be above and below the cavitation threshold, respectively, as calculated from Equation (4.20). As in Section 4.4.1, there were additional constraints from the MD simulations for these equations. It was assumed that the maximum contact angle that could be sustained on a pinning site was $90^\circ$; also, due to the axisymmetric pinning, the contact line would now jump in increments of $2\lambda_S$, i.e. $L_n = L_0 + 2n\lambda_S$. Equations (4.19) and (4.20) predicted the corrected cavitation threshold to be $P_{\infty,c} = -9.18\,\text{MPa}$, and so the two simulation cases were run with final applied pressures of $-7.5\,\text{MPa}$ and $-10.5\,\text{MPa}$.

Simulations were run for 5 ns after the pressure drop, as it was shown in Section 4.4.1 that the 2D surface nanobubble simulations demonstrated their respective stability/instability within $\sim 4\,\text{ns}$. The $P_\infty = -7.5\,\text{MPa}$ was found to be stable, while the $P_\infty = -10.5\,\text{MPa}$ case was found to be unstable, in good agreement with the predicted threshold above. The variations in the 3D surface nanobubble volume with time for the stable and unstable cases are shown in Figure 4.11.

The stable growth case shown in Figure 4.11(a) reaches a steady size around $650\,\text{nm}^3$ within 1 ns. The unstable growth case in Figure 4.11(b) continues to grow after 1 ns and clearly does not achieve a stable state, reaching a final volume a magnitude larger than the stable case by the end of the simulation[2]. Towards 5 ns, the unstable growth case starts its rapid or "explosive" growth phase, characteristic of cavitation (Borkent *et al.*, 2007; Brennen, 2013).

The Blake threshold, Equation (2.3), predicts the cavitation threshold of a spherical bubble with radius $R_0 = 10.5\,\text{nm}$ to be $P_{\infty,c} = -4.08\,\text{MPa}$. This is nearly 3.5 MPa higher than observed in the stable growth case where $P_\infty = -7.5\,\text{MPa}$. Again, it is confirmed that the Blake threshold is unsuitable for predicting the cavitation threshold for surface nanobubbles, as suggested by Borkent *et al.* (2007).

Using similar parameters as above: $P_{\infty,0} = 10\,\text{MPa}$ and $\gamma = 57.35\,\text{mJ/m}^2$, the variation in the predicted cavitation threshold for different 3D surface nanobubble shapes and sizes is shown in Figure 4.12. The cavitation threshold depends strongly on the contact angle and lateral contact diameter. Smaller bubbles have a lower cavitation threshold, while the cavitation threshold for larger bubbles tends towards $P_v$, as with the Blake threshold (Blake, 1949; Brennen, 2013). Moving from isothermal $(k = 1)$ to adiabatic $(k = 7/5)$ expansion reduces the cavitation

2. Supplementary videos showing the growth cases in Figures 4.11(a) and 4.11(b) can be found at `https://pubs.acs.org/doi/10.1021/acs.langmuir.8b02887`.

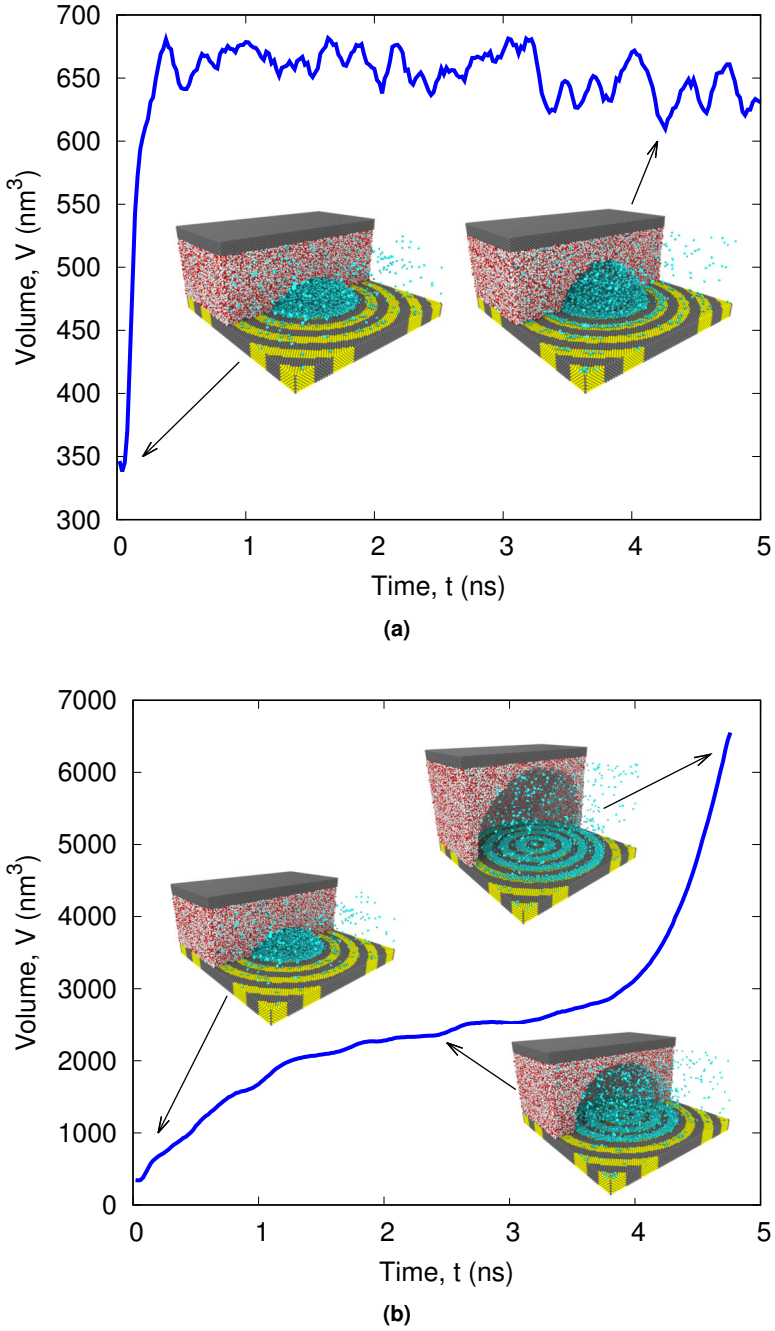


**Figure 4.11:** Variations in bubble volume for (a) stable, $P_\infty = -7.5\,\mathrm{MPa}$, and (b) unstable, $P_\infty = -10.5\,\mathrm{MPa}$, growth cases. Insets show renderings at different times during the MD simulations.

threshold, which again is a feature of the Blake threshold (Blake, 1949; Brennen, 2013). Qualitatively, the variation in cavitation thresholds shown in Figure 4.12 is similar to the 2D surface nanobubbles in Figure 4.12, however, the 3D surface nanobubbles appear to be resistant to much lower pressures. This is a result of the Laplace pressure (whose function in this case is

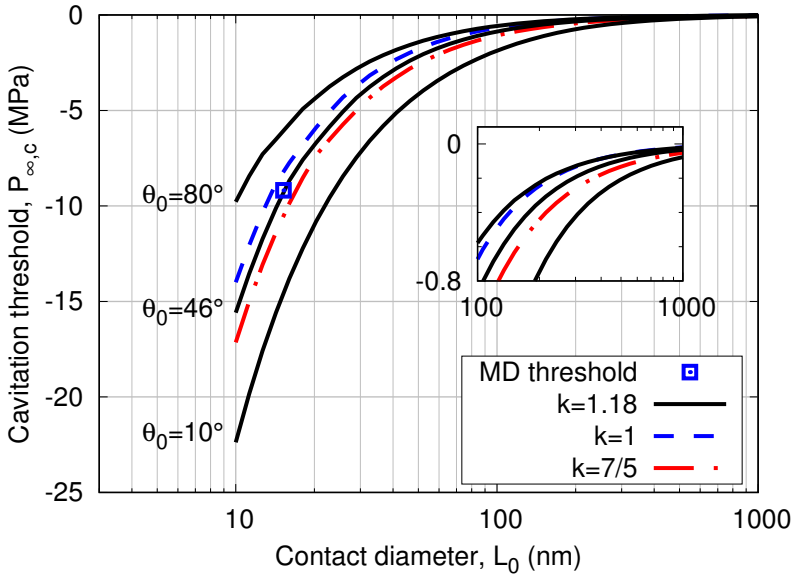


**Figure 4.12:** Variation in the predicted 3D surface nanobubble cavitation threshold with initial contact angle and contact diameter, for $P_{\infty,0} = 10\,\text{MPa}$ and $\gamma = 57.35\,\text{mJ}/\text{m}^2$. The inset shows the variations for large surface nanobubbles. Changes in polytropic exponent are also shown for the $\theta_0 = 46^\circ$ bubble.

to suppress excessive growth) being double the Laplace pressure for the 2D cylindrical bubbles (Maheshwari *et al.*, 2016).

### Comparison to experiments

There have been reports of surface nanobubbles being stable at pressures as low as $-6\,\text{MPa}$ (Borkent *et al.*, 2007). Using more appropriate experimental parameters, i.e. $P_{\infty,0} = 0.1\,\text{MPa}$ and $\gamma = 71.69\,\text{mJ}/\text{m}^2$ (Lemmon *et al.*, 2017), the variations in cavitation threshold with bubble size and shape are predicted by Equations (4.19) and (4.20) and shown in Figure 4.13(a).

Figure 4.13(a) shows that for $L < 20\,\text{nm}$, most surface nanobubbles should be stable at $P_\infty = -6\,\text{MPa}$. For very small surface nanobubbles, e.g. $\theta_0 = 10^\circ$ and $L_0 = 10\,\text{nm}$, the cavitation threshold can be as low as $P_{\infty,c} = -28\,\text{MPa}$. This value is very similar to results discussed in Chapter 2; using methods similar to Berthelot (1850), cavitation thresholds of $P_{\infty,c} = -30\,\text{MPa}$ were obtained (Brennen, 2013; Caupin and Herbert, 2006). This suggests that cavitation nucleating from surface nanobubbles could have been occurring in these studies. While these results seem low, it is worth remembering that the cavitation threshold for pure water, with homogeneous vapour bubble nucleation, is predicted to be $\sim -160\,\text{MPa}$ (Caupin and Herbert, 2006; El Mekki Azouzi *et al.*, 2012; Menzl *et al.*, 2016; Pallares *et al.*, 2014).

With similar initial size as in the MD simulations described above, i.e. $\theta_0 = 46^\circ$ and $L_0 = 15.22\,\text{nm}$, the cavitation threshold is predicted to be around $-15\,\text{MPa}$. For $L_0 > 50\,\text{nm}$, however,

most surface nanobubbles would be expected to cavitate at $P_\infty = -6\,\mathrm{MPa}$, as shown in Figure 4.13(a). So, the results of Borkent *et al.* (2007), which produced stable surface nanobubbles

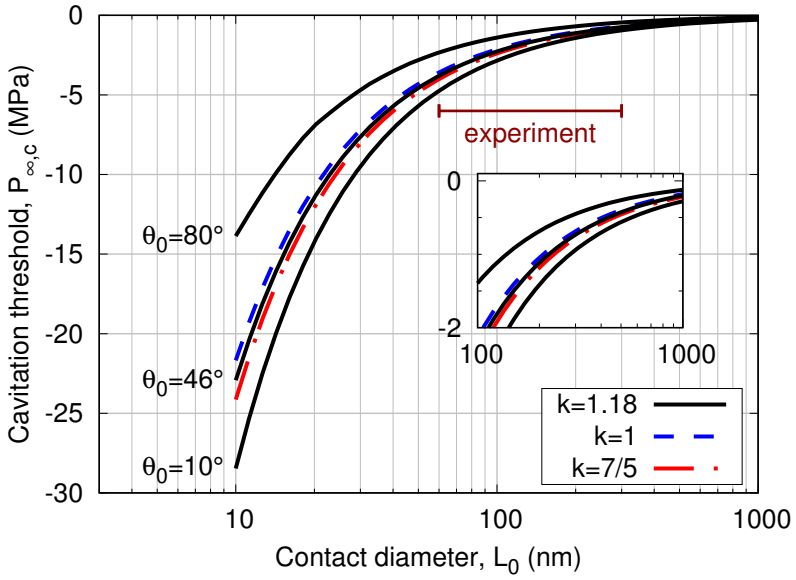


**(a)**

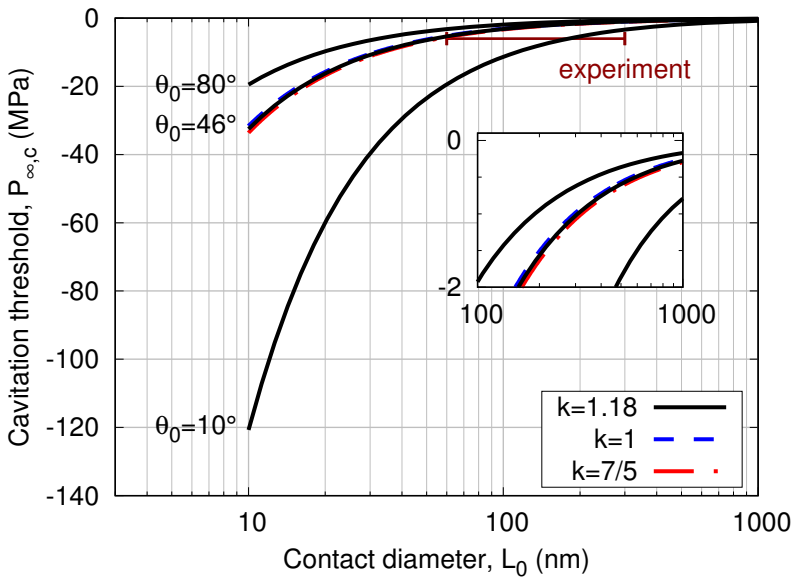


**(b)**

**Figure 4.13:** Variation in the predicted cavitation threshold for different 3D surface nanobubble initial contact angles and contact diameters, with $P_{\infty,0} = 0.1\,\mathrm{MPa}$ and $\gamma = 71.69\,\mathrm{mJ/m^2}$; (a) results of the proposed model; (b) results of the Blake threshold for an equivalent spherical bubble with equal mass to the surface nanobubbles in (a). Also shown is the range of experimental results from Borkent *et al.* (2007). Insets show the variations for large bubbles. Changes in polytropic exponent are also shown for the $\theta_0 = 46^\circ$ bubble.

at $P_\infty = -6\,\text{MPa}$ with sizes up to $L_0 = 300\,\text{nm}$ do not agree with the theoretical predictions in this work; these range of results are also shown in Figure 4.13(a). Equations (4.19) and (4.20) predict the cavitation threshold for $L_0 = 300\,\text{nm}$ to be around $-1\,\text{MPa}$. The proposed models cannot account for this anomalous stability.

One possible explanation for this discrepancy is by considering what would happen if the surface nanobubbles detached from the substrate during growth. The Blake threshold has already been shown to be unsuitable for predicting the cavitation threshold of a surface nanobubble, considering its initial radius of curvature $R_0$. However, consider a spherical bubble with a radius $R_m$, and equal mass to the surface nanobubble. Combining Equations (2.1) and (2.2), and the volume of a spherical bubble, $V = 4\pi R_m^3/3$, the radius of this new spherical bubble can be obtained numerically from:

$$R_m^{3k-1}\left[R_m + \frac{2\gamma}{P_\infty - P_v}\right] = \left(1 + \frac{2\gamma}{R_0\,(P_\infty - P_v)}\right)\left(\frac{3V_0}{4\pi}\right)^k. \tag{4.21}$$

By substituting $R_m$ into Equation (2.3), a new range of cavitation thresholds can be obtained, assuming the surface nanobubble detaches from the surface during growth and forms a spherical bubble, as shown in Figure 4.13(b). The effect of detachment would allow the nanobubbles to resist many mega-Pascals lower pressures than they would if they were still pinned to the substrate. Figure 4.13(b) shows better, although not complete, agreement with results from Borkent *et al.* (2007). Larger surface nanobubbles with $L_0 = 300\,\text{nm}$, for example, would still be expected to experience unstable growth for $P_\infty = -6\,\text{MPa}$.

Another explanation for the discrepancy in these results is the possibility of contamination in the experiments of Borkent *et al.* (2007) (Lohse and Zhang, 2015b). Berkelaar *et al.* (2014) found that droplets of polydimethylsiloxane (PDMS) could be easily mistaken for surface nanobubbles, resulting in erroneous experimental findings, and noted that results from Borkent *et al.* (2007) (among many other publications) could be affected.

Unfortunately, due to the large difference in scale between the MD simulations presented here and the experiments of Borkent *et al.* (2007), direct comparisons cannot be made. There is still uncertainty in the possible mechanism for stability of large surface nanobubbles with $L_0 \sim 300\,\text{nm}$. Further research in this area could explore the exact nature of this apparent enhanced stability during cavitation growth for these larger surface nanobubbles, specifically investigating the influence of polymer contamination, and the possible mechanism for detachment during rapid growth.

## 4.5 Summary

The cavitation threshold for unstable growth of surface nanobubbles cannot be predicted by the classical Blake threshold equation. A new cavitation threshold model has been proposed in this chapter, for 2D cylindrical cap and 3D spherical cap surface nanobubbles, which takes into account the pinned CCR mode of growth. During CCR growth, the radius of curvature $R$ decreases, which increases the surface tension contribution to the pressure balance, i.e. the Laplace pressure $2\gamma/R$. The cavitation threshold and growth paths of a 2D cylindrical cap surface nanobubbles were in good agreement with quasi-2D MD simulations.

The predicted cavitation threshold for a 3D surface nanobubble was also in good agreement with MD simulations. Applying the model to more suitable experimental parameters, $P_{\infty,0} = 0.1\,\text{MPa}$ and $\gamma = 71.69\,\text{mJ/m}^2$, the cavitation threshold for small surface nanobubbles ($\theta_0 = 46^\circ$ and $L_0 = 15\,\text{nm}$) was predicted to be as low as $P_{\infty,c} = -15\,\text{MPa}$; this was many mega-Pascals lower than expected from the Blake threshold.

The proposed models are in good agreement with MD simulations performed in this research. However, experiments by Borkent *et al.* (2007) reported that surface nanobubbles with sizes in the range of $60\,\text{nm} < L_0 < 300\,\text{nm}$ should be stable down to at least $-6\,\text{MPa}$, which could not be validated with the proposed models. Detachment of the surface nanobubbles during growth, which was not observed in the MD simulations, could be a possible mechanism for this enhanced stability. A new radius $R_m$ could be defined for a free spherical bubble with equal mass to the surface nanobubble, and used in the Blake threshold calculation to obtain even lower predicted cavitation thresholds. Even with this proposed explanation, the stability of the larger reported surface nanobubbles ($L_0 \approx 300\,\text{nm}$) could still not be accounted for, and these cited experiments could, instead, have been adversely affected by polymer contamination (Berkelaar *et al.*, 2014). That is not to say that this detachment phenomenon is impossible, however, it is more commonly associated with larger bubbles ($R \sim 1\,\text{mm}$) where buoyancy forces are dominant (Gupta *et al.*, 2017), and not so much during cavitation. Further work could investigate the nature of detachment for rapidly expanding surface nanobubbles.

The proposed models were also constrained such that the maximum contact angle that could be sustained on a particular pinning site was $\theta = 90^\circ$, as observed in the MD simulations. The $S_i/S_o$ patterned substrate provided multiple pinning sites for the bubble contact line. During expansion, the bubble exhibited CCR growth, with "stick-jump" contact line motion between pinning sites. For larger bubbles, this stick-jump behaviour could manifest as the "stick-slip" motion, more commonly observed for droplet wetting dynamics, which would likely result in CCA mode of growth (Li *et al.*, 2014). Further research in this area could investigate how the relative wettabilities of the different substrate types could alter this contact line behaviour.

This concludes this chapter, and the first stage of cavitation for a pinned surface nanobubble. The primary outcome of this work was to determine the pressure at which a surface nanobubble

would begin to experience unstable growth, which would lead to further cavitation effects. By operating in pressures above the thresholds presented here, the effects of cavitation from surface nanobubbles should be mitigated.

Chapter 5

# Oscillation and Growth Dynamics of Surface Nanobubbles

Parts of this chapter have been submitted in a manuscript to *Journal of Fluid Mechanics* and is currently under review: Dockar, D., Gibelli, L., and Borg, M. K. "Mechanical growth dynamics and natural frequencies of surface nanobubbles".

## 5.1 Introduction

It has already been shown in the previous chapter how the threshold for unstable cavitation growth can be predicted for surface nanobubbles. This is often sufficient to mitigate the deleterious effects of cavitation (Brennen, 2013). However, some interesting applications depend on the dynamics of these cavitating bubbles, such as in ultrasound contrast agents where the natural frequency of the bubble strengthens the signal in medical ultrasound imaging (Martynov *et al.*, 2011; Stride and Saffari, 2003), as discussed in Chapter 2. It is also important to understand the rate at which these surface nanobubbles grow for applications in which the collapsing jet dynamics are to be utilised (Brems *et al.*, 2014; Dular *et al.*, 2016; Lukianova-Hleb *et al.*, 2014, 2016).

The most commonly used model for spherical bulk bubble dynamics is the Rayleigh-Plesset equation (Brennen, 2013; Plesset, 1949), reproduced from Equation (2.4):

$$R\ddot{R} + \frac{3}{2}\dot{R}^2 + \frac{4\nu\dot{R}}{R} = \frac{1}{\rho}\left[P_{g,0}\left(\frac{R_0}{R}\right)^{3k} - (P_\infty - P_v) - \frac{2\gamma}{R}\right]. \tag{2.4}$$

Equation (2.4) is a second order, ordinary differential equation, from which it is possible to obtain the bubble's natural frequency (Minnaert, 1933). In a real cavitation event, there are many more complicated phenomena not captured by Equation (2.4), such as compressibility of the liquid (Keller and Miksis, 1980; Trilling, 1952; Vokurka, 1986), non-sphericity during collapse (Klaseboer and Khoo, 2006; Zhang and Duncan, 1994), and even quantum effects (Nagashima *et al.*, 2017); however, its simplicity and enduring use is testament to its importance

in cavitation science. Several authors have used Rayleigh-Plesset dynamics to model nanoscale bubble dynamics with Molecular Dynamics (MD) simulations (Man *et al.*, 2018; Menzl *et al.*, 2016; Tsuda *et al.*, 2015).

In Chapter 4, it was shown that the radius of curvature $R$ for a surface nanobubble decreases during the early stages of growth, contrary to what is expected for a spherical bubble. The resulting change to the Laplace pressure component was enough for the classical Blake threshold model (which assumes spherical bubble growth) to over predict the cavitation threshold of surface nanobubbles by many mega-Pascals. The Rayleigh-Plesset equation is also derived for a spherical bubble, in which it is assumed that bubble growth is accompanied by an increase in $R$. Figure 2.3 shows how Equation (2.4) predicts a bubble to increase in $R$ with a pressure drop. This is the opposite to what was found in Chapter 4, where surface nanobubble growth was better evaluated in terms of its contact angle $\theta$. So, it becomes immediately clear that the Rayleigh-Plesset equation in its current form is unsuitable for modelling the cavitation growth of a spherical cap surface nanobubble. In this chapter, a new model will be proposed for the pinned growth stage of a surface nanobubble, and will be extended to analyse the oscillation dynamics of the surface nanobubble.

## 5.2 Pinned growth model derivation

Leighton (2008) derived a "volume frame" Rayleigh-Plesset equation, in terms of the bubble volume $V$:

$$\frac{1}{4\pi R_{eq}}\left(\ddot{V}-\frac{\dot{V}^2}{6V}\right)+\frac{4\dot{V}\nu}{3V}=\frac{1}{\rho}\left[P_{g,0}\left(\frac{V_0}{V}\right)^k-(P_\infty-P_v)-\frac{2\gamma}{R_{eq}}\right], \tag{5.1}$$

where an equivalent radius is defined $R_{eq}=(3V/4\pi)^{1/3}$. Leighton was not the first author to suggest a volume frame model for non-spherical bubble growth (Klaseboer and Khoo, 2006; Zabolotskaya and Soluyan, 1973), as this is a common procedure for predicting the collapsing dynamics of cavitation bubbles. However, previous attempts at a volume frame model did not capture the appropriate viscous dissipation at the bubble surface, and either used approximations or ignored this viscous term altogether; Equation (5.1) was derived specifically such that Equation (2.4) could be obtained in full by setting $V=4\pi R^3/3$ (Leighton, 2008).

Equation (5.1) was still derived assuming a spherical bubble, and so the equivalent radius will increase with increasing volume. As such, the equivalent Laplace pressure term $2\gamma/R_{eq}$ will still decrease with increasing bubble size. This is usually suitable for "weakly" non-spherical bubbles, which might deviate slightly from a perfectly spherical shape, as in the case of a bubble expansion close to a wall (Benjamin and Ellis, 1966; Brennen, 2013). In these cases, the $R_{eq}$ term acts like the mean radius of curvature to estimate the equivalent Laplace pressure. As found in Chapter 4, the appropriate steady-state pressure balance across a pinned surface

nanobubble interface can only be obtained by considering the radius of curvature variation during constant contact radius (CCR) growth, and not using this equivalent radius $R_{eq}$. The pressure balance on the right-hand side of Equation (5.1) will need to be modified so the *actual* radius of curvature $R$ is used. This pressure balance then becomes $1/\rho[P_{g,0}(V/V_0)^k - (P_\infty - P_v) - 2\gamma/R]$, as rearranged from Equation (4.17).

The inertial and viscous components (on the left-hand side) of Equation (5.1) can then be found with the volume of a spherical cap, reproduced from Equation (4.16):

$$V = \frac{\pi L^3}{24\sin^3\theta}\left[2 - 3\cos\theta + \cos^3\theta\right]. \tag{4.16}$$

Differentiating Equation (4.16) with respect to time twice gives:

$$\dot{V} = \frac{\pi L^3}{8}\frac{1}{(1+\cos\theta)^2}\dot{\theta}, \tag{5.2}$$

and:

$$\ddot{V} = \frac{\pi L^3}{8(1+\cos\theta)^2}\left[\ddot{\theta} + \frac{2\sin\theta}{(1+\cos\theta)}\dot{\theta}^2\right]. \tag{5.3}$$

The equivalent radius for the spherical cap shape is found:

$$R_{eq} = \frac{L}{2\sin\theta}\left[\frac{1}{4}(2+\cos\theta)(1-\cos\theta)^2\right]^{\frac{1}{3}}. \tag{5.4}$$

By substituting in Equations (4.16), (5.2), (5.3), and (5.4) into Equation (5.1), and by considering the correct pressure balance across the surface nanobubble interface, a new "contact angle frame" form of the Rayleigh-Plesset equation can be obtained for spherical cap surface nanobubbles[1]:

$$\ddot{\theta} + \dot{\theta}^2\left[\frac{2\sin\theta}{(1+\cos\theta)} - \frac{1}{2}\frac{1}{\sin\theta(2+\cos\theta)}\right] + \frac{4\nu}{R_{eq}^2}\dot{\theta} = \frac{\sin\theta(2+\cos\theta)}{\rho R_{eq}^2}\left[P_{g,0}\left(\frac{V_0}{V}\right)^k - (P_\infty - P_v) - \frac{4\gamma\sin\theta}{L}\right], \tag{5.5}$$

where the expressions for $V$ and $R_{eq}$ can be found from Equations (4.16) and (5.4), respectively. Equation (5.5) is to be validated using MD simulations in the following sections.

---

1. While the model presented here is in units of radians, results in the following sections will be presented in degrees for readability.

## 5.3 MD simulation set-up

MD simulations were performed of pinned surface nanobubble growth using different time-varying pressure cases and compared to the bubble's size predicted from Equation (5.5). The simulation set-up was similar to that in Section 3.6, with a piston used to control the pressure. The monatomic water (mW) and monatomic nitrogen (mN) models were predominantly used in this chapter for simulations, with potentials given in Tables 3.2 and 3.3. Contact line pinning was provided by a concentric ring pattern of alternating hydrophobic ($S_o$) and hydrophilic ($S_i$) Lennard-Jones (LJ) substrate atoms, with potentials also given in Tables 3.2 and 3.3. Some surface nanobubble simulations with the TIP4P/2004 water ($H_2O$) and two-site nitrogen ($N_2$) models from the previous chapter were also investigated, with potentials as given in Table 3.1.

All simulations were initialised and equilibrated at constant $T = 300\,\mathrm{K}$ temperature using a Nosé-Hoover thermostat until the bubble had reached a steady size, after around 1 ns (Martínez *et al.*, 2009). During the main production simulations (i.e. when the pressure variations were applied), the thermostat was applied only to the liquid, which allowed the nitrogen gas phase to expand without enforcing an adiabatic or isothermal behaviour, as per Chapter 4. A timestep of $\Delta t = 2\,\mathrm{fs}$ was used for all mW–mN simulations, and $\Delta t = 1\,\mathrm{fs}$ for the $H_2O$–$N_2$ simulations.

The volume of the bubble as it changed with time was measured as the volume underneath the normalised fluid density 50% isodensity surface contour. A spherical cap profile was fitted to this surface contour to measure the contact angle and lateral contact diameter.

## 5.4 Results and discussion

### 5.4.1 Response to stable pressure drop

To first confirm Equation (5.5) could accurately predict the growth rate of a pinned surface nanobubble, the simulation results from the 3D stable pressure drop case from Chapter 4 were compared to the proposed model. To recap, the equilibrated surface nanobubble had size $L = 15.22\,\mathrm{nm}$ and contact angle $\theta_0 = 46°$, at initial pressure $P_{\infty,0} = 10\,\mathrm{MPa}$. The TIP4P/2005 $H_2O$ and two-site $N_2$ models were used for the liquid and gas phases, respectively. The pressure was dropped to $P_\infty = -7.5\,\mathrm{MPa}$, over a period of 0.1 ns, using a smoothed hyperbolic tangent function to ensure there was no liquid detachment. The viscosity of the TIP4P/2005 water model is $\mu = 8.441 \times 10^{-4}\,\mathrm{Pa\,s}$, and surface tension is $\gamma = 57.35\,\mathrm{mJ/m^2}$, as given in Chapter 3. Density was assumed constant, $\rho = 1000\,\mathrm{kg/m^3}$ (Lemmon *et al.*, 2017); vapour pressure of the liquid at 300 K was assumed $P_v = 3.353\,68 \times 10^{-3}\,\mathrm{MPa}$ (Lemmon *et al.*, 2017).

Equation (5.5) was solved numerically using the *ode15s* numerical differentiation solver in MATLAB (Shampine and Reichelt, 1997). The variation in contact angle with time with the predicted "pinned model" is shown in Figure 5.1(a). The polytropic exponent was chosen as

$k = 1.18$, as obtained from Chapter 4. The predicted growth rates assuming isothermal $(k = 1)$ and adiabatic $(k = 7/5)$ expansion are also shown. Equation (4.16) was used to model the surface nanobubble's volume with time, using the variation in contact angle from Figure 5.1(a) and constant $L$, and compared to the results from the MD simulation in Figure 5.1(b). The MD simulation data given in Figure 5.1(b) is identical to that in Figure 4.11(a) up to 1.25 ns.

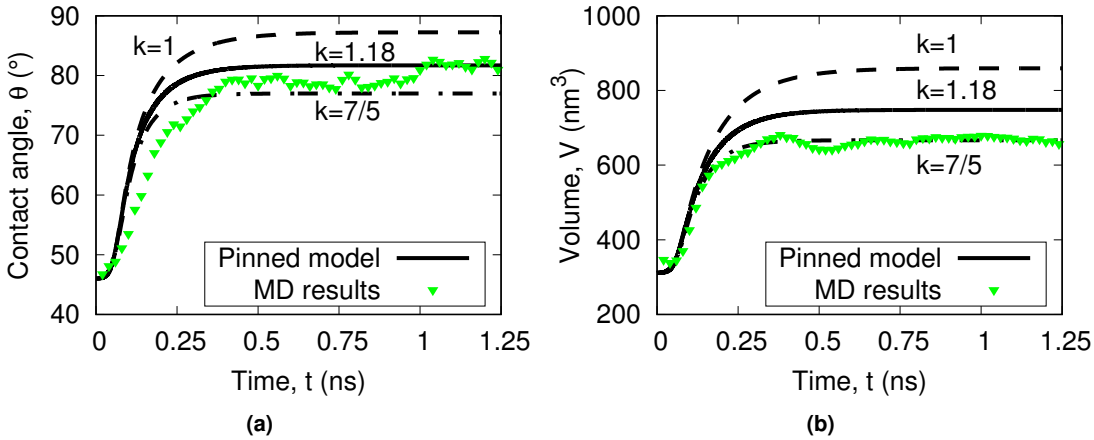


**Figure 5.1:** Time variation of: (a) contact angle, and (b) bubble volume, for a 3D surface nanobubble with $P_\infty = -7.5\,\text{MPa}$ applied pressure drop, using $H_2O$–$N_2$ MD results from Chapter 4, and compared to results predicted from Equations (5.5) and (4.16). Three values of polytropic exponent in Equation (5.5) are shown: $k = 1$ (isothermal, dashed black line), $k = 7/5$ (adiabatic, dot-dashed black line), and the value obtained in Chapter 4, $k = 1.18$ (solid black line).

Equation (5.5) predicts the contact angle and volume of the bubble grows quicker than what is observed in the MD results. However, it should be noted that a relatively small fluid domain was used in these previous simulations, which could have inhibited the growth rate of the bubble, although does not affect the steady-state response which is only dependent on applied pressure. The results appear to better match the adiabatic expansion. The value $k = 1.18$ was obtained for the 2D stable pressure drop cases in Chapter 4, after around 15 ns, which is significantly longer than the 1.25 ns shown here. The 3D surface nanobubble simulation could have grown with adiabatic expansion during this initial stage of growth (as is also observed in the following simulations), although the $k = 1.18$ exponent suggests it would gradually increase in temperature if the simulation was run up to 15 ns.

More MD simulations were performed in which a 3D surface nanobubble was subjected to a rapid change in pressure, using the mW and mN models. These models were computationally cheaper to run than the $H_2O$–$N_2$ pairing, so larger domains could be simulated. A surface nanobubble was equilibrated at $P_{\infty,0} = 10\,\text{MPa}$, as shown in Figure 5.2, with an enhanced view of the bubble in inset A. The substrate was patterned with $S_i$ and $S_o$ atom types directly under the bubble, as shown in inset B. The $S_i/S_o$ patterning was *not* extended across the whole

substrate, as done in Chapter 4, to prevent the contact line jumping across multiple pinning sites during growth. The initial contact angle and lateral contact diameter were measured at $\theta_0 = 50.5^\circ$ and $L = 15.11\,\text{nm}$, respectively. The liquid-bubble system consisted of $3 \times 10^6$ water molecules for the bulk liquid, 7700 nitrogen molecules in the bubble, with a further 1872 nitrogen molecules dissolved in the liquid to provide supersaturation, as per Equations (2.1) and (2.10). The equilibrated fluid domain measured $56.4 \times 56.4 \times 28.5\,\text{nm}^3$ in the $x$, $y$, and $z$ directions, respectively, although was allowed to expand in the $z$ direction to allow variations in pressure. This domain size was approximately 12 times larger than the 3D MD simulation

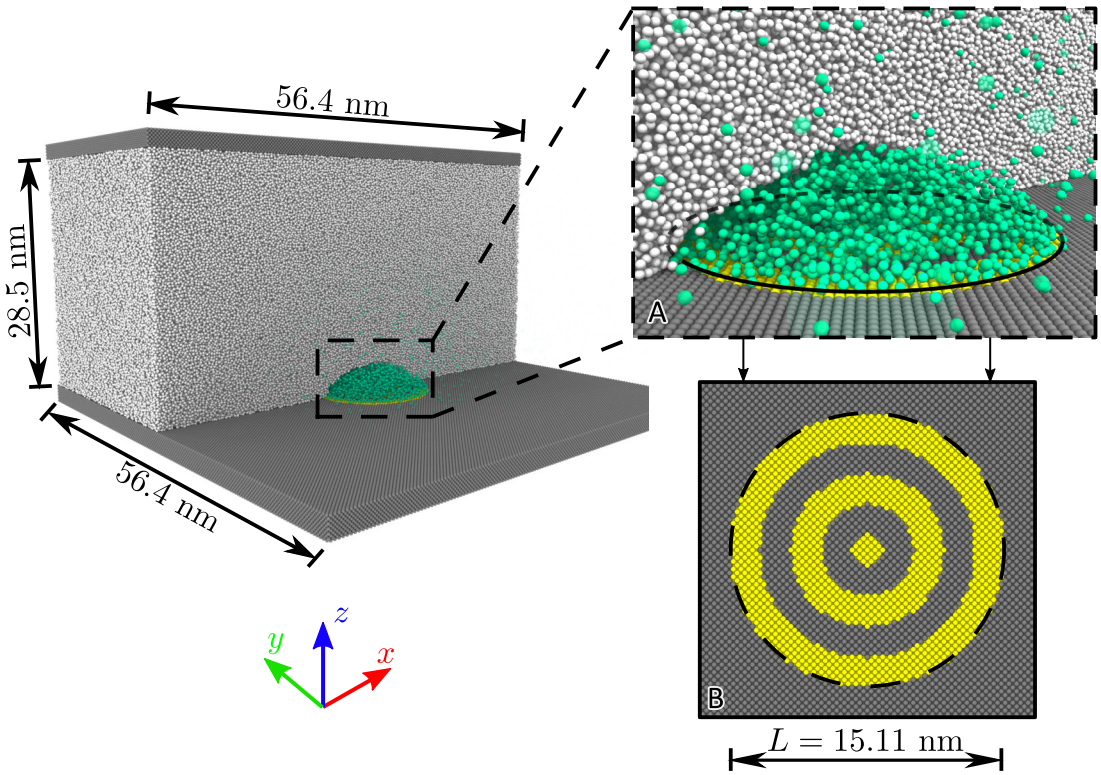


**Figure 5.2:** Schematic of the MD simulation of a 3D surface nanobubble. The white particles are the mW water molecules, green particles are the single-site mN nitrogen molecules, and the dark-grey and yellow atoms are the hydrophilic ($S_i$) and hydrophobic ($S_o$) substrate atoms, respectively. Some of the mW molecules, piston atoms, and dissolved $N_2$ molecules are not shown for clarity. Inset A shows the surface nanobubble in more detail, and inset B shows the $S_i/S_o$ substrate patterning directly below the bubble.

domain employed in Chapter 4. This was found to be necessary to achieve agreement with the proposed models, particularly for the oscillation cases in Section 5.4.2.

Pressure in the liquid was dropped to $P_\infty = -7.5\,\text{MPa}$ over a period of 0.1 ns using a smooth hyperbolic tangent function. This change in pressure to $P_\infty = -7.5\,\text{MPa}$ was specifically chosen as this would result in the largest growth of the surface nanobubble (which would make it easier to measure over the noise in the MD simulations) while still remaining stable, as observed

in Chapter 4. Surface tension for the mW model was $\gamma = 65.384\,\mathrm{mJ/m^2}$, and viscosity $\mu = 3.550 \times 10^{-4}\,\mathrm{Pa\,s}$, from Chapter 3. A total of $3.73 \times 10^5$ atoms were employed in the piston, with an overall piston mass of: $m_p = 1.21 \times 10^{-19}\,\mathrm{kg}$.

Using the parameters described above, Equation (5.5) was used to model the surface nanobubble's variation of contact angle with time and compared to the results from the MD simulation, as shown in Figure 5.3(a). The predicted volume change of the bubble was estimated using Equation (4.16), and is shown in Figure 5.3(b).

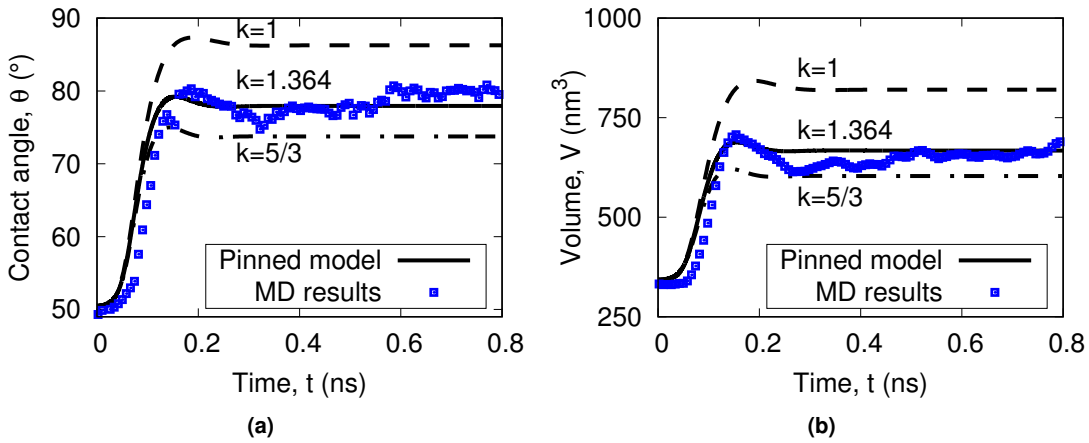


**Figure 5.3:** Time variation of: (a) contact angle, and (b) bubble volume, for a $P_\infty = -7.5\,\mathrm{MPa}$ applied pressure drop to the 3D surface nanobubble using mW–mN MD results, and compared to results predicted from Equations (5.5) and (4.16). Three values of polytropic exponent in Equation (5.5) are shown: $k = 1$ (isothermal, dashed black line), $k = 5/3$ (adiabatic, dot-dashed black line), and the fitted value, $k = 1.364$ (solid black line).

The polytropic exponent $k$ was used as a fitting parameter to match the volume of the bubble from the MD simulations. An appropriate value was found by fitting a line to the variation in gas pressure with bubble volume, as shown in Figure 5.4; the fitted value was found to be $k = 1.364$. The value of $k$ can also qualitatively describe the thermodynamic behaviour of the gas with $k = 1$ indicating isothermal expansion, and $k = 5/3$ being adiabatic expansion for a monatomic gas[2]. These two limits are also shown in the predicted model in Figure 5.3.

Figure 5.3 shows that Equation (5.5) and MD simulations both predict that the surface nanobubble completes most of its growth within the first 0.25 ns. As the gas behaviour changes from adiabatic ($k = 5/3$) to isothermal ($k = 1$), the final steady-state size of the bubble increases as expected; aside from this final size, the qualitative growth behaviour appears visually similar, although reaches a steady-state quicker for the adiabatic case. There are also some higher-frequency variations in the MD simulations, not captured by the proposed model, as can be seen

2. In reality, nitrogen gas is diatomic, however, the single-site nitrogen model used in these simulations is monatomic.

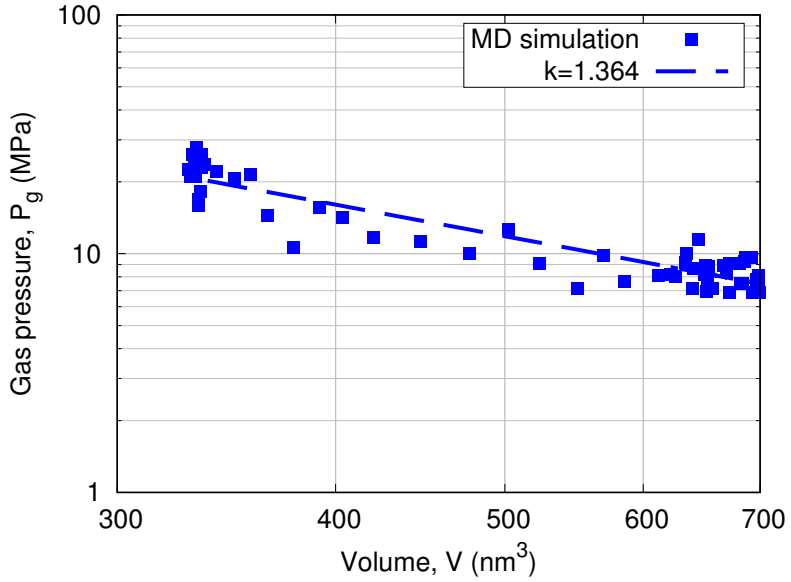


**Figure 5.4:** Variation in gas pressure with bubble volume for the $P_\infty = -7.5\,\mathrm{MPa}$ applied pressure drop to the 3D surface nanobubble, plotted on logarithmic axes. A line is also plotted, corresponding to the fitted polytropic exponent $k = 1.364$.

in Figure 5.3. These are most likely caused by thermal fluctuations, which are more prevalent at the nanoscale (Menzl *et al.*, 2016; Perumanath *et al.*, 2019); these fluctuations would be expected to be negligible for larger surface nanobubble sizes.

For the fitted value of $k = 1.364$, which is in between the isothermal and adiabatic limits, a temperature drop in the bubble would be expected during growth. This is confirmed by the temperature variation in Figure 5.5. Also shown is the liquid temperature, which is thermostatted to 300 K and so does not exhibit any temperature drop.

### Piston inertia effects on pinned growth model

Equation (5.5) derived in Section 5.2 should be suitable for modelling the growth rate of pinned surface nanobubbles surrounded by a semi-infinite liquid. However, the MD simulations in this thesis are clearly not semi-infinite. With computational constraints, a finite number of molecules are used to approximate this semi-infinite liquid domain, which could lead to possible discrepancies. The mass of the piston is found to contribute to the dynamics of the surface nanobubble system. The piston used in the simulations moves up and down in the $z$ direction to allow changes in the system pressure (see Chapter 3). It is assumed that for an incompressible liquid, the volume displaced by the bubble is equal to the volume of liquid displaced, and hence the vertical velocity of the piston $\dot{z}_p$ can be easily obtained:

$$\dot{z}_p = \frac{\dot{V}}{A_p}, \tag{5.6}$$

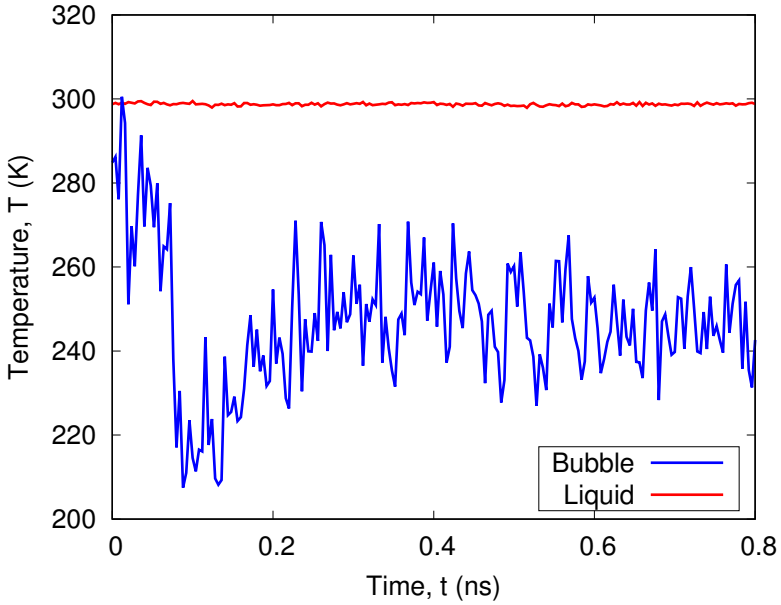


**Figure 5.5:** Variation in the bubble and surrounding liquid temperatures with time for the $P_\infty = -7.5\,\mathrm{MPa}$ pressure drop simulation on the 3D surface nanobubble.

where $A_p$ is the plane area of the piston in contact with the fluid. Equation (5.6) can be differentiated to calculate the piston acceleration:

$$\ddot{z}_p = \frac{\ddot{V}}{A_p}. \tag{5.7}$$

By balancing the pressures across the piston, the far-field liquid pressure $P_\infty$ can be estimated from:

$$P_\infty = P_{in} + \frac{m_p \ddot{z}_p}{A_p}. \tag{5.8}$$

Equation (5.8) can be substituted into Equation (5.5), using Equations (5.3) and (5.7), to obtain a modified model to be used for comparison with the following MD simulations, for small but finite values of $m_p$:

$$\ddot{\theta}\left[1+\frac{4\pi m_p}{A_p^2\rho}R_{eq}\right] + \dot{\theta}^2\left[\frac{2\sin\theta}{(1+\cos\theta)}\left(1+\frac{4\pi m_p}{A_p^2\rho}R_{eq}\right) - \frac{1}{2}\frac{1}{\sin\theta\,(2+\cos\theta)}\right] + \frac{4\nu}{R_{eq}^2}\dot{\theta}$$
$$= \frac{\sin\theta\,(2+\cos\theta)}{\rho R_{eq}^2}\left[P_{g,0}\left(\frac{V_0}{V}\right)^k - (P_{in}-P_v) - \frac{4\gamma\sin\theta}{L}\right]. \tag{5.9}$$

Equation (5.5) can be obtained again by setting $m_p = 0$; only the inertial terms, containing $\ddot{\theta}$ and $\dot{\theta}^2$, have changed.

The inertial terms in Equation (5.9) have a dependence on the piston's mass $m_p$. Figure 5.6 shows the difference in the predicted contact angle variations for Equations (5.5) and (5.9),

including the mass of the "heavy" piston as used earlier. There is a small increase in the

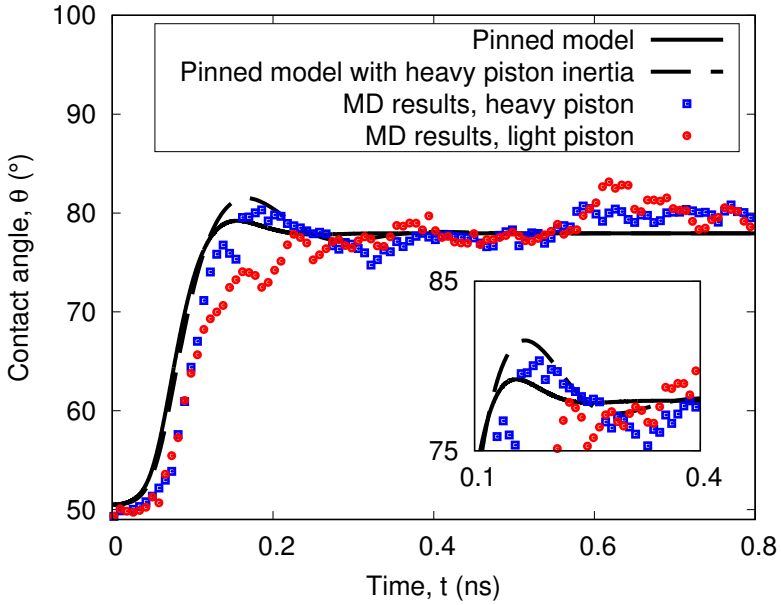


**Figure 5.6:** Time variation of contact angle for the $P_\infty = -7.5\,\mathrm{MPa}$ pressure drop applied to the 3D surface nanobubble, with a correction to the proposed model for piston inertia effects. Also shown is MD simulation results of the $P_\infty = -7.5\,\mathrm{MPa}$ pressure drop case with pressure applied by the "heavy" and "light" pistons.

"overshoot" response at around $t = 0.15\,\mathrm{ns}$ when accounting for the inertia of the piston, and this is also observed in the MD simulations. The piston's inertial effect on the liquid pressure $P_\infty$ in the MD simulations is shown in Figure 5.7 and compared to Equations (5.8) and (5.9). The variations in gas pressure ($P_g = P_{g,0}(V_0/V)^k$), and Laplace pressure ($4\gamma\sin\theta/L$) are also shown in Figure 5.7 and are in good agreement with the pressures obtained from the MD simulations.

Also shown in Figure 5.6 is a similar simulation with a "light" piston, where the piston atoms have a similar mass as an mW water molecule (see Chapter 3). The total mass of the light piston is $m_p = 1.12 \times 10^{-20}\,\mathrm{kg}$. There is not a significant difference in the time taken to reach the equilibrium size for the lighter piston, however, the lighter piston experiences stronger effects from random thermal fluctuations in the liquid, as can be seen by the "bump" at around $t = 0.6\,\mathrm{ns}$, and larger deviations from the proposed model. The liquid thermal fluctuations impacting the piston might also be the cause for the lack of overshoot in the light piston MD simulations.

This difference in behaviour between the piston masses can also be examined in the mean $z$ displacement during the pressure drop simulation, as shown in Figure 5.8. Both pistons reach the same final mean position of $z_p = 28.719\,\mathrm{nm}$ after around $0.2\,\mathrm{ns}$. Both pistons experience fluctuations around this mean position due to the nearby liquid thermal fluctuations; the lighter

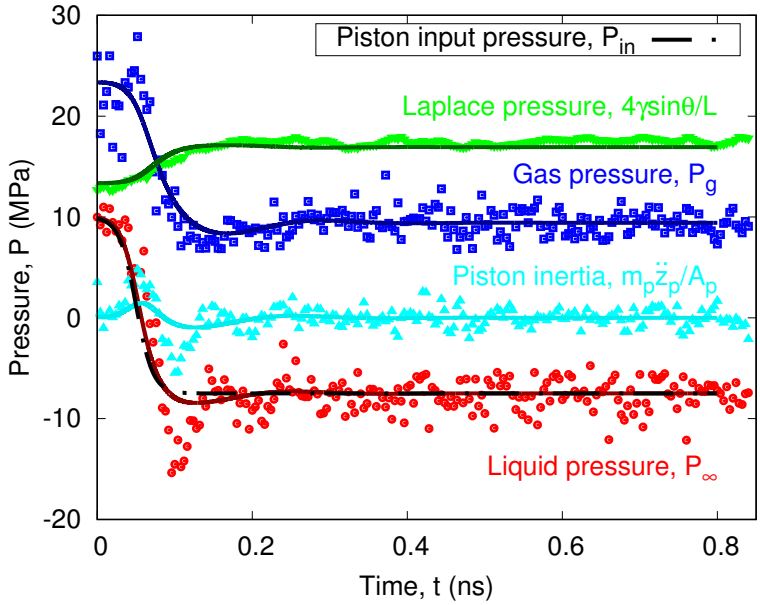


**Figure 5.7:** Time variation of liquid, gas and Laplace pressures with time for the pressure drop simulation. Also shown is the input piston pressure variation, and the resulting contribution to the pressure from the piston's inertia. The different pressure contribution terms from Equation (5.9) are shown as solid lines, and MD simulation results are shown as symbols.

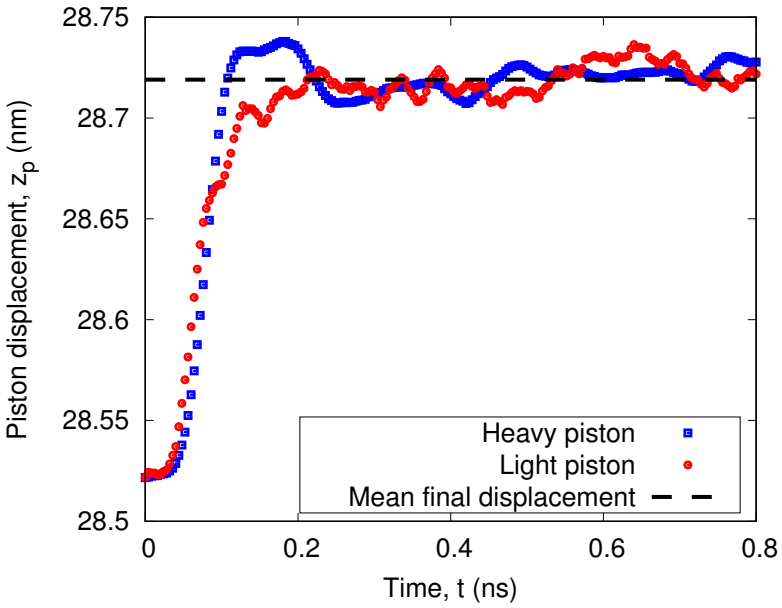


**Figure 5.8:** Piston displacement for the heavy and light pistons during the $P_\infty = -7.5\,\mathrm{MPa}$ pressure drop MD simulations.

piston experiences a greater frequency of these fluctuations due to the stronger effects on the lower piston mass. The same bump at around $t = 0.6\,\text{ns}$ is also observed in the lighter piston results, in Figure 5.6. These results show that variations in the bubble's volume, both during growth and at a steady-state, can be affected by the mass of the piston. The heavier piston appears better at enforcing the pressure in steady-state conditions, however, in Section 5.4.2 the suitability of this piston for rapid dynamic systems will be examined in more detail.

### 5.4.2 Oscillation dynamics of pinned surface nanobubbles

Various MD simulations were performed in which the surface nanobubbles were subjected to an oscillating pressure field at different frequencies. The same initial surface nanobubble from the previous section was used, with $P_{in,0} = P_{\infty,0} = 10\,\text{MPa}$. The piston pressure was varied with a sinusoidal function $P_{in}(t) = P_{in,0} + \Delta P_{in} \sin(\Omega_d t)$, where $\Delta P_{in}$ was the input pressure amplitude, and $\Omega_d$ was the driving frequency. For all the simulations in this section, $\Delta P_{in} = 5\,\text{MPa}$. The driving frequency $\Omega_d$ was varied to investigate the surface nanobubble's response.

#### Discussions on the MD simulation set-up

The simulation set-up in Section 5.4.1 was found to be suitable for modelling simple pressure drop cases. However, in oscillating pressure-driven simulations, large amplitudes and growth rates can develop, particularly near the bubble's natural frequency $\omega_0$, which can invalidate the assumptions of a semi-infinite surrounding liquid. The set-up of the surface nanobubble MD simulations is examined here to evaluate whether they are suitable for accurately modelling the dynamic nature of the oscillating cases, particularly concerning the fluid viscous and inertial effects.

The viscous boundary layer of an oscillating droplet has a thickness of the order $\delta \sim \sqrt{\nu/\omega_0}$ (Prosperetti, 2012). For oscillating droplets, dissipation in the viscous boundary layer near the liquid-gas interface can be considered the dominant dissipation mechanism if this length scale is much smaller than the liquid droplet radius (Prosperetti, 2012). For a nanobubble, which can be treated as the inverse of a droplet, this viscous boundary layer can be assumed negligible compared to the extent of the domain boundaries. For the nanobubbles investigated in this section, the natural frequency is of the order $\omega_0 \sim 10\,\text{rad/ns}$; the expected viscous boundary layer would then be $\delta \sim 6\,\text{nm}$, compared to the 28.5 nm length of the MD simulation domain boundaries and so was regarded as sufficiently small for this simulation. The ratio of damping in this viscous boundary layer to damping in the bulk liquid in the MD simulations is also checked, and given by $kP_{g,0}L^2/4\rho\nu^2 \sim 20$ (Gelderblom *et al.*, 2012); this ratio is deemed sufficiently large to neglect the effects of viscous dissipation within the bulk liquid for the proposed model.

A new length scale was derived in Appendix A to find the far-field limit $r_\infty$ at which the inertial effects of the liquid are uninhibited by the domain's limited size, during bubble dynamics

driven by oscillating pressures. It is found that the ideal simulation domain should have a size $r_\infty \gg \left[\Delta P_\infty \rho R_0^6/32\mu^2\right]^{1/4}$, where $\Delta P_\infty$ is the far-field oscillating pressure amplitude. This limit was derived strictly for a spherical bubble simulation, however, it can give a rough estimate for a surface nanobubble simulation domain by setting $R_0 = R_{eq,0}$, where $R_{eq,0}$ is the equivalent radius of the initial surface nanobubble volume $V_0$. In practical terms, $r_\infty$ can be thought of as the distance to the closest domain boundary. Interestingly, despite being an analysis on the inertial effects of the surrounding liquid, the liquid viscosity has a more significant role, as it dictates the amplitudes of the bubble oscillations during pressure-driven dynamics. Due to the $R_0^6$ term, the effect of viscosity weakens for simulations of larger bubbles, and the relative domain-to-bubble size would need to increase. For the current simulation set-up, it was found that $\left[\Delta P_\infty \rho R_0^6/32\mu^2\right]^{1/4} \sim 1.7\,\text{nm}$, which was considered suitably small compared to the 28.5 nm simulation domain lengths.

Due to the mass of the piston, the inertia of the whole system increases. In Section 5.4.1, Equation (5.5) was modified to account for the piston mass to obtain Equation (5.9). It was assumed that the motion of the piston was directly related to the volume expansion of the bubble, such that the velocity and acceleration of the piston could be calculated using Equations (5.6) and (5.7), respectively. For this to be true, the piston and bubble would need to act in phase, i.e. as a one degree of freedom (DoF) system. This assumption was acceptable for "slow" changes in pressure, such as the simulations in Section 5.4.1. However, for oscillation dynamics, where the pressure is enforced at high sinusoidal frequencies, there is the risk of the piston and bubble "decoupling" and acting as a two DoF system, where the piston's own natural frequency in the system becomes more dominant. If the piston and bubble interacted as a two DoF system, the amplitude of the bubble's oscillations could not be reliably analysed, and it would not represent a realistic system of a surface nanobubble surrounded by a semi-infinite liquid.

A new dimensionless number was derived in Appendix A to evaluate the relative effects of the piston inertia to the driving pressures:

$$\beta = \frac{m_p \pi R_{eq,0}^3 \Omega_d}{A_p^2 \mu}. \tag{5.10}$$

An ideal system should have $\beta \ll 1$, for forcing frequencies close to the natural frequency $\Omega_d \sim \omega_0$. This dimensionless number does not depend on the pressure variation amplitude but instead depends on the forcing frequency $\Omega_d$, and the liquid viscosity. The mass and area of the piston are important with a lighter and larger piston most likely to avoid these adverse effects. While the dimensionless number in Equation (5.10) contains an $A_p^2$ term in the denominator, the piston mass is typically dependent on the plane area, so the number typically scales with $m_p/A_p^2 \propto 1/A_p$ for a fixed piston density.

Figure 5.9(a) shows the variation in the measured liquid pressure and pressure contributed from the piston inertia from an MD simulation of a surface nanobubble subjected to an oscillating

pressure input with amplitude $\Delta P_{in} = 5\,\text{MPa}$ and frequency $\Omega_d = 60\,\text{rad/ns}$, using the heavier piston. Also shown in Figure 5.9(a) is the input piston pressure, given by $P_{in}(t) = P_{in,0} + \Delta P_{in} \sin(\Omega_d t)$. For this set-up $\beta = 0.52$, which is not desirable as it is only slightly smaller than unity. The effective pressure contributed from the piston's inertia is significant, and the resulting pressure measured in the liquid is nearly 10 MPa larger than maximum input pressure. The liquid pressure also resembles a sinusoidal shape but can be seen to *not* be in phase with the input pressure function. This suggests that in this particular simulation, the bubble and piston have become a two DoF system, and so would not be suitable for investigating the bubble's oscillation dynamics.

To minimise this effect, the lighter piston, as used in Figure 5.8, was used to enforce the pressure in another oscillating pressure MD simulation, using the same input pressure function as Figure 5.9(a). Figure 5.9(b) shows the variation in the measured liquid pressure and pressure from the piston inertia with the lighter piston. For the lighter piston set-up $\beta = 0.048$, which is an order of magnitude smaller than for the previous set-up in Figure 5.9(a). The contribution of the piston's inertia on the liquid pressure is significantly reduced compared to Figure 5.9(a), and the measured liquid pressure more closely matches the input pressure function. By subtracting the measured piston inertia from the measured liquid pressure in the MD simulations, a curve closely matching the piston input pressure variation can be obtained, seen in both cases in Figure 5.9. This confirms the suitability of the assumptions taken for Equation (5.8).

The effect from this piston's inertia on the bubble's oscillation dynamics is also examined. The variation in the contact angle, with pressure enforced by the heavy piston, do not match the proposed models, even accounting for the increased piston's inertia with Equation (5.9), as shown in Figure 5.10(a). The amplitude and phase of the resulting surface nanobubble oscillation do not match the prediction, for either isothermal $(k = 1)$ or adiabatic $(k = 5/3)$ expansion. The MD simulation results obtained using the lighter piston much better match the predicted oscillation of the surface nanobubble, as shown in Figure 5.10(b).

For the remainder of the research in this section, the lighter piston was used to apply the pressure oscillations. Since the lighter piston was used, the contribution to the pressure from the piston inertia was considered negligible, and so the input forcing on the piston could be approximated to the liquid pressure $P_{in} = P_\infty$ (and $\Delta P_{in} = \Delta P_\infty$). This is important for accurately modelling the surface nanobubble's frequency response, since a constant value of $\Delta P_\infty$ will be achieved across the full oscillation frequency range, and so the peak oscillation amplitude can be observed near the natural frequency.

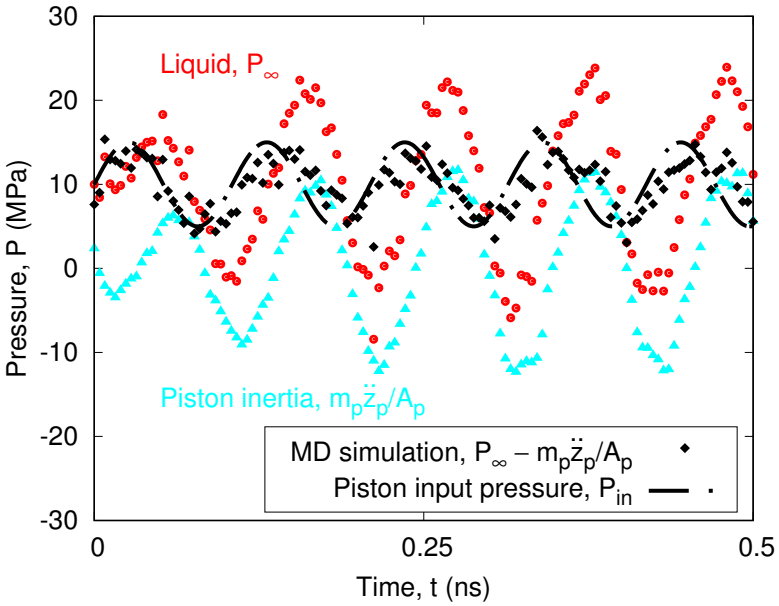


(a)

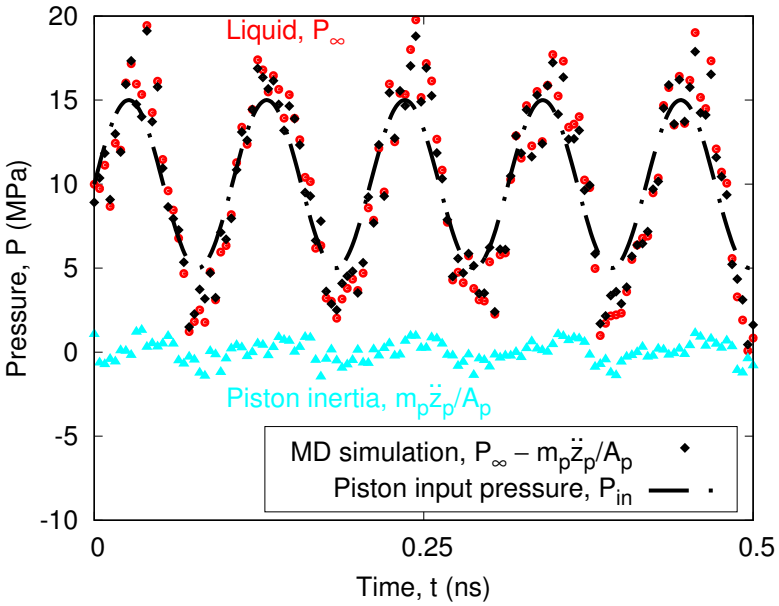


(b)

**Figure 5.9:** Variation in the measured liquid pressure and piston inertia contribution in the MD simulations of an oscillating surface nanobubble, with pressure enforced by the: (a) heavy piston ($\beta = 0.52$), and (b) light piston ($\beta = 0.048$). Also shown is the sinusoidal input pressure function, $\Delta P_{in} = 5\,\mathrm{MPa}$ and $\Omega_d = 60\,\mathrm{rad/ns}$.

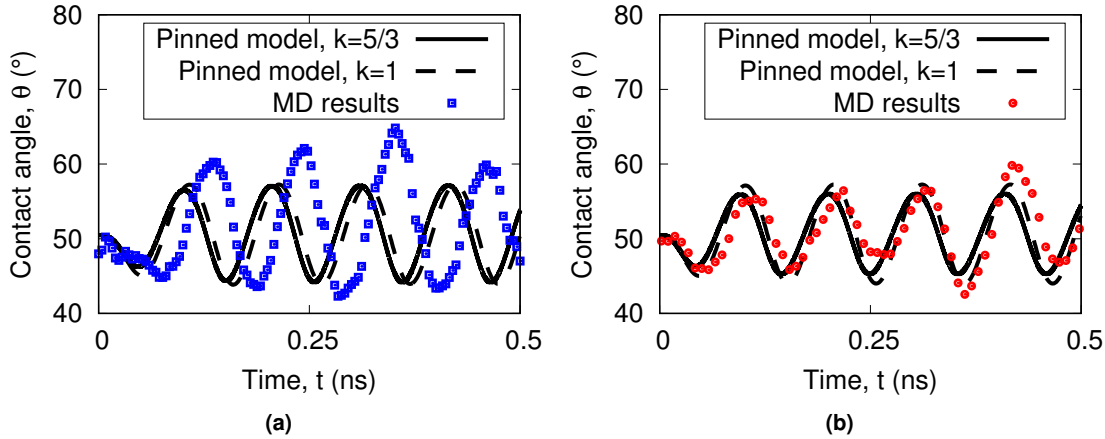


**Figure 5.10:** Variation in the contact angle from the MD simulations of an oscillating surface nanobubble, with pressure enforced by the: (a) heavy piston ($\beta = 0.52$), and (b) light piston ($\beta = 0.048$), for the sinusoidal input pressure function, with $\Delta P_{in} = 5\,\text{MPa}$ and $\Omega_d = 60\,\text{rad/ns}$. Results are compared to the proposed model in Equation (5.9), with two values of $k$: adiabatic expansion ($k = 5/3$), and isothermal expansion ($k = 1$), respectively, and using the appropriate piston mass from each simulation.

### Surface nanobubble oscillation frequency response

Once the correct simulation set-up had been established, a further 14 MD simulations were run with surface nanobubbles subjected to pressure oscillations at varying driving frequency between $\Omega_d = 10\,\text{rad/ns}$ to $\Omega_d = 120\,\text{rad/ns}$. The input pressure amplitude was kept at $\Delta P_\infty = 5\,\text{MPa}$. Each case was run for 2 ns which was found to be enough time to establish a steady sinusoidal response. The variation in the contact angle and volume for the $\Omega_d = 10\,\text{rad/ns}$ case is shown in Figures 5.11(a) and 5.11(b), respectively.

The polytropic exponent $k$ was found again for the $\Omega_d = 10\,\text{rad/ns}$ case by fitting a line to the variation in gas pressure with bubble volume, as shown in Figure 5.12. The fitted polytropic exponent $k = 1.658$ is very close to the adiabatic limit of $k = 5/3$. Also shown in Figure 5.11 are the predicted contact angle and volume variations, using Equations (4.16) and (5.9), with adiabatic ($k = 5/3$) and isothermal ($k = 1$) expansions; the MD results are in better agreement with the adiabatic prediction, compared to the isothermal expansion, as expected from the fitted value of $k$.

Prosperetti (1991, 1977) analysed the thermal behaviour and effective damping of the internal gas phase for spherical bubble oscillations; the Peclet number $Pe = R_0^2 \Omega_d / D_g$ can also give an estimate on the thermal gas behaviour during oscillations. The thermal diffusivity of the gas is given by $D_g = K_g / \rho_g C_p$, where $K_g$ is the thermal conductivity of the gas, $\rho_g$ is the gas density, and $C_p$ is the specific heat capacity of the gas at constant pressure. Prosperetti (1991, 1977) suggested that for $Pe \lesssim 1$, the gas expansion can be considered isothermal, while adiabatic

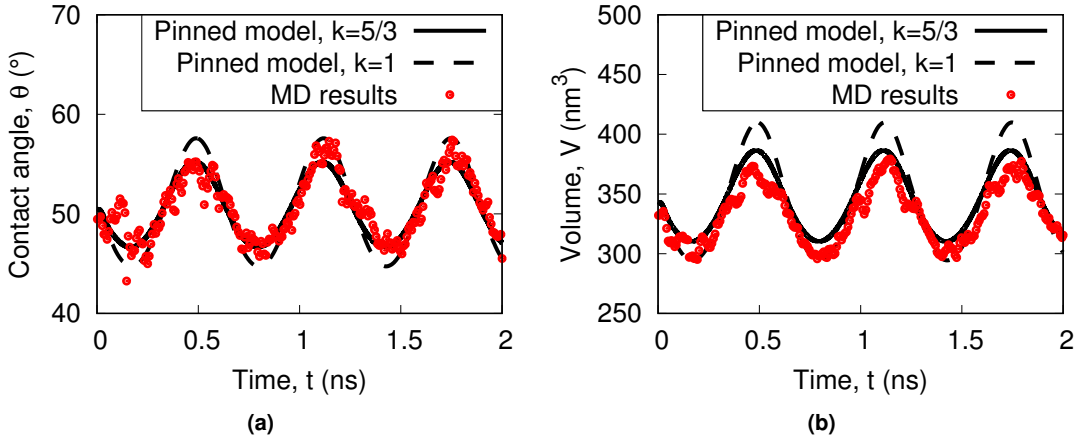


**Figure 5.11:** Variation in the: (a) contact angle, and (b) bubble volume, from the MD simulations of an oscillating surface nanobubble, with pressure enforced by a sinusoidal input function, $\Delta P_\infty = 5\,\mathrm{MPa}$ and $\Omega_d = 10\,\mathrm{rad/ns}$. Also shown is the predicted model for adiabatic expansion ($k = 5/3$), and isothermal expansion ($k = 1$).

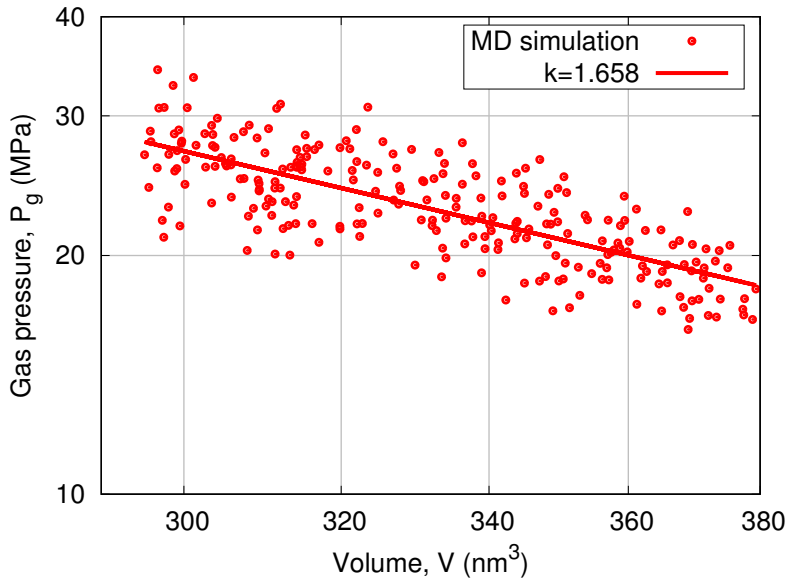


**Figure 5.12:** Variation in gas pressure with bubble volume for a surface nanobubble subjected to an oscillating pressure, with $\Delta P_\infty = 5\,\mathrm{MPa}$ and $\Omega_d = 10\,\mathrm{rad/ns}$, plotted on logarithmic axes. A line is also plotted, corresponding to the fitted polytropic exponent $k = 1.658$.

behaviour would be expected for Peclet numbers approaching $\sim 10^5$. For the bubble cases run here, setting $R_0 = R_{eq,0}$, with the gas initially at $P_{g,0} = 23.4\,\mathrm{MPa}$, gives $Pe \sim 2$ (Lemmon *et al.*, 2017), for the slowest oscillation frequency $\Omega_d = 10\,\mathrm{rad/ns}$. For such small bubbles close to the surface, it may seem surprising that the observed gas behaviour in Figure 5.12 is not isothermal, since the Peclet number is not much greater than 1. However, it should be noted that with the

current MD simulation set-up, the LJ solid atoms of the lower substrate are kept rigid. This effectively creates an insulated boundary, where no heat transfer is possible across the gas-solid interface, and this could artificially lead the gas to more adiabatic behaviour. If the substrate was thermostatted like the liquid, it might result in nearer isothermal gas expansion, which could be investigated in future work. Alternatively, other nanoscale interfacial phenomena not considered in the analyses by Prosperetti (1991, 1977), such as the Kapitza resistance, could have inhibited heat transfer to the bubble. For the rest of the oscillating pressure cases, it was assumed all the bubbles expanded adiabatically, since $Pe$ increases with increasing $\Omega_d$ (Prosperetti, 1991).

The variation in the pressures acting on the bubble as it oscillated in the MD simulation was also well predicted by the proposed models, as shown in Figure 5.13. Equations (5.8) and (5.9) were used to predict the piston inertia effect on the liquid pressure, and was confirmed to provide a negligible contribution, as shown in Figure 5.13(b).

For all driving frequency cases, the surface nanobubble contact angle variations all exhibited an oscillatory response, as in Figure 5.11(a), and a sinusoidal function could be fitted to the response in each case. The contact angle oscillation amplitude was measured, and is shown as a function of driving frequency in Figure 5.14. The full surface nanobubble response, as predicted by Equation (5.5), and the MD simulation results for each oscillation frequency case can be found in Appendix B. Figure 5.14 shows that the oscillation amplitude of the surface nanobubble from the MD simulations is maximum around $\Omega_d = 70\,\mathrm{rad/ns}$. Various models in literature have been proposed to estimate the natural frequency of a bubble, as will be discussed below (Blue, 1967; Miller and Nyborg, 1983; Minnaert, 1933).

Equations (2.4) and (5.5) are both second order non-linear ordinary differential equations, which are intended to capture the cavitation dynamics of spherical and surface nanobubbles, respectively. However, their non-linear forms make them difficult to solve analytically, and so need to be simplified in order to gain a better understanding of the bubble's oscillatory behaviour. Equation (2.4) can be linearised by assuming small radial perturbations $\xi$, i.e. $R(t) = R_0 + \xi(t)$, where $\dot{R} = \dot{\xi}$, and $\ddot{R} = \ddot{\xi}$. Ignoring higher orders of $\xi$, a simplified expression for the oscillation dynamics of a spherical bubble can be obtained:

$$\ddot{\xi} + \frac{4\nu}{R_0^2}\dot{\xi} + \frac{1}{\rho R_0^2}\left[3kP_{g,0} - \frac{2\gamma}{R_0}\right]\xi = \frac{\Delta P_\infty}{\rho R_0} f(t), \tag{5.11}$$

where $f(t)$ is some time-dependent function, e.g. a sinusoidal function as used in these simulations. Equation (5.11) resembles the classical equation for a damped oscillator $\ddot{x} + \alpha\dot{x} + \omega_0^2 x = G(t)$, where $x$ is a generic coordinate frame, $\omega_0$ is the system natural frequency, $\alpha$ is the damping coefficient, and $G(t)$ is the forcing function. From this damped oscillator analysis,

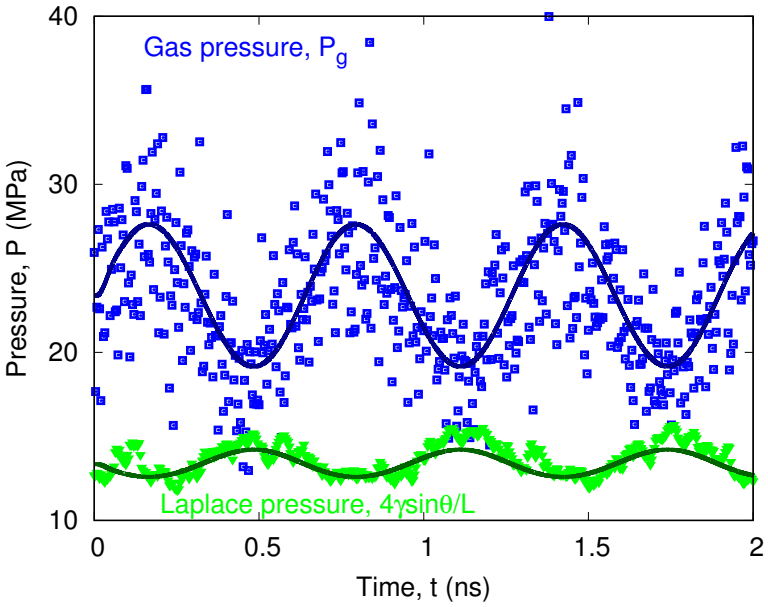


**(a)**

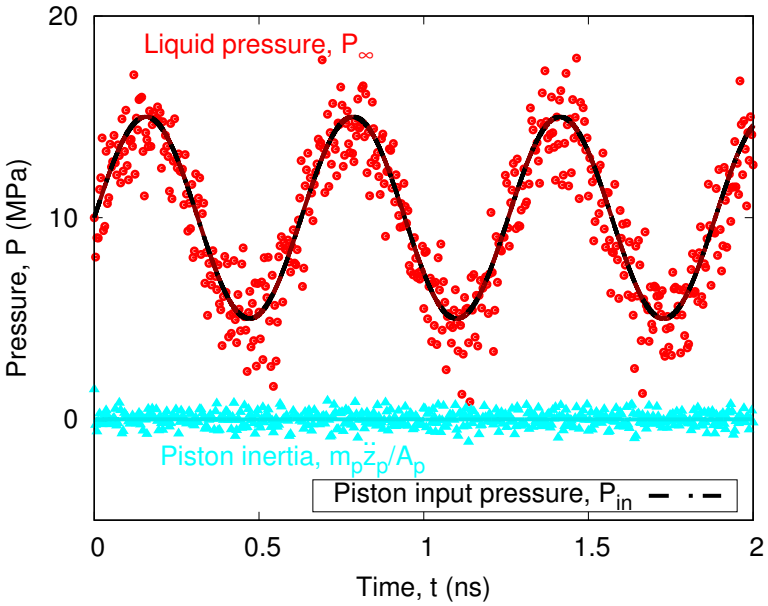


**(b)**

**Figure 5.13:** Time variation of: (a) surface nanobubble gas and Laplace pressures, and (b) liquid pressure, piston input pressure and resulting pressure from piston inertia, for a surface nanobubble subjected to an oscillating pressure, with $\Delta P_\infty = 5\,\mathrm{MPa}$ and $\Omega_d = 10\,\mathrm{rad/ns}$. The different pressure contribution terms from Equation $(5.9)$ are shown as solid lines, and MD simulation results are shown as symbols.

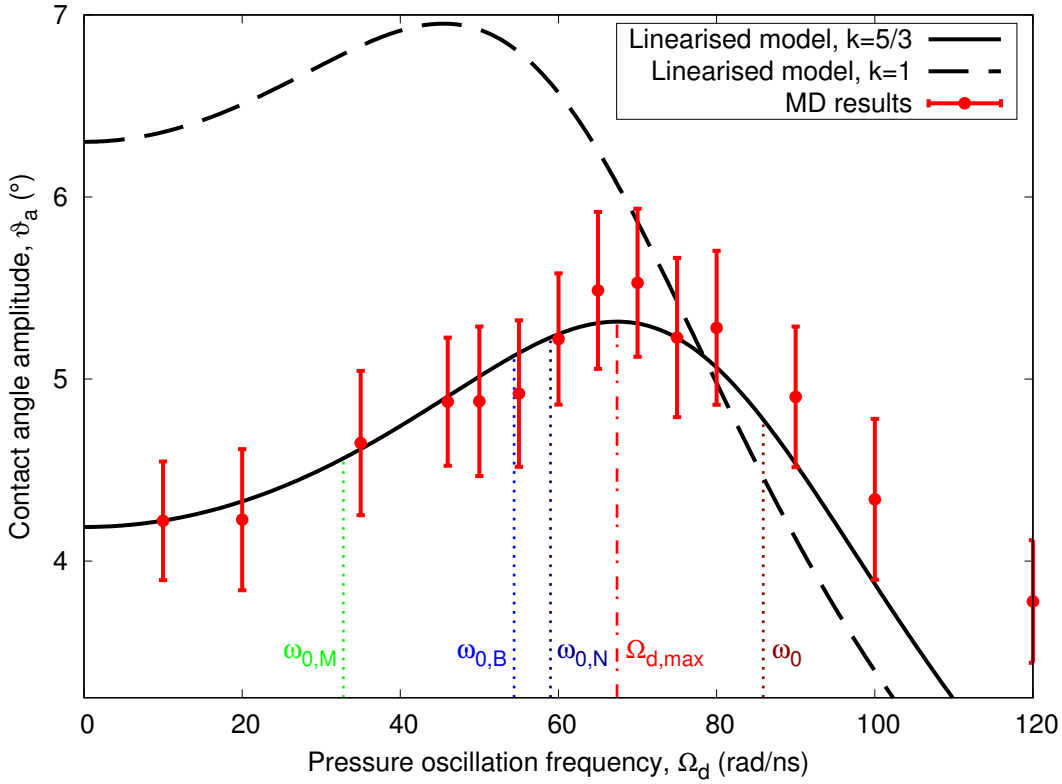


**Figure 5.14:** Variation in the surface nanobubble contact angle amplitude, with pressure oscillation frequency $\Omega_d$, and with $\Delta P_\infty = 5\,\text{MPa}$. The MD simulations are compared with the oscillation amplitude of the linearised model in Equation (5.18) for various values of $k$, assuming adiabatic ($k = 5/3$) and isothermal ($k = 1$) expansion. The natural frequency $\omega_0$ and oscillation frequency for maximum amplitude $\Omega_{d,max}$ are shown, predicted from Equations (5.16) and (5.19), respectively. The Minnaert frequency $\omega_{0,M}$, Blue frequency $\omega_{0,B}$ (both modified to account for surface tension), and Miller-Nyborg frequency $\omega_{0,N}$, are also labelled, from Equations (5.12), (5.13) and (5.14), respectively (Blue, 1967; Miller and Nyborg, 1983; Minnaert, 1933).

the natural frequency of a spherical bubble can be found from Equation (5.11):

$$\omega_{0,M} = \left[\frac{3kP_{g,0} - 2\gamma/R_0}{\rho R_0^2}\right]^{\frac{1}{2}}, \tag{5.12}$$

where $P_{g,0} = P_{\infty,0} - P_v + 2\gamma/R_0$. Minnaert (1933) first determined the natural frequency of a spherical bubble, neglecting surface tension effects; in this case, Equation (2.5) is obtained when setting $P_{g,0} = P_{\infty,0}$ and $\gamma = 0$. Due to its similar form to Equation (2.5), Equation (5.12) is also referred to as the Minnaert frequency, although modified to account for the effects of surface tension.

Equation (5.12) predicts the natural frequency of a spherical nanobubble to be $\omega_{0,M} = 32.8\,\text{rad/ns}$. Figure 5.14 clearly shows peak oscillations for the surface nanobubbles at frequencies approx-

imately double this Minnaert frequency. Analyses of linearised damped oscillators should estimate the natural frequency to be greater than the frequency where peak oscillation amplitudes are observed when damping effects are considered, and so the Minnaert frequency does not seem suitable for predicting the surface nanobubble's natural frequency.

The natural frequency of a surface bubble expanding with constant contact angle (CCA) growth mode has also been derived (Blue, 1967):

$$\omega_{0,B} = \left[\frac{3kP_{g,0} - 2\gamma/R_0}{\rho R_0^2 (1-\cos\theta_0)}\right]^{\frac{1}{2}}. \tag{5.13}$$

Equation (5.13) has a similar form to Equation (5.12), except there is a $(1-\cos\theta_0)$ term in the denominator to account for the bubble's spherical cap shape. Equation (5.13) has been modified from Blue (1967) to include the effects of surface tension (like in Equation (5.12)), and predicts the natural frequency of the surface nanobubble modelled here to be $\omega_{0,B} = 54.4\,\mathrm{rad/ns}$. This is larger than the Minnaert frequency but is still less than the MD simulation results shown in Figure 5.14. Similar to spherical bubble growth, models based on CCA growth for spherical capped bubbles assume that $R$ increases with bubble size, and so does not properly account for the Laplace pressure variation during oscillations.

Previous investigations into pinned nano and microbubble resonance have so far been dominated by gas trapped in micropores (Bolaños-Jiménez *et al.*, 2017; Gelderblom *et al.*, 2012; Miller and Nyborg, 1983). Most of these analyses differ from this work in that they generally assume a flat liquid-gas interface at equilibrium and that during oscillation the interface profile is parabolic, rather than maintaining a spherical cap profile. The most commonly used micropore model is by Miller and Nyborg (1983):

$$\omega_{0,N} = \left[\frac{480\pi\gamma h + 15\pi k P_\infty L^2}{16\rho L^3 h}\right]^{\frac{1}{2}}, \tag{5.14}$$

where $h$ is the depth of the cylindrical pore, with diameter $L$. The model of Miller and Nyborg (1983) assumes a flat interface at equilibrium, since the gas is contained within a micropore, and so the initial gas pressure would be expected to be equal to the external liquid pressure; surface nanobubble pressures have been shown to exceed the external liquid pressure by up to $\sim$1 MPa (Huang *et al.*, 2013; Zhang *et al.*, 2008), which may affect the stiffness of the bubble spring model. By defining an equivalent pore depth for the surface nanobubble: $h_{eq} = 4V/\pi L^2$, Equation (5.14) predicts a natural frequency of $\omega_{0,N} = 59.0\,\mathrm{rad/ns}$, which is higher than the previous Minnaert frequency and Blue frequency models but still lower than the peak from the MD simulations in Figure 5.14.

To estimate the surface nanobubble natural frequency based on the proposed model in Section 5.2, Equation (5.5) is linearised by assuming small contact angle perturbations $\vartheta$, i.e.

$\theta(t) = \theta_0 + \vartheta(t)$, where $\dot{\theta} = \dot{\vartheta}$, and $\ddot{\theta} = \ddot{\vartheta}$:

$$\ddot{\vartheta} + \frac{4\nu}{R_{eq,0}^2}\dot{\vartheta} + \frac{1}{\rho R_{eq,0}^2}\left[3kP_{g,0} + \frac{4\gamma\sin\theta_0}{L}\cos\theta_0\,(2+\cos\theta_0)\right]\vartheta = \Delta P_\infty \frac{(2+\cos\theta_0)\sin\theta_0}{\rho R_{eq,0}^2} f(t). \tag{5.15}$$

Equations (5.11) and (5.15) have similar forms, although Equation (5.15) is in terms of the surface nanobubble contact angle, while Equation (5.11) is in terms of the spherical bubble's radius. From this damped oscillator analysis, the natural frequency of a pinned surface nanobubble undergoing CCR growth can be obtained from Equation (5.15), neglecting damping effects:

$$\omega_0 = \left[\frac{3kP_{g,0} + (4\gamma\sin\theta_0/L)\cos\theta_0\,(2+\cos\theta_0)}{\rho R_{eq}^2}\right]^{\frac{1}{2}}, \tag{5.16}$$

where $P_{g,0} = P_{\infty,0} - P_v + 4\gamma\sin\theta_0/L$. Equations (5.16) and (5.12) again appear similar. There is a $3kP_{g,0}$ term that contributes to the system stiffness, however, the surface tension contributions now differ. In Equation (5.16) the effect of the Laplace pressure ($4\gamma\sin\theta_0/L$, which is equivalent to $2\gamma/R_0$) has a different sign to that in Equation (5.12), which is a result of the pinned contact line and CCR growth that have been observed in surface nanobubble growth. This change in sign means an increase in the natural frequency of the surface nanobubble compared to the Minnaert frequency. In Equation (5.16), there is an additional $\cos\theta_0\,(2+\cos\theta_0)$ coefficient in this Laplace pressure term, which is a result of the surface nanobubble's spherical cap shape. The inertial terms are also similar, except Equation (5.16) is in terms of the equivalent radius $R_{eq}$, while Equation (5.12) is in terms of the radius of curvature $R_0$.

Equation (5.16) predicts the natural frequency of the surface nanobubble to be $\omega_0 = 85.9\,\mathrm{rad/ns}$, which is higher than the peak oscillation frequency of $\Omega_d = 70\,\mathrm{rad/ns}$ from the MD simulations. Due to the effects of viscous dissipation (predominantly in the boundary layer near the bubble surface), this natural frequency does not match the frequency in which peak oscillation amplitude is observed in the MD simulations, as shown in Figure 5.14. Equation (5.16) does not account for the viscosity of the liquid, which is important to the bubble's oscillation amplitude. The frequency for the peak oscillation amplitude can be found by continuing with the damped oscillator analysis of the surface nanobubble below.

For a sinusoidal external pressure field $P_\infty(t) = P_{\infty,0} + \Delta P_\infty \sin(\Omega_d t)$, a sinusoidal solution for the bubble's contact angle response can be assumed:

$$\vartheta = \vartheta_a \sin(\Omega_d t + d), \tag{5.17}$$

where $\vartheta_a$ is the oscillation amplitude of the bubble response, out of phase by $d$ radians with the forcing function. Note that Equation (5.17) is simply the sinusoidal solution to Equation (5.15). In reality, long-term pressure oscillations could result in a gradual increase in the bubble's mass contents via rectified diffusion (Brotchie and Zhang, 2011; Lohse and Zhang, 2015b).

This diffusive effect should occur over a time scale of $\sim 10\,\mu$s for surface nanobubbles, and so is considered to be negligible compared due to the 2 ns times of these simulations (Brennen, 2013).

It can be shown from Equation (5.15) that the bubble's oscillation amplitude is:

$$\vartheta_a = \frac{p_a}{\sqrt{\left(\Omega_d^2 - \omega_0^2\right)^2 + \alpha^2\Omega_d^2}}, \tag{5.18}$$

where $p_a = (2+\cos\theta_0)\sin\theta_0\Delta P_\infty/\rho R_{eq,0}^2$, and $\alpha = 4\nu/R_{eq,0}^2$. The damping coefficient $\alpha$, which is proportional to the liquid viscosity, limits the bubble's oscillation amplitude, particularly at driving frequencies close to the natural frequency $\Omega_d \sim \omega_0$. Equation (5.18) indicates that the amplitude of the bubble oscillation is dependent on the forcing frequency, as shown by the linearised response in Figure 5.14 for $k = 5/3$, and is in good agreement with the MD simulations. Also shown in Figure 5.14 is the predicted response for isothermal expansion $k = 1$, which shows the peak oscillation frequency would decrease, although with an increased oscillation amplitude. The distribution of the MD results is in better agreement with the proposed model assuming adiabatic expansion, as opposed to isothermal expansion. This also follows from the earlier analysis (in Figure 5.12), where the slowest oscillation case exhibited near-adiabatic expansion.

The driving frequency that results in maximum oscillation amplitude can be found by differentiating Equation (5.18) with respect to driving frequency, and solving for $\partial\vartheta_a/\partial\Omega_d = 0$. The maximum bubble oscillation amplitude occurs at a driving frequency:

$$\Omega_{d,max} = \sqrt{\omega_0^2 - \frac{\alpha^2}{2}}. \tag{5.19}$$

Equation (5.19) shows that due to the damping coefficient (which is proportional to viscosity and is always positive), the driving frequency at which the maximum oscillation amplitude occurs is always less than the natural frequency, $\Omega_d < \omega_0$. Equation (5.19) predicts the peak oscillation amplitude to occur at $\Omega_{d,max} = 67.4\,\text{rad/ns}$. This is in very good agreement with the MD simulations which show the expected peak oscillation frequency to be in between $\Omega_d = 65\,\text{rad/ns}$ and $\Omega_d = 70\,\text{rad/ns}$.

As the frequency increases towards $\Omega_d = 120\,\text{rad/ns}$, the discrepancy between the MD simulations and the linearised model increases. This is due to the piston inertia dimensionless number increasing with increasing frequency: $\beta = 0.10$ for $\Omega_d = 120\,\text{rad/ns}$ (ideally $\beta \ll 1$). The result to the liquid pressure in this simulation case is shown in Figure 5.15. The piston's contribution to the pressure is now around 2.8 MPa amplitude for $\Omega_d = 120\,\text{rad/ns}$, compared to the slower speed $\Omega_d = 60\,\text{rad/ns}$ and $\Omega_d = 10\,\text{rad/ns}$ cases in Figures 5.9(b) and 5.13(b), respectively, where the piston effect on the pressure was negligible. This effect from the piston inertia would need to be addressed in future work if attempting to model oscillations at higher

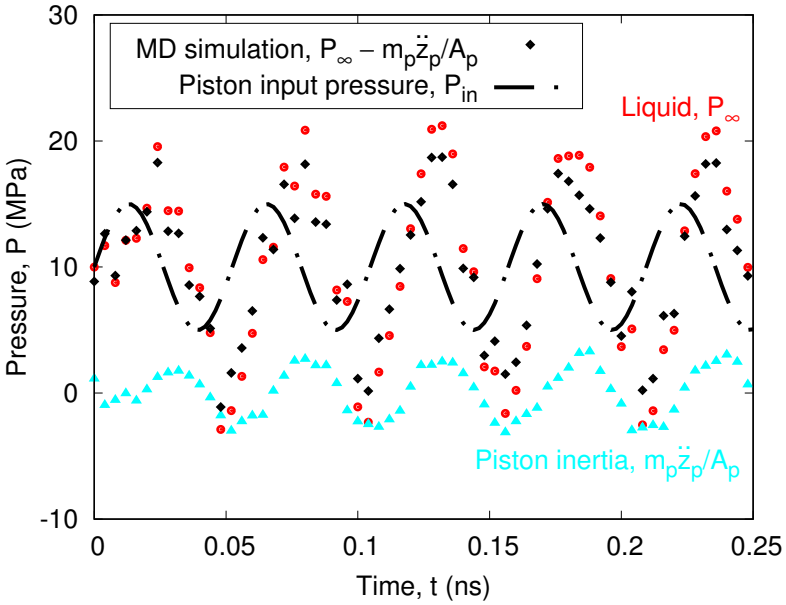


**Figure 5.15:** Variation in the measured liquid pressure and piston inertia pressure contribution in MD simulations of an oscillating surface nanobubble, with $\beta = 0.10$. Also shown is the sinusoidal input pressure function, with $\Delta P_{in} = 5\,\mathrm{MPa}$ and $\Omega_d = 120\,\mathrm{rad/ns}$.

frequencies, either by employing a lighter piston or a larger domain to reduce $\beta$.

Equations (5.5) and (5.16) assume that the bubble retains its spherical cap shape during its pinned growth mode. The Weber number can be used to assess the relative effects of the inertial forces on the surface tension, $We = \rho R_0^3 \omega_0^2 / \gamma$. Prosperetti (2012) used the square root of this Weber number to non-dimensionalise the frequency of a constrained surface droplet. For the MD simulation case, with natural frequency estimated from Equation (5.16), $We \sim 10$. For larger, bubbles the relative effects of the surface tension would be reduced, and so this assumption of spherical cap shape could become less valid. However, this assumption is also essential for the natural frequency of a surface bubble undergoing CCA mode of growth, as in Equation (5.13). Blue (1967) performed experiments of $\mu$m sized, CCA surface bubbles, oscillating at frequencies in the kHz range, equivalent to $We \sim 300$, and so it is suggested that the proposed models for bubble growth rate and natural frequency are also suitable at similar Weber numbers, due to the similar assumptions taken in Blue (1967).

### 5.4.3 Non-linear oscillation dynamics

One of the strengths of the Rayleigh-Plesset equation is the ability to model non-linear oscillations of spherical bubbles. One final simulation is performed with a sinusoidal pressure function as before, although now the pressure amplitude is $\Delta P = 20\,\text{MPa}$, and the driving frequency is $\Omega_d = 15\,\text{rad/ns}$. Figure 5.16 shows the non-linear variation in the contact angle and volume of the surface nanobubble in response to this pressure wave, as predicted from Equations (5.5) and (4.16). Also shown is the expected linearised response of the surface nanobubble as predicted from Equation (5.15), to highlight this difference in behaviour.

The linearised response in Equation (5.15) was derived for a small amplitude perturbation in contact angle, and assumes simple oscillation dynamics of the surface nanobubble. As such, it does not capture the exact contact angle and volume responses from the MD simulation. Equation (5.5) predicts the surface nanobubble's response well, and considerably better than the linearised response. This discrepancy from the linearised response is due to the gas pressure and Laplace pressure's non-linear spring behaviour as the bubble experiences larger contact angle and volume responses from the larger changes in pressure. Some of the finer details of the bubble's oscillation observed in the MD simulations, such as the more spread out trough and sharper peak, are also captured.

The variations in pressure were also plotted and compared to the MD simulations as shown in Figure 5.17. Some non-linear behaviour in the gas and Laplace pressures can be seen in Figure 5.17(a). The light piston was confirmed to have a negligible effect on the sinusoidal liquid pressure, as shown in Figure 5.17(b).

The polytropic exponent was found again by plotting the variation in gas pressure with bubble volume and fitting the polytropic exponent $k = 1.661$, as shown in Figure 5.18. This was very close to the adiabatic limit of $k = 5/3$, as assumed in Figure 5.16

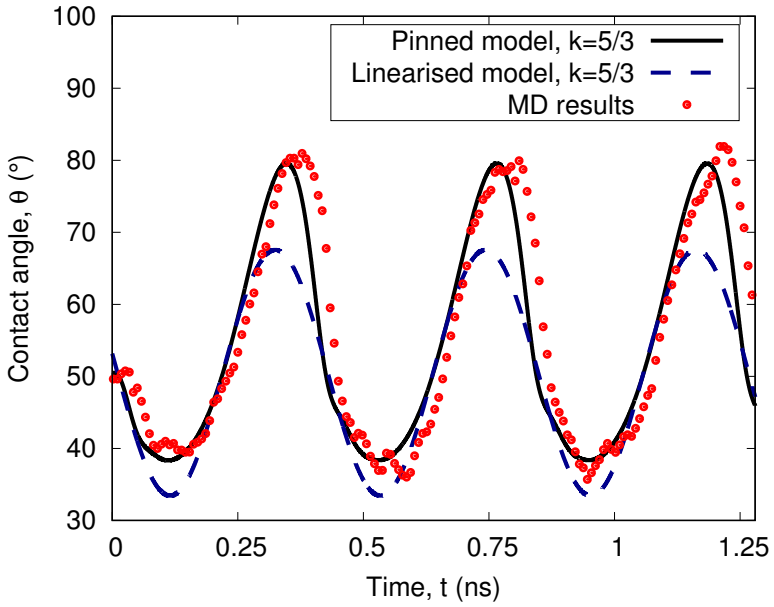


**(a)**

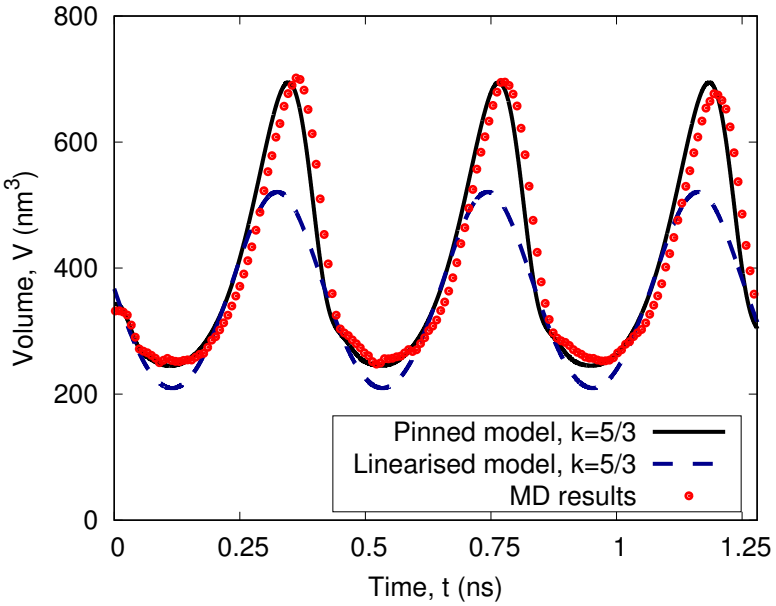


**(b)**

**Figure 5.16:** Variation in the: (a) contact angle, and (b) bubble volume, for a surface nanobubble subjected to an oscillating pressure, with pressure enforced by a sinusoidal input function, $\Delta P_{in} = 20\,\mathrm{MPa}$ and $\Omega_d = 15\,\mathrm{rad/ns}$. Also shown is the predicted model from Equation (5.5), and the linearised model, Equation (5.15), both assuming adiabatic expansion $k = 5/3$.

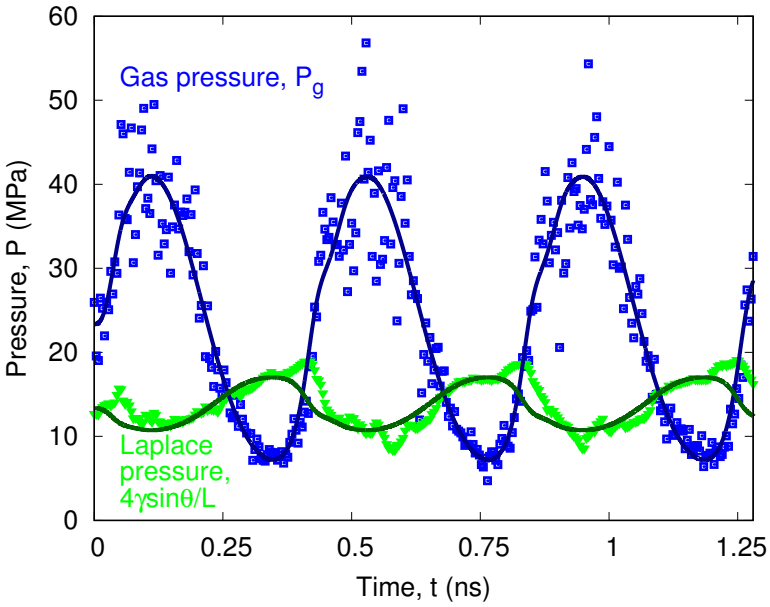


**(a)**

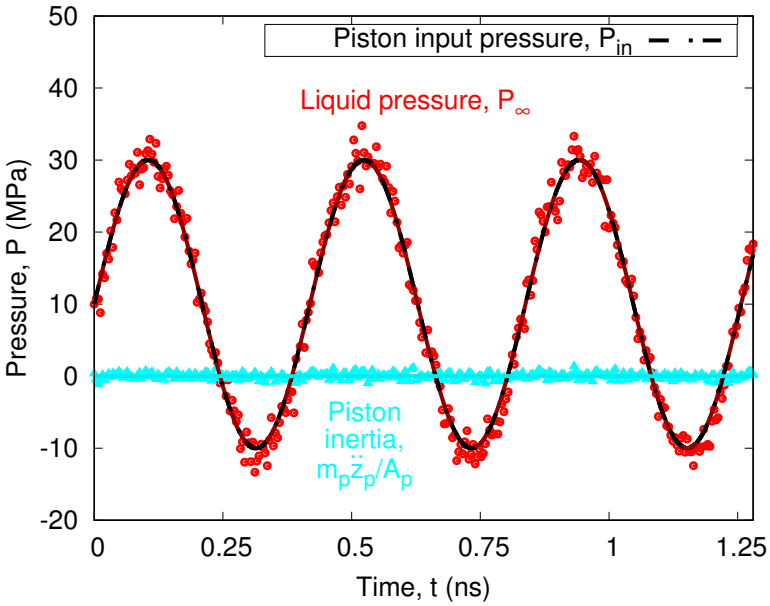


**(b)**

**Figure 5.17:** Time variation of: (a) bubble gas and Laplace pressures, and (b) liquid pressure, piston input pressure and resulting pressure from piston inertia, for a surface nanobubble subjected to an oscillating pressure, with $\Delta P_\infty = 20\,\mathrm{MPa}$ and $\Omega_d = 15\,\mathrm{rad/ns}$. The different pressure contribution terms from Equation $(5.5)$ are shown as solid lines, and MD simulation results are shown as symbols.

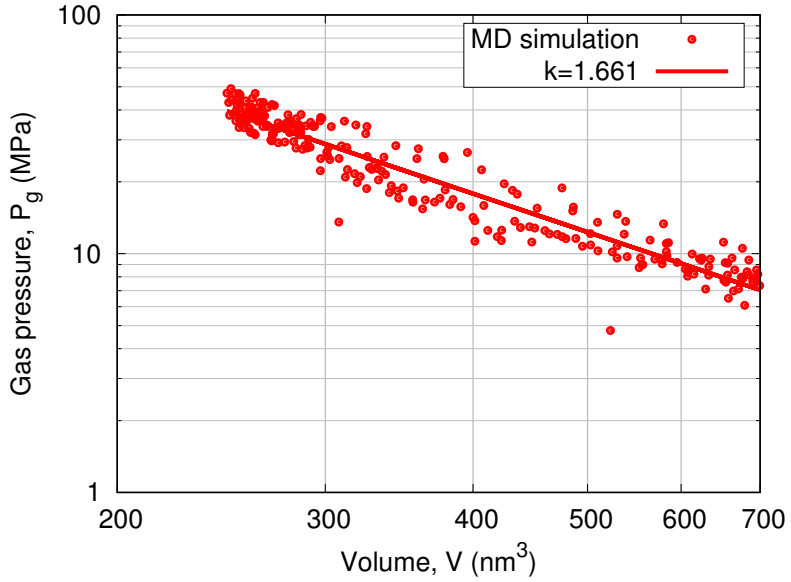


**Figure 5.18:** Variation in gas pressure with bubble volume for a surface nanobubble subjected to an oscillating pressure, with $\Delta P_\infty = 20\,\mathrm{MPa}$ and $\Omega_d = 15\,\mathrm{rad/ns}$, plotted on logarithmic axes. A line is also plotted, corresponding to the fitted polytropic exponent $k = 1.661$.

## 5.5 Summary

The Rayleigh-Plesset equation cannot be used to predict the growth rate of a cavitating pinned surface nanobubble. A volume frame equivalent of the Rayleigh-Plesset equation (Leighton, 2008) was modified such that the dynamics of the surface nanobubble could be accurately modelled. These modifications included expressing the bubble volume as a spherical cap shape, and correcting the pressure balance across the liquid-gas interface to ensure the bubble was in mechanical equilibrium under steady-state conditions.

The proposed model was in good agreement with MD simulations under a variety of different pressure-driven cases. The model could predict the final size and approximate time to reach this state for a simple pressure drop case, with simulations employing the $H_2O$–$N_2$ and mW–mN model pairings. The oscillation dynamics of the surface nanobubbles were also modelled in MD simulations and could be analysed using simple damped oscillator analysis. The natural frequency and peak amplitude frequency, predicted by the linearised form of the model, were found to agree well with the MD simulations under pressure-driven oscillating flow. Other models for the natural frequency, such as the Minnaert frequency, Blue frequency (both modified to account for surface tension), and the Miller-Nyborg frequency for bubble oscillations within a cylindrical micro-pore, were also examined and found not to be suitable for predicting the surface nanobubble natural frequency (Blue, 1967; Miller and Nyborg, 1983; Minnaert, 1933). Non-linear oscillation dynamics were also observed in MD simulation under larger pressure variations, and still in good agreement with the proposed model. Most of the bubbles expanded

with near adiabatic behaviour in the MD simulations, despite their small size and proximity to liquid and solid surfaces. It is suggested that the rigid solid surface could have provided an insulating effect on the internal gas phase, leading to zero heat transfer across the gas-solid interface. Alternatively, other interfacial nanoscale phenomena, such as the Kapitza resistance could have inhibited heat transfer into the bubble. Further investigation is required into the surface nanobubble's thermal expansion behaviour.

The suitability of the MD simulation set-up for approximating a semi-infinite liquid field was also critically discussed. It was found that the proposed set-up was suitable for accounting for the liquid's inertial and viscous effects within the oscillating pressure simulations. The main limitations at the scales modelled actually arose from the piston mechanism used to enforce the pressure in the system (see Chapter 3). For high piston masses, the inertia of the piston was found to contribute significantly to the pressure measured in the liquid. For low-speed simulations, such as the simple pressure drop cases, the dynamics of the piston could be accounted for, when using a small but finite piston mass. A heavier piston in these cases was preferred as they experienced reduced effects from the liquid's random thermal fluctuations at the piston-liquid interface, which was found to influence some of the surface nanobubble measurements for the lighter piston cases. For the high oscillation frequencies, the inertia of the piston was found to contribute significantly and a lighter piston was more appropriate to control the pressure. The effect of the thermal motion on the lighter piston was not so important in these oscillation cases as the surface nanobubble dynamics were averaged over many cycles.

This concludes this chapter on the oscillation and growth dynamics of surface nanobubbles during expansion. This phase is critical during the initial stages for cavitation growth of a surface nanobubble. The natural frequency dynamics could be useful in attempting to detach surface nanobubbles from substrates, such as on catalysts (Lohse and Zhang, 2015b). The oscillation dynamics presented here can predict the natural frequency of a surface nanobubble in pinned CCR growth mode, assuming no diffusive growth. For long-term oscillations, diffusive growth may occur via rectified diffusion, particularly as surface nanobubbles are commonly found in supersaturated solutions (Brennen, 2013; Brotchie and Zhang, 2011; Lohse and Zhang, 2015b).

Chapter 6

# Shock-Induced Collapse of Surface Nanobubbles

## 6.1 Introduction

The previous chapters have addressed how surface nanobubbles respond to drops and oscillations in external pressure, and the onset of unstable growth. The knowledge gained in these areas should be sufficient to mitigate the adverse effects of collapsing nanobubbles. However, in cases where surface nanobubbles have become unstable, or if the possible jet dynamics are to be utilised for engineering applications, the collapsing dynamics of these surface nanobubbles are still of interest and are to be covered here.

The collapsing dynamics of spherical bubbles has been frequently analysed through a variety of experimental (Akhatov *et al.*, 2001; Benjamin and Ellis, 1966; Philipp and Lauterborn, 1998; Supponen *et al.*, 2016) and simulation methods (Blake *et al.*, 2015; Koukouvinis *et al.*, 2016; Zhang and Duncan, 1994). However, there is still difficulty in observing the simultaneous bubble and solid response during bubble collapse, due to the large changes in time and length scales that arise in cavitation. The solid response is sometimes modelled with finite element solvers, although some form of coupling to a fluid solver is required to capture the preceding bubble behaviour (Chahine and Hsiao, 2015; Fivel *et al.*, 2015).

Molecular Dynamics (MD) simulations are capable of modelling both fluid and solid material behaviours concurrently, and more recently have been used to model the pitting and poration in solids and membranes from spherical bubble collapse (Adhikari *et al.*, 2016; Choubey *et al.*, 2011; Shekhar *et al.*, 2013; Vedadi *et al.*, 2010). The issues with MD simulations found in previous chapters have the same restrictions for these simulations; with limited domain sizes, only very small bubbles can be simulated, and shock waves are normally required to induce violent collapse, due to the stronger effects of viscosity and surface tension at this scale (Choubey *et al.*, 2011; Vedadi *et al.*, 2010). Despite these advances, cavitation collapse is still a complex topic and there remains to be found a simplified model (like the Blake threshold and Rayleigh-Plesset equations used previously in this research), which can capture the non-spherical collapse shape or resulting solid damage.

Most of the phenomena so far covered in this thesis have generally been dependent on pressure, as seen in Chapters 4 and 5. However, it is the *impulse* that has been shown to be most important in quantifying collapsing dynamics due to the rapid nature of the jets formed (Adhikari *et al.*, 2015, 2016; Benjamin and Ellis, 1966; Blake *et al.*, 2015; Brennen, 2013; Philipp and Lauterborn, 1998; Supponen *et al.*, 2016). Impulse is defined here as the time integral of pressure:

$$I = \int P \mathrm{d}t. \tag{6.1}$$

The Kelvin impulse is a theoretical concept in which the asymmetric collapse of a spherical bubble can be analysed via potential flow theory. The "impulsive wrench" was a term coined to describe the global change in momentum that would be required to induce a particular fluid motion from rest at any time instant; this impulsive wrench must balance the (Kelvin) impulse across the bubble and solid surfaces at that particular time instant (Benjamin and Ellis, 1966; Blake *et al.*, 2015). A perfectly spherical bubble collapse would result in a vanishing of the Kelvin impulse (and hence fluid momentum) upon complete closure of the bubble surfaces, and so circulatory flows are generated to conserve this Kelvin impulse, which manifests as the typical re-entrant jet formation and the final toroidal bubble shape (Benjamin and Ellis, 1966; Blake *et al.*, 2015). The Kelvin impulse analysis assumes an inviscid fluid and so is of limited application here due to the strong effects of viscosity at the nanoscale. However, the concept of impulse is useful in quantifying the effect of the shock wave driving collapse, as well as the effect of the re-entrant jet on the wall.

Collapse can be induced by a variety of drivers, such as large variations in liquid pressure, the presence of nearby surfaces, external force fields e.g. gravity, and impinging shock waves. It has been shown that the distinct collapsing shape, as shown in Figure 2.4, and re-entrant jet formation is a common result of collapse, regardless of the driver (Supponen *et al.*, 2016). For collapse near a solid wall, the bubble dynamics can be characterised in terms of the stand-off parameter $\chi = z_c/R_{max}$, where $z_c$ is the perpendicular distance from the wall to the centre of the bubble and $R_{max}$ is the maximum radius of curvature before collapse, as shown in Figure 6.1(a) (Philipp and Lauterborn, 1998; Supponen *et al.*, 2016).

As the stand-off parameter decreases, i.e. the bubble is nearer the wall before collapse, the resulting solid damage is typically enhanced (Philipp and Lauterborn, 1998). Cavitation bubbles can also accelerate towards the wall during collapse from the pressure gradient driving the jet formation (Brennen, 2013; Philipp and Lauterborn, 1998). There have been several investigations into the dynamics of spherical bubble growth and collapse very close to a solid substrate (with $0 < \chi < 1$), where the bubble is initially spherical, then deforms as it interacts with the wall (Benjamin and Ellis, 1966; Philipp and Lauterborn, 1998; Supponen *et al.*, 2016). Philipp and Lauterborn (1998) found that the greatest damage on aluminium substrates from millimetre size bubbles occurred with stand-off parameters $\chi \approx 0.3$ in experiments of laser-induced bubble formation; bubble growth was driven by the rapid vapour formation from

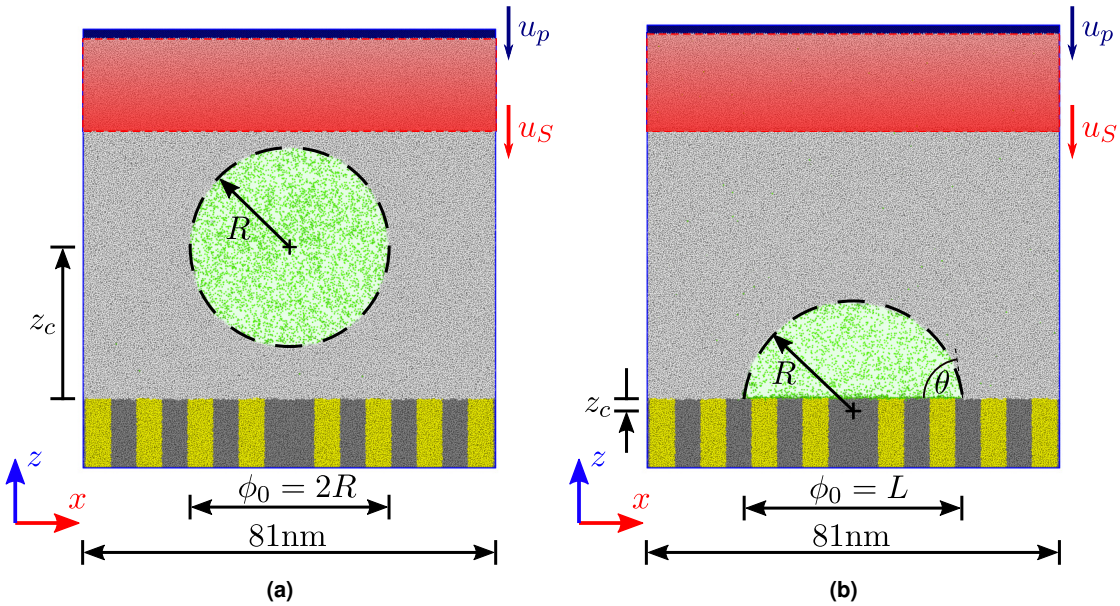


**Figure 6.1:** Schematics of the: (a) spherical, and (b) surface nanobubble, collapsing MD simulations. The mW water molecules are shown in white, mN nitrogen molecules in green, piston atoms in dark-blue, and $aSi_i$ and $aSi_o$ atom types in yellow and grey, respectively. The renderings show a thin slice of the 3D MD simulations, through the centre of the bubble. The red highlighted region shows the propagation of the shock wave with velocity $u_S$, driven by the piston at velocity $u_p$.

the concentrated heating by the lasers. In these cases, the bubbles deform during expansion such that the distal (lower) bubble surface was pressed flat against the solid substrate at maximum size; the re-entrant jet would impact both the distal bubble surface and solid substrate at approximately the same time, causing maximum damage to the solid. For larger stand-off parameters ($\chi \sim 1$), the re-entrant jet would first impact the distal bubble surface and is decelerated by the water layer, such that the jet's second impact (on the solid substrate) is significantly weakened (Philipp and Lauterborn, 1998). This understanding holds for collapse under low driving pressures, however, for shock-induced collapse, the effect of stand-off is not so obvious, with peak substrate pressures and damaging effects being observed for $\chi \sim 2$ in simulations (Johnsen and Colonius, 2009; Shekhar *et al.*, 2013).

The above analyses were for spherical bubbles. The collapsing dynamics of surface nanobubbles, which have only been recently discovered to exist, have not been extensively investigated. In this chapter, the key differences in collapsing behaviour between spherical bubbles and surface nanobubbles are analysed and compared through MD simulations. The stand-off parameter can similarly be applied to surface nanobubbles, where for $\theta < 90^\circ$ the centre of the bubble's spherical cap shape is below the solid surface, i.e. $\chi = -\cos\theta < 0$, as shown in Figure 6.1(b).

## 6.2 MD simulation set-up

MD simulations were set-up similar to those in Chapters 4 and 5, where 3D gas-filled surface nanobubbles and spherical nanobubbles were individually initialised and equilibrated on (or above) a solid substrate, as shown in Figure 6.1. Concentric ring pinning sites were employed again in all simulations (including the spherical cases for uniformity). Another benefit of the patterning was that it provided a clear visualisation of the damage on the substrate.

A variety of different bubble sizes and shapes were investigated, each equilibrated individually to achieve appropriate starting conditions. The spherical bubbles were each initialised to have a stand-off of $\chi = 1.5$, comparable to previous simulations of collapsing spherical bubbles (Johnsen and Colonius, 2009; Shekhar *et al.*, 2013). The high contact angle (HCA) surface nanobubble cases were initialised with a relatively high contact angle of 80°, while the low contact angle (LCA) surface nanobubble cases had an initial contact angle around 40°, equivalent to stand-off parameters $\chi = -0.17$ and $\chi = -0.77$, respectively. The various bubble sizes refer to the maximum width of the bubble before collapse $\phi_0$, which was equivalent to the lateral contact diameter $L$ for the surface nanobubbles, and double the radius of curvature $R$ for the spherical bubbles, as shown in Figure 6.1. Three additional simulations were also performed in which the larger ($\phi_0 = 40$ nm) spherical and surface nanobubble simulations were repeated from the same equilibrated states, except the gas molecules were all removed immediately before the shock wave was propagated to investigate the differences in vapour bubble collapse. Another final "no-bubble" case was equilibrated and simulated with no bubble present to evaluate the shock wave's contribution to the solid substrate damage (Adhikari *et al.*, 2015, 2016). All simulation cases are summarised in Table 6.1. The equilibrated contact angles for the surface nanobubble cases before collapse are also given in Table 6.1.

| Bubble case | Equilibrated size $\phi_0$ (nm) | Equilibrated contact angle $\theta_0$ (°) |
|---|---|---|
| 40 nm Spherical nanobubble* | 38.9 | - |
| 40 nm Surface nanobubble (HCA)* | 44.0 | 83 |
| 40 nm Surface nanobubble (LCA)* | 38.0 | 38 |
| 20 nm Spherical nanobubble | 17.7 | - |
| 20 nm Surface nanobubble (HCA) | 23.2 | 84 |
| 20 nm Surface nanobubble (LCA) | 22.1 | 40 |
| No-bubble | - | - |

**Table 6.1:** Different cases for the collapsing nanobubble MD simulations. The "contact angle" column applies only to the surface nanobubble cases. The asterisk (*) refers to cases in which an additional simulation was performed with nitrogen molecules removed before collapse, representing a vapour bubble.

The monatomic water (mW) and monatomic nitrogen (mN) models were used for the liquid and gas phases, respectively. The piston was modelled as a rigid hydrophilic ($S_i$) solid, and the main substrate was modelled with the flexible amorphous silicon (aSi) model. The piston had a mass $m_p = 2.00 \times 10^{-19}$ kg. The hydrophilic ($aSi_i$) and hydrophobic ($aSi_o$) silicon atoms were employed for the substrate ring patterning; potentials are given in Tables 3.2 to 3.5.

During the equilibration process, the piston applied a force as described in Chapter 3, equivalent to $P_\infty = 0.1$ MPa until the bubble reached mechanical equilibrium. A lower equilibration pressure was employed than for previous chapters, to minimise the effect of the higher gas pressures potentially inhibiting jet formation, while also being more realistic. For equilibration, a timestep of $\Delta t = 2 \times 10^{-6}$ ns was used, however, due to the high particle velocities and pressures expected from the shock waves, it was found to be necessary to reduce the timestep to $\Delta t = 1 \times 10^{-6}$ ns during the main simulation run to prevent numerical instabilities. Each of the surface nanobubble cases was initialised as a spherical cap with appropriate supersaturation conditions found from Equation (2.10). However, due to the very large number of atoms used, these surface nanobubbles were only equilibrated up to a maximum of 0.1 ns. The initial supersaturation of the spherical (and no-bubble case) was considered less important, since spherical bubbles cannot be held in stable diffusive equilibrium (Attard, 2016; Brennen, 2013; Epstein and Plesset, 1950). The spherical and no-bubble cases were equilibrated with a supersaturation ratio of $\zeta \equiv C_\infty / C_s - 1 = 4$, however, it was generally assumed that diffusive dynamics, which would occur over $\sim 10\,\mu$s timescales (Epstein and Plesset, 1950), were unimportant during the shock-induced collapsing process, which occurs over $\sim 10$ ps (Brennen, 2013). Approximately $17 \times 10^6$ mW molecules were used per simulation, with an additional 800 to $55 \times 10^3$ mN molecules, depending on the simulation case. The amorphous silicon substrate was composed of $4.20 \times 10^6$ aSi atoms, with a thickness of 13 nm. No thermostat was applied to the fluid molecules, but was applied to the amorphous silicon to maintain the temperature at 300 K. The bottom layer of solid atoms were kept rigid to prevent displacement of the wall from the impinging shock waves. These are unusually large MD simulations containing in excess of $20 \times 10^6$ molecules.

Periodic boundary conditions were applied in the $x$ and $y$ directions, with fixed boundaries in the $z$ direction to prevent unintended periodic interactions with the piston and lower wall, particularly for the reflection of shock waves. The equilibrated fluid domains had sizes of $81 \times 81 \times 82\,\text{nm}^3$ in the $x$, $y$ and $z$ directions, respectively, although were allowed to vary in the $z$ direction to allow vertical displacement of the piston.

When the collapsing simulations began, the piston was used to propagate a shock wave towards the bubble, as described in Chapter 3, Section 3.4.7. Instead of defining a pressure for the piston, as done in Chapters 4 and 5, the piston was set to move at a high velocity $u_p$ to drive the shock formation, which propagated with speed $u_S$, as shown in Figure 6.1 (Adhikari *et al.*, 2016; Choubey *et al.*, 2011; Shekhar *et al.*, 2013; Vedadi *et al.*, 2010).

All cases were driven with a piston velocity $u_p = 2500\,\mathrm{m/s}$ (equivalent to Mach number $Ma = 1.07$ with the mW model) for a duration $\tau_s = 4\,\mathrm{ps}$, after which the piston was then set to enforce pressure again, using the standard method defined in Chapter 3. It was normal for shock waves to reflect off the bubble and substrate surfaces, and travel back towards the piston. Subsequent shock wave reflections off the piston were also observed; all simulations were stopped after 35 ps, to prevent further reflected shock waves re-interacting with the already collapsed bubbles.

## 6.3 Results and discussion

### 6.3.1 Early shock formation

During the first 4 ps, while the piston was moving with constant velocity, a shock wave propagated towards the substrate and bubbles with a velocity of $u_S = 7800\,\mathrm{m/s}$, as measured from the no-bubble case. The pressure jump across the shock front was found to be approximately 22.5 GPa, as shown in Figure 6.2(a). This was close in magnitude to the estimated pressure jump of $\rho_0 u_S u_p = 19.5\,\mathrm{GPa}$ (Heymann, 1969; Huang *et al.*, 1973; Vedadi *et al.*, 2010). The mean density of the shock wave was $1480\,\mathrm{kg/m^3}$ as shown in Figure 6.2(b), similar to previous MD simulations of shock wave propagation in water (Choubey *et al.*, 2011; Shekhar *et al.*,

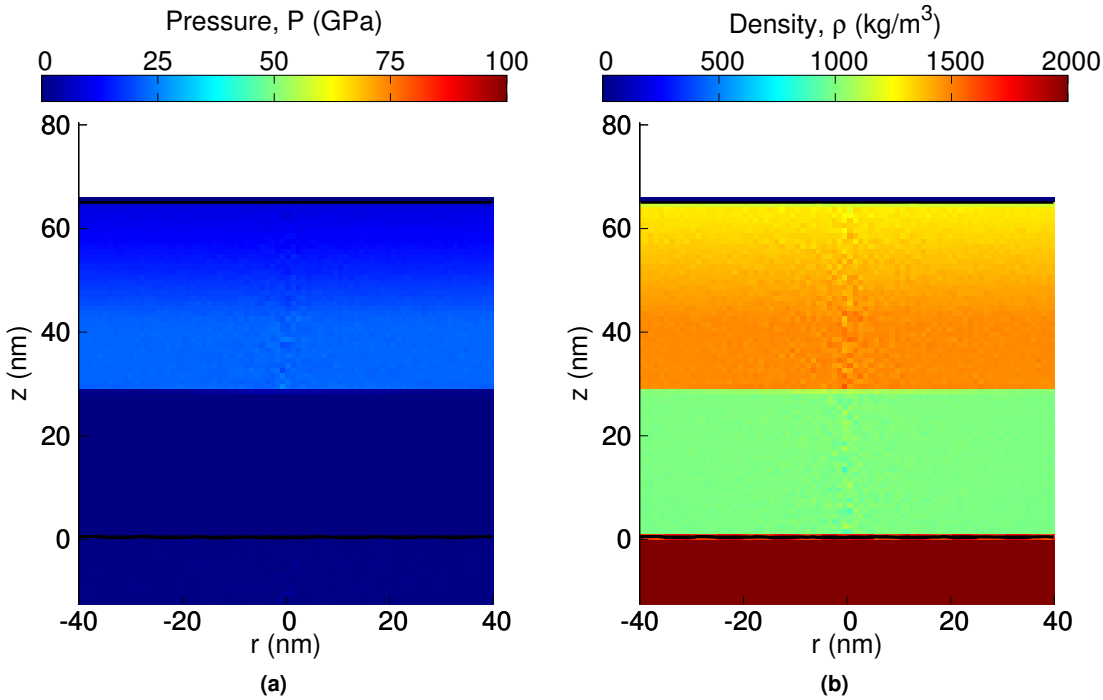


**Figure 6.2:** Shock wave propagation in the no-bubble simulation showing jumps in: (a) pressure, and (b) density, across the shock wave at 6.6 ps. The shock wave front is located around $z = 30\,\mathrm{nm}$.

2013).

Pressure was measured across the solid substrate (at $z = 1\,\text{nm}$), and Equation (6.1) was used to calculate the impulse. Figure 6.3 shows the variation in the pressure and impulse within this measurement region for the no-bubble case. The shock wave impacted the substrate around

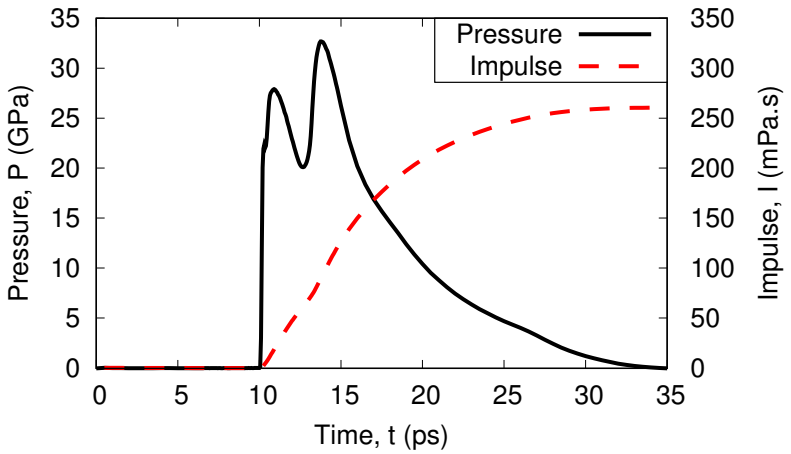


**Figure 6.3:** Variation in pressure and impulse across the silicon substrate for the no-bubble case.

10.3 ps, and a partial shock wave reflection was observed off the top of the wall. Figure 6.3 shows the pressure across the substrate reaches a first peak value around 28 GPa at 10.9 ps, higher than the shock wave pressure in Figure 6.2(a) due to the interference of this reflected shock wave. The pressure begins to decay before abruptly peaking again around 33 GPa at 13.8 ps, due to another shock wave reflecting off the rigid solid atoms in the bottom of the wall. This "double peak" is not uncommon in shock wave pressure measurements (Obara *et al.*, 1995), and was difficult to mitigate in the MD simulations. For the no-bubble case, the incident and reflected shock waves were all parallel to the substrate, and there was little variation in pressure with radial distance $r$ from the impact centre. The shock wave dynamics in the bubble simulations had more complex interference patterns, due to the curved interfaces and collapsing jet dynamics; the effect of shock wave reflections and "water hammer" from the cavitation jet impacts will be further examined in Section 6.3.3.

Despite such high values of pressure across the substrate exceeding the maximum tensile strength of the amorphous silicon model (5.5 GPa, see Chapter 3), no permanent deformation was observed in the solid by the end of the no-bubble simulation. The impulse is more important in assessing the relative damage to the substrate during high-speed jet impacts, such as cavitation bubble collapse; the effect of the impulse on the resulting substrate damage will be further examined in Section 6.3.4. After reaching a peak, the pressure across the substrate decayed rapidly until reaching an ambient value towards the end of the simulation. The impulse across the substrate tended to a steady value of $I = 260\,\text{mPa s}$, and this value is considered the

"impulsive wrench" which acts on all the bubble cases.

### 6.3.2 Collapsing bubble dynamics

All the collapsing bubble simulations exhibited the classical jet formation commonly observed in the literature (Akhatov *et al.*, 2001; Benjamin and Ellis, 1966; Koukouvinis *et al.*, 2016; Supponen *et al.*, 2016; Zhang and Duncan, 1994); for example, renderings of the 40 nm spherical collapsing case at varying timesteps are shown in Figure 6.4. The shock wave can be seen by

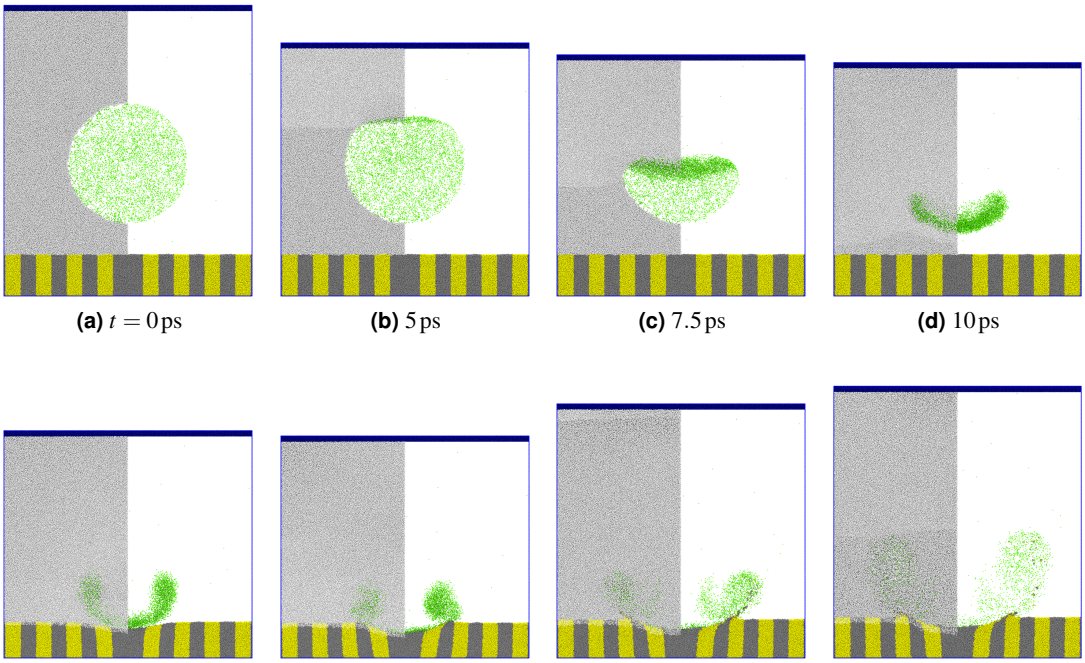

**(a)** $t = 0$ ps **(b)** 5 ps **(c)** 7.5 ps **(d)** 10 ps

**(e)** 12.5 ps **(f)** 15 ps **(g)** 25 ps **(h)** 35 ps

**Figure 6.4:** Renderings of the collapsing 40 nm spherical bubble MD simulation case at various timesteps. Some of the water molecules are not shown for clarity.

the slight lighter change in colour of liquid molecules in the top left-hand side of Figure 6.4(b), as the molecules are more closely packed. Figures 6.4(c)-(e) show the jet formation during the bubble collapse up to the moment it impacted the solid substrate. Figures 6.4(f)-(h) show the latter stages of the simulation where the pit forms on the substrate; the fluid flow is directed away from the impact centre and a toroidal rebounding bubble begins to form, albeit with a high density content. Some substrate material was removed from the substrate and circulated with the fluid flow.

The surface nanobubble cases also exhibited jet formation, as shown in Figures 6.5(a)-(d) and Figures 6.5(e)-(h) for the 40 nm HCA and LCA cases, respectively. Since the top surfaces of the surface nanobubbles were much closer to the substrate than for the spherical case, the jets did not appear to fully develop before they had already impacted the substrate. This jetting

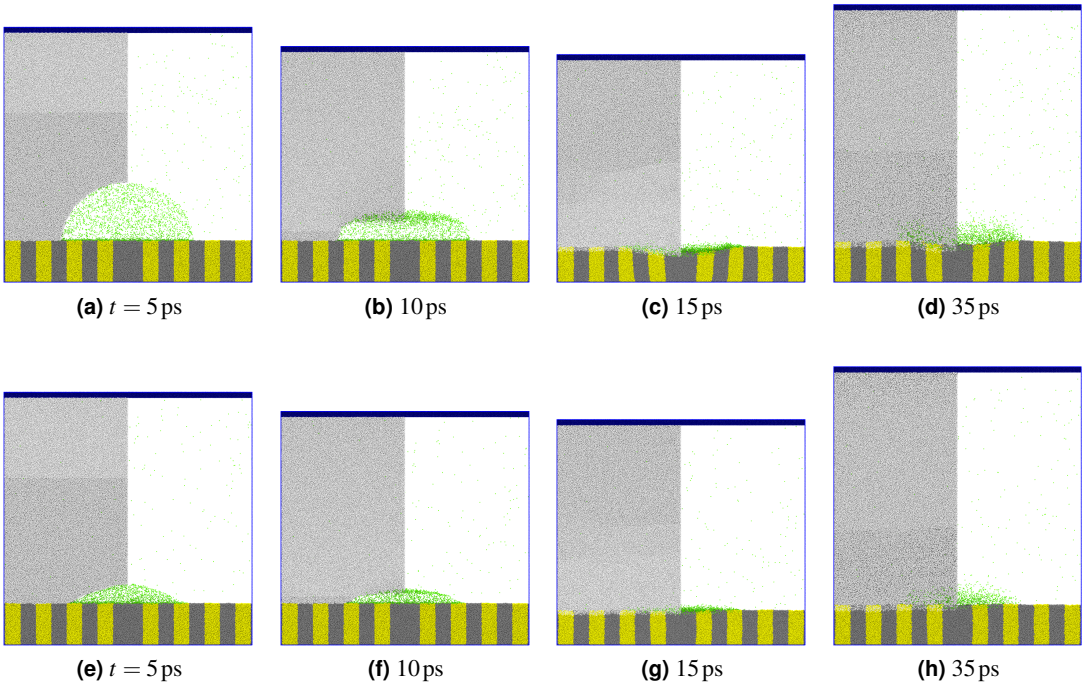

**(a)** $t = 5\,\text{ps}$ **(b)** $10\,\text{ps}$ **(c)** $15\,\text{ps}$ **(d)** $35\,\text{ps}$

**(e)** $t = 5\,\text{ps}$ **(f)** $10\,\text{ps}$ **(g)** $15\,\text{ps}$ **(h)** $35\,\text{ps}$

**Figure 6.5:** Renderings of the collapsing $40\,\text{nm}$ surface nanobubble MD simulations at various timesteps: (a)-(d) HCA surface nanobubble, and (e)-(h) LCA surface nanobubble. Some of the water molecules are not shown for clarity.

effect was even less pronounced in the LCA case, where the top surface was even closer to the solid than in the HCA case. With the inhibited jet formation, there was visibly less damage to the solid substrate compared to the spherical case (see Section 6.3.4). There was also less outward flow from the impact centre, and no rebounding bubbles observed, as with the spherical cases. Most of the nitrogen molecules remained dissolved, with a high concentration near the substrate, whereas in the spherical case, the nitrogen molecules end further away from the solid substrate by the end of the simulation.

The volume of the bubbles was measured, as shown for all cases in Figure 6.6. The insets show the rapid collapsing phase of the bubbles in more detail. There were some uncertainties in the measured surface nanobubble volume at the time close to complete collapse, due to the difficulty in measurements on the flexible substrate. The collapses all began when the shock wave first hit the bubble. The shock waves took longer to reach the surface nanobubbles, as they were closer to the solid substrate, but they also collapsed quicker due to their reduced volume. The $40\,\text{nm}$ spherical vapour bubble collapsed quicker than the equivalent sized gas-filled bubble, as shown in Figure 6.6(a), indicating that the gas phase inhibits the collapsing dynamics of the bubble. The vapour surface nanobubbles did not collapse much quicker than for the equivalent gas-filled cases. The rebounding behaviour of all the spherical bubbles can also be seen towards the end of the simulations.

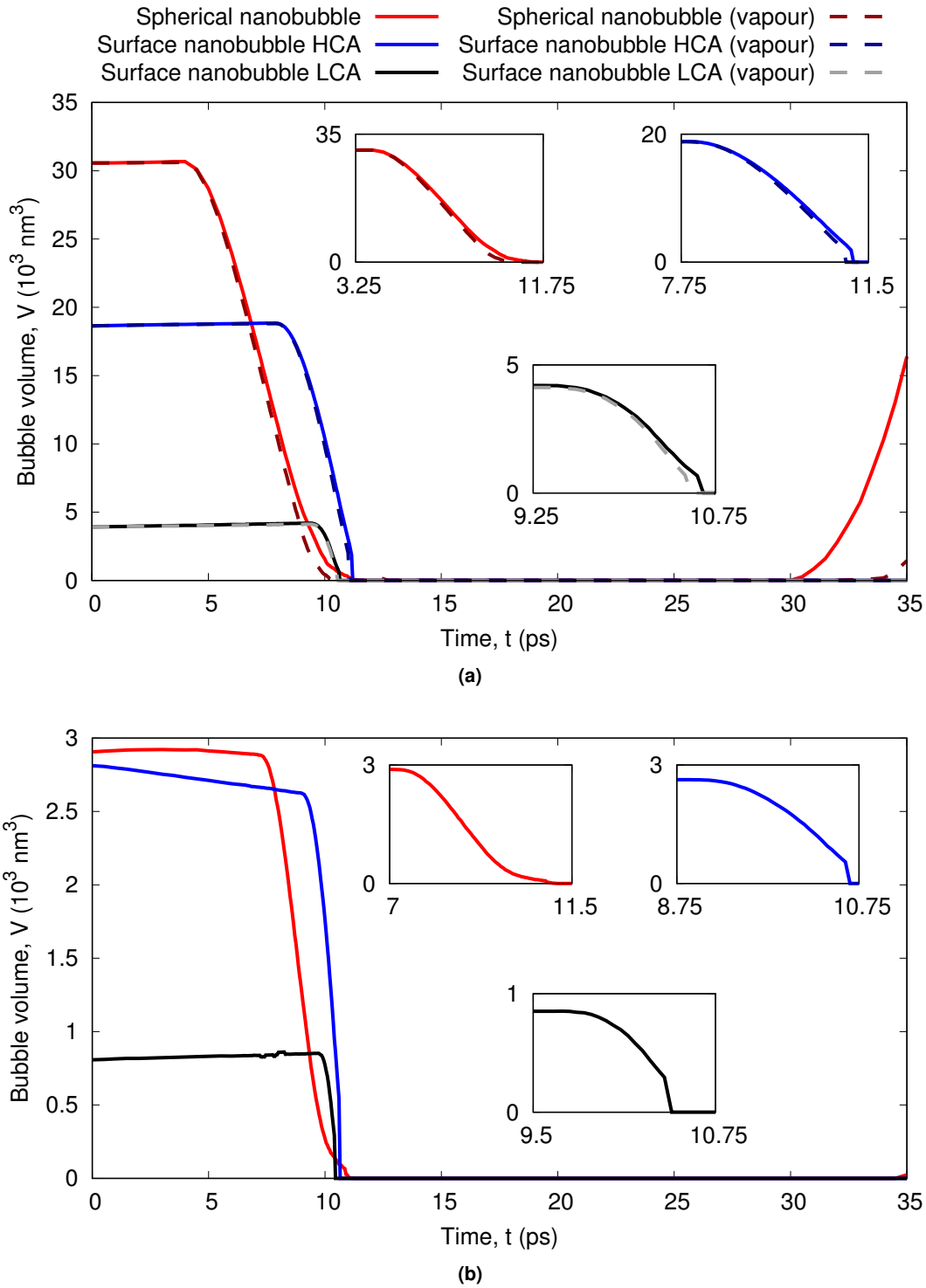


**Figure 6.6:** Time variation of bubble volume during collapse for: (a) $40\,\mathrm{nm}$ spherical bubble, and HCA and LCA surface nanobubbles (also shown are the equivalent vapour bubbles); (b) $20\,\mathrm{nm}$ spherical, and HCA and LCA surface nanobubbles. Insets show the collapsing phase in more detail for each case.

The time taken for a spherical bubble to collapse could be estimated from the Rayleigh collapse time, reproduced below from Equation (2.6):

$$\tau_c \approx 0.9147 R_{max} \sqrt{\frac{\rho}{P_\infty - P_v}}. \tag{2.6}$$

In the case of shock-driven collapse, the pressure of the incoming shock wave was taken as the liquid pressure, i.e. $P_\infty = 22.5\,\text{GPa}$, as found in Section 6.3.1. The vapour pressure was assumed negligible. Table 6.2 shows the measured collapse time for all bubble cases and predicted collapse times from Equation (2.6). For the surface nanobubbles, the equivalent radius was used again (see Chapter 5): $R_{eq} = (3V/4\pi)^{1/3}$, and substituted into Equation (2.6) instead of $R_{max}$.

| Bubble case | Actual collapse time (ps) | Rayleigh collapse time $\tau_c$ (ps) |
|---|---|---|
| 40 nm Spherical nanobubble | 8.00 | 4.32 |
| 40 nm HCA Surface nanobubble | 3.30 | 3.67 |
| 40 nm LCA Surface nanobubble | 1.20 | 2.23 |
| 20 nm Spherical nanobubble | 4.05 | 1.97 |
| 20 nm HCA Surface nanobubble | 1.65 | 1.95 |
| 20 nm LCA Surface nanobubble | 0.65 | 1.31 |
| 40 nm Spherical nanobubble (vapour) | 6.90 | 4.32 |
| 40 nm HCA Surface nanobubble (vapour) | 3.10 | 3.67 |
| 40 nm LCA Surface nanobubble (vapour) | 1.10 | 2.21 |

**Table 6.2:** Measured collapse time and predicted Rayleigh collapse time for all bubble simulation cases.

The Rayleigh collapse time does not agree with the collapsing times for the spherical bubbles. This is not unexpected, since Equation (2.6) has been previously shown to underpredict the shock-induced collapse of spherical bubbles, particularly at high driving pressures (Kapahi *et al.*, 2015; Vedadi *et al.*, 2010). This discrepancy is often put down to asymmetry during collapse and presence of nearby walls (Johnsen and Colonius, 2009), as well as the increased effects of surface tension and viscosity at the nanoscale (Vedadi *et al.*, 2010). The 40 nm spherical vapour bubble collapsed quicker than the respective gas-filled bubble, however, this still did not agree with Equation (2.6). The Rayleigh collapse time appears in better agreement with the surface nanobubble cases, although as already discussed, the effect of shock-induced collapse may be influencing this apparent agreement. It is clear that the surface nanobubbles collapsed quicker than the equivalently size spherical cases, due to the reduced volume of their spherical cap shape; however, as will be discussed in the next section, this quicker collapse did

not result in faster jet dynamics. Despite the lack of agreement with the Rayleigh collapse time, the different bubble shapes did show a size-dependent relationship, with the collapse times for the 20 nm bubbles approximately half that of the equivalent 40 nm bubbles.

### 6.3.3 Re-entrant jet dynamics

The most significant observation from Figure 6.5 was that the jets did not appear to fully develop during the collapsing surface nanobubble simulations. Figure 6.7(a) shows the development of the jet velocity $u_j$ for the 40 nm spherical and surface nanobubble cases, starting from the times the bubbles each began their collapse, denoted by $t_c$. Also shown are the 40 nm vapour bubble cases.

For all cases, the jet velocity gradually increased until it impacted the nearest surface, either the solid substrate for the surface nanobubble cases, as shown for the 40 nm HCA bubble in Figure 6.7(b), or the distal bubble surface for the spherical bubble cases, as shown for the 40 nm spherical bubble in Figure 6.7(c). After these impacts, the jet velocities began to decelerate; for the spherical cases, the jet would decelerate as it passed through the lower liquid layer before eventually impacting the solid substrate and finally dissipating (Philipp and Lauterborn, 1998), as shown in Figure 6.7(d). The jet profile was determined by the 50% isomomentum ($\rho u_j$) contour within the fluid (Thomas *et al.*, 1990), as shown by the solid grey lines in Figures 6.7(b)-(d).

All the jets from the 40 nm bubble cases developed at a similar rate for the first 1 ps. The jet velocities began around 2500 m/s, the same as the piston velocity $u_p$, and started rapidly developing before each jet made its first impact. The HCA surface nanobubble jet velocity developed from 2500 m/s to 4500 m/s, an increase of 2000 m/s after 3 ps, before impacting the substrate. The spherical bubble jet also reached a similar velocity by 3 ps, but continued to develop and experienced an almost 4000 m/s increase before impacting the distal bubble surface. Even after an initial deceleration, the jet velocity was still over 1000 m/s faster than the jets from the surface nanobubble cases upon impacting the substrate. It is clear that the substrate is prematurely halting the jet's development during the surface nanobubble collapses. The jets from the vapour bubbles develop higher velocities than their respective equivalent bubble sizes, due to the lack of the high density gas phase that would otherwise decelerate the fluid.

The jets from the collapsing spherical bubbles were also observed to be narrower than for the surface nanobubble cases, as seen in Figures 6.7(b)-(d). This can be explained from continuity: as the jet velocity increases, the diameter decreases. The jets from the surface nanobubbles appeared to be close to the full width of the bubble $\phi_0$, which could have been influenced by the contact line pinning of the surface nanobubble. The jet profiles from the surface nanobubble cases also had a much flatter leading surface, compared to the jets in the spherical cases. This could be due to more uniform gas density within the surface nanobubbles during collapse.

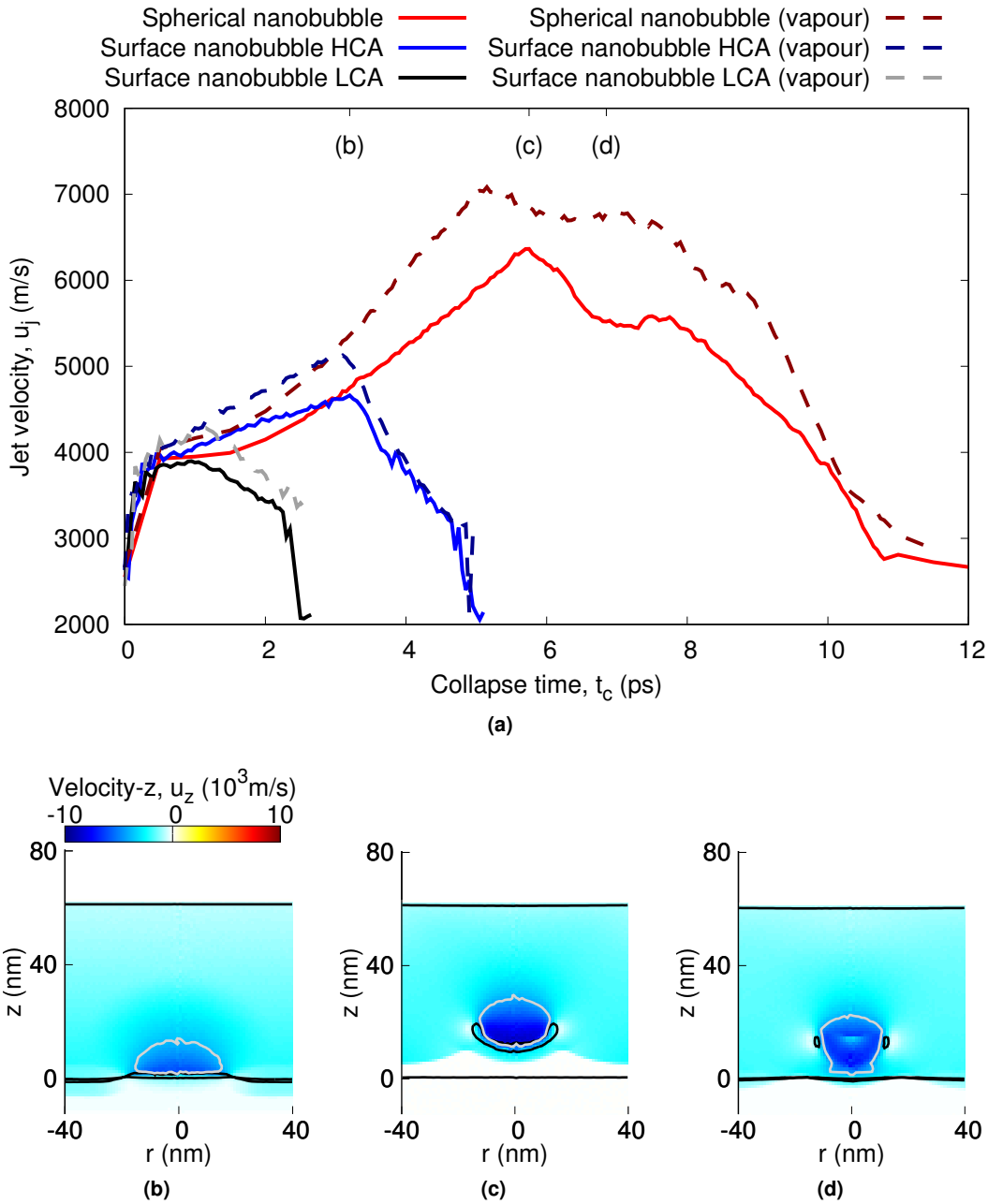


**Figure 6.7:** (a) Time variation of jet velocity $u_j$ for each of the $40\,\mathrm{nm}$ bubble cases; variation in $z$-component velocity across the: (b) $40\,\mathrm{nm}$ HCA surface nanobubble at jet impact on the substrate, (c) $40\,\mathrm{nm}$ spherical bubble at jet impact on the distal bubble surface, and (d) $40\,\mathrm{nm}$ spherical bubble at jet impact on the substrate. Solid black lines show the bubble interface, and the solid grey line shows the liquid jet. The (b), (c) and (d) labels in (a) correspond to the times of the other subfigures. The colour key in (b) also applies to subfigures (c) and (d).

The jet profile shape also has implications for the resulting pressure increase after impact, as discussed below (Dear and Field, 1988; Heymann, 1969).

Similar jetting behaviour was observed for the $20\,\mathrm{nm}$ spherical and surface nanobubble cases,

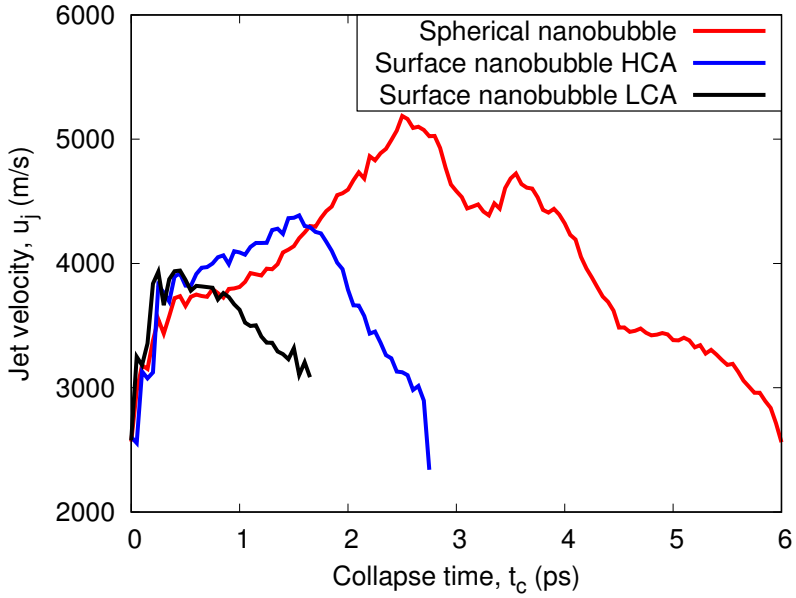


**Figure 6.8:** Time variation of jet velocity $u_j$ for each of the 20 nm bubble cases.

as shown in Figure 6.8.

After each of the jet impacts, high local pressures were observed, due to reflection and recombination of shock waves (Dear and Field, 1988; Heymann, 1969; Huang *et al.*, 1973). This spike increase in pressure is sometimes attributed as the main damage mechanism during cavitation (Kornfeld and Suvorov, 1944), although the impulsive effects of these pressures should also be considered, as discussed in Section 6.1.

There also appeared to be some unusual acceleration of the jet from the 40 nm spherical bubble collapse, just after it had impacted the solid substrate, at around 7.5 ps in Figure 6.7(a). This was a result of the water hammer (see below) causing a sudden increase in liquid density, and hence momentum, which caused a brief fluctuation in the jet's properties.

The pressure variations across the 40 nm spherical bubble collapse can be seen in Figure 6.9, showing the pressure peaking at each of the jet impacts. Figure 6.9(a) shows the shock wave with approximately the same pressure jump as seen in Figure 6.2(a) for the no-bubble case. As the shock wave impacted the top surface of the bubble a reflected expansion wave can be seen that travelled back upwards, as shown in Figure 6.9(b). Figures 6.9(c)-(f) show the brief spikes in pressure, as the jet impacted the distal bubble surface and then the solid substrate. A very localised pressure reaching almost 100 GPa can be seen at the distal bubble surface jet impact in Figure 6.9(d).

The pressure distribution across the substrate was also measured in the fluid 1 nm above the substrate, as shown at various time frames for the 40 nm bubble cases in Figure 6.10. Also shown is the initial bubble diameter $\phi_0$ (dashed black line), and final pit perimeter $\phi_d$ (solid

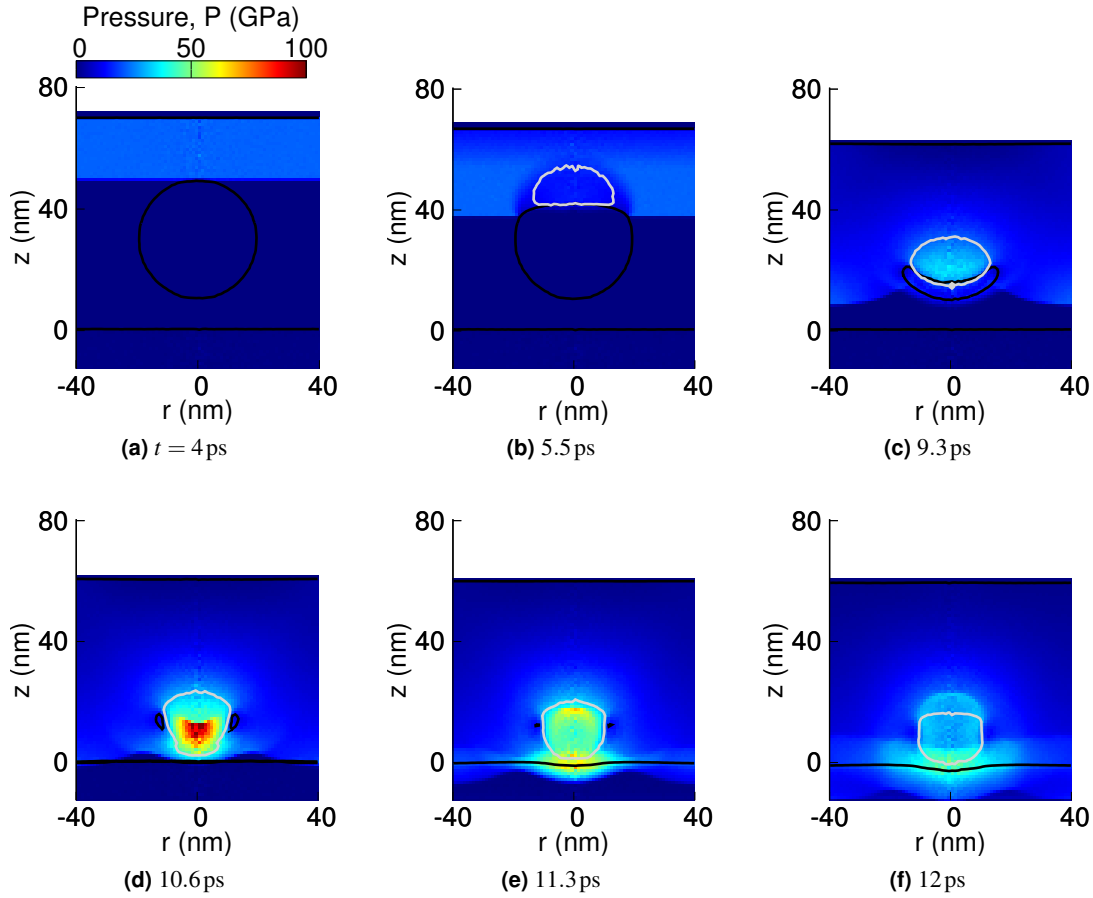


**Figure 6.9:** Variation in pressure across the 40 nm spherical bubble at various timesteps. The solid black line shows the bubble 50% isodensity contour. The solid grey line shows the development of the re-entrant jet. The colour key in (a) applies to all subfigures.

black line, see Section 6.3.4). The shock waves all impacted the substrate around 10.3 ps, as shown in Figures 6.10(a), (d), (g), similar to the no-bubble case as discussed in Section 6.3. The pressure across the substrates after jet impacts are shown in Figures 6.10(b), (h), (e) for the spherical bubble, and HCA and LCA surface nanobubble cases, respectively, in order of decreasing peak pressure. As the shock waves and jet flows were reflected off the substrate, the pressure across the substrate decreased back to ambient conditions as shown in Figures 6.10(c), (f), (i).

The peak pressures after each jet impact $P_j$ are shown for all bubble cases as a function of the incident jet momentum, as shown in Figure 6.11. The impact pressure was averaged across the jet and initial bubble diameters, for the distal bubble surface and solid substrate impacts, respectively, and the shock wave pressure (22.5 GPa) was subtracted from all results to show the pressure increase. There was a clear increase in the resulting impact pressure with impinging jet momentum. For the spherical bubble collapses, the jet momentum increased with increasing bubble size, and further increased with the vapour bubble collapse, for the

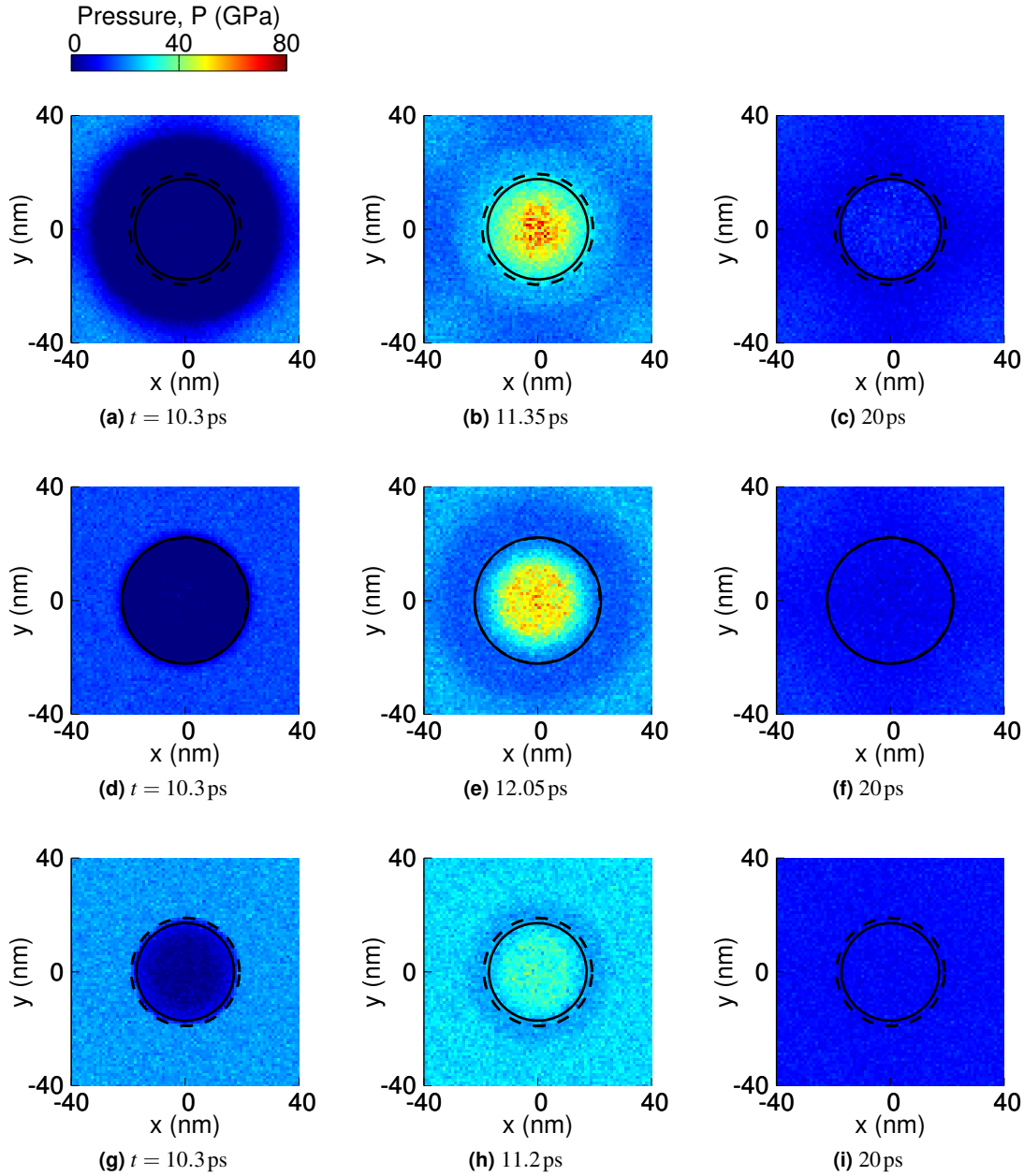


**(a)** $t = 10.3\,\mathrm{ps}$ **(b)** $11.35\,\mathrm{ps}$ **(c)** $20\,\mathrm{ps}$

**(d)** $t = 10.3\,\mathrm{ps}$ **(e)** $12.05\,\mathrm{ps}$ **(f)** $20\,\mathrm{ps}$

**(g)** $t = 10.3\,\mathrm{ps}$ **(h)** $11.2\,\mathrm{ps}$ **(i)** $20\,\mathrm{ps}$

**Figure 6.10:** Pressure distribution in fluid $z = 1\,\mathrm{nm}$ above solid substrate at various time frames for the collapsing $40\,\mathrm{nm}$ spherical and surface nanobubbles: (a)-(c) spherical bubble; (d)-(f) HCA surface nanobubble; (g)-(i) LCA surface nanobubble. The solid black circle shows the final perimeter of the pit damage $\phi_d$ and the dashed black circle shows the initial size of the bubble $\phi_0$. The colour key in (a) applies to all subfigures.

distal bubble surface impact in Figure 6.11(a) and the substrate impact in Figure 6.11(b). Contrary to this, the impinging jet momentum for the collapsing surface nanobubble cases was less dependent on size or the vapour contents. All the jets from the HCA cases had momentum $\sim 5.5 \times 10^6\,\mathrm{kg/m^2s}$, and for the LCA cases were $\sim 4.5 \times 10^6\,\mathrm{kg/m^2s}$. Similar jet

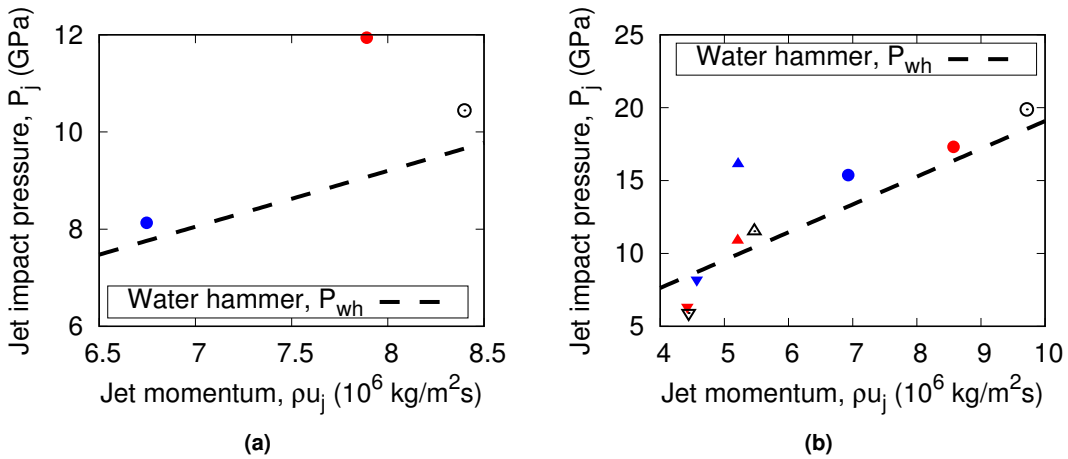


**Figure 6.11:** Variation of resulting liquid pressure increase with incident jet momentum immediately after each jet impact: (a) jet impact on the distal bubble surface for spherical bubble cases; (b) jet impact on the solid substrate for all bubble cases. Also shown is the predicted variation in water hammer pressure with jet momentum, from Equation (6.2), for each jet impact. Circles (◯) are for the spherical bubble cases, triangles (△) are for the HCA surface nanobubble cases, and inverted triangles (▽) are for the LCA surface nanobubble cases. The 20 nm sized gas-filled bubble cases are given by blue filled symbols, 40 nm sized gas-filled bubble cases are given by red filled symbols, and 40 nm vapour bubble cases are given by empty black symbols.

impact pressures were also observed in the respective surface nanobubble cases, although, as will be discussed in Section 6.3.4, the variation in pit damage was more dependent on the impulse. The resulting impact pressures for the surface nanobubble cases were generally all lower than the equivalently size spherical bubbles, which is a result of the weaker jet formations. The collapse of the LCA surface nanobubbles resulted in a lower pressure than for the equivalently sized HCA surface nanobubbles, due to the relatively lower jet velocity again.

Water hammer is a phenomenon where sudden changes in liquid flow momentum (such as quickly closing a valve in a pipe) can result in sharp increases in pressure, which can even lead to structural damage of engineering components. Dear and Field (1988) proposed the water hammer pressure for a liquid impacting a non-rigid solid surface:

$$P_{wh} = \rho u_j c_{0,l} \frac{\rho_s c_{0,s}}{\rho_s c_{0,s} + \rho c_{0,l}}, \tag{6.2}$$

where $\rho_s$ is the solid density, and $c_{0,l}$ and $c_{0,s}$ are the speeds of sound in the liquid and solid phases, respectively (Dear and Field, 1988). For the distal bubble surface jet impact, the liquid parameters ($\rho$, $c_{0,l}$) can be substituted instead of the solid parameters ($\rho_s$, $c_{0,s}$), and Equation (6.2) reduces to $P_{wh} \approx 0.5\rho u_j c_{0,l}$ (Johnsen and Colonius, 2009; Supponen *et al.*, 2017). This shows a roughly linear function of water hammer with jet momentum, as shown

in Figure 6.11(a). Similarly, using equilibrium values for the amorphous silicon wall from Chapter 3: $\rho_s = 2200\,\mathrm{kg/m^3}$ and $c_{0,s} = 5100\,\mathrm{m/s}$, Equation (6.2) reduces to $P_{wh} \approx 0.830\rho u_j c_{0,l}$, as shown in Figure 6.11(b).

Equation (6.2) was derived for low Mach flows, where the shock waves propagate at roughly the speed of sound within each medium; there are other much more complicated phenomena which influence this water hammer, such as the increased shock wave speed at high Mach flows (Heymann, 1969), as well as curvature of the impacting jet (Dear and Field, 1988; Heymann, 1969). These additional effects result in a much higher localised water hammer pressure at the impact centre, as can be seen in Figures 6.9 and 6.10. Predicting this localised peak pressure, while also taking into account the effect of the non-rigid impacted surface as in Equation (6.2), is not trivial and so the water hammer pressure distributions were averaged across the jet and bubble diameters to achieve better agreement, as in Figures 6.11(a) and (b), respectively.

Despite the deceleration between jet impacts in the collapsing spherical bubbles, the resulting pressure was larger for the second impacts, since the solid material properties are also important. This was also because the jets did not fully decelerate in between the two impacts, as already discussed. For non-shock-induced collapse of larger bubbles, which can be assumed mostly incompressible and with lower jet velocities, the jet's second impact on the substrate has been shown to be weaker due to this deceleration (Philipp and Lauterborn, 1998; Supponen *et al.*, 2016).

During collapse of the spherical bubbles, strong vortex flows were generated by the jet formation, which led to the toroidal shapes of the rebounding bubbles (Blake *et al.*, 2015; Johnsen and Colonius, 2009; Supponen *et al.*, 2016; Zhang and Duncan, 1994). The vorticity of the fluid flow is given by the curl of the velocity:

$$\vec{\eta} = \vec{\nabla} \times \vec{u}. \tag{6.3}$$

The vorticity around the 40 nm spherical and surface nanobubbles as they collapsed is plotted in Figure 6.12. The azimuthal component of vorticity $\eta_\varphi$ was found to be dominant, and is the only component plotted in Figure 6.12. Vortices were observed to be generated during the jet formation, as shown in Figure 6.12(a), with a maximum vorticity magnitude of nearly $4000\,\mathrm{ns^{-1}}$. Even as the jet impacted the silicon substrate in Figure 6.12(b), strong vortices remained within the fluid flow that continued for the remainder of the simulation where the toroidal rebounding bubble still had significant circulating fluid flow, as shown in Figure 6.12(c).

In comparison, the surface nanobubbles did not generate such strong vortices during their collapse, with a maximum magnitude of around $1000\,\mathrm{ns^{-1}}$ for the HCA surface nanobubble case, as shown in Figure 6.12(d). Since the jets did not fully develop during the surface nanobubble collapses, the vortices also did not fully develop, and so after the bubble had fully collapsed in

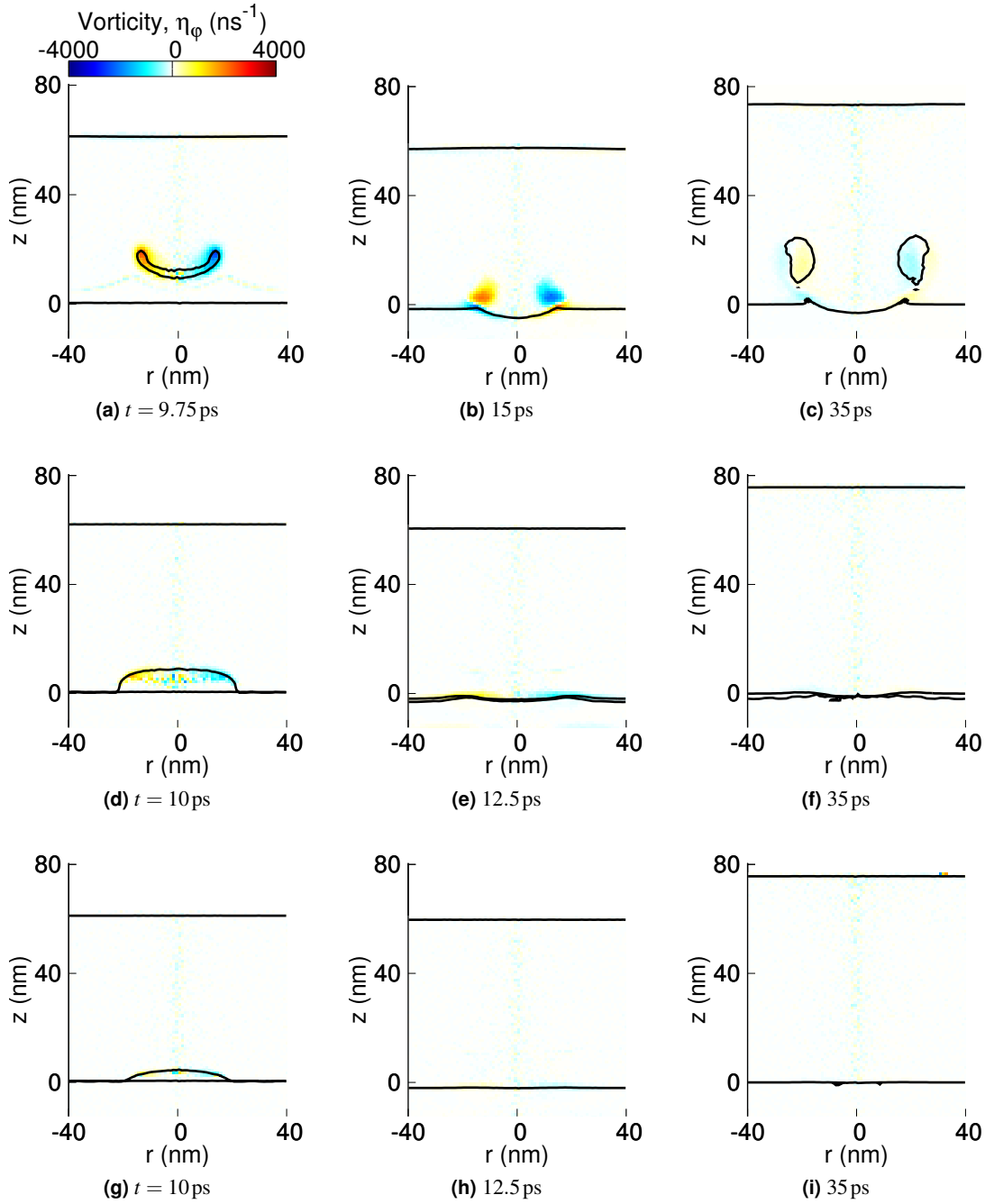


**(a)** $t = 9.75\,\text{ps}$ **(b)** $15\,\text{ps}$ **(c)** $35\,\text{ps}$

**(d)** $t = 10\,\text{ps}$ **(e)** $12.5\,\text{ps}$ **(f)** $35\,\text{ps}$

**(g)** $t = 10\,\text{ps}$ **(h)** $12.5\,\text{ps}$ **(i)** $35\,\text{ps}$

**Figure 6.12:** The variation in the azimuthal component of vorticity $\eta_\varphi$ during the collapse of $40\,\text{nm}$ spherical and surface nanobubbles: (a)-(c) spherical bubble collapse; (d)-(f) HCA surface nanobubble collapse; (g)-(i) LCA surface nanobubble collapse. The colour key in (a) applies to all subfigures.

Figures 6.12(e), (f) the vorticity generated rapidly diminished. With the weaker jet and vortices upon collapse, the fluid did not flow as quickly away from the substrate afterwards, which could explain why no toroidal rebound bubbles were observed in any of the collapsing surface nanobubble cases.

### 6.3.4 Pitting damage

Pitting damage was observed in all but one collapsing bubble simulations (the LCA 20 nm surface nanobubble case). A spherical cap shape could be fitted to the resulting pit damage on the solid substrate (Shekhar *et al.*, 2013), as shown in Figure 6.13 from the 40 nm spherical bubble case.

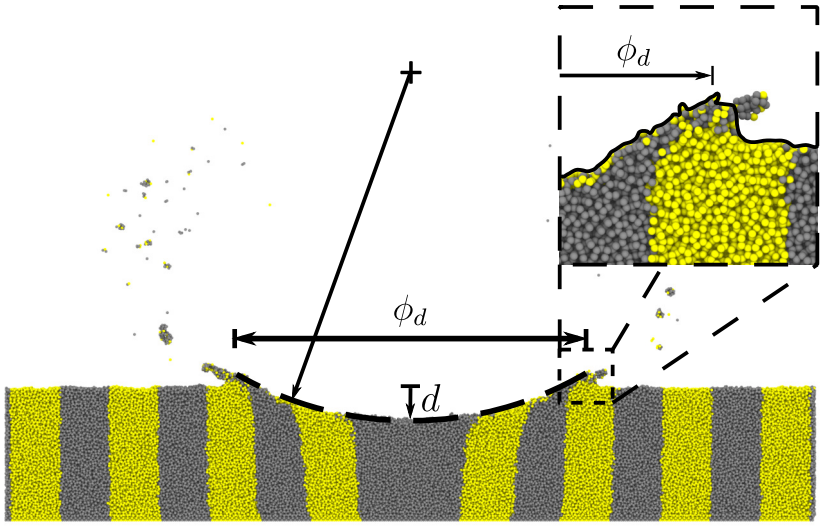


**Figure 6.13:** Schematic showing the typical solid substrate pitting damage at the end of the MD simulation. The dashed black line shows the fitted spherical cap shape to the pit. The inset shows a closer view of lip formed around the pit perimeter.

A small lip was also observed around the perimeter of the pit, caused by the deformation of the solid substrate as the fluid flowed away from the impact centre, with some of the material removed from the substrate ending up immersed in the liquid. A circle was fitted to the perimeter of this lip for all bubble cases, and the diameters of these pit perimeters $\phi_d$ were nearly identical to the initial bubble sizes $\phi_0$, as shown in Figure 6.14(a). Previous investigations have also found that the final pit size scales with initial bubble size for spherical bubble collapse (Philipp and Lauterborn, 1998; Shekhar *et al.*, 2013), consistent with these findings. As discussed in Section 6.3.1, no damage was observed in the case with no bubble, confirming that the collapsing nature of the cavitation bubbles is important for the resulting pit damage shape, and damage is not just the result of an impinging shock wave.

Although similar sized bubbles produced pits with similar perimeters, the depths of these pits $d$ varied significantly depending on the dynamics of the jet just before impact with the substrate, as shown in Figure 6.14(b). The spherical bubbles always produced the deepest pits for a given size. Removing the gas phase from the 40 nm spherical bubble almost doubled the pit depth, despite a relatively small change in pit perimeter. The depths of the pits from the collapsing surface nanobubbles did not differ much with the size of the bubbles; the HCA surface nanobubble cases all produced pits with depths of around 1.2 nm, regardless of bubble

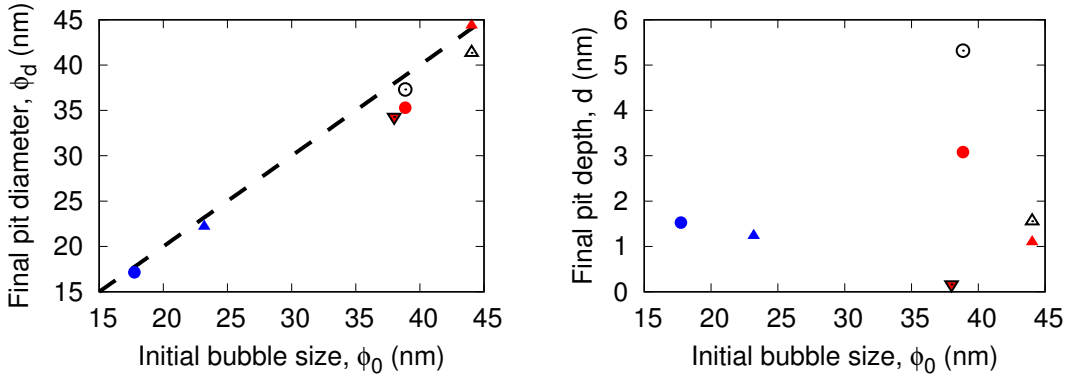


**Figure 6.14:** Variation in: (a) final pit diameter with initial bubble size (the dashed line shows $\phi_d = \phi_0$), and (b) final pit depth with initial bubble size. Circles (◯) are for the spherical bubble cases, triangles (△) are for the HCA surface nanobubble cases, and inverted triangles (▽) are for the LCA surface nanobubble cases. The 20 nm sized gas-filled bubble cases are given by blue filled symbols, 40 nm sized gas-filled bubble cases are given by red filled symbols, and 40 nm vapour bubble cases are given by empty black symbols.

size. Removing the gas from the HCA 40 nm surface nanobubble did increase the pit depth to around 1.5 nm, although was not as significant an increase compared to the 40 nm spherical bubbles. The pit depth from the 20 nm HCA case was also around 1.5 nm, which could be due to the similar pressures observed in Figure 6.11(b). The LCA 40 nm surface nanobubble cases produced pits around 0.15 nm; overall there was little effect from removing the gas phase from the LCA surface nanobubble case on the final pit shape, due to the limited effect of the gas-phase on the jet's already weak development.

Using Equation (6.1), the radial distribution in impulse across the substrate could be determined, and is shown for all bubble cases in Figure 6.15. The impulse across the substrate from just the shock wave was 260 mPa s as measured from the no-bubble case (see Section 6.3.1), which is also shown as the dashed line in Figure 6.15. For all bubble cases, the impulse was maximum around the impact centre and decreases towards a steady value, approximately equal to the mean impulse from the driving shock wave, at a distance close to the initial bubble radius.

For each size, the spherical cases had a higher peak impulse at the impact centre than for the surface nanobubble cases. The LCA surface nanobubble case had a peak 266 mPa s, which was not much greater than the 260 mPa s impulse from the no-bubble case; this relatively small increase in impulse at the impact centre could explain why no damage was observed in this particular case. Comparing the vapour bubbles to the equivalent gas-filled bubbles, there were no significant differences in the impulse distributions for either of the 40 nm surface nanobubble cases. This is in contrast to the spherical case, where the peak impulse increased from 390 mPa s to 425 mPa s when the internal gas phase was removed before collapse.

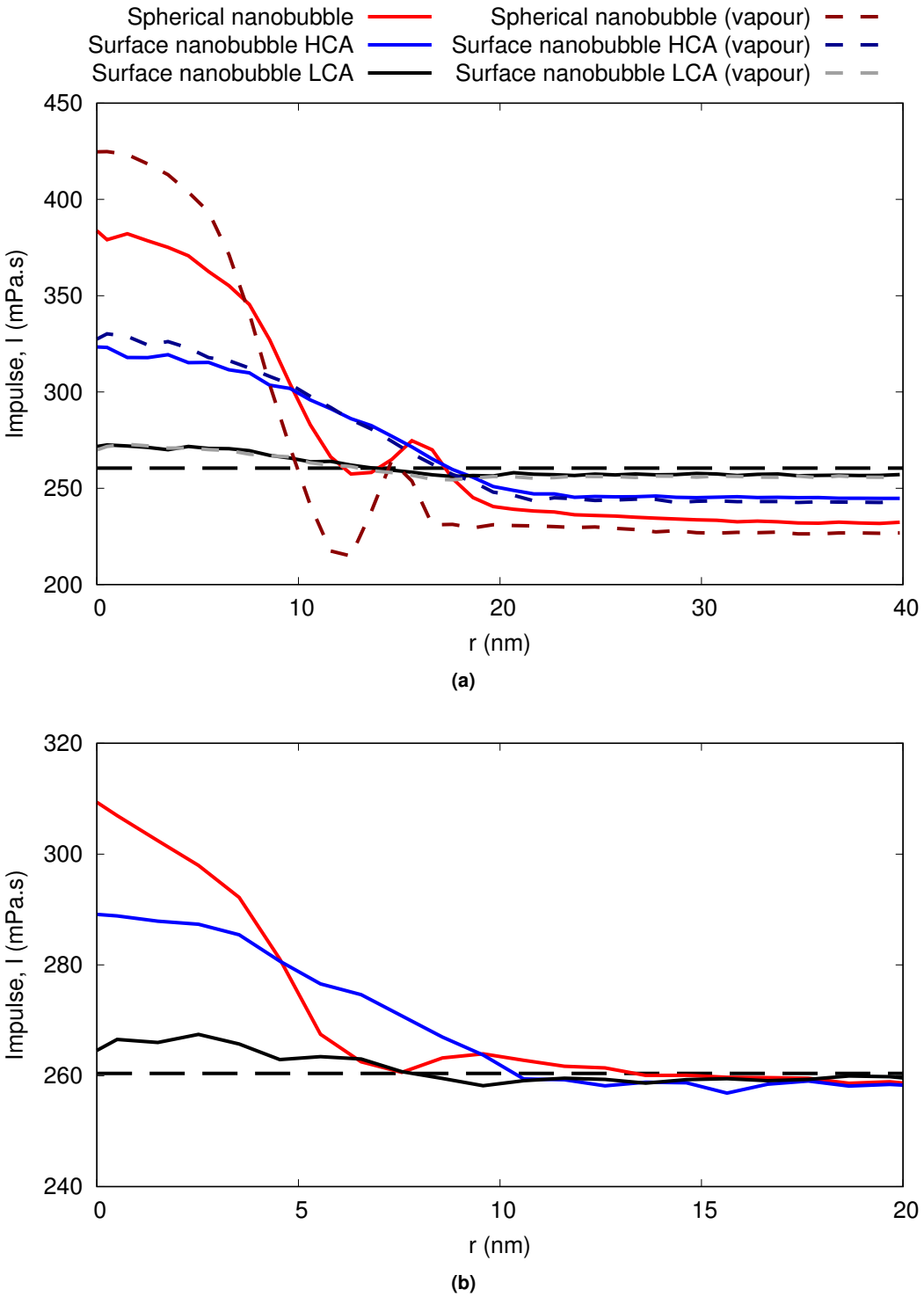


**Figure 6.15:** Radial distribution in impulse across the substrate for the: (a) $40\,\mathrm{nm}$ size bubble cases, and (b) $20\,\mathrm{nm}$ size bubble cases. The mean impulse from the no-bubble case is shown as the black dashed line at $I = 260\,\mathrm{mPa\,s}$.

The impulse distributions from all the spherical bubble cases exhibited an interim trough and peak around $r = 12\,\text{nm}$ in Figure (a) and $r = 7.5\,\text{nm}$ in Figure 6.15(b). These interim troughs were observed to be all approximately the radius of the maximum jet sizes. This feature of the impulse distribution could be due to the circulatory motion of the fluid as it flowed away from the impact centre after collapse, as discussed in Section 6.3.3. These interim peaks and troughs cannot be seen for the surface nanobubble cases; in these cases, circulatory flow and a toroidal rebounding bubble were not observed after collapse, which could explain the absence of these impulse features.

Despite the large variations in the maximum impulse measured at the impact centre for each bubble case from Figure 6.15, the mean impulse across the substrate did not deviate as much from the 260 mPa s no-bubble value, as shown in Figure 6.16. All the collapsing bubble cases

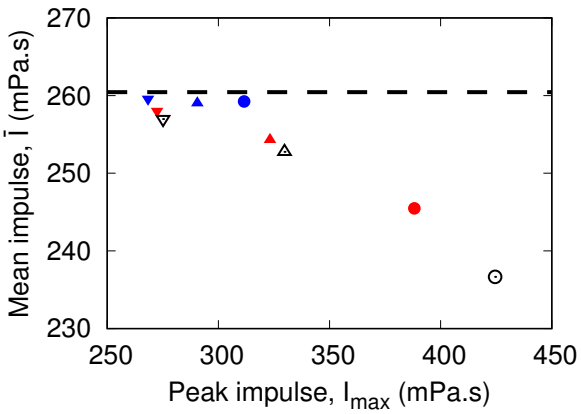


**Figure 6.16:** Variation in the mean and peak impulse across the substrate for each collapsing bubble case (the dashed line shows the mean impulse for the no-bubble case.)

recorded a mean impulse lower than the no-bubble case. This was not unexpected since the impulse produced from the shock wave would be dissipated through other means, e.g. deformation of the solid, shock wave reflections and viscous dissipation during vortex formation. Also, the impulse across the toroidal rebounding bubbles' surfaces (which was not considered in Figure 6.16) would contribute to the total system impulse. The larger 40 nm bubble cases deviated the most from the no-bubble case, due to these dissipation mechanisms. The vapour 40 nm bubbles also led to lower mean impulses across the substrate, possibly from the increased jet velocities and resulting solid deformation.

The damage to the substrate was quantified as the volume of silicon displaced from its mean $z$ position at the end of the simulation. Figure 6.17 shows the variation in the final damage volume with the jet impact pressures (from Figure 6.11(b)) and peak impulse $I_{max}$ at the impact centre for the collapsing bubble simulations. There is no clear trend in the damage volume variation with the jet impact pressure; instead, the impulse needs to be considered. The resulting pit damage increases with increasing peak impulse, as shown in Figure 6.17(b). The 20 nm

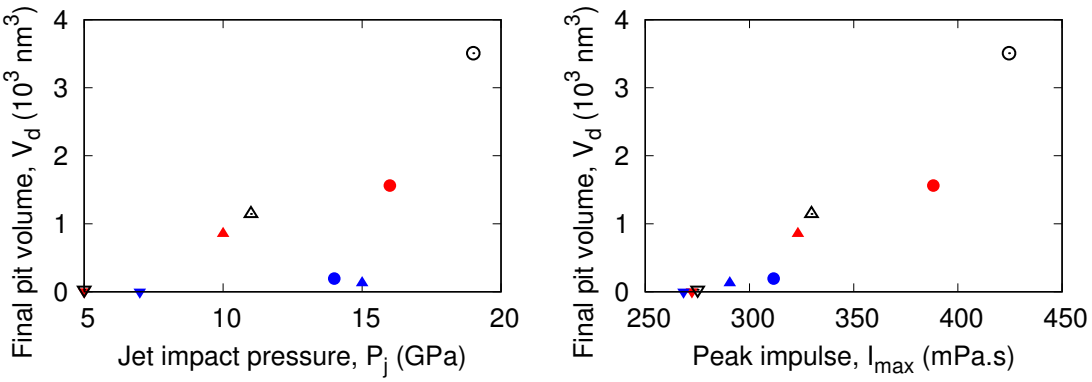


**Figure 6.17:** (a) Variation in final pit damage volume with jet impact pressure; and (b) variation in final pit volume damage with peak impulse at the impact centre. Circles (◯) are for the spherical bubble cases, triangles (△) are for the HCA surface nanobubble cases, and inverted triangles (▽) are for the LCA surface nanobubble cases. The 20 nm sized gas-filled bubble cases are given by blue filled symbols, 40 nm sized gas-filled bubble cases are given by red filled symbols, and 40 nm vapour bubble cases are given by empty black symbols.

LCA surface nanobubble case is also shown in Figure 6.17(b), although with zero damage $V_d = 0\,\text{nm}^3$ at $I_{max} = 266\,\text{mPa s}$. Figures 6.15 and 6.17 show that it is not the mean impulse that dictates the extent of the damage to the substrate, in agreement with Adhikari *et al.* (2015); indeed, the maximum mean impulse on the substrate was recorded for the no-bubble case, in which no damage was recorded. The maximum impulse at the impact centre, as well as general distribution of impulse across the surface, provides a better understanding of the preceding re-entrant jet dynamics and resulting pit damage.

## 6.4 Summary

The shock-induced collapse of surface nanobubbles of varying size and contact angle has been investigated and compared to the collapse of a spherical bubble close to a solid substrate (with stand-off parameter $\chi = 1.5$). The re-entrant jet formation, typical in cavitation collapse, was observed in all bubble simulations. The jets were found to develop and increase in velocity until impacting the nearest surface. For the spherical bubbles, this was the distal bubble surfaces; after this first impact, the jet began decelerating before impacting the solid substrate very soon after. For the surface nanobubbles, the jets impacted the solid substrate before they could fully develop, and never reached the same peak velocities compared to the jets from the equivalently sized spherical bubbles. The "weaker" jets from the collapsing surface nanobubbles were characterised by lower jet velocities, and larger jet diameters (in comparison to the initial bubble size) due to the effects of the pinned contact line. A toroidal rebounding bubble was

observed in all the spherical cases, but not in any of the surface nanobubble cases; there was less outward flow away from the impact centre after the surface nanobubble collapses. For the proposed surface cleaning application, surface nanobubbles might require an external bulk fluid flow to remove the contaminant particles after collapse, due to this lack of outward flow.

This abrupt obstruction to the jet had a greater effect for the lower contact angle surface nanobubbles, where the top surface of the bubble was already close to the substrate. The jets reached a greater peak velocity for the higher contact angle surface nanobubble cases, however, never achieved the same peak velocities of the equivalently sized spherical bubble cases. The underdeveloped jets from the collapsing surface nanobubbles were found to lead to lower pressures across the substrate after impact. The resulting pressure immediately after impact was proportional to the incident jet's momentum, and also dependent on the mechanical properties of the liquid and substrate (for non-rigid solids); this was in good agreement with the predictions of water hammer pressure. Local variations in the pressure were also observed close to the impact centre which arose from complex reflections and interference of shock waves, due to the high Mach number jets and curvature of the leading jet surfaces. Further research could investigate the water hammer from the impact of high Mach number liquid jets on flexible solid surfaces, including the effect of jet curvature.

The collapse of the surface nanobubbles resulted in less permanent damage to the substrate, compared to equivalently sized spherical bubbles. This would appear to be in contrast to the findings of Philipp and Lauterborn (1998), who found that bubbles closer to the surface (for stand-off of $\chi \approx 0.3$) caused larger pits after collapse. This difference in results is partly down to using shock waves to induce collapse here, since substrate damage has been shown to be less dependent on stand-off parameter for $\chi > 0$ (Johnsen and Colonius, 2009; Shekhar *et al.*, 2013). However, the main reason is due to the weaker jets formed during surface nanobubble collapse for $\chi < 0$, which resulted in reduced peak impulse across the substrate. No permanent damage was observed for the no-bubble case or the smallest bubble volume case (20 nm LCA surface nanobubble).

The pit perimeters had diameters which scaled with the initial sizes of the bubbles, as has been previously shown (Philipp and Lauterborn, 1998; Shekhar *et al.*, 2013). The pitting damage was found to be dependent on the peak impulse at the impact centre, as opposed to the mean impulse across the solid substrate during collapse, or the jet impact pressure. The mean impulse across the substrate was found to decrease with increasing peak impulse, as momentum was dissipated by solid deformation and viscous dissipation during jet formation and rebound. The impulse distribution also revealed some of the main features of the preceding jet formation and resulting pit damage shape; for the spherical cases, an interim peak and trough in the impulse distribution were found near the radius of the jet before impact, which is suggested to be due to the toroidal rebounding bubble after collapse.

Due to nanoscale bubbles modelled in the MD simulations, shock waves had to be introduced in

order to induce a violent collapse typical in cavitation. These shock waves can often arise from the collapse of larger bubbles (Supponen *et al.*, 2017), however, they did make analyses of the collapsing bubbles more difficult from shock reflections and interference effects. Eliminating some of the shock wave reflections, such as from the piston and the bottom of the domain, was difficult in the MD simulations (although is also a problem in other simulation and experimental techniques). Further research could investigate suitable methods for mitigating the effects of these shock wave reflections so the long-term behaviour of the fluid (and toroidal rebounding bubble) post-collapse could be suitably modelled.

# Chapter 7

# Summary and Concluding Remarks

This concludes all the research conducted for this thesis, which has broadly covered the life of a cavitating surface nanobubble, from the onset of instability, growth rate, oscillation dynamics, and finally collapse. If there is a general theme to the findings, it is that of enhanced stability. In Chapter 4, surface nanobubbles were found to be able to sustain pressures many mega-Pascals lower than an equivalently sized spherical bubble before experiencing unstable growth, due to pinning of the contact line. In Chapter 5, surface nanobubbles were shown to oscillate with a higher natural frequency than spherical bubbles, which is often associated with an increased "stiffness" in damped oscillator analysis, again, a result of their pinned growth mode. Finally, in Chapter 6, the substrate damage resulting from surface nanobubble collapse was found to be reduced compared to spherical bubble collapse, due to the solid substrate prematurely stopping the re-entrant jet development before impact.

This enhanced stability would seem to fit in with the general nature of surface nanobubbles; their existence was originally considered interesting in the field of multiphase fluid mechanics due to their diffusive stability and long lifetimes. This diffusive stability is commonly attributed, in part, to the pinning of the three-phase contact line, which was also found in this research to be important to their cavitation dynamics. To summarise, the pinned contact line causes a constant contact radius (CCR) mode of growth of the surface nanobubble; the result is an increased Laplace pressure contribution across the interface which suppresses excessive expansion of the internal gas phase. This makes surface nanobubbles more resistant to the effects of cavitation.

However, this apparent stability appears to contradict the prevailing understanding of cavitation being commonly associated with heterogeneous nucleation and collapse on solids. It is worth considering the higher probability of finding surface nanobubbles on an immersed solid, due to their diffusive stability, as opposed to spherical bubble nuclei in the nearby bulk liquid, which have comparatively shorter lifetimes. Cavitation would more likely be observed to nucleate from these longer-lasting surface nanobubbles, than the short-lived spherical nanobubbles in the bulk. Also, the effects of cavitation are interpreted by the evidence they leave behind, i.e. the permanent damage on solids after a prolonged period of time, since the rapid nature of the collapse is difficult to observe in real time.

The long lifetimes of surface nanobubbles make them appealing for a variety of engineering applications, as discussed in Chapter 2. How does the knowledge gained in this research align with some of these proposed applications? Firstly, the enhanced resistance to cavitation means lower pressures will be required to induce instability. This may be beneficial in applications where the surface nanobubbles will be able to operate over a larger range of pressures and flow situations. The oscillation dynamics of bubbles can be used in diagnostics and medicine, such as in ultrasound contrast agents. The increased natural frequency of surface nanobubbles would result in more power required by the ultrasonic transducers to achieve resonance, although this change in natural frequency could provide additional insight when investigating the surface characteristics of a solid, e.g. increased surface roughness would result in an increased number density of surface nanobubbles, and stronger response signal. For applications such as ultrasonic cleaning, jets from the collapse of cavitation bubbles are used to displace contaminant particles from a solid. As discussed in Chapter 6, the collapsing jets of surface nanobubbles are weaker than for spherical bubbles, and so they may be better suited to avoid damage to the substrate for more delicate parts such as in Micro-Electro-Mechanical Systems (MEMS) devices. However, unlike spherical bubble collapse, there is a lack of outward flow immediately after collapse of the surface nanobubble, so an external flow in the surrounding bulk liquid would be required to remove the contaminant particles after being displaced from the substrate.

The cavitation dynamics of surface nanobubbles have been extensively investigated here, however, there remains some questions on their behaviour. For example, could surface nanobubbles detach from the substrate during explosive growth, as suggested in Chapter 4? This detachment mechanism was not directly modelled, although the collapse of spherical bubbles close to solid substrates was simulated in Chapter 6. In Chapter 5, the growth rate and natural frequency models proposed assume contact line pinning and a spherical cap shape; further research could investigate how these assumptions hold for larger surface nanobubbles. Also, the bubbles in Chapter 5 were found to oscillate adiabatically, which was not expected from the (spherical) bubble analyses by Prosperetti (1991, 1977), that suggest more isothermal behaviour. Further investigations could examine the possibility of nanoscale interfacial phenomena, such as the Kapitza resistance, influencing the thermal expansion of surface nanobubbles.

Molecular Dynamics (MD) simulations were used successfully throughout this research to model the surface nanobubbles, due to their superior accuracy at modelling nanoscale physics, which could not be achieved by other simulation techniques. However, the high computational cost, particularly for simulating larger domains as in Chapters 5 and 6, make them less suitable for larger bubbles and time scales. More efficient Computational Fluid Dynamics (CFD) solvers (e.g. OPENFOAM (Weller *et al.*, 1998)) could be used in the future, coupled with MD to capture the contact line stick-slip dynamics, polytropic gas behaviour, diffusive bubble growth, and fluid-solid interaction during collapse. These hybrid solvers would also be well suited to model the wide range of bubble sizes that are observed during cavitation. Other phenomena

could then be modelled, such as rectified diffusion (as discussed in Chapter 5), the effects of close neighbouring bubbles on oscillation and collapse, and the proposed detachment process as discussed above.

What should be clear from this research is that surface nanobubbles have unique dynamics during cavitation, and cannot be simply modelled from the classical spherical bubble equations, such as the Blake threshold and Rayleigh-Plesset equation. This does not make them unsuitable for their proposed applications outright, more that they require proper modelling, as done here, to establish the role of the solid, contact line pinning and surface tension effects to their behaviour. With further investigation and improved modelling techniques for larger length and time scales, more understanding could be gained in some specific cavitation-related phenomena, which could lead to engineering applications tailored to the unique behaviour of these surface nanobubbles.

# Appendix A

# Molecular Dynamics Simulation Length Scales and Dimensionless Numbers

Due to the dynamic nature of the simulations in Chapter 5, certain checks need to be taken to ensure that the simulation set-up would be suitable to approximate surface nanobubbles oscillating within a semi-infinite liquid. There is a risk that due to the small finite sizes of Molecular Dynamics (MD) simulation domains, the effects of confinement could influence the dynamics of the surface nanobubbles (Leighton, 2011; Martynov *et al.*, 2011; Tsuda *et al.*, 2015; Vincent and Marmottant, 2017). The following length-scales and dimensionless numbers are derived to assess the limits at which these effects can be considered negligible, i.e. when we can approximate the MD domain as a semi-infinite liquid. The analyses follow for spherical bubbles, although are useful in giving a rough estimate for the domain sizes for surface nanobubble simulations.

The analyses assume the linearised form of the Rayleigh-Plesset equation, reproduced below from Equation (5.11):

$$\ddot{\xi} + \frac{4\nu}{R_0^2}\dot{\xi} + \frac{1}{\rho R_0^2}\left[3kP_{g,0} - \frac{2\gamma}{R_0}\right]\xi = \frac{\Delta P_\infty}{\rho R_0} f(t). \tag{5.11}$$

Equation (5.11) takes the form of a general damped harmonic oscillator $\ddot{\xi} + \alpha\dot{\xi} + \omega_0^2\xi = p(t)$.

For oscillations driven by a sinusoidal pressure field $P_\infty(t) = P_{\infty,0} + \Delta P_\infty \sin\Omega_d t$, the amplitude of the bubble oscillations is:

$$\xi_a = \frac{p_a}{\sqrt{\left(\Omega_d^2 - \omega_0^2\right)^2 + \alpha^2\Omega_d^2}}, \tag{A.1}$$

where for a spherical bubble, $p_a = \Delta P_\infty/\rho R_0$ and $\alpha = 4\nu/R_0^2$, obtained from Equation (5.11).

## A.1 Effect of domain size on liquid inertia

Due to the restricted number of atoms that can be modelled in the MD simulations, the inertial effects of the surrounding liquid during bubble growth will certainly be less than that expected for a semi-infinite liquid. To assess this discrepancy, the dynamic pressure of the liquid $\frac{1}{2}\rho u(r)^2$ is investigated at a radial position $r$. For an ideally large system, the dynamic pressure far away from the bubble should be negligible compared to the far-field pressure variation inducing growth $\Delta P_\infty$:

$$\Delta P_\infty \gg \frac{1}{2}\rho u_r(r)^2, \tag{A.2}$$

where $u_r(r)$ is the radial velocity at a distance $r$. For a spherical bubble, this is given by (Brennen, 2013):

$$u_r(r) = \frac{\dot{R}R_0^2}{r^2}. \tag{A.3}$$

For small amplitudes, the bubble can be assumed to undergo linear oscillations, in which the bubble has a sinusoidal response to a sinusoidal input pressure, as discussed in Section 5.4.2. The amplitude response as a function of driving frequency is given in Equation (A.1). For a bubble driven at its natural frequency $\Omega_d = \omega_0$, Equation (A.1) reduces to:

$$\xi_a = \frac{p_a}{\alpha\omega_0}. \tag{A.4}$$

The maximum wall velocity of the bubble oscillating at its natural frequency is simply:

$$\dot{R}_{max} = \xi_a\omega_0 = \frac{\Delta P_\infty R_0}{4\mu}. \tag{A.5}$$

Substituting Equations (A.3) and (A.5) into Equation (A.2), and rearranging to find the far-field limit at $r_\infty = r$, gives:

$$r_\infty \gg \left[\frac{\Delta P_\infty \rho R_0^6}{32\mu^2}\right]^{\frac{1}{4}}. \tag{A.6}$$

Equation (A.6) shows that the required far-field distance relates the inertial and applied pressure forces driving the bubble oscillation, to the viscous dissipation forces limiting this oscillation amplitude. For nanobubbles, this viscous effect becomes dominant, which allows the MD simulations to be able to run with reasonable domain sizes.

## A.2 Effect of piston inertia on pressure dynamics

Equation (5.8) shows how the inertia of the piston can contribute significantly to the pressure in the liquid during high frequency oscillations. For the pressure-driven oscillation cases, the contribution of the piston's inertia should ideally be negligible compared to the desired pressure variation in the liquid:

$$\Delta P_\infty \gg \frac{m_p \ddot{V}}{A_p^2}. \tag{A.7}$$

Differentiating the volume of a sphere twice with respect to time, and ignoring the non-linear $\dot{R}^2$ term, gives:

$$\ddot{V} = 4\pi R_0^2 \ddot{R} + 8\pi \dot{R}^2 R_0 \approx 4\pi R_0^2 \ddot{R}. \tag{A.8}$$

For the linearised analysis, the maximum acceleration of the bubble surface for a driving frequency $\Omega_d$ is:

$$\ddot{R}_{max} = \xi_a \Omega_d^2. \tag{A.9}$$

For driving frequencies close to the natural frequency $\Omega_d \sim \omega_0$, it is assumed that $\xi_a \Omega_d^2 \approx \Delta P_\infty R_0 \Omega_d / 4\mu$, from Equation (A.4). Substituting in Equations (A.8) and (A.9) into Equation (A.7), and rearranging into a non-dimensional form gives:

$$\beta \equiv \frac{m_p \pi R_0^3 \Omega_d}{A_p^2 \mu} \ll 1. \tag{A.10}$$

This newly derived *piston inertia number* $\beta$ represents the relative effect of the piston's inertia on the pressures in the liquid driving the bubble oscillations and allows proper sizing of the domains for the MD simulations. Interestingly, despite being derived in terms of the applied pressure amplitude $\Delta P_\infty$, this pressure amplitude is not actually present in Equation (A.10), since the piston inertia amplitude is proportional to the bubble oscillation amplitude, which is also proportional to $\Delta P_\infty$. Instead, it is the viscosity which counteracts this piston inertia, since the viscous damping limits the oscillation amplitude near the natural frequency from Equation (A.1). Again, this allows proper sizing of the domains for the MD nanobubble simulations.

# Appendix B

# Oscillating Surface Nanobubble Results

This appendix gives the simulation results for each MD simulation oscillation frequency case, as given in Chapter 5, Section 5.4.2, and compared to results from the proposed model in Equation (5.9) for adiabatic expansion ($k = 5/3$), as shown in Figure B.1. Also shown is the fitted sine wave to results, with amplitudes plotted in Figure 5.14.

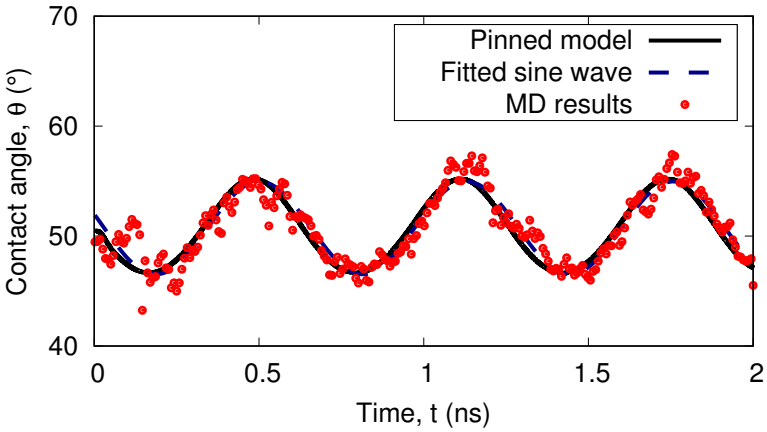


**(a)** $\Omega_d = 10\,\mathrm{rad/ns}$

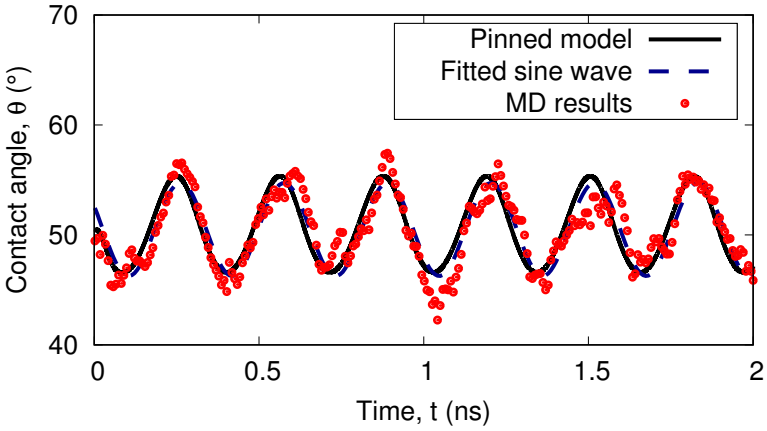


**(b)** $\Omega_d = 20\,\mathrm{rad/ns}$

**Figure B.1:** Variation in contact angle with time for various pressure oscillation frequencies $\Omega_d$, as indicated in each graph. Figure continues on next page.

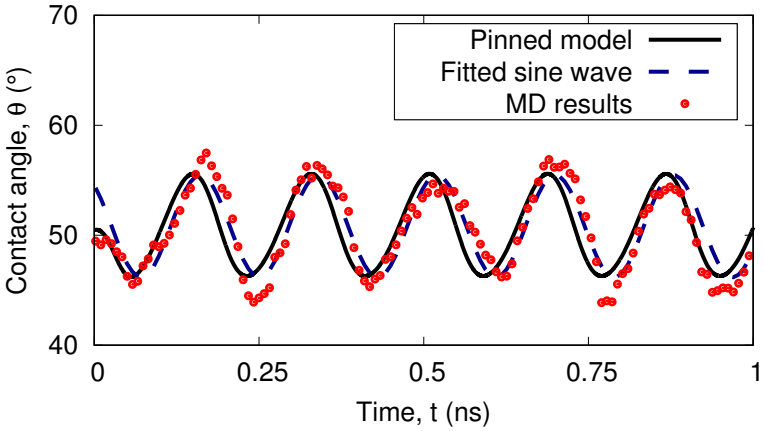


**(c)** $\Omega_d = 35\,\mathrm{rad/ns}$

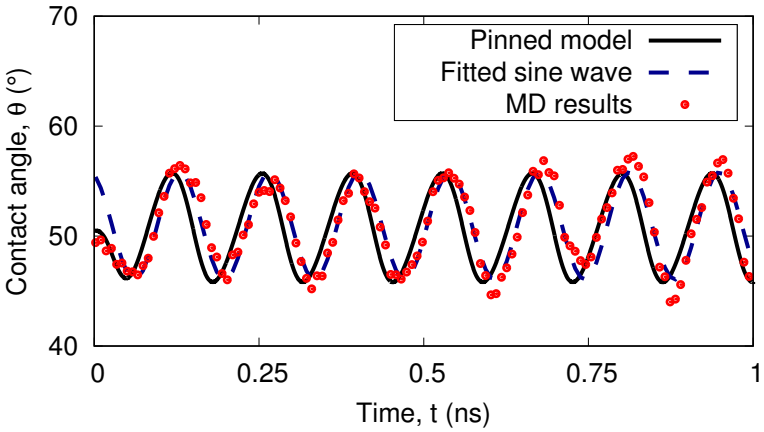


**(d)** $\Omega_d = 46\,\mathrm{rad/ns}$

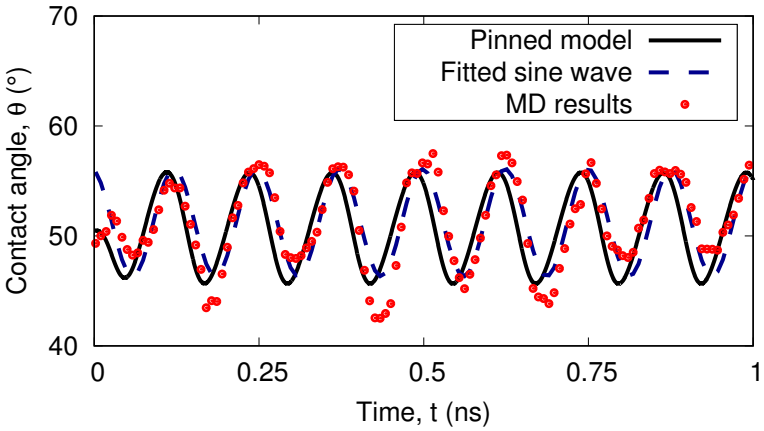


**(e)** $\Omega_d = 50\,\mathrm{rad/ns}$

**Figure B.1:** *Continued:* variation in contact angle with time for various pressure oscillation frequencies $\Omega_d$, as indicated in each graph. Figure continues on next page.

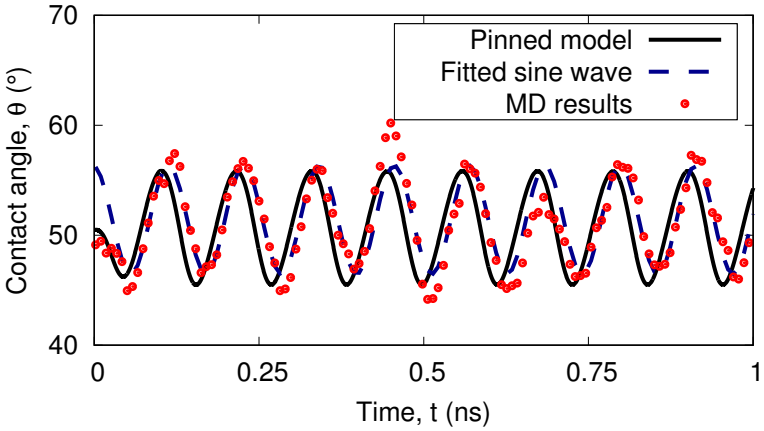


**(f)** $\Omega_d = 55\,\mathrm{rad/ns}$

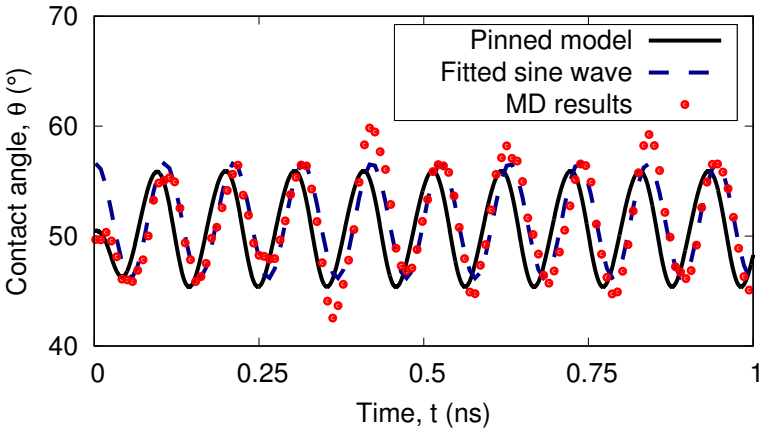


**(g)** $\Omega_d = 60\,\mathrm{rad/ns}$

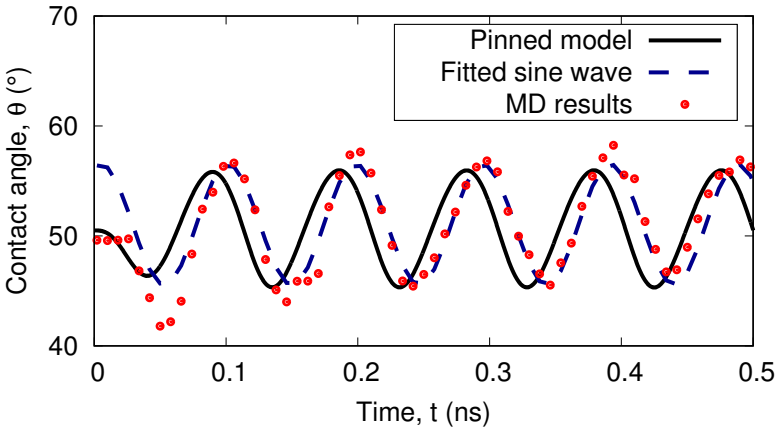


**(h)** $\Omega_d = 65\,\mathrm{rad/ns}$

**Figure B.1:** *Continued:* variation in contact angle with time for various pressure oscillation frequencies $\Omega_d$, as indicated in each graph. Figure continues on next page.

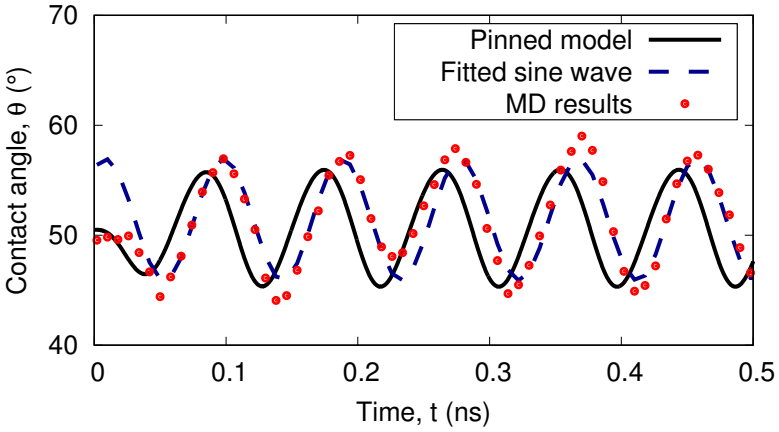


**(i)** $\Omega_d = 70\,\mathrm{rad/ns}$

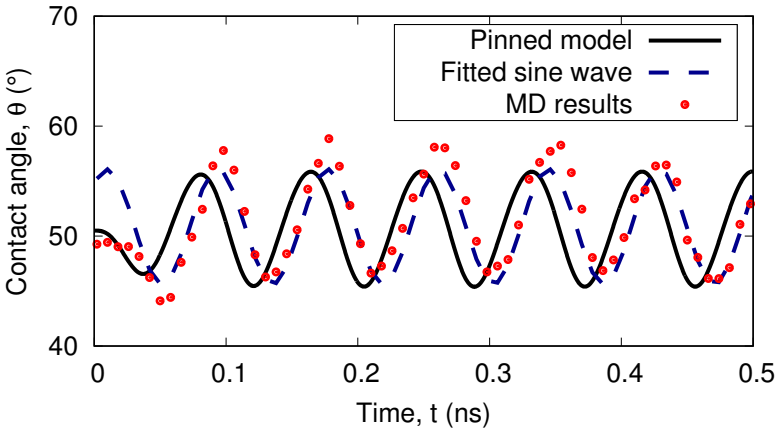


**(j)** $\Omega_d = 75\,\mathrm{rad/ns}$

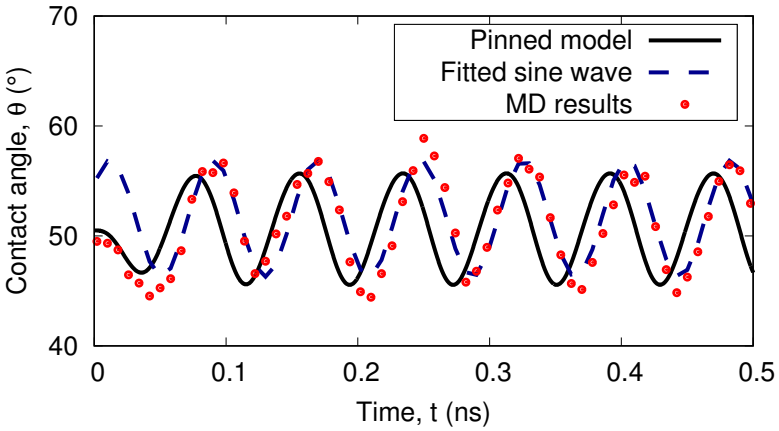


**(k)** $\Omega_d = 80\,\mathrm{rad/ns}$

**Figure B.1:** *Continued:* variation in contact angle with time for various pressure oscillation frequencies $\Omega_d$, as indicated in each graph. Figure continues on next page.

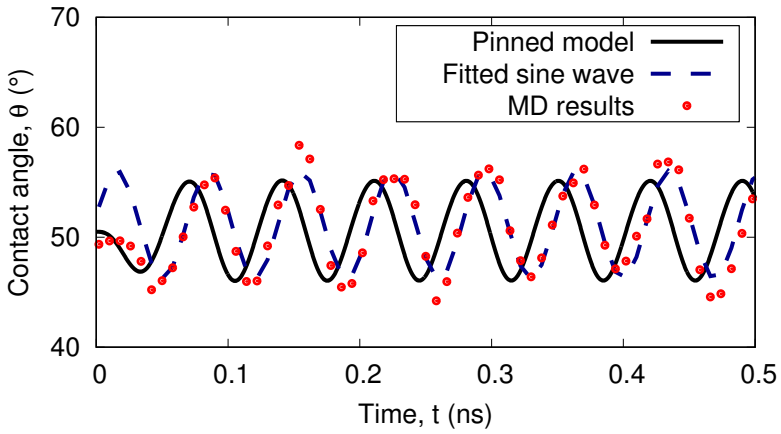


**(l)** $\Omega_d = 90\,\mathrm{rad/ns}$

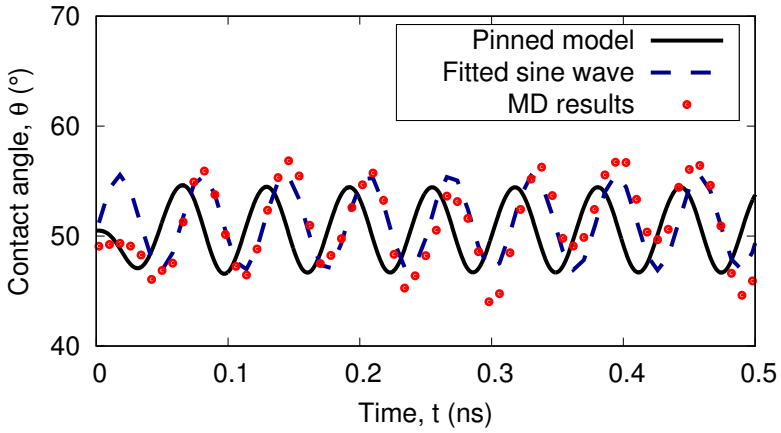


**(m)** $\Omega_d = 100\,\mathrm{rad/ns}$

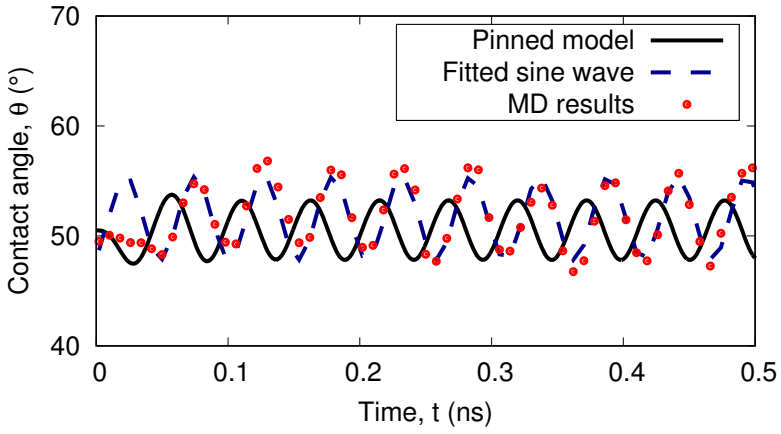


**(n)** $\Omega_d = 120\,\mathrm{rad/ns}$

**Figure B.1:** *Continued:* variation in contact angle with time for various pressure oscillation frequencies $\Omega_d$, as indicated in each graph.

# References


Abascal, J. L. F. and Vega, C. "A General Purpose Model for the Condensed Phases of Water: TIP4P/2005". *J. Chem. Phys.*, 123(23):234505, 2005.

Adhikari, U., Goliaei, A., and Berkowitz, M. L. "Mechanism of Membrane Poration by Shock Wave Induced Nanobubble Collapse: A Molecular Dynamics Study". *J. Phys. Chem. B*, 119 (20):6225–6234, 2015.

Adhikari, U., Goliaei, A., and Berkowitz, M. L. "Nanobubbles, cavitation, shock waves and traumatic brain injury". *Phys. Chem. Chem. Phys.*, 18:32638–32652, 2016.

Ahmar, E. E., Creton, B., Valtz, A., Coquelet, C., Lachet, V., Richon, D., and Ungerer, P. "Thermodynamic study of binary systems containing sulphur dioxide: Measurements and molecular modelling". *Fluid Phase Equilib.*, 304(1):21–34, 2011.

Akhatov, I., Lindau, O., Topolnikov, A., Mettin, R., Vakhitova, N., and Lauterborn, W. "Collapse and rebound of a laser-induced cavitation bubble". *Phys. Fluids*, 13(10):2805–2819, 2001.

Andersen, A. and Mørch, K. A. "Cavitation Nuclei in Water Exposed to Transient Pressures". *J. Fluid Mech.*, 771:424–448, 2015.

Atchley, A. A. and Prosperetti, A. "The Crevice Model of Bubble Nucleation". *J. Acoust. Soc. Am.*, 86(3):1065–1084, 1989.

Attard, P. "Pinning Down the Reasons for the Size, Shape, and Stability of Nanobubbles". *Langmuir*, 32(43):11138–11146, 2016.

Barber, B. P., Wu, C. C., Löfstedt, R., Roberts, P. H., and Putterman, S. J. "Sensitivity of sonoluminescence to experimental parameters". *Phys. Rev. Lett.*, 72:1380–1383, 1994.

Benjamin, T. B. and Ellis, A. T. "The Collapse of Cavitation Bubbles and the Pressures thereby Produced against Solid Boundaries". *Philos. Trans. R. Soc., A*, 260(1110):221–240, 1966.

Berendsen, H. J. C., Postma, J. P. M., van Gunsteren, W. F., DiNola, A., and Haak, J. R. "Molecular dynamics with coupling to an external bath". *J. Chem. Phys.*, 81(8):3684–3690, 1984.

Berendsen, H. J. C., Grigera, J. R., and Straatsma, T. P. "The missing term in effective pair potentials". *J. Phys. Chem.*, 91(24):6269–6271, 1987.

Berkelaar, R. P., Dietrich, E., Kip, G. A. M., Kooij, E. S., Zandvliet, H. J. W., and Lohse, D. "Exposing nanobubble-like objects to a degassed environment". *Soft Matter*, 10:4947–4955, 2014.

Berla, L. A., Lee, S. W., Ryu, I., Cui, Y., and Nix, W. D. "Robustness of amorphous silicon during the initial lithiation/delithiation cycle". *J. Power Sources*, 258:253–259, 2014.

Berthelot, M. "Sur Quelques Phenomemes de Dilation Force de Liquids". *Ann, Chimie Phys.*, 30:232–237, 1850.

Blake, F. G., Jr. "Onset of Cavitation in Liquids: I". Technical Memorandum 12, 1949.

Blake, J. R., Leppinen, D. M., and Wang, Q. "Cavitation and bubble dynamics: the Kelvin impulse and its applications". *Interface Focus*, 5(5):20150017, 2015.

Blue, J. E. "Resonance of a Bubble on an Infinite Rigid Boundary". *J. Acoust. Soc. Am.*, 41 (2):369–372, 1967.

Bolaños-Jiménez, R., Rossi, M., Fernandez Rivas, D., Kähler, C. J., and Marin, A. "Streaming flow by oscillating bubbles: quantitative diagnostics via particle tracking velocimetry". *J. Fluid Mech.*, 820:529–548, 2017.

Borg, M. K., Macpherson, G. B., and Reese, J. M. "Controllers for imposing continuum-to-molecular boundary conditions in arbitrary fluid flow geometries". *Mol. Simul.*, 36(10): 745–757, 2010.

Borg, M. K., Lockerby, D. A., and Reese, J. M. "The FADE mass-stat: A technique for inserting or deleting particles in molecular dynamics simulations". *J. Chem. Phys.*, 140(7):074110, 2014.

Borkent, B. M., Dammer, S. M., Schönherr, H., Vancso, G. J., and Lohse, D. "Superstability of Surface Nanobubbles". *Phys. Rev. Lett.*, 98:204502, 2007.

Borkent, B. M., Gekle, S., Prosperetti, A., and Lohse, D. "Nucleation threshold and deactivation mechanisms of nanoscopic cavitation nuclei". *Phys. Fluids*, 21(10):102003, 2009.

Bremond, N., Arora, M., Ohl, C.-D., and Lohse, D. "Cavitation on surfaces". *J. Phys.: Condens. Matter*, 17(45):S3603–S3608, 2005.

Brems, S., Hauptmann, M., Camerotto, E., Pacco, A., Kim, T.-G., Xu, X., Wostyn, K., Mertens, P., and De Gendt, S. "Nanoparticle Removal with Megasonics: A Review". *ECS J. Solid State Sci. Technol.*, 3(1):N3010–N3015, 2014.

Brennen, C. E. *Cavitation and Bubble Dynamics.* Cambridge University Press, 2013.

Brotchie, A. and Zhang, X. H. "Response of interfacial nanobubbles to ultrasound irradiation". *Soft Matter*, 7:265–269, 2011.

Caupin, F. and Herbert, E. "Cavitation in water: a review". *C. R. Phys.*, 7(9):1000–1017, 2006. Nucleation.

Chahine, G. L. and Hsiao, C.-T. "Modelling cavitation erosion using fluid–material interaction simulations". *Interface Focus*, 5(5):20150016, 2015.

Chakraborty, I. "Numerical modeling of the dynamics of bubble oscillations subjected to fast variations in the ambient pressure with a coupled level set and volume of fluid method". *Phys. Rev. E*, 99:043107, 2019.

Chakraborty, I., Biswas, G., and Ghoshdastidar, P. "A coupled level-set and volume-of-fluid method for the buoyant rise of gas bubbles in liquids". *Int. J. Heat Mass Transfer*, 58(1): 240–259, 2013.

Chan, C. U., Arora, M., and Ohl, C.-D. "Coalescence, Growth, and Stability of Surface-Attached Nanobubbles". *Langmuir*, 31(25):7041–7046, 2015.

Che, Z. and Theodorakis, P. E. "Formation, dissolution and properties of surface nanobubbles". *J. Colloid Interface Sci.*, 487:123–129, 2017.

Chen, Y.-X., Chen, Y.-L., and Yen, T.-H. "Investigating Interfacial Effects on Surface Nanobubbles without Pinning Using Molecular Dynamics Simulation". *Langmuir*, 34(50): 15360–15369, 2018.

Choubey, A., Vedadi, M., Nomura, K.-I., Kalia, R. K., Nakano, A., and Vashishta, P. "Poration of lipid bilayers by shock-induced nanobubble collapse". *Appl. Phys. Lett.*, 98(2):023701, 2011.

Coasne, B., Galarneau, A., Di Renzo, F., and Pellenq, R. J. M. "Molecular Simulation of Nitrogen Adsorption in Nanoporous Silica". *Langmuir*, 26(13):10872–10881, 2010.

Cosden, I. A. and Lukes, J. R. "Effect of Cutoff Radius on the Surface Tension of Nanoscale Bubbles". *J. Heat Transfer*, 133(10):101501, 2011.

Creux, P., Lachaise, J., Graciaa, A., and Beattie, J. K. "Specific Cation Effects at the Hydroxide-Charged Air/Water Interface". *J. Phys. Chem. C*, 111(9):3753–3755, 2007.

De Beer, M. and Maina, J. W. "Some fundamental definitions of the elastic parameters for homogenous isotropic linear materials in road design and analysis". In *Proceedings of the 27$^{th}$ Southern African Transport Conference (SATC 2008)*, 2008.

de Gennes, P. G. "Wetting: statics and dynamics". *Rev. Mod. Phys.*, 57:827–863, 1985.

Dear, J. P. and Field, J. E. "High-speed photography of surface geometry effects in liquid/solid impact". *J. Appl. Phys.*, 63(4):1015–1021, 1988.

Debenedetti, P. G. "Supercooled and glassy water". *J. Phys.: Condens. Matter*, 15(45):R1669–R1726, 2003.

Denner, F., Evrard, F., Serfaty, R., and van Wachem, B. G. "Artificial viscosity model to mitigate numerical artefacts at fluid interfaces with surface tension". *Comput. Fluids*, 143: 59–72, 2017.

Dockar, D., Borg, M. K., and Reese, J. M. "Mechanical Stability of Surface Nanobubbles". *Langmuir*, 35(29):9325–9333, 2019.

Ducker, W. A. "Contact Angle and Stability of Interfacial Nanobubbles". *Langmuir*, 25(16): 8907–8910, 2009.

Dular, M., Griessler-Bulc, T., Gutierrez-Aguirre, I., Heath, E., Kosjek, T., Klemenčič, A. K., Oder, M., Petkovšek, M., Rački, N., Ravnikar, M., Šarc, A., Širok, B., Zupanc, M., Žitnik, M., and Kompare, B. "Use of hydrodynamic cavitation in (waste)water treatment". *Ultrason. Sonochem.*, 29:577–588, 2016.

El Mekki Azouzi, M., Ramboz, C., Lenain, J.-F., and Caupin, F. "A coherent picture of water at extreme negative pressure". *Nat. Phys.*, 9:38–41, 2012.

Epstein, P. S. and Plesset, M. S. "On the Stability of Gas Bubbles in Liquid-Gas Solutions". *J. Chem. Phys.*, 18(11):1505–1509, 1950.

Fivel, M., Franc, J.-P., and Roy, S. C. "Towards numerical prediction of cavitation erosion". *Interface Focus*, 5(5):20150013, 2015.

Flannigan, D. J. and Suslick, K. S. "Plasma formation and temperature measurement during single-bubble cavitation". *Nature*, 434(7029):52–55, 2005.

Flannigan, D. J. and Suslick, K. S. "Inertially confined plasma in an imploding bubble". *Nat. Phys.*, 6(8):598–601, 2010.

Frenkel, Y. I. *Kinetic theory of liquids*. Dover, 1955.

Gelderblom, H., Zijlstra, A. G., van Wijngaarden, L., and Prosperetti, A. "Oscillations of a gas pocket on a liquid-covered solid surface". *Phys. Fluids*, 24(12):122101, 2012.

González, M. A., Valeriani, C., Caupin, F., and Abascal, J. L. F. "A comprehensive scenario of the thermodynamic anomalies of water using the TIP4P/2005 model". *J. Chem. Phys.*, 145 (5):054505, 2016.

Grady, D. "Shocks and structured waves". In *Physics of Shock and Impact, Volume 1*, 2053-2563, pages 1–1–1–103. IOP Publishing, 2017.

Green, M. S. "Markoff Random Processes and the Statistical Mechanics of Time-Dependent Phenomena. II. Irreversible Processes in Fluids". *J. Chem. Phys.*, 22(3):398–413, 1954.

Gupta, M. K., Sharma, D. S., and Lakhera, V. J. "Detachment forces on Spherical bubble during formation". *Mater. Today: Proc.*, 4(2, Part A):4130–4136, 2017. 5th International Conference of Materials Processing and Characterization (ICMPC 2016).

Han, B., Zhu, R., Guo, Z., Liu, L., and Ni, X.-W. "Control of the liquid jet formation through the symmetric and asymmetric collapse of a single bubble generated between two parallel solid plates". *Eur. J. Mech. B Fluids*, 72:114–122, 2018.

Harvey, E. N., Barnes, D. K., McElroy, W. D., Whiteley, A. H., Pease, D. C., and Cooper, K. W. "Bubble formation in animals. I. Physical factors". *J. Cell. Comp. Physiol.*, 24(1): 1–22, 1944.

Heymann, F. J. "High-Speed Impact between a Liquid Drop and a Solid Surface". *J. Appl. Phys.*, 40(13):5113–5122, 1969.

Hockney, R. W. and Eastwood, J. W. *Computer simulation using particles*. CRC Press, 1988.

Hoover, W. G. "Canonical dynamics: Equilibrium phase-space distributions". *Phys. Rev. A*, 31:1695–1697, 1985.

Huang, T.-W., Liu, S.-Y., Chuang, Y.-J., Hsieh, H.-Y., Tsai, C.-Y., Wu, W.-J., Tsai, C.-T., Mirsaidov, U., Matsudaira, P., Chang, C.-S., Tseng, F.-G., and Chen, F.-R. "Dynamics of hydrogen nanobubbles in KLH protein solution studied with in situ wet-TEM". *Soft Matter*, 9:8856–8861, 2013.

Huang, Y. C., Hammitt, F. G., and Mitchell, T. M. "Note on shock-wave velocity in high-speed liquid-solid impact". *J. Appl. Phys.*, 44(4):1868–1869, 1973.

Ishida, N., Inoue, T., Miyahara, M., and Higashitani, K. "Nano Bubbles on a Hydrophobic Surface in Water Observed by Tapping-Mode Atomic Force Microscopy". *Langmuir*, 16 (16):6377–6380, 2000.

Ivashchenko, V. I., Turchi, P. E. A., and Shevchenko, V. I. "Simulations of the mechanical properties of crystalline, nanocrystalline, and amorphous SiC and Si". *Phys. Rev. B*, 75: 085209, 2007.

J. H. Irving and J. G. Kirkwood. "The Statistical Mechanical Theory of Transport Processes. IV. The Equations of Hydrodynamics". *J. Chem. Phys.*, 18(6):817–829, 1950.

Janeček, J. "Long Range Corrections in Inhomogeneous Simulations". *J. Phys. Chem. B*, 110 (12):6264–6269, 2006.

Johnsen, E. and Colonius, T. "Numerical simulations of non-spherical bubble collapse". *J. Fluid Mech.*, 629:231–262, 2009.

Jorgensen, W. L., Chandrasekhar, J., Madura, J. D., Impey, R. W., and Klein, M. L. "Comparison of simple potential functions for simulating liquid water". *J. Chem. Phys.*, 79(2): 926–935, 1983.

Joseph, D. D. "Potential flow of viscous fluids: Historical notes". *Int. J. Multiphase Flow*, 32 (3):285–310, 2006.

Kapahi, A., Hsiao, C.-T., and Chahine, G. L. "Shock-Induced Bubble Collapse versus Rayleigh Collapse". *J. Phys.: Conf. Ser.*, 656:012128, 2015.

Keller, J. B. and Miksis, M. "Bubble oscillations of large amplitude". *J. Acoust. Soc. Am.*, 68 (2):628–633, 1980.

Kilymis, D., Gerard, C., and Pizzagalli, L. "Mechanical Properties of Amorphous Silicon Nanoparticles". In *TMS 2019 148th Annual Meeting & Exhibition Supplemental Proceedings*, pages 1347–1354, Cham, 2019. Springer International Publishing.

Kirova, E. M. and Norman, G. E. "Viscosity calculations at molecular dynamics simulations". *J. Phys.: Conf. Ser.*, 653:012106, 2015.

Kitchen, D. B., Hirata, F., Westbrook, J. D., Levy, R., Kofke, D., and Yarmush, M. "Conserving energy during molecular dynamics simulations of water, proteins, and proteins in water". *J. Comput. Chem.*, 11(10):1169–1180, 1990.

Klaseboer, E. and Khoo, B. C. "A modified Rayleigh–Plesset model for a non-spherically symmetric oscillating bubble with applications to boundary integral methods". *Eng. Anal. Bound. Elem.*, 30(1):59 –71, 2006.

Kornfeld, M. and Suvorov, L. "On the Destructive Action of Cavitation". *J. Appl. Phys.*, 15 (6):495–506, 1944.

Koukouvinis, P., Gavaises, M., Supponen, O., and Farhat, M. "Numerical simulation of a collapsing bubble subject to gravity". *Phys. Fluids*, 28(3):032110, 2016.

Kubo, R. "Statistical-Mechanical Theory of Irreversible Processes. I. General Theory and Simple Applications to Magnetic and Conduction Problems". *J. Phys. Soc. Jpn.*, 12(6):570–586, 1957.

Lauterborn, W., Lechner, C., Koch, M., and Mettin, R. "Bubble models and real bubbles: Rayleigh and energy-deposit cases in a Tait-compressible liquid". *J. Inst. Math. Its Appl.*, 83(4):556–589, 2018.

Leighton, T. G. "The inertial terms in equations of motion for bubbles in tubular vessels or between plates". *J. Acoust. Soc. Am.*, 130(5):3333–3338, 2011.

Leighton, T. G. "The Rayleigh–Plesset equation in terms of volume with explicit shear losses". *Ultrasonics*, 48(2):85–90, 2008.

Lemmon, E. W., McLinden, M. O., and Friend, D. G. *NIST Chemistry WebBook, NIST Standard Reference Database Number 69, Eds. P.J. Linstrom and W.G. Mallard.* National Institute of Standards and Technology, Gaithersburg, 20899, 2017.

Levi, B. G. "Skepticism Greets Claim of Bubble Fusion". *Phys. Today*, 55(4):16–18, 2002.

Li, J., Chen, H., Zhou, W., Wu, B., Stoyanov, S. D., and Pelan, E. G. "Growth of Bubbles on a Solid Surface in Response to a Pressure Reduction". *Langmuir*, 30(15):4223–4228, 2014.

Lohse, D. and Zhang, X. "Pinning and gas oversaturation imply stable single surface nanobubbles". *Phys. Rev. E*, 91:031003, 2015a.

Lohse, D. and Zhang, X. "Surface Nanobubbles and Nanodroplets". *Rev. Mod. Phys.*, 87: 981–1035, 2015b.

Lorentz, H. A. "Ueber die Anwendung des Satzes vom Virial in der kinetischen Theorie der Gase". *Ann. Phys. (Berlin, Ger.)*, 248(1):127–136, 1881.

Lou, S.-T., Ouyang, Z.-Q., Zhang, Y., Li, X.-J., Hu, J., Li, M.-Q., and Yang, F.-J. "Nanobubbles on Solid Surface Imaged by Atomic Force Microscopy". *J. Vac. Sci. Technol., B: Microelectron. Nanometer Struct.–Process., Meas., Phenom.*, 18(5):2573–2575, 2000.

Lukianova-Hleb, E. Y., Ren, X., Sawant, R. R., Wu, X., Torchilin, V. P., and Lapotko, D. O. "On-Demand Intracellular Amplification of Chemoradiation with Cancer-Specific Plasmonic nanobubbles". *Nat. Med.*, 20(7):778–784, 2014. Technical Report.

Lukianova-Hleb, E. Y., Kim, Y.-S., Belatsarkouski, I., Gillenwater, A. M., O'Neill, B. E., and Lapotko, D. O. "Intraoperative diagnostics and elimination of residual microtumours with plasmonic nanobubbles". *Nat. Nanotechnol.*, 11:525–532, 2016.

Maheshwari, S., van der Hoef, M., Zhang, X., and Lohse, D. "Stability of Surface Nanobubbles: A Molecular Dynamics Study". *Langmuir*, 32(43):11116–11122, 2016.

Maheshwari, S., van der Hoef, M., Rodríguez Rodríguez, J., and Lohse, D. "Leakiness of Pinned Neighboring Surface Nanobubbles Induced by Strong Gas-Surface Interaction". *ACS Nano*, 12(3):2603–2609, 2018.

Mahoney, M. W. and Jorgensen, W. L. "A five-site model for liquid water and the reproduction of the density anomaly by rigid, nonpolarizable potential functions". *J. Chem. Phys.*, 112 (20):8910–8922, 2000.

Man, V. H., Li, M. S., Derreumaux, P., and Nguyen, P. H. "Rayleigh-Plesset equation of the bubble stable cavitation in water: A nonequilibrium all-atom molecular dynamics simulation study". *J. Chem. Phys.*, 148(9):094505, 2018.

Martínez, L., Andrade, R., Birgin, E. G., and Martínez, J. M. "PACKMOL: A Package for Building Initial Configurations for Molecular Dynamics Simulations". *J. Comput. Chem.*, 30(13):2157–2164, 2009.

Martynov, S., Kostson, E., Saffari, N., and Stride, E. "Forced vibrations of a bubble in a liquid-filled elastic vessel". *J. Acoust. Soc. Am.*, 130(5):2700–2708, 2011.

Matsumoto, M. and Kataoka, Y. "Study on liquid–vapor interface of water. I. Simulational results of thermodynamic properties and orientational structure". *J. Chem. Phys.*, 88(5): 3233–3245, 1988.

Menzl, G., Gonzalez, M. A., Geiger, P., Caupin, F., Abascal, J. L. F., Valeriani, C., and Dellago, C. "Molecular Mechanism for Cavitation in Water Under Tension". *Proc. Natl. Acad. Sci. U. S. A.*, 113(48):13582–13587, 2016.

Miller, D. L. and Nyborg, W. L. "Theoretical investigation of the response of gas-filled micropores and cavitation nuclei to ultrasound". *J. Acoust. Soc. Am.*, 73(5):1537–1544, 1983.

Minnaert, M. "XVI. On musical air-bubbles and the sounds of running water". *London, Edinburgh Dublin Philos. Mag. J. Sci.*, 16(104):235–248, 1933.

Molinero, V. and Moore, E. B. "Water Modeled As an Intermediate Element between Carbon and Silicon". *J. Phys. Chem. B*, 113(13):4008–4016, 2009.

Nagashima, H., Tsuda, S., Tsuboi, N., Hayashi, A. K., and Tokumasu, T. "A molecular dynamics study of nuclear quantum effect on diffusivity of hydrogen molecule". *J. Chem. Phys.*, 147(2):024501, 2017.

Nosé, S. "A unified formulation of the constant temperature molecular dynamics methods". *J. Chem. Phys.*, 81(1):511–519, 1984.

Obara, T., Bourne, N. K., and Field, J. E. "Liquid-jet impact on liquid and solid surfaces". *Wear*, 186-187:388–394, 1995. 8th International Conference on Erosion by Liquid and Solid Impact.

Padrino, J. C. and Joseph, D. D. "Correction of Lamb's dissipation calculation for the effects of viscosity on capillary-gravity waves". *Phys. Fluids*, 19(8):082105, 2007.

Pallares, G., El Mekki Azouzi, M., González, M. A., Aragones, J. L., Abascal, J. L. F., Valeriani, C., and Caupin, F. "Anomalies in bulk supercooled water at negative pressure". *Proc. Natl. Acad. Sci. U. S. A.*, 111(22):7936–7941, 2014.

Pallares, G., Gonzalez, M. A., Abascal, J. L. F., Valeriani, C., and Caupin, F. "Equation of state for water and its line of density maxima down to $-120$ MPa". *Phys. Chem. Chem. Phys.*, 18:5896–5900, 2016.

Perumanath, S., Borg, M. K., Chubynsky, M. V., Sprittles, J. E., and Reese, J. M. "Droplet Coalescence is Initiated by Thermal Motion". *Phys. Rev. Lett.*, 122:104501, 2019.

Philipp, A. and Lauterborn, W. "Cavitation erosion by single laser-produced bubbles". *J. Fluid Mech.*, 361:75–116, 1998.

Plesset, M. S. "The dynamics of cavitation bubbles". *J. Appl. Mech.*, 16:277–282, 1949.

Plesset, M. S. and Prosperetti, A. "Bubble Dynamics and Cavitation". *Annu. Rev. Fluid Mech.*, 9(1):145–185, 1977.

Plimpton, S. "Fast Parallel Algorithms for Short-Range Molecular Dynamics". *J. Comput. Phys.*, 117(1):1–19, 1995.

Prosperetti, A. "Linear oscillations of constrained drops, bubbles, and plane liquid surfaces". *Phys. Fluids*, 24(3):032109, 2012.

Prosperetti, A. "The thermal behaviour of oscillating gas bubbles". *J. Fluid Mech.*, 222:587–616, 1991.

Prosperetti, A. "Thermal effects and damping mechanisms in the forced radial oscillations of gas bubbles in liquids". *J. Acoust. Soc. Am.*, 61(1):17–27, 1977.

Ramisetti, S. B., Borg, M. K., Lockerby, D. A., and Reese, J. M. "Liquid slip over gas nanofilms". *Phys. Rev. Fluids*, 2:084003, 2017.

Saltmarsh, M. J. and Shapira, D. "Questions Regarding Nuclear Emissions in Cavitation Experiments". *Science*, 297(5587):1603, 2002.

Sander, R. *NIST Chemistry WebBook, NIST Standard Reference Database Number 69, Eds. P.J. Linstrom and W.G. Mallard.* National Institute of Standards and Technology, Gaithersburg, 20899, 2017.

Seddon, J. R. T., Lohse, D., Ducker, W. A., and Craig, V. S. J. "A deliberation on nanobubbles at surfaces and in bulk". *ChemPhysChem*, 13(8):2179–2187, 2012.

Shampine, L. F. and Reichelt, M. W. "The MATLAB ODE Suite". *SIAM J. Sci. Comput*, 18 (1):1–22, 1997.

Shekhar, A., Nomura, K.-I., Kalia, R. K., Nakano, A., and Vashishta, P. "Nanobubble Collapse on a Silica Surface in Water: Billion-Atom Reactive Molecular Dynamics Simulations". *Phys. Rev. Lett.*, 111:184503, 2013.

Shi, B., Sinha, S., and Dhir, V. K. "Molecular dynamics simulation of the density and surface tension of water by particle-particle particle-mesh method". *J. Chem. Phys.*, 124(20): 204715, 2006.

Stillinger, F. H. and Weber, T. A. "Computer simulation of local order in condensed phases of silicon". *Phys. Rev. B*, 31:5262–5271, 1985.

Stride, E. and Saffari, N. "Microbubble ultrasound contrast agents: A review". *Proc. Inst. Mech. Eng., Part H*, 217(6):429–447, 2003.

Stukowski, A. "Visualization and Analysis of Atomistic Simulation Data with OVITO–the Open Visualization Tool". *Modell. Simul. Mater. Sci. Eng.*, 18(1):015012, 2010.

Supponen, O., Obreschkow, D., Tinguely, M., Kobel, P., Dorsaz, N., and Farhat, M. "Scaling laws for jets of single cavitation bubbles". *J. Fluid Mech.*, 802:263–293, 2016.

Supponen, O., Obreschkow, D., Kobel, P., Tinguely, M., Dorsaz, N., and Farhat, M. "Shock waves from nonspherical cavitation bubbles". *Phys. Rev. Fluids*, 2:093601, 2017.

Suslick, K. S. and Price, G. J. "Applications of ultrasound to materials chemistry". *Annu. Rev. Mater. Sci.*, 29(1):295–326, 1999.

Taleyarkhan, R. P., West, C. D., Cho, J. S., Lahey, R. T., Nigmatulin, R. I., and Block, R. C. "Evidence for Nuclear Emissions During Acoustic Cavitation". *Science*, 295(5561):1868–1873, 2002.

Theodorakis, P. E. and Che, Z. "Surface nanobubbles: Theory, simulation, and experiment. A review". *Adv. Colloid Interface Sci.*, 272:101995, 2019.

Thomas, J. D., Liu, C. M., Flachskampf, F. A., O'Shea, J. P., Davidoff, R., and Weyman, A. E. "Quantification of jet flow by momentum analysis. An in vitro color Doppler flow study.". *Circulation*, 81(1):247–259, 1990.

Trilling, L. "The Collapse and Rebound of a Gas Bubble". *J. Appl. Phys.*, 23(1):14–17, 1952.

Tsuda, S., Hyodo, H., and Watanabe, S. "Validation of Bubble Dynamics Equation for a Nano-scale Bubble via Molecular Dynamics Simulation". *J. Phys.: Conf. Ser.*, 656:012039, 2015.

Tyrrell, J. W. G. and Attard, P. "Images of Nanobubbles on Hydrophobic Surfaces and Their Interactions". *Phys. Rev. Lett.*, 87:176104, 2001.

Vedadi, M., Choubey, A., Nomura, K., Kalia, R. K., Nakano, A., Vashishta, P., and van Duin, A. C. T. "Structure and Dynamics of Shock-Induced Nanobubble Collapse in Water". *Phys. Rev. Lett.*, 105:014503, 2010.

Vincent, O. and Marmottant, P. "On the statics and dynamics of fully confined bubbles". *J. Fluid Mech.*, 827:194–224, 2017.

Vink, R. L. C., Barkema, G. T., van der Weg, W. F., and Mousseau, N. "Fitting the Stillinger–Weber potential to amorphous silicon". *J. Non-Cryst. Solids*, 282(2):248–255, 2001.

Vokurka, K. "Comparison of Rayleigh's, Herring's, and Gilmore's Models of Gas Bubbles". *Acta Acust. Acust.*, 59(3):214–219, 1986.

Wang, F.-C. and Wu, H.-A. "Pinning and depinning mechanism of the contact line during evaporation of nano-droplets sessile on textured surfaces". *Soft Matter*, 9(24):5703–5709, 2013.

Weijs, J. H., Marchand, A., Andreotti, B., Lohse, D., and Snoeijer, J. H. "Origin of line tension for a Lennard-Jones nanodroplet". *Phys. Fluids*, 23(2):022001, 2011.

Weijs, J. H., Seddon, J. R. T., and Lohse, D. "Diffusive Shielding Stabilizes Bulk Nanobubble Clusters". *ChemPhysChem*, 13(8):2197–2204, 2012a.

Weijs, J. H., Snoeijer, J. H., and Lohse, D. "Formation of Surface Nanobubbles and the Universality of Their Contact Angles: A Molecular Dynamics Approach". *Phys. Rev. Lett.*, 108:104501, 2012b.

Weller, H. G., Tabor, G., Jasak, H., and Fureby, C. "A tensorial approach to computational continuum mechanics using object-oriented techniques". *Comput. Phys.*, 12(6):620–631, 1998.

Zabolotskaya, E. and Soluyan, S. "Emission of harmonic and combination-frequency waves by bubbles". *Acoust. Phys.*, 18(3):396–398, 1973.

Zambrano, H. A., Walther, J. H., and Jaffe, R. L. "Molecular Dynamics Simulations of Water on a Hydrophilic Silica Surface at High Air Pressures". *J. Mol. Liq.*, 198:107–113, 2014.

Zhang, S. and Duncan, J. H. "On the nonspherical collapse and rebound of a cavitation bubble". *Phys. Fluids*, 6(7):2352–2362, 1994.

Zhang, X., Uddin, M. H., Yang, H., Toikka, G., Ducker, W., and Maeda, N. "Effects of Surfactants on the Formation and the Stability of Interfacial Nanobubbles". *Langmuir*, 28 (28):10471–10477, 2012.

Zhang, X. H., Maeda, N., and Craig, V. S. J. "Physical Properties of Nanobubbles on Hydrophobic Surfaces in Water and Aqueous Solutions". *Langmuir*, 22(11):5025–5035, 2006.

Zhang, X. H., Quinn, A., and Ducker, W. A. "Nanobubbles at the Interface between Water and a Hydrophobic Solid". *Langmuir*, 24(9):4756–4764, 2008.

Zienkiewicz, O., Taylor, R., and Nithiarasu, P. *The Finite Element Method for Fluid Dynamics (Seventh Edition)*. Butterworth-Heinemann, 2014.